University of Trento

University of Brescia

University of Padova

University of Trieste

University of Udine

University IUAV of Venezia

Anil Kumar

INVESTIGATION OF THE DYNAMIC PERFORMANCE OF A CABLE-STAYED FOOTBRIDGE

Tutor: Prof. Oreste S. Bursi

April, 2011

UNIVERSITY OF TRENTO

Structural Engineering - Modelling, Preservation and Control of Materials and Structures

Cycle: XXIII

Head of the Doctoral School: Prof. Davide Bigoni

Board of Examiners:

Prof. Maurizio Piazza (Università degli Studi di Trento)

Prof. Joan Ramon Casas (Universitat Politecnica de Catalunya)

Prof. Francesco Marotti de Sciarra (Università degli Studi di Napoli – Federico II)

SUMMARY

The developments in conceptual design, material technology and efficient construction techniques enabled the creation of longer, lighter, slender and stylish Cable-Stayed Foot Bridges (CSFB). Hence, modern CSFB can be characterized by interacting phenomena like cable nonlinearities, deck dynamic instability and deck lateral oscillations due to pedestrian walking. These phenomena, if intertwined, may bring these structures out of service or to failure. In view of a better performance, additional damping can be provided by passive dampers. However, amplitude dependent behaviour of dampers and slip in connections can make them effective only above a threshold amplitude. Hence, due to high uncertainties in the complex CSFB-damper system, usually, dynamic tests are performed to investigate the performance of the overall system.

In this thesis, the effectiveness of the passive vibration reduction system in a complex cable-stayed footbridge characterised by two curved decks was investigated. The amplitude dependent behaviour was found both with the output-only ambient vibration and free decay tests. In order to clarify these outcomes, modal quantities were calculated instantaneously, based on time-frequency identification techniques. A thorough analysis of dynamic response signals revealed that the structure with dampers actually behaved like a threshold system: i) for low vibration levels the dampers were still, so that they performed as constraints that stiffened the structure; ii) for high vibration levels, the dampers became fully working. Moreover, a deck-cable interaction between one of the longest cables and the first global mode was detected. Initially, the modal properties estimated from the dynamic tests did not match those of the numerical model. In order to have a robust FE model capable to simulate the actual behaviour of the footbridge, model updating was performed. The sensitivity-based model updating techniques and Powell's Dog-Leg method of optimisation based on the Trust-Region approach were used. The final updated model showed a considerable reduction in the percentage error of frequencies. The updated model was able to reproduce the response of the footbridge under actual wind conditions. The revealed cable-deck interaction phenomenon was a motivation to investigate in depth the dynamics of long stay cables. Therefore, efforts were made towards the identification of the nonlinear behaviour of stay cables from measured response data. In view of the fact that actual measured data contained the response of a MDoF system, the first step in this direction was to investigate the feasibility of the nonlinear identification method, i.e. a non-parametric approach applied to a SDoF cable system. The results revealed a good fitting between identified and numerical data, where only a cubic type of nonlinearity was identified. Moreover, an increase of the parameter related to damping and a decrease of the parameter relevant to linear-frequency were observed versus the loading amplitude. However, the values of the parameters stabilised at higher load amplitudes and superharmonics were present in the response. The proposed non-parametric method exhibited a good capability in the nonlinear parameter identification of cables.

Approaching towards a more complete understanding of the performance of cable-stayed footbridges, it was realized that the modern footbridges are more prone to pedestrian-induced vibrations that, eventually, degrades their serviceability performance. Moreover, several researchers tried to investigate the problem of synchronous lateral excitation of footbridges, but

there is no general consensus on pedestrian models. Therefore, a model of pedestrian-footbridge interaction was proposed. In detail, pedestrian was represented by a modified hybrid Van der Pol/Rayleigh (MHVR) self-sustained oscillator. Amplitude, stability and phase of the MHVR oscillator solution under a harmonic external force associated with the floor motion were analytically evaluated by the harmonic balance method and was compared with numerical results. It was shown that the phase difference tended to become constant at high excitation amplitudes. Moreover, the stability domain was found useful in predicting the percentage of pedestrians synchronized to a given oscillating floor. The numerical results of MHVR oscillator was, then, compared with the experimental result of a shake table with harmonic floor motion. A good agreement in amplitude ratio was found, however, the phase difference resulted to be underestimated by the MHVR model.

To my beloved parents
LALITA & RAMASHANKER

ACKNOWLEDGEMENTS

I would like to express my deepest gratitude and thanks to Professor Oreste S. Bursi for his constant encouragement, guidance, kindness and his patience with me. I feel honoured to be the student of Prof. Bursi.

Second, I would like to give my deep thanks to Dr. Silvano Erlicher (Ecole Nationale des Ponts et Chaussees,-ENPC- France) and Dr. Rosario Ceravolo (Politecnico di Torino, Italy) for helping me with their experiences and knowledge in the course of my research work. Here, I would like to thank also to my colleagues Mr. Philippe Pecol from ENPC and Mr. Luca Zanotti Fragonara from the Politecnico di Torino, with whom I developed some of the parts of my research work.

I also owe my sincere gratitude to my colleagues in Trento, Dr. Alessio Bonelli, Dr. Nicola Tondini, Dr. Fabio Ferrario, Dr. Marco Molinari, Mr. Stefano Francescotti, Mr. Shahin Reza, Mr. Zhen Wang, Mr. Giuseppe Abbiati, Ms. Alessia Ussia and Mr. Yue Yanchao for the help, suggestions and good time spent together. Here, I would also like to remember my past colleague and friend Dr. Huayong Wu for good time spent together and discussions made on various topics.

Moreover, I want to remember all the nice people I met during my PhD career.

Finally, I am grateful to my beloved parents and family for their love and blessings in my endeavour.

CONTENTS

LIST OF FIGURES

LIST OF TABLES

CHAPTER 1

INTRODUCTION

Bridges are indispensable components of the infrastructure of modern society. They are of many different types, e.g. beam, arch, cantilever, suspension, cable-stayed etc., depending on application and design. Compared to other bridge types, the cable-stayed bridges (CSB) are optimal for spans longer than typically seen in cantilever bridges and shorter than those typically requiring a suspension bridge. Cable-stayed bridges mainly consist of cables, pylons and girders (bridge decks).

Due to their aesthetic appearance, efficient utilization of structural materials and other notable advantages, cable-stayed bridges have gained much popularity in recent decades. Nowadays, as their properties have been more fully understood, very long span slender cable-stayed bridges are being built, and the ambition is to further increase the span length and use shallower and more slender girders for future bridges. Bridges of this type are entering a new era with main span lengths reaching 1000 m, e.g. Sutong CSB in China spans 1088 m (Janjic). This fact is due to the relatively small size of the substructures required, the development of efficient construction techniques and the rapid progress in the analysis and design of this type of bridges. They have recently proved to be highly cost-effective for short to medium spans.

Cable-stayed bridges with modern distinctive styles are increasing in number worldwide. These bridges are now built in more unusual styles for structural and aesthetic/architectural reasons (Menn, 1996; Rito, 1996). Some of the examples include the Lerez Bridge (Troyano et al., 1998)- a single inclined tower bridge; the Katsushika Harp Bridge (Takenouchi, 1998)- with a single pylon and S shaped deck; the Marian Bridge (Kominek, 1998)- with a single L-shaped pylon; the Alamillo Bridge (Casas,

1995)- with a single inclined pylon; the Safti Link Bridge (Brownjohn and Xia, 2000)- which has a curved deck and single offset pylon; circular cable stayed footbridge (Rebelo et al., 2010) and twin curved deck footbridges (Gentile et al., 2004; Tondini et al., 2010). The unique structural styles of these bridges beautify the environment, however, add to the difficulties in accurate structural analysis due to their complex shape. It is, therefore necessary to perform experimental identification tests to measure the actual dynamic properties, for e.g. resonant frequency, mode shape and modal damping, of the bridges to understand better their dynamic behavior. These measured properties can be used to correct and update numerical FE model to better reflect the reality. The updated FE model can be useful to predict the damage and safety conditions of the bridge under the extreme loading events, such as typhoon or earthquake.

For cable supported bridges and in particular long span cable-stayed bridges, energy dissipation is very low and is often not enough on its own to suppress vibrations (Forsterling and Furtner, 2004; Hikami, 1986). To increase the overall damping capacity of the bridge structure, one possible option is to incorporate external dampers, i.e. discrete damping devices such as viscous dampers and MR dampers, into the system. Such devices are frequently used nowadays for cable supported bridges. However, it is not believed that this is always the most effective and the most economic solution. Therefore, a great deal of research is needed to investigate the damping capacity of modern cable-stayed bridges and to find new alternatives to increase the overall damping of the bridge structure. Moreover, it is deemed necessary to investigate the effectiveness of the dampers after installing on the bridge.

Modern cable-stayed bridges exhibit geometrically nonlinear behaviour, they are very flexible and undergo large displacements before attaining their equilibrium configuration. Stay cables impart major part of the geometrical nonlinearity in the global dynamics; a well known deck-cable interaction phenomenon was reported by several researchers in cable-stayed footbridges (Caetano et al., 2000, 2008). To identify the nonlinear behaviour of the cables from the response data, special techniques are required.

The recent developments in material technology and efficient construction techniques enable the construction of not only longer but also lighter and more slen-

der footbridges. Therefore, the modern cable-stayed footbridges have become more prone to vibrations due to the wind and pedestrian actions. The very large amplitude lateral vibrations of Millenium bridge (Dallard et al., 2001a) decks on its opening day 10 June 2000, has realized the complexity of the serviceability problems in pedestrian-footbridge interaction. Several researchers have introduced models to explain the phenomenon of synchronous lateral excitation of footbridges, but there is no consensus on the general applicability of these models. Hence, there is still effort to model the pedestrian-footbridge behaviour in order to understand this complex phenomenon.

1.1 Objectives of the research

As discussed in the previous section, modern cable-stayed bridges are made in distinctive styles, that adds complexity to the structure. However, flexible, slender and lighter CSB are more prone to wind- and pedestrian- induced vibrations. A performance-based approach of cable-stayed footbridges requires the consideration of both ultimate as well as serviceability limit states. Even though a footbridge may be endowed with a robust design against failure, serviceability problems may arise from many sources, such as wind, pedestrians, nonlinear behaviour of cables and their interaction to the deck, ineffectiveness of damper system, etc. A more complete approach towards the investigation of the performance of a cable-stayed footbridge was considered in this thesis.

In brief, this thesis aims to investigate in depth several issues crucial to the performance of cable-stayed footbridges. In particular, it focusses on the: i) investigation of the effectiveness of the vibration reduction system in a complex cable-stayed footbridge characterised by two curved decks; ii) model updating of the ‘Ponte del mare’ footbridge in Pescara, Italy; iii) nonliner-identification of stay cables; and iv) modelling of the synchronous lateral excitation phenomenon for the pedestrian-footbridge interaction.

1.2 Structure of the thesis

This thesis presents the research work performed by the author on the system identification and pedestrian-induced vibration of cable-stayed footbridges. The research was sponsored by “HITUBES: Design and Integrity Assessment of High Strength Tubular Structures for Extreme Loading Conditions”- a Research Fund for Coal and Steel (RFCS) funded project of the European Commission to the University of Trento.

The second chapter provides the state of the art on the dynamic response of cable-stayed footbridges (CSFB). As the CSFB are mainly subjected to wind and pedestrian loadings in their everyday life, the review focuses on the dynamic response of the CSFB due to wind and anthropic actions. Moreover, it also discusses some damping system applicable to the main deck as well as stay cables.

Structural identification techniques are summarised in chapter 3. Both linear and nonlinear techniques are reviewed. Then, techniques relevant to cable-stayed footbridges are described.

In chapter 4, the design and outcomes of the dynamic identification tests of the ‘Ponte del mare’ footbridge are described. Moreover, the instantaneous identification is performed in order to investigate the effectiveness of the installed dampers.

The model updating is carried out on the FE model in view of the measured identification data in chapter 5. The updated model is used to simulate the actual behaviour of the footbridge under a measured wind excitation.

In chapter 6, the numerical analysis is carried out to investigate the applicability of time-frequency techniques for the nonlinear identification of cables.

The pedestrian-footbridge behaviour is analytically modelled and numerical comparisons are made in chapter 7.

The main findings of the thesis are summarised in chapter 8, where the conclusions of the research are underlined together with future perspectives.

CHAPTER 2

DYNAMIC RESPONSE OF CABLE-STAYED FOOTBRIDGES: A STATE-OF-THE-ART

2.1 Introduction

Footbridges are mainly subjected to the action of the wind and pedestrians in their everyday life. This chapter reviews the literature concerning the three aspects of the cable-stayed footbridges (CSB): i) dynamic response due to the wind; ii) dynamic response due to pedestrians; and iii) vibration reduction techniques for cable-stayed footbridges. Factors affecting the behaviour of bridges are discussed, both due to the wind and pedestrians. Finally, some vibration reduction techniques are reviewed.

Although, the general theories of highway bridges can be applied also to the footbridges in case of wind loadings, however cable-stayed footbridges can be differentiated to the cable-stayed highway bridges in the sense that footbridges are more slender and lower static weight and subjeted to a different traffic, i.e. pedestrians.

2.2 Dynamic response due to the wind

2.2.1 Wind loading phenomena

The criteria for the design of long spanned cable-stayed bridges are concerned with the static and dynamic responses of the bridge under wind loading. The design of long span bridges is often governed by aeroelastic instability. Aerodynamic design involves calculation of the critical velocity for the onset of flutter. It is to be ensured that the wind velocity does not exceed the predicted critical velocity to avoid failure due to flutter (Selvam and Govindaswamy, 2001). A list of bridges failure due to the wind can be found in (Rutz and Rens, 2007).

Arrol and Chatterjee (Arrol and Chatterjee, 1981) mention that designers should remember that the position of maximum stress would not always be at mid-span, or a support, and the stress value will depend upon the mode shape. In a simply supported span the second mode maximum stress is at the quarter points and will have a value four times that of the fundamental mode maximum stress, occurring at mid span.

When designing a bridge, one has to take into account the wind effects on the structure. Wind loading can be categorised into two categories; Static and dynamic wind loading. Static wind load is the most basic wind effect considered when designing a structure. For bridges, the static behaviour is less critical to the dynamic effects. There are many types of dynamic wind load. The one that will be addressed are buffeting, vortex shedding, galloping, torsional divergence, and flutter.

Dynamic behavior includes the responses due to vortex shedding excitation, self-excited oscillations and buffeting by wind turbulence (Selvam, 1998). Bridges could oscillate in two natural modes, vertical and torsional. In the vertical mode, all joints at any cross-section move the same distance in the vertical plane, while in the torsional mode every cross-section rotates about a longitudinal axis parallel to the roadway.

Unlike the static behavior, the dynamic behavior is critical and important to be considered during design. A basic knowledge of the wind forces that are required to

understand the issues involved in the design is explained in the following sub-section.

2.2.1.1 Aeroelastic Instability

Aeroelasticity is the discipline concerned with the study of phenomena wherein the aerodynamic forces and structural motions interact significantly. When a structure is subjected to wind flow, it may vibrate or suddenly deflect in the airflow. This structural motion results in a change in the flow pattern around the structure. If the modification of wind pattern around the structure by aerodynamic forces is such that it increases rather than decreasing the vibration, thereby giving rise to succeeding deflections of oscillatory and/or divergent character, aeroelastic instability is said to occur (Simiu and Scanlan, 1996). The aeroelastic phenomena that are considered in wind engineering are vortex shedding, torsional divergence, galloping, flutter and buffeting.

Vortex Shedding

Simiu and Scanlan (Simiu and Scanlan, 1996) state that when a body is subjected to wind flow, the separation of flow occurs around the body. This produces force on the body, a pressure force on the windward side and a suction force on the leeward side. The pressure and suction forces result in the formation of vortices in the wake region causing structural deflections on the body. The shedding of vorticity balances the change of fluid momentum along the entire body surface. The shed vortices are convected downwind by local mean wind speed and viscous diffusion but will also interact to form large-scale coherent structures. The frequency in which the vortices are shed dictates the structural response. The structural member acts as if rigidly fixed, when the frequency of vortex shedding (also called wake frequency) is not close to the natural frequency of the member. On the other hand, when the vortex-induced and the natural-frequencies coincide, the resulting condition is called lock-in. During lock-in condition, the structural member oscillates with increased amplitude but rarely exceeding half of the across wind dimension of the body (Simiu and Scanlan, 1996). The lock-in condition is illustrated in Figure 2.1.

In the Figure 2.1, we see that the wake frequency remains locked to that of natural frequency for a range of wind velocities. As the velocity further increases, the wake frequency will again break away from the natural frequency. The extent of the shedding depends on the Reynolds number (Re) and Strouhal number (S_t), which is

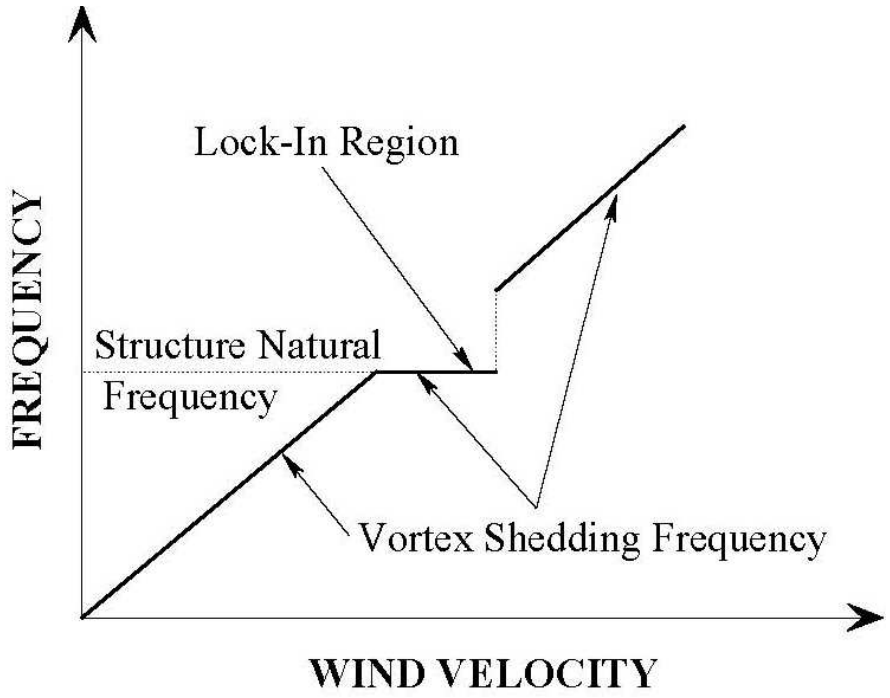

Figure 2.1: Qualitative trend of vortex shedding frequency with wind velocity during lock-in (after Simiu and Scanlan 1996)

defined as:

$$\text{Re} = \frac{\rho UD}{\mu} \tag{2.1}$$

$$S_t = \frac{N_s D}{U} \tag{2.2}$$

where, ρ = wind density, U = wind velocity, D = diameter, μ = viscosity, and Ns = frequency of vortex cycle shedding.

For a very low Reynolds number (Selvam and Govindaswamy, 2001; Simiu and Scanlan, 1996) the flow remains the same, just circumventing the obstruction on its way. For higher Reynolds numbers, the flow starts to separate around the edges of the obstruction and vortices are generated in the immediate wake of the obstruction. Thereafter further increase in the Reynolds number causes the creation of cyclically alternating vortices and they are carried over with the flow downstream. From there on, the inertial effects become dominant over the viscous effects and turbulence sets in, resulting in shear of the flow. So this reasonably illustrates the vorticity phenomenon starting from a smooth and low speed flow to a turbulent and high-speed flow.

Galloping

Simiu and Scanlan (Simiu and Scanlan, 1996) state that galloping is an instability typical of slender structures. This is a relatively low-frequency oscillatory phenomenon of elongated, bluff bodies acted upon by a wind stream. The natural structural frequency at which the bluff object responds is much lower than the frequency of vortex shedding. It is in this sense that galloping may be considered a low-frequency phenomenon. There are two types of galloping: Wake and Across-wind.

Wake galloping: It is considered of two cylinders one windward, producing a wake, and one leeward, within that wake separated at a few diameters distance away from each other. In wake galloping the downstream cylinder is subjected to galloping oscillations induced by the turbulent wake of the upstream cylinder. Due to this, the upstream cylinder tends to rotate clockwise and the downstream cylinder, anti-clockwise thus inducing torsional oscillations.

Across wind galloping: Across wind galloping in a bridge, is an instability that is initiated by a turbulent wind blowing transversely across the deck. Across-wind galloping causes a crosswise vibration in the bridge deck (Liu, 1991). As the section vibrates crosswise in a steady wind velocity (*U*), the relative velocity changes, thereby changing the angle of attack (α). Due to the change in α, an increase or decrease on the lift force of the cylinder occurs. If an increase of α causes an increase in the lift force in the opposite direction of motion, the situation is stable. But on the other hand if the vice versa occurs, i. e., an increase of α causes a decrease in lift force, then the situation is unstable and galloping occurs.

Torsional divergence

Torsional divergence is an instance of a static response of a structure. Torsional divergence was at first associated with aircraft wings due to their susceptibility to twisting off at excessive air speeds (Simiu and Scanlan, 1996). Liu (Liu, 1991), reports that when the wind flow occurs, drag, lift, and moment are produced on the structure. This moment induces a twist on the structure and causes the angle of incidence α to increase. The increase in α results in higher torsional moment as the wind velocity increases. If the structure does not have sufficient torsional stiffness to resist this increasing moment, the structure becomes unstable and will be twisted to failure. Simiu and Scanlan (Simiu and Scanlan, 1996) report that the phenomenon depends upon structural flexibility and the manner in which the aerodynamic moments develop with twist; it does not depend upon ultimate strength. They say that in most cases the critical divergence velocities are extremely high, well beyond the range of velocities normally considered in design.

Flutter

The phenomenon of flutter (classical flutter) is a very serious concern in the design of bridges. The failure of the Tacoma's narrows bridge was due to the flutter. The term flutter has been variously used to describe different types of wind-induced behavior. Flutter can be defined as a condition of negative aerodynamic damping wherein the deflection in the structure grows to enormous levels till failure once started. The other types of flutter reported by Simiu and Scanlan (Simiu and Scanlan, 1996) are stall flutter and panel flutter.

Stall flutter is a single-degree-of-freedom oscillation of airfoils in torsion due to the

nonlinear characteristics of the lift (Simiu and Scanlan, 1996). The stall flutter phenomenon can also occur with structures having broad surfaces depending on the angle of approaching wind. The torsional oscillation of a traffic stop sign about its post is an example of this phenomenon.

Panel flutter is a sustained oscillation of panels typically the sides of large rockets, caused by the high-speed passage of air along the panel. The most prominent cases have been in supersonic flow regimes and so have not appeared in the wind engineering context. Flag flutter is closely related to panel flutter.

The motion that is caused by the wind flow will either be damped out or will grow indefinitely until failure. The theoretical dividing line between these two states is the critical flutter condition and the wind speed at this condition is called critical wind speed.

Critical wind speeds for Flutter

When the critical wind speed for flutter is exceeded, the structure will become unstable and experience excessive deflections. Hence it is an important factor to be considered in design. Arrol and Chatterjee (Arrol and Chatterjee, 1981) mention the following guidelines.

Vortex shedding: With respect to vortex shedding, if the critical wind speed for resonance in vertical and torsional modes (vertical modes only for trusses) is greater than the reference wind speed, the static and fatigue stress effects need to be checked from amplitude calculations appropriate to the mode shape.

Turbulence Response: If the natural frequency in first mode for vertical or torsional deflection is greater than 1 Hz, a dynamic analysis for stress effects need to be carried out to account for it.

Classical and Stall flutter: For prevention of this type of instability, the critical wind speed is to be greater than 1.3 times reference speed. The designer must ensure one of the following. The critical wind speed exceeds the practical limiting value for the given site or the resulting amplitudes are of allowable levels. Criteria for acceptability may include considerations of fatigue or of user reaction as well as of ultimate strength.

Buffeting

Buffeting is defined as the unsteady loading of a structure by velocity fluctuations

in the incoming flow and not self-induced (Simiu and Scanlan, 1996). Buffeting vibration is the vibration produced by turbulence. There are two types of buffeting. One type is caused by turbulence in the airflow, and the other type is caused by disturbances generated by an upwind neighboring structure or obstacle. The first type of buffeting can produce significant vertical and torsional motions of a bridge even at low speeds. This buffeting induced motion results in a gradual transition to large amplitude torsional oscillations, which could lead to the failure of a bridge. If the velocity fluctuations are clearly associated with the turbulence shed in the wake of an upstream body, the unsteady loading is referred to as wake buffeting. Wake buffeting is common in urban areas with many tall structures.

2.2.1.2 Wind load model

The aerodynamic loads acting on a body can be divided into static (*St*), buffeting (*b*) and self-excited (*Se*) parts by the formula (Kiviluoma, 1998)

$$\begin{cases} L = L_{st} + L_b + L_{se} \\ D = D_{st} + D_b + D_{se} \\ M = M_{st} + M_b + M_{se} \end{cases} \tag{2.3}$$

in which L, D and M are the time dependent lift, drag and (pitching) moment, respectively.

Applying the dimensionless steady aerodynamic lift C_L, drag C_D, and moment C_M coefficients of a typical cross-section (Fig. 2.2) the static terms are (Kiviluoma, 1998)

$$\begin{cases} L_{st} = \frac{1}{2}\rho U^2 BIC_L \\ D_{st} = \frac{1}{2}\rho U^2 BIC_D \\ M_{st} = \frac{1}{2}\rho U^2 BIC_M \end{cases} \tag{2.4}$$

where U is the mean wind velocity, ρ is the density of air and B and I are the width and the length of the body, respectively. Here, the horizontal component of the wind velocity at instant t is divided into the form $U(t) = U + u(t)$, in which $u(t)$ is the longitudinal component of the fluctuating velocity. If the direction of the mean wind velocity is assumed horizontal, the vertical wind velocity component is characterized

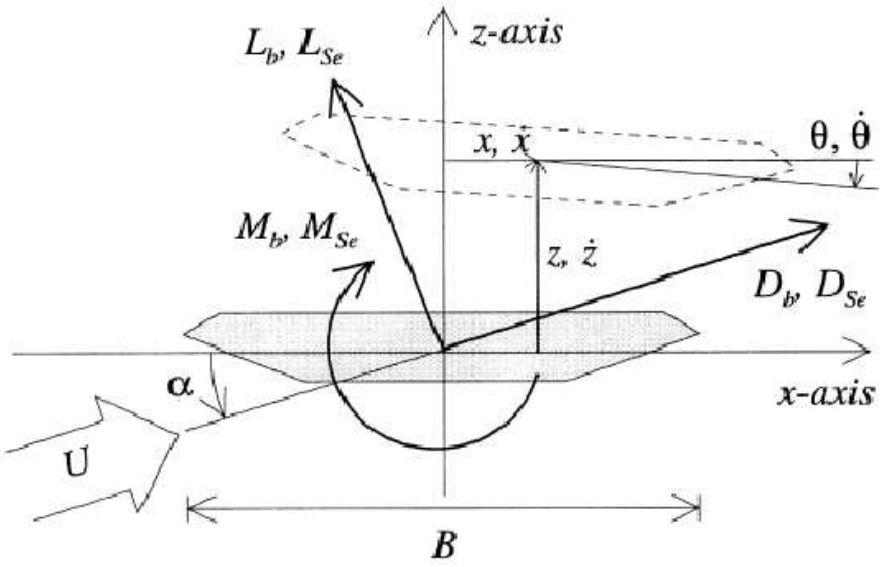

Figure 2.2: Wind load (after Kiviluoma 1998)

by the corresponding transverse fluctuating velocity component $w(t)$. In Eq. 2.3 the buffeting terms take into account the fluctuations in wind speed and direction relative to a body at rest while the self-excited forces take into account the aerodynamic forces caused by motion of the body itself. The approximations $\alpha \approx w/U$ and $Ci(\alpha) \approx Ci + \alpha\, dCi/d\alpha$, ($i = C, D$ *or* M) yield the widely used quasi-steady formulation for the buffeting terms (Kiviluoma, 1998)

$$\begin{cases} L_b = \rho U B l (C_L u + \frac{1}{2}\frac{dC_L}{d\alpha} w) \\ D_b = \rho U B l (C_D u + \frac{1}{2}\frac{dC_D}{d\alpha} w) \\ M_b = \rho U B^2 l (C_M u + \frac{1}{2}\frac{dC_M}{d\alpha} w) \end{cases} \tag{2.5}$$

where α is the angle of attack. Using the typical American notation of flutter derivatives and applying the sign convention of Fig. 2.2, the self-excited terms for sinusoidal motion can be expressed by the formula (Kiviluoma, 1998)

$$\begin{cases} L_{se} = \frac{1}{2}\rho U^2 B l (K H_1^* \frac{z}{U} + K H_2^* \frac{B\theta}{U} + K^2 H_3^* \theta + K^2 H_4^* \frac{z}{B}) \\ D_{se} = \frac{1}{2}\rho U^2 B l (K P_1^* \frac{x}{U} + K P_2^* \frac{B\theta}{U} + K^2 P_3^* \theta + K^2 P_4^* \frac{x}{B}) \\ M_{se} = \frac{1}{2}\rho U^2 B^2 l (K A_1^* \frac{z}{U} + K A_2^* \frac{B\theta}{U} + K^2 A_3^* \theta + K^2 A_4^* \frac{z}{B}) \end{cases} \tag{2.6}$$

in which the flutter derivatives and P_i, H_i and A_i (i=1, 2, 3 or 4) are functions of the reduced frequency $K = B\omega/U$ only, where ω is the circular frequency of the motion. The notation used here is the same as that used in (Scanlan, 1993) except the positive direction of the vertical coordinate z and the vertical force component L. Thus, flutter derivatives H_2, H_3, A_1 and A_4 possess negative signs compared to American literature.

In Eq. 2.6 no terms proportional to translational or rotational accelerations are given and thus the effect of the apparent mass of fluid is neglected. This restricts the usage of the equation to structural members that are relatively dense in comparison to the density of the fluid. Furthermore, usage of the mean wind velocity in Eq. 2.6 implies some inconsistency in analysis of wind-speeds just below the flutter velocity, since the latter velocity is probably exceeded in short duration gusts.

2.2.2 Wind effect on bridges

Wind loading has long played a significant role in bridge design. Some spectacular failures, such as the Tay Bridge (Scotland, 1879), or the Tacoma Narrow Bridge (Washington state,1940) acted as painful reminder to the engineers in case they had forgotten the importance of wind loading. Very long span cable-stayed bridges are flexible structural systems. These flexible systems are susceptible to the dynamic effects of wind loads. Wind can produce the following effects on cable-stayed bridges (Farran, 1999):

1. Wind lift and drag forces,
2. Aeroelastic effects (torsional divergence or lateral buckling),
3. Oscillations induced by vortex effects,
4. Flutter phenomena,
5. Galloping effects, and
6. Buffeting.

All of the above effects require wind tunnel tests. It is very important to understand here that studies are needed for the partially complete structure as well as the completed structure. The performance of the structure under the effect of wind loads should be investigated during the various construction stages of the long cable-stayed

bridge. There are 3 types of wind tunnel tests on a suspension bridge:

1. Models of the entire bridge,

2. Taut strip models, and

3. Sectional models.

The first category of wind tunnel models provides the engineer with the advantages of similitude between model and prototype. These models are expensive to build and constitute a large initial capital expenditure. Experience from previous designs indicates that a scale of 1 to 300 is desirable. Other scales are also possible. The distribution of the mass in such complete scale models is identical to the mass distribution of the real life structure or prototype.

The second category, or the taut strip model, consists of 2 wires that are stretched across the wind tunnel. The response of such models to applied fluid flows in the wind tunnel is similar to the response of the center section of the suspension structure.

The third category is made up of sections of the bridge deck in the span-wise direction. The ends of these sections are supported on spring type foundations to allow motion in the vertical direction as well as the rotational sense. The usual scales for such deck sections are within the 1/50 to 1/25 range. These sectional models are very important in determining the aeroelastic stability of the proposed deck system. These models allow us to further investigate the steady state coefficients for drag, lift, and moment.

These 3 quantities are fundamental characteristics of the cable supported bridge deck. These coefficients are a function of the air density, the deck width of the bridge, the mean wind speed at the height of the deck, as well as the drag, lift, and moment per unit span length, see Eq. 2.4. The science of aerodynamics is very important here since various plots of these functions are usually done versus the angle of attack of the oncoming wind flow. It is also possible from a study of these sectional models to determine the aerodynamic coefficients attributed to the self-excited forces acting on the vibrating structure (Farran, 1999).

2.2.3 Wind effect on stay cables

Stay cables are susceptible to wind (and rain) induced vibration in cable-stayed bridges. Matsumoto et al. (Matsumoto et al., 1992) observed double amplitude (peak to peak) on the Bridge Islands (Denmark) up to 2 m due to the combined effect of rain and wind.

There are a number of mechanisms that can potentially lead to vibrations of stay cables. Some of these types of excitation are more critical or probable than others but all are listed here for completeness (Kumarasena et al., 2005):

- Vortex excitation of an isolated cable;
- Vortex excitation of groups of cables;
- Wake galloping for groups of cables;
- Galloping of single cables inclined to the wind;
- Rain/wind-induced vibrations of cables;
- Galloping of cables with ice accumulations;
- Galloping of cables in the wakes of other structural components (e.g., arches, towers, truss members);
- Aerodynamic excitation of overall bridge modes of vibration involving cable motion (e.g., vortex shedding off the deck may excite a vertical mode that involves relatively small deck motions but substantial cable motions);
- Motions caused by wind turbulence buffeting; and
- Motion caused by fluctuating cable tensions.

For a detail discussion of the above mechanisms of stay cables, the reader can refer to the FHWA report (Kumarasena et al., 2005). The FHWA report, a first report, that provides a design guidelines for the mitigation of wind-induced vibrations of stay cables. FHWA report concludes its initial review with that- while the rain/wind problem is known in sufficient detail (Phelan et al., 2006), galloping of dry inclined cables was the most critical wind-induced vibration mechanism in need of further experimental research.

Rain-wind vibrations

The combination of rain and moderate wind speeds can cause high-amplitude cable vibrations at low frequencies. This phenomenon has been observed on many

cable-stayed bridges and has been researched in detail. Rain/wind-induced vibrations were first identified by Hikami and Shiraishi on the Meiko-Nishi cable-stayed bridge (Hikami, 1986). Since then, these vibrations have been observed on other cable-stayed bridges, including the Fred Hartman Bridge in Texas, the Sidney Lanier Bridge in Georgia, the Cochrane Bridge in Alabama, the Talmadge Memorial Bridge in Georgia, the Faroe Bridge in Denmark, the Aratsu Bridge in Japan, the Tempohzan Bridge in Japan, the Erasmus Bridge in Holland, and the Nanpu and Yangpu Bridges in China. These vibrations occurred typically when there was rain and moderate wind speeds (8–15 m/s) in the direction angled 20° to 60° to the cable plane, with the cable declined in the direction of the wind. The frequencies were low, typically less than 3 Hz. The peak amplitudes were very high, in the range of 0.25 to 1.0 m, violent movements resulting in the clashing of adjacent cables observed in several cases (Kumarasena et al., 2005).

Wind tunnel tests have shown that rivulets of water running down the upper and lower surfaces of the cable in rainy weather were the essential component of this aeroelastic instability(Hikami, 1986). The water rivulets changed the effective shape of the cable and moved as the cable oscillated, causing cyclical changes in the aerodynamic forces which led to the wind feeding energy into oscillations. The following criterion can be used to specify the amount of damping that must be added to the cable to mitigate rain/wind-induced vibrations:

$$S_c = \frac{m\zeta}{\rho d^2} > 10 \tag{2.7}$$

where, S_c = Scruton number, m = mass of cable per unit length (kg/m), ζ = damping as ratio of critical damping, ρ = air density (kg/m^3), and d = cable diameter (m).

Since the rain/wind oscillations are due to the formation of rivulets on the cable surface, several researchers have tried using small protrusions, for e.g. helical fillets 1.5 mm high (Flamand, 1994), on the cable surface to solve the problem. The technique has proven successful, with a minimal increase in drag coefficient. This type of cable surface treatment is becoming a popular design feature for new cable-stayed bridges.

On the basis of the test results, FHWA report (Kumarasena et al., 2005) suggests that if even a low amount of structural damping is provided ($\zeta > 0.003$), then vortex shedding and inclined cable galloping vibrations are not significant. This damping

corresponds to a Scruton number of approximately 3, which is less than the minimum of 10 established for suppression of rain/wind vibrations (Eq. 2.7). Therefore dry cable instability should be suppressed by default if enough damping is provided to mitigate rain/wind vibrations.

2.3 Dynamic response due to pedestrians

Although there have been several cases of footbridges experiencing excessive vibrations by pedestrians in the past, this problem attracted considerably greater public and professional attention only after the infamous swaying of the London Millennium Footbridge located across the Thames River in Central London, see Figure 2.3. The Millennium Bridge problem attracted more than 1000 press articles and over 150 broadcasts in the media around the world (Zivanovic et al., 2005).

The bridge was opened to the public on 10 June 2000 and during the first day between 80,000 and 100,000 people crossed the bridge, resulting in a maximum crowd density of between 1.3 - 1.5 persons per square meter at any one time (Dallard et al., 2001a). On the first day, the Millennium Bridge experienced horizontal vibrations induced by a synchronized horizontal pedestrian load. The horizontal vibrations took place mainly on the south span, at a frequency of around 0.8 Hz and on the central span, at frequencies of just under 0.5 Hz and 0.9 Hz, the first and second lateral modes respectively (Dallard et al., 2001a). The oscillations had maximum amplitudes of 50mm on the southern span and 70 mm on the central span (Dallard et al., 2001b). The maximum lateral acceleration of the bridge was estimated to be between 1.9 and 2.45 ms^{-2}.The bridge's lateral movements caused many pedestrians to have difficulty walking— pedestrians had to hold onto the balustrades, or stop walking to retain their balance. Furthermore, these movements would only die out if the pedestrians on the bridge decreased in number, or stopped walking. Two days after the opening, the bridge was closed in order to investigate the cause of the vibrations and to design a solution.

Figure 2.3: London Millenium Bridge

Figure 2.4: Toda Park Bridge, Japan

One of the earliest reported incidences of excessive horizontal vibrations due to synchronized horizontal pedestrian load occurred on the Toda Park Bridge (T-bridge), Toda City, Japan (Fujino et al., 1993; Nakamura and Fujino, 2002). The T-bridge is a pedestrian cable-stayed bridge which was completed in 1989. It has a main span of 134 meters, a side span of 45 meters, and two cable planes with 11 stays per plane, see Figure 2.4. It was observed that several stays and the girder vibrated when a large number of people (some 2000) were crossing the T-bridge after big boat races. The girder vibrated laterally with amplitude of about 10 mm and a frequency of about 0.9 Hz, the natural frequency of the first lateral mode. Although this amplitude does not seem to be large, some pedestrians felt uncomfortable and unsafe (Fujino et al., 1993; Nakamura and Fujino, 2002; Nakamura, 2004). By video recording and observing the movement of people's heads in the crowd, and by measuring the lateral response, Fujino et al. (Fujino et al., 1993) concluded that 20% of the people in the crowd perfectly synchronized their walking.

In 1975, the north section of the Auckland Harbour Road Bridge in New Zealand, experienced lateral vibrations during a public demonstration, when the bridge was being crossed by between 2000 and 4000 demonstrators. The span of the north section is 190 meters and the bridge deck is made of a steel box girder. Its lowest natural horizontal frequency is 0.67 Hz (Dallard et al., 2001a).

In addition, horizontal vibrations were among several reasons behind the closure of the Solferino Bridge in Paris immediately after its opening in December 1999. Also, a 100 year-old footbridge, Alexandra Bridge in Ottawa, experienced strong lateral vibrations in July 2000, when subjected to crowd loading by spectators of a fireworks display (Dallard et al., 2001b). Other types of bridges such as conventional suspension bridges such as the Groves Suspension Bridge in Chester have also been reported to experience similar lateral vibrations (Dallard et al., 2001a).

The previous cases show that the problem of pedestrian-induced lateral vibrations has occurred on a range of different structural types (suspension, cable-stayed and steel girder bridges) as well as on footbridges made of different materials (steel, composite steel-concrete and reinforced and prestressed concrete) (Zivanovic et al., 2005). In almost all previously reported problems related to footbridge vibrations, the excessive vibrations were caused by a near resonance of one or more modes of

lateral vibration. The reason for this is that the range of footbridge natural (lateral) frequencies often coincides with the dominant frequencies of the human-induced load (Zivanovic et al., 2005). It is therefore stated, that pedestrians can induce excessive lateral vibrations on a footbridge of any structural form, if there is a lateral natural frequency below or near to the lateral human loading frequency – for e.g. about 1 Hz, in case of walking.

2.3.1 Synchronous Lateral Excitation (SLE)

When a pedestrian walks on a lively footbridge human-structure interaction can occur. The interaction takes place in two ways (Venuti and Bruno, 2010). First of all, the presence of the pedestrians modifies the bridge dynamic properties. A first effect is the change of natural frequencies due to the pedestrian added mass, and the change is much higher if the ratio of the dead load to live load is small, that is, if a very light bridge is crossed by a high density crowd. A second effect is a change in damping (Zivanovic et al., 2005). This effect is well-known in the case of stationary people, but it is not completely understood in the case of moving people. According to some authors (e.g. (Zivanovic et al., 2005)), walking pedestrians cause an increase in damping in the vertical direction, due to human's inability to synchronize their pace with surfaces that move in the vertical direction. On the contrary, damping can be reduced by walking pedestrians, when the second interaction effect takes place, that is, the possibility of synchronization between the pedestrians and the structure, when the vibrations become perceptible. This phenomenon is more likely to occur in the horizontal direction, since pedestrians are more sensible to lateral vibrations which affect their balance during gait. This phenomenon is called Synchronous Lateral Excitation (SLE) and has come to the world attention after the closure of the London Millennium Bridge.

The SLE has been the leading research topic in footbridge dynamics in the last decade. The phenomenon is due to the development of two kinds of synchronization (Ricciardelli and Pizzimenti, 2005). The first is the pedestrian-structure synchronization, which takes place when the lateral vibrations become perceptible and the pedestrian unconsciously adapts his/her frequency to that of the bridge in order to maintain

balance. This first type of synchronization is also known as lock-in, in analogy to the well-known fluid-structure interaction phenomenon. The second kind of synchronization develops between the pedestrians themselves and it depends on the crowd density. As a matter of fact, when the crowd density is very high, each pedestrian cannot move freely and is conditioned by the surrounding people, so he/she tends to walk at the same frequency and in phase with the pedestrians in front. In the SLE these two synchronization effects are strictly related and it is very difficult to separate their contribution.

Moreover, the experiments devoted to the comprehension of the synchronization among pedestrians are very scarce, therefore further research in this field is required (Venuti and Bruno, 2010). The SLE is a self-excited phenomenon, since the lateral force exerted by the pedestrians grows for increasing amplitude of the deck lateral motion, as well as the probability of lock-in (Venuti and Bruno, 2010). On the other hand the phenomenon is also selflimited, in the sense that when the vibrations exceed a certain value, pedestrians can no more maintain balance, so they stop, detune or touch the handrails, causing the vibrations to decay. For this reason the SLE has never caused structural failure, but only a serviceability problems for the users. Nevertheless, in the last few years, a great number of footbridges have been closed after the construction in order to install damping devices, therefore it is very important to avoid the occurrence of this problem by taking it into account in the design stage.

Finally, a few words should be spent about vandal loading, which is the deliberate movement of pedestrians in order to magnify the footbridge vibrations through knee-bending, skipping or shaking handrails. The data about this kind of loading are scarce and the debate is still open. What is clear is that it deserves greater attention, especially nowadays when footbridges are very lively and easy to excite. Therefore, a clarification of the exact definition of the vandal loading, regarding its duration, type of load and number of people involved, as well as its force modelling is a task for further investigation.

2.3.2 Dynamic forces induced by pedestrians

During walking, pedestrians induce dynamic forces on the surface they walk. These forces have components in all three directions, vertical, lateral and longitudinal and they depend on parameters such as pacing frequency, walking speed and step length. The vertical component is applied at the footfall frequency (typically around 2 Hz) and is about 40% of their body weight. The lateral component is applied at half the footfall frequency and on a stationary surface is about 10 times smaller than the vertical component (Dallard et al., 2001a), see Figure 2.5. Table 2.1 shows a classification of frequency ranges for different activities, that is, walking, running and jumping and for different velocities, as proposed by Bachmann (Bachmann, 2002). This has been confirmed with several experiments, for example by Matsumoto who investigated a sample of 505 persons that the pacing frequency follows a normal distribution with a mean of 2.0 Hz and a standard deviation of 0.173 Hz, see Fig.2.6 (Matsumoto et al., 1978).

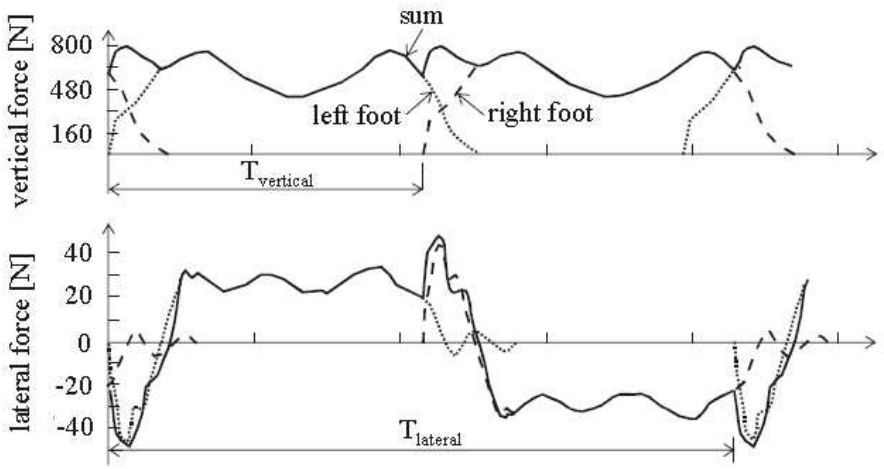

Figure 2.5: Periodic walking time histories: vertical and lateral direction (after Zivanovic 2005)

Usually, the force exerted by a single pedestrian is modelled as a periodic force. Therefore, each force component, vertical, lateral and longitudinal, can be decom-

Table 2.1: Walking frequency ranges (Hz) for different activities (after Bachmann 2002)

	Total range	Slow	Normal	Fast
Walking	1.4 – 2.4	1.4 – 1.7	1.7 – 2.2	2.2 – 2.4
Running	1.9 – 3.3	1.9 – 2.2	2.2 – 2.7	2.7 – 3.3
Jumping	1.3 – 3.4	1.3 – 1.9	1.9 – 3.0	3.0 – 3.4

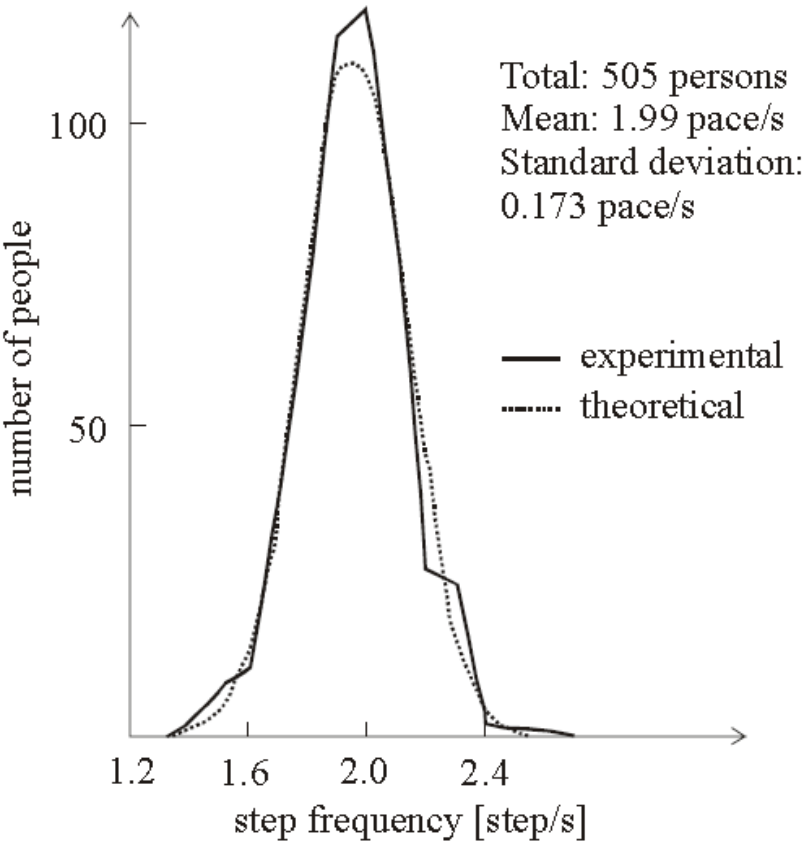

Figure 2.6: Normal distribution of pacing frequencies for normal walking (after Matsumoto et al. 1978)

posed in a Fourier series:

$$\begin{cases} F_{vert}(t) = G + \sum_{i=1}^{n} \left[G\alpha_{i,vert} \sin\left(2\pi ift - \phi_{i,vert}\right) \right] \\ F_{lat}(t) = \sum_{i=1}^{n} \left[G\alpha_{i,lat} \sin\left(\pi ift - \phi_{i,lat}\right) \right] \\ F_{long}(t) = \sum_{i=1}^{n} \left[G\alpha_{i,long} \sin\left(2\pi ift - \phi_{i,long}\right) \right] \end{cases} \tag{2.8}$$

where G is the pedestrian's weight (usually taken as 700 N), α_i is the Dynamic Load Factor (DLF) of the ith harmonic, ϕ_i is the phase shift of the ith harmonic, i the order number of the harmonic, n a suitable number of harmonics and f the pacing frequency [Hz]. Different authors have tried to measure the DLFs related to the different force components. A complete review is reported by Zivanovic (Zivanovic et al., 2005); as an example, only the measurements of Bachmann & Ammann (Bachmann and Ammann, 1987) for the vertical and lateral component are reported in Table 2.2.

Table 2.2: DLFs according to Bachmann & Ammann (1987)

	α_1	α_2	α_3	α_4	α_5
Vertical	0.37	0.10	0.12	0.04	0.08
Lateral	0.039	0.01	0.043	0.012	0.015

The action of a group or stream of pedestrians is generally modelled by multiplying the action of (or the acceleration induced by) a single pedestrian by a multiplication factor, which should account for randomness of the loading or for synchronization effects. This general approach can be summarised in the following formula (Venuti and Bruno, 2010):

$$F_n(t) = C \cdot N \cdot k \cdot F_0 \cos\left(2\pi ft\right) \tag{2.9}$$

where N is the number of pedestrians in the group or stream, C is a synchronization factor, k is a reduction factor, which account for the probability of occurrence of step frequencies, and F_0 is the amplitude of the force component (Table 2.3). The multiplication factor is, therefore, given by the product $C \cdot N \cdot k$.

Table 2.3: Amplitude F_0 [N] in codes and guidelines

Code	Vertical	Longitudinal	Horizontal
UK N.A.to Eurocode1	280 (walk)	-	-
	910 (jogging)		
Setra/AFGC	280	140	35

It should be noted that the periodic load models, for single and multiple pedestrians, described above do not account for the human-structure interaction.

2.3.3 Comfort criteria in codes and design guidelines

The comfort criteria proposed in standard codes are based on the fulfillment of one of two requirements (Venuti and Bruno, 2010). The first is that the footbridge natural frequencies should not fall in the typical ranges of walking frequencies. Table 2.4 summarises the frequency ranges that should be avoided, according to international standards (Eurocode 5 2004, BS EN 1991-2 2003, BS5400 2006). This first requirement is rarely satisfied in newly built footbridges. In that case a dynamic calculation with suitable load models is required, and the second requirement to be satisfied is that the maximum vertical and lateral accelerations do not exceed a limit value. Table 2.5 summarises the limit values of vertical and horizontal accelerations reported by international standards (ISO 10137 2007, Eurocode 5 2004, BS5400 2006). It should be pointed out that ISO 10137 refers to the root mean square (rms) values of acceleration, instead of the peak values.

In comparison to the comfort requirements proposed in standard codes, the new design guidelines (Sétra /AFGC 2006, Hivoss 2008) adopt a different approach. Comfort criteria are not proposed as absolute values but depend on the footbridge class and required comfort level, which can be decided by the footbridge Owner. Since the Sétra /AFGC and the Hivoss guidelines propose a very similar design methodology, the common features will be outlined in the following.

Footbridges are classified into traffic classes (4 in Sétra /AFGC, 5 in Hivoss) (SE-

Table 2.4: Frequency ranges to be avoided

Code	Vertical	Horizontal
Eurocode 5	< 5	< 2.5
UK N.A.to Eurocode1	$< 8^{*}$	$< 1.5^{**}$
BS 5400	< 5	< 1.5

* unloaded bridge

** loaded bridge

Table 2.5: Limits on accelerations

Code	Vertical (m/s^2)		Horizontal (m/s^2)
ISO 10137*	$0.6/f^{0.5}$,	$1 < f^{**} < 4$ Hz	0.2
	0.3,	$4 < f < 8$ Hz	
Eurocode 5		0.7	0.2
BS 5400		$0.5/f^{0.5}$	

* values referred to walking pedestrians

** f = first natural frequency

TRA., 2006; HIVOSS, 2008) depending on the traffic level which they undergo. Besides, four comfort levels (maximum, average, minimum, discomfort) and related acceleration limits are defined (Table 2.6). If the occurrence of SLE has to be avoided (maximum comfort), a lateral acceleration of 0.1 m/s^2 should not be exceeded. It is worth pointing out that the Sétra /AFGC and Hivoss guidelines consider the triggering of the lock-in in terms of an acceleration threshold. This approach seems to be more appropriate than the one proposed by Arup (Dallard et al., 2001a), which is based on the calculation of a critical number of pedestrians which trigger the lock-in (Dallard et al., 2001a). However, the Hivoss guideline considers the two approaches as equivalent, therefore it is possible to calculate the triggering number of pedestrians by means of the Arup formula or to verify the lateral acceleration does not exceed 0.1-0.15 m/s^2.

Table 2.6: Comfort classes and related cceleration limits

Comfort level	Vertical (m/s^2)	Horizontal (m/s^2)
Maximum	< 0.5	< 0.1
Average	$0.5 - 1$	$0.1 - 0.3$
Minimum	$1 - 2.5$	$0.3 - 0.8$
Discomfort	> 2.5	> 0.8

2.3.4 Models for human-structure interaction

There have been several efforts, so far, to model the human-structure interaction phenomenon to understand the SLE of footbridges. The available models are listed below.

- Fujino's model (Fujino et al., 1993)
- Arup's model (Dallard et al., 2001a,b)
- Newland's model (Newland, 2003)
- Nakamura's model (Nakamura, 2004)
- Abrams' model (Strogatz et al., 2005; Abrams, 2006)

- Robert's model (Roberts, 2005)

- Macdonald's model (Macdonald, 2008)

- Venuti's model (Venuti et al., 2007)

- Bodgi et al. (Bodgi et al., 2007)

- Erlicher et al. model (Erlicher et al., 2010)

A recent review of the different models is already made in some of the papers (Venuti and Bruno, 2010; Marcheggiani and Lenci, 2010) and the thesis (Abrams, 2006). However, to facilitate the reader and continue the subject, the salient features of the various models are presented here.

Fujino et al. (Fujino et al., 1993) have adopted a model of harmonic forcing by empirically tuning a synchronization parameter for the lateral vibrations of the T-Bridge (according to their experimental data. This model assumes a continuous increase in the vibration amplitude as the number of pedestrians increases. Dallard et al. (Dallard et al., 2001a,b) have conducted a series of controlled crowd tests on the Millennium Bridge and consequently they have proposed a load model based on empirical observations. Their phenomenological approach assumes but does not explain the observed synchronization effect, and cannot predict the steady state amplitude for bridge motion, as it is due to unmodelled nonlinearities. In any case a formula has been yielded to evaluate the critical number of pedestrians, by tuning a proportionality constant on the specific real casestudy. Newland (Newland, 2003) has approached the problem by referring to the interaction phenomenon between fluid flow and structures (lock-in) which is widely studied in wind engineering (Borri and Hffer, 2000). His model includes the empirical assumption that the 40% of the pedestrians are synchronized with bridge lateral frequency, independently on the amplitude of the oscillations. Nakamura (Nakamura, 2004) has proposed an interactive forcing model which allows the schematization of the self-limiting nature of the synchronization phenomenon and the prediction of the steady state amplitude. Also this model is based on coefficients which have been estimated from experimental tests (Nakamura and Kawasaki, 2006; Fujino et al., 1993). Strogatz et al. (Strogatz et al., 2005; Abrams, 2006) have been the first, up to our knowledge, to mathematically describe and predict the simultaneous growth of bridge movement and crowd synchronization, an observation that was unexplained in previous models but that is confirmed by analyses of video footages

recorded during overcrowding conditions on lively footbridges (Fujino et al., 1993; Dallard et al., 2001a). They adapted ideas originally developed to explain the collective synchronization of biological oscillators, such as neurons and fireflies, or other nonlinear systems able to phase-lock to an external periodic drive (Strogatz, 2000). The basic idea is just the observation that also human walking is governed by unconscious rhythmic biological signals, so an analogy for example with the rhythmic flashing of fireflies seems to be possible.

Roberts (Roberts, 2005) has schematized the interaction between the pedestrians and the footbridge assuming that synchronization occurs when the pedestrians motion is larger than the bridge motion; from this critical condition, he obtains a limit number of pedestrians. Blekherman (Blekherman, 2007) has explained the excessive lateral vibrations on the Solferino Bridge in Paris on the basis of autoparametric resonance by using a double pendulum model. He highlights the possibility of a non linear parametric resonance as the reason for excessive lateral vibration, due to the fact that the first vertical frequency of bridge deck and the lateral one are in the ratio 2:1 in many cases (Blekherman, 2005). Piccardo and Tubino (Piccardo and Tubino, 2008) have performed an interesting extensive critical analysis of the excitation mechanisms identified in the literature and they have proposed a new forcing model based on experimental tests carried out on harmonically moving platforms: the force exerted by pedestrians is modelled as harmonic with an amplitude depending on the deck lateral displacement, and a simple criterion defining the limit pedestrian mass is introduced. Venuti et al. (Venuti et al., 2007) modelled the human-structure interaction based on a substructure approach– the structure and the crowd are the two subsystems. Venuti et al. (Venuti et al., 2007; Venuti and Bruno, 2009) have developed a first-order model based on the mass conservation equation, in order to macroscopically describe the dynamics of the crowd in the framework of hydrodynamic modelling. Their model permits to take into account the triggering of the lock-in and its self-limited nature, previously explained only by Strogatz et al. (Strogatz et al., 2005). The effects of two different kinds of synchronization, i.e. between pedestrians and structure and among pedestrians, are introduced. Some parameters, used in the formulation of the model, would require specific experimental tests to be confirmed. Bodgi et al. (Bodgi et al., 2007), independently and almost at the same time of (Venuti et al., 2007), have

adopted a similar approach to simulate the mechanics of synchronous lateral excitation. Ricciardelli and Pizzimenti (Ricciardelli and Pizzimenti, 2005, 2007) performed a systematic experimental campaign aimed at characterizing dynamically the lateral force exerted by pedestrians on footbridges, both in case of still deck and in case of laterally moving deck; deterministic and stochastic lateral loading models for the static case have been provided. The mechanism of crowd synchronization has been investigated only from the qualitative point of view.

To model pedestrians-induced lateral vibrations it is necessary to have some understanding of the mechanics which describes human walking, with special attention to the lateral component of the ground reaction force; therefore, some authors (Bauby and Kuo (Bauby and Kuo, 2000), Belli et al. (Belli et al., 2001), Vaughan (Vaughan, 2003), Hof et al. (Hof et al., 2005, 2007), Macdonald (Macdonald, 2008), Trovato et al. (Trovato et al., 2008, 2009), especially in the area of biomechanics, have recently investigated this topic developing and reorganizing theories on bipedal walking, forcing and frequency of human footfall during walking and balance control.

Macdonald's model of human balance comprises an inverted pendulum- for which the most effective means of lateral stabilization is by the control of the position, rather than the timing, of foot placement. The model gives a reasonable representation of the lateral pedestrian forces applied to the ground (or bridge) in the absence of bridge motion, compared against previous measurements. The same balance strategy as for normal walking on a stationary surface is applied to walking on a laterally oscillating bridge. As a result, without altering their pacing frequency (unsynchronized with the bridge), averaged over a large number of cycles, the pedestrian effectively acts as a negative (or positive) damper to the bridge motion, which may be at a different frequency. This is in agreement with the empirical model developed by Arup from the measurements on the London Millenium Bridge, leading to divergent amplitude vibrations above a critical number of pedestrians. However, with the chosen parameters, the model does not accurately match the numerical results from the full-scale measurements, although it is possible to modify the results considerably using different parameters or balance strategies. In addition, the model does not cover the behaviour for larger bridge amplitudes for which pedestrians may change their gait, possibly including synchronizing their motion with the bridge or stopping walking. Therefore, to

refine the model, further data are required on pedestrian behaviour when perturbed by bridge motion.

2.3.4.1 Erlicher's model on rigid floor (Erlicher et al., 2010) and extension to the moving floor

Erlicher et al. (Erlicher et al., 2010) proposed a model to represent the lateral oscillation of a pedestrian walking on a rigid floor by an autonomous self-sustained oscillator by modifying the so-called hybrid Van der Pol/Rayleigh oscillator, already used for applications in the field of robotics. They defined a nonlinear Single-Degree-of-Freedom oscillator able to accurately predict the lateral walking force of a pedestrian. The force exerted on the floor corresponds to its restoring force. Although, such an oscillator is a simplified representation of the human body, it is able to reproduce two experimentally observed phenomena: (i) the time-history of lateral force is an approximately periodic signal; (ii) the walking motion is self-sustained, in the sense that the pedestrian/oscillator produces by itself the energy needed to sustain its motion. This implies that such an oscillator must be self-sustained. In addition, the self-sustained character entails that the autonomous oscillation has a natural amplitude and frequency, representing the natural walking amplitude and frequency of the pedestrian. A dynamic analysis of this oscillator was performed through an energetic approach and a perturbation technique in order to get the stable limit cycle. The model parameters were finally identified from the experimental force signals, resulting from a test campaign on a population of twelve pedestrians: the agreement between model and experimental results was very good.

The next step, that is to model the behaviour of a pedestrian on a moving floor to explain the SLE phenomenon is addressed in this thesis.

The motivation to extend this model to the moving floor case is that in certain situations, it is useful to replace a self-sustained oscillator with a simpler dynamic model, based on the so-called phase equation (Erlicher et al., 2010). Roughly speaking, the response of a self-sustained oscillator can be described in terms of amplitude and angle variable. If the amplitude is supposed constant, then the angle variable suffices to describe the oscillation. In this case, the so-called total phase, strictly related to the angle variable (Pikowski et al., 2001; Kuramoto, 2000), governs the system evo-

lution by a suitable equation of phase. This idea has been used in (Strogatz et al., 2005) and (Eckhardt et al., 2007) for modelling the crowd behavior: each pedestrian is represented by a phase equation. The time-derivative of the phase represents the instantaneous walking frequency.

By definition, this approach neglects the amplitude variations of the pedestrian oscillations. However, several experimental tests, e.g. (Nakamura et al., 2008), show that the variations of the lateral oscillation amplitude of pedestrians are not negligible. In this respect, Macdonald (Macdonald, 2008) has suggested the use of a model for the pedestrian lateral oscillation where only the amplitude variations are accounted for and no frequency modulation due to the external excitation is considered. The modified hybrid Van der Pol/Rayleigh model proposed here accounts for both phase and amplitude variations due to external excitation.

2.4 Vibration reduction techniques for cable-stayed footbridges

The discussion made in the previous sections reveals the vibration problems associated of the cable-satyed bridges due to the wind and pedestrian loadings. It was found that the cable-satyed bridges are flexible and have low damping. Therefore, it has been a general practice, nowadays, to introduce external dampers in order to increase the damping of the bridge system.

However, it is concluded by the previous studies on several cable-stayed bridges (Yamaguchi and Ito, 1997) that the modal damping-frequency relation shows considerable scatter, moreover, the modal damping of cable-stayed bridges is highly dependent on the coupling characteristics of mode shapes. The damping value of coupled mode becomes large (or small) if the sub-structure coupled with the girder motion has higher (or lower) damping than the girder. Due to the coupling between the components of the CSB, for e.g. deck and cables; it is important to consider the damping devices for both- the deck and stay cables.

A detail description of the types, principles and application of the dampers in civil engineering field including cable-stayed bridges can be found in (Weber et al., 2006; Nyawako and Reynolds, 2007). However, a brief description of the damper system used in bridges is given as follows (Anusas et al., 2007).

- absorbing dampers;
- mass dampers ;
- active tuned dampers;
- structural or physical damping.

Absorbing damper

Two types of dampers can be distinguished: mechanical dampers and hydraulic dampers. In mechanical dampers the structure's oscillation damping is achieved by springs or elastic pieces, in hydraulic dampers - by liquids, oil or gas. Hydraulic or viscous damper is made of hydraulic cylinder, surrounding a piston, the head of which forms two chambers. A relative motion applied to the actuator results in a pressure difference between the two chambers, creating a potential for flow and energy dissipation. See Figure 2.7.

Tuned mass damper (TMD)

TMD is a device absorbing vibrations by vibration of the self mass (See Figure 2.7). A vibration absorber consists of a mass-spring damper system which is attached to the structure and carefully tuned with the structure‘s vibration characteristics. When the counterweight of the damper moves in one direction as the structure moves in the other, the damping of the structure‘s oscillation is achieved. A limitation of the device, however, that it is only being effective over a narrow band of frequencies. However, TMD system might not be a good countermeasure for mitigating the buffeting response of a long-span bridge (Chang et al., 2003).

Active tuned damper

This type of vibration absorbers can suppress and tune the vibrations over a range of frequencies by incorporating a variable stiffness element that can be adjusted in real-time. Among others the magneto-rheological (MR) fluid dampers can be mentioned. MR fluids, which typically consist of micrometer-sized, magnetically polarizable particles in a water, oil or silicon. When a magnetic field is applied to the fluids, the fluids become semisolid and exhibit viscoplasticity adjusting their tuning to the

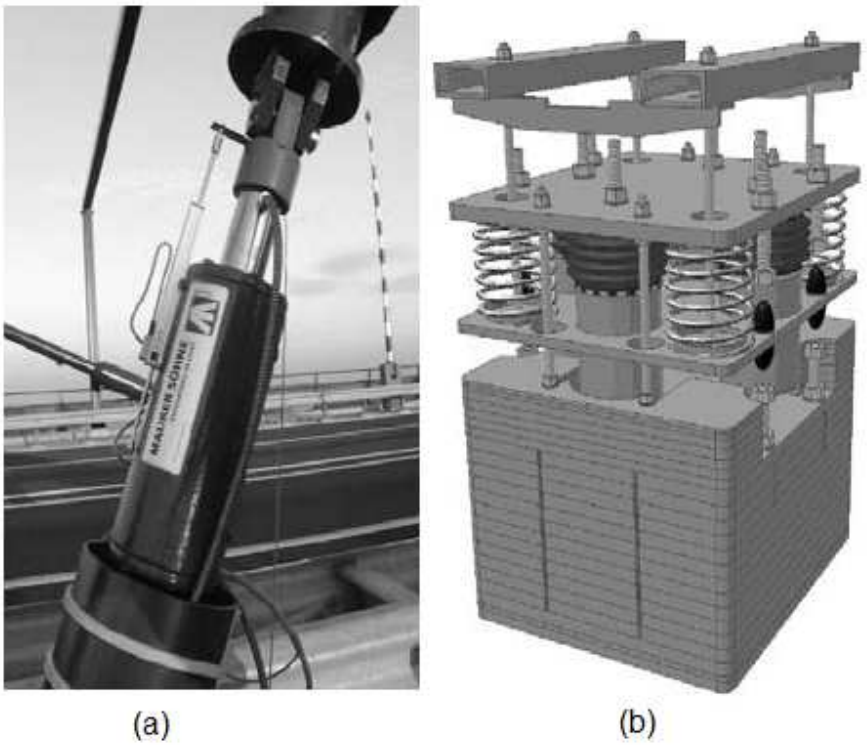

Figure 2.7: (a) Absorbing and (b) mass damper

dynamic parameters of the structure and help to reduce the structure vibration. The absorbers viscosity and elasticity are controlled by an external electric source. At present implementation of multiple absorbers activated when bridge motion exceeds admissible bounds is carried out.

Structural or physical damping

It consists of local or total structural modifications by changing mainly the stiffness or the mass of a structure. Such as local strengthening of members, introducing of additional beams in the crosssections, installing a stiffer hand rail by truss or solid wall construction, intermediate piers, additional hangers, ties or cables can be mentioned. By these measures the natural frequencies could be changed, leading to frequency tuning of the bridge structures.

For the mitigation of rain/wind induced vibrations of stay cables, it is recommended (Kumarasena et al., 2005) to an effective surface treatment by using double-helical beads for cable pipes. $S_c > 5$ may be acceptable in this case. However, such reductions should be made only for regularly spaced, single cable arrangements. In general, it is recommended to keep the Scruton number as high as possible by providing external dampers and/or crossties.

A damper can be tuned to yield optimal damping in any one selected mode. For other modes the level of damping will be less than this optimal value. Rain/wind-induced vibrations occur predominantly in mode 2. Therefore, if a damper is to be tuned to a particular mode to mitigate rain/wind-induced vibrations, it appears logical to select mode 2.

With some dampers (such as dashpot type), an initial static friction force must be overcome before engaging of the viscous element. Field experiments have shown the presence of this stick-move-stick-move behavior associated with such dampers. This may effectively provide a fixed node instead of the intended damping for the cable at low-amplitude oscillations and should be considered. The visco-elastic type dampers where an elastomeric element is permanently engaged between the cable and the supporting elements, theoretically, are free of such initial frictional thresholds. On the other hand, there are also damper designs that rely on friction as the energy dissipation mechanism, and the static friction threshold for such dampers may be higher than for the other types.

The crossties are used to suppress the vibrations by tying multiple cables together with secondary cables to form cable networks so that the energy in individual cables can be redistributed either to the higher modes of vibration or to adjacent cables in the network (Ehsan and Scanlan, 1990). The use of crossties creates local modes, which must be considered in design. Cable crossties must be provided with initial tension sufficient to prevent slack of the crossties during design wind events. However, the crossties between the stays are considered a distraction to the aesthetic beauty of cable-stayed bridges (Pacheco et al., 1993) and, due to the large stresses to which they are subjected, there have been incidents of crosstie failures, such as that reported on the Erasmus Bridge in the Netherlands (Virlogeux, 1993).

External devices, such as high-damping rubbers (Yamaguchi and Fujino, 1999) and dampers attached at the vicinity of the cable anchorages are used to supplement the inherent mechanical damping in the cables. This inherent structural damping is believed to be at an extremely low level and a critical contributory factor to the susceptibility of stay cables to aerodynamic excitations (Kiviluoma, 1998). Among these damping supplementing devices, passive viscous dampers have been extensively studied (e.g., (Zuo and Jones, 2005; Kumarasena et al., 2005; Pacheco et al., 1993; Tabatabai and Mehrabi, 2000; Achs and Adam, 2005) and their effectiveness in suppressing stay cable vibrations has been widely accepted (Yamaguchi and Fujino, 1999). In recent years, the potential application of active and semi-active dampers has also been investigated in attempt to achieve improved damping performance over other damping supplementing devices e.g., (Johnson et al., 2003; Wu et al., 2004). Although the effectiveness of such active and semi-active dampers has been confirmed by experimental tests, there still remain many theoretical as well as practical issues to be resolved (Yamaguchi and Fujino, 1999). In most cases, these three types of countermeasures have been applied separately. On some bridges, however, more than one of them has been employed, for e.g. the Normandie Bridge (Fuzier and Stubler, 1994). Whether or not these countermeasures can work together effectively is also a subject of further study.

Although the above-discussed types of countermeasures have been demonstrated to be effective in suppressing some or all types of wind- and rain-wind-induced vibrations, the design still remains semi-empirical. For example, in the design of dampers,

an efficient and reliable means to estimate the inherent damping in the cables is still not available, and it is still not fully clear how much supplemental damping is needed to suppress the vibrations. To enable more rational and efficient design of counter-measures, a better understanding of the mechanisms of wind- and rain-wind-induced stay cable vibrations, as well as the key parameters involved, is needed.

2.5 Conclusions

The state of art for the dynamic behaviour of the cable-stayed footbridges was provided both due to wind and pedestrian loading. Also some vibration reduction systems were reviewed. It was derived that wind load effects are getting bigger on the design of a cable-stayed bridge with its longer span lengths. The wind vibrations are conventionally classified into buffeting, vortex excitations, galloping and torsional flutter of the whole bridge. Wind induced vibrations are to be verified also for various stages during the erection as well as, for such structural elements as pylon and stay cables, after completion. The most important wind effect in case of stay cables is that of due to the rain-wind phenomenon. However, dry cable instability should be suppressed by default if enough damping is provided to mitigate rain/wind vibrations.

The pedestrian induced loading produces SLE phenomenon. This phenonmenon is complex and still under research. There is need of new models that can describe better this behaviour. In this view modified hybrid Van der Pol/Rayleigh oscillator will be used to model the synchronous behaviour of pedestrians on a moving floor in chapter 7.

Finally, the application of external dampers is increasing in cable-stayed footbridges for the mitigation of wind and pedestrian induced vibrations. Not only the main deck but also stay cables need special attention and design of damping devices. Some viscous dampers (such as dashpot type), may not be effective at low-amplitude oscillations as an initial static friction force must be overcome before engaging of the viscous element, showing a particular stick-move-stick-move behavior. Moreover, the

research on active and semiactive dampers, e.g. MR dampers, is increasing that work in a wide frequency ranges.

CHAPTER 3

STRUCTURAL (SYSTEM) IDENTIFICATION TECHNIQUES FOR CABLE-STAYED BRIDGES

3.1 Introduction

Structural (system) identification of civil engineering structures refers to any systematic approach for identifying structural modal parameters -frequencies, damping ratios and mode shapes- through the use of input and output test data. These parameters serve as basis or input to the finite element model updating, detecting and locating the possible damage, long-term health monitoring and the safety evaluation of structures against extreme circumstances like earthquake, wind loads etc. (Natke et al., 1993; Ghanem and Shinozuka, 1995; Maia and Silva, 1998). Even if the age of virtual prototyping has already started (Auweraer Van Der, 2002), experimental testing and system identification still play a key role because they help the structural dynamicist to reconcile numerical predictions with experimental investigations. The term 'system identification' is sometimes used in a broader context in the technical literature and may also refer to the extraction of information about the structural behaviour directly from experimental data, i.e., without necessarily requesting a model, e.g., identification of the number of active modes or the presence of natural frequencies within a certain frequency range. The field of system identification techniques traversed through a long journey and nowadays various advanced techniques are available. The following section 3.2 presents a state-of art on the development of the system identification techniques. Then, section 3.3 describes the various structural

identification techniques applicable to the bridge structures, in particular, relevant to the cable-stayed bridges. Finally, the important conclusions are drawn.

3.2 Structural (system) identification techniques: a state-of-art

3.2.1 Linear identification

Linear system identification is a discipline that has evolved considerably during the last 30 years (Soderstrom and Stoica, 1989). Experimental modal analysis is by all means the most popular approach to performing linear system identification in structural dynamics. The model of the system is expressed in the form of modal parameters, namely the natural frequencies, mode shapes and damping ratios. The popularity of modal analysis stems from its great generality; modal parameters can describe the behaviour of a system for any input type and any range of the input.

The field of linear identification now offers a vast range of effective techniques. In recent years, time domain techniques have been used rather successfully, thanks to the great spectral resolution offered and to their modal uncoupling capability (Masri et al., 1982; Shinozuka et al., 1982; Safak, 1991; Safak and Celebi, 1991; Peeters and DeRoeck, 1999; Loh et al., 2000). One of the basic shortcomings of these methods is that they often produce spurious modes, whose true nature, however, can usually be identified by means of simple modal form correlation indicators (Ewins, 2000), or, as an alternative, with the aid of numerical models.

An important family of time domain methods makes use of time series autoregressive models and exploits the theoretical results coming from research in the field of system control (Ljung, 1999). These techniques provide a very general and attractive formulation, and are frequently applied to civil structures. The most critical aspect resides in the computational complexity associated with applications to Multi-Degree-of-Freedom (MDoF) systems. The extension of the parameter estimation techniques

to stochastic multi-variate models, in fact, is far from being trivial, and additional difficulties arise from local minimum points and algorithmic instabilities (Fassois and Lee, 1993).

Among the deterministic methods, in addition to the historic Ibrahim Time Domain (Ibrahim and Mikulcik, 1977), we should mention the Eigensystem Realisation Algorithm (ERA) (Juang. and Pappa, 1984), which, based on a Single Value Decomposition (SVD) of Hankel's matrix, has been closely studied in the literature (e.g. (Lew et al., 1993)), and the Polyreference Time Domain (PRTD) stemming from a generalisation of Prony's method (Vold et al., 1982).

Since the beginning of the nineties, there has been an increasing interest in so-called Stochastic Subspace Identification (SSI) methods, in which statistical, algebraic and numerical concepts and algorithms cooperate, leading to user-friendly software for linear system identification (Zeiger and McEwen, 1974; James et al., 1995; Peeters and DeRoeck, 1999). Contrary to classical algorithms, subspace algorithms do not suffer from the problems caused by a-priori parametrisations and non-linear optimisations. Van Overschee and De Moor (Van Overschee and De Moor, 1996) studied three different subspace algorithms for the identification of combined deterministic-stochastic systems. This comparison is done through the introduction of a unifying theorem, of which the three algorithms are special cases.

For a description and classification of various input-output modal analysis techniques the reader may consult specialized texts (Heylen et al., 1997; Maia and Silva, 1998; Ewins, 2000). Unification of the theoretical development of modal identification algorithms was also attempted, e.g., in (Allemang and Brown, 1998; Allemang and Phillips, 2004), which is another sign of the maturity of this research field.

Different is the situation with modal analysis algorithms that, being conceived to work with output data (output-only or input-unknown techniques), are of special interest for structures exposed to natural vibration (bridges, towers, buildings etc.). These issues in the nineties gave rise to a new research area, officially inaugurated in a special session of IMAC-XIV organised by Felber and Ventura (Felber and Ventura, 1996), which today is often referred to as "in operation" (or improperly "operational") modal analysis, e.g., (Cunha and Caetano , eds; Brincker and Moller , eds.; Reynders et al.; Giraldo et al., 2009). In ambient vibration conditions, there is still a need

to determine to what extent the use of these techniques in non-ideal conditions, as is in the typical case, can be deemed acceptable, or whether it proves necessary to resort to techniques specially conceived for dealing with non-stationarity. Inherently non-stationary techniques include stochastic approaches (e.g. (Yuen and Katafygiotis, 2002)), time-frequency instantaneous estimators (e.g. (Ceravolo, 2004)) or time-varying estimators (e.g. (A.G. and S.D., 2008; Du and Wang, 2009)).

3.2.2 Nonlinear identification

Though the word nonlinearity has a tautological meaning, a classification of possible sources of nonlinearity might still retain a practical interest in structural dynamics. A drawback in using this term in a survey is rather due to the vast range of problems and techniques that deserve a proper coverage. This section on nonlinear identification is not intended as a comprehensive review by any means. In fact, such a review already exists in the form of the textbook Nonlinearity in Structural Dynamics: Detection, Identification and Modelling by Worden and Tomlinson (Worden and Tomlinson, 2001) and in several comprehensive state-of-the-art papers (e.g. (Hemez and Doebling, 2001)). For a much more comprehensive overview the reader is directed to these and other documents. The present survey is intended to illustrate the use of a small number of vibration-based methods of direct or potential interest for understanding the structure under exam.

A first category includes identification methods using various strategies to by-pass non-linearity. Other methods can be framed respectively in the parametric and the non parametric approach: in the former case, a priori selection of a specific model for the dynamic behaviour of the system is needed and the identification process consists of determining the coefficients for such model. Non parametric methods, instead, do not require any assumption on the type and localisation of structural non-linearities but, generally, the quantities identified cannot be directly correlated to the equation system of motion.

3.2.2.1 By-passing non-linearity

Traditional techniques for the analysis of the dynamics of nonlinear structures are based on the assumptions of weak nonlinearities and of a non-linear modal structure that is similar or a small perturbation of the underlying linearised system.

Caughey in 1959 proposed to replace a nonlinear oscillator with external Gaussian excitation by a linear one with the same excitation such that the mean-square error between the actual nonlinear and linearised systems is minimised in a statistical sense. The procedure, known as equivalent linearisation, operated directly on the equations of motion. Many developments have been proposed since the work of Caughey (Roberts and Spanos, 1990). This commonly used approach has proved useful in most applications, particularly for the random vibration analysis of systems where the nonlinear restoring force is hysteretic. For experimental applications, the extraction of a linear model requires the knowledge of the functional form of the restoring force, which is generally not the case. Hagedorn and Wallaschek (Hagedorn and Wallaschek, 1987) have developed an effective experimental procedure for doing precisely this. This work triggered the development of the concept of equivalent linear systems with random coefficients which has enjoyed some success for system identification of nonlinear systems (Soize C., 1997; Bellizzi and Defilippi, 2003).

The harmonic balance method described by Nayfeh and Mook (Nayfeh and Mook, 1995) can be also employed for linearising nonlinear equations of motion with harmonic forcing. This method has been the basis of several nonlinear system identification techniques (among others see (Yasuda et al., 1988; Benhafsi Y., 1992; Meyer et al., 2003; Ozer et al., 2005)).

For MDoF systems a suggestive way to make a transition between linear and nonlinear dynamics is through the extension of the concept of normal mode of classical linear vibration theory to nonlinear systems. In particular conditions, the concept of nonlinear normal mode (NNM) has been introduced by Rosenberg (R.M., 1966) and developed by Vakakis (Vakakis, 1997). The identification of individual NNMs may represent a limitation when considering the arbitrary motion of a nonlinear system; in this case, the NNMs are bound to interact. Several authors have used other types of non-linear modes for the identification of non-linear systems from free vibration (Hasselman et al., 1998; Hemez and Doebling, 2001).

3.2.2.2 Parametric approaches

Apart for linearization techniques, that usually are parametric, a very direct strategy to obtain a typically parametric identification algorithm consists of extending the use of time series models (Ljung, 1999) to non-linear systems. A suggestive extension is represented by NARMAX (Nonlinear ARMA with eXogeneous input) model proposed by Leontaritis and Billings (Leontaritis and Billings, 1985a,b). The NARMAX structure is general enough to admit many forms of model including neural networks, although the estimation problem becomes nonlinear and the orthogonal estimator will not work (Billings et al., 1991). In fact, the application of NARMAX to structures is extremely complex an no relevant applications to real structures are reported to date.

3.2.2.3 Non-parametric approaches

The Volterra series representation of the input/output relationship is one of the principal tools for studying weakly non-linear systems is: in this theoretical framework the problem of identification is the determination of the higher-order frequency response functions, in the frequency domain, or higher-order impulse response functions, in the time-domain, from experimental data. Usually, methods based on Volterra series representation are classed as non-parametric, like all those making use of non-linear functionals.

The structures can be tested applying loads deterministic (i.e. stepped-sine test) or stochastic in nature. In the latter case, there is quite an extensive literature about the techniques for identifying Volterra systems: one of the first attempts to determine the linear and quadratic frequency response functions of a quadratic system was performed by Tick (Tick, 1961), under the assumption that system excitation is white Gaussian noise. The hypothesis of gaussianity greatly simplifies the problem of identification but can lead to unrealistic results. This difficulty has been overcome with the formulation of identification methods which can be applied in conditions characterised by excitation with arbitrary spectral properties, defined both in the time domain (e.g. (Koukoulakis and Kalouptsidis, 2000)) and in the frequency domain (e.g. (Kim and Powers, 1993)). All these methods require the calculation of higher order statistical moments: in structural engineering applications it is not possible to obtain a number

of experimental measurements large enough as necessary to get a consistent estimate of the statistical moments of interest. The availability of a limited number of experimental data can be obviated through the time-frequency representation of the signals and the definition of instantaneous estimators of the mechanical properties to be identified (Demarie et al., 2005b).

We underline that a vast majority of identification techniques, especially non-parametric ones, variously admit heuristic versions. In this connection we shall mention neural networks, because of their universal approximation features, and neuro-fuzzy models, because of their semantic transparency (e.g. (Juditsky et al., 1995; Chassiakos A.G., 1996; Kosmatopoulos et al., 2001; Riche et al., 2001; Song et al., 2004; Liang et al., 2001; Fan and Li, 2002)).

3.2.3 Approaches based on instantaneous estimation

This class of methods was already considered in the 1960s for problems in acoustics and vibrations (Priestley, 1967), but it is only from the 1990s that it gained widespread popularity within the structural dynamics community. A survey of the analysis of non-stationary signals using time–frequency methods is available in (Hammond and White, 1996), (Hammond and Waters, 2001) and (Ceravolo, 2009).

Feldman showed how to use the traditional definition of the analytic signal and the time-domain Hilbert transform in order to identify nonlinear models of SDOF systems. The FREEVIB approach proposed in (Feldman, 1994a) is based on free vibration whereas the FORCEVIB approach proposed in (Feldman, 1994b) deals with forced vibration. These approaches can be used to construct the instantaneous damping and stiffness curves for a large class of nonlinear systems, but are only suitable for monocomponent signals (Feldman, 1997). We mention that a method for the decomposition of signals with multiple components into a collection of monocomponents signals, termed intrinsic mode functions (IMFs), was proposed in (Huang et al., 1998) and is now referred to as Huang– Hilbert transform in the time-frequency literature. The IMFs are constructed such that they have the same number of extrema and zero-crossings, and only one extremum between successive zero-crossings. As a result, they admit a well-behaved Hilbert transform. The method now enjoys several

applications in structural dynamics including linear system identification (Yang et al., 2003a,b) and damage detection (Yang J.N., 2004).

Other time–frequency representations are also suitable for the analysis of nonlinear oscillations. Linear representations have been used for instance by (Spina et al., 1996) and (Demarie et al., 2005b). An overview of the use of the wavelet transform in nonlinear dynamics can be found in (Staszewski, 2000), while among others interesting applications are reported by Newland (Newland, 1999) and Erlicher and Argoul (Erlicher and Argoul, 2007). Quadratic representations which include the Wigner–Ville distribution and the Cohen-class of distributions have also received some attention (Feldman and Braun, 1995; Bonato et al., 1997; Wang et al., 2003).

3.3 Structural identification of cable-stayed bridges

Structural identification techniques have been implemented successfully in the case of cable-stayed bridges for the identification of main structure as well as stay cables; followed by updating of numerical models (Casas, 1995; Cunha et al., 2001; Gentile et al., 2004; Casas and Aparicio, 2010). A summary of dynamic excitation methods for modal parameter identification on bridges is given in (Farrar et al., 1999) and (Cunha et al., 2001). There are mainly three types of testing methods: (1) Forced vibration tests; (2) Ambient vibration tests; and (3) Free vibration tests. Structural identification techniques are classified mainly in two types: Input-output techniques and Output-only techniques.

3.3.1 Input-output Techniques

The conventional modal testing is based on the estimation of a set of frequency response functions (FRFs) relating the applied force and the corresponding measured response at several pairs of points along the structure, with enough high spatial and

frequency resolution. The construction of FRFs requires the use of an instrumentation chain for structural excitation, vibration measurement and data acquisition and signal processing. A summary of input-output modal identification methods is given in (Cunha et al., 2006).

As input-output techniques require input force measurement for FRFs calculation, the structure undergoes forced vibration tests. Impulse hammers and electrodynamic shakers can be used with success in forced vibration tests of relatively small and medium size structures like pedestrian bridges (Cunha et al., 2006). However, when dealing with large structures, much heavier and more expensive equipments are needed, like eccentric mass or servo-hydraulic shakers. In case of large and flexible cable-stayed bridges, with significant natural frequencies in a low range, e.g. 0-1 Hz, it becomes still more difficult and costly to provide controlled excitation at high levels (Cunha et al., 2001). Moreover, the input-output methods relevant to the linear identification of cable-stayed bridges can be summarised as followings (Cunha et al., 2006):

1. Frequency domain methods: rational fraction polynomial (RFP), complex exponential frequency domain (CEFD), polyreference frequency domain (PRFD);

2. Time domain methods: autoregressive moving average (ARMA), complex exponential (CE), least square complex exponential (LSCE), polyreference complex exponential (PRCE), ibrahim time domain (ITD), eigensystem realization algorithm (ERA).

The reader can refer some literature- (Ewins, 2000) for theoretical details and (Cunha et al., 2006) for application of the above named input-output techniques.

3.3.2 Output-only techniques

In contrary to the input-only techniques, output-only techniques use only output response of the structure for modal parameter identification. The structure can undergo ambient or free vibration tests. The technological advancement in the fields of transducers and A/D converters during the last years made feasible the very accurate measurement of very low levels of dynamic response induced by ambient excitations, like wind or traffic, strongly encouraging the development of output-only modal identification methods. Moreover, for larger bridges ambient excitation is the only practical

means of exciting the structure as the ability to input significant energy into the structure, particularly at higher frequencies, by some mechanical device becomes more impractical as the size of the structure increases. Ambient excitation is also used with smaller bridges when other constraints prevent the bridge from being taken out of service during the tests. The advantages of ambient vibration tests for modal identification of bridges are listed as follows:

i) inexpensive and efficient, as no input forcing device and instrumentation is needed;

ii) avoids the shut down of traffic on the bridge;

iii) represents a real operating condition of the structure during its daily use; and

iv) applicable to small, medium and large bridge structures.

A drawback of using ambient excitation is that this type of input is often non-stationary. Also, because the input is not measured it is not known if this excitaion source provides input at the frequencies of interest or how uniform the input is over a particular frequency range. Even when measured-input excitations are used, ambient vibration sources are often still present producing undesirable and often unavoidable extraneous inputs to the structure (Farrar et al., 1999). The modal analysis involving output-only measurements presents a challenge that requires the use of special modal identification technique, which can deal with very small magnitude of ambient vibration contaminated by noise.

Though modal damping can be also identified using ambient vibration tests, the corresponding estimates are often not so accurate, and this may be a major point of concern in some applications. For instance, in case of large and slender cable-stayed bridges, where knowledge of certain damping factor is crucial for the assessment of aeroelastic instability problems, the accurate identification of modal damping factors is required (Cunha et al., 2007). In such cases, it is appropriate to perform a free vibration test, introducing an initial perturbation that can induce a free vibration response significantly higher than the ambient response. This can be done by provoking a sudden release of a mass appropriately suspended from the deck.

The output-only methods relevant to the linear identification of cable-stayed bridges can be summarised as followings (Cunha et al., 2006):

1. Frequency domain (non-parametric) methods: peak-picking (PP), frequency domain decomposition (FDD);

2. Time domain (parametric) methods: autoregressive moving average (ARMA), random decrement (RD), eigensystem realization algorithm (ERA), polyreference time domain (PRTD), Stochastic subspace identification (SSI).

The basic frequency domain peak-picking (PP) method is based on the evaluation of normalized average power spectral densities involving all the measurement points and ambient response transfer functions relating the response at each measurement point with the response at a reference point. This approach can be improved by performing a single value decomposition (SVD) of the matrix of response spectra (FDD-frequency domain decomposition method), so as to obtain power spectral densities of a set of SDoF systems, and enhanced (EFDD method) in order to extract modal damping factors estimates, through inspection of the decay of auto-correlation functions, evaluated by performing the inverse Fourier transform of the SDoF systems' power spectral densities. For theoretical details reader can refer the papers- (Brincker et al., 2001) and (Ren and Zong, 2004).

The time domain parametric methods involve the choice of an appropriate mathematical model to idealise the dynamic structural behaviouur (usually time-discrete state-space stochastic models, ARMAV or ARV models) and the identification of the values of the modal parameters so as that model fits as much as possible the experimental data, following some appropriate criterion. These methods can be directly applied to discrete response time series or, alternatively, to response correlation functions. The evaluation of these functions can be made based on their definition, using the FFT algorithm or applying the random decrement (RD) method.

A brief theoretical description of some of the techniques used in this thesis is given in the following sub-subsections.

3.3.2.1 Peak-picking method (PP)

The peak pick method is the simplest known method for identifying the modal parameters of civil engineering structures subjected to ambient excitation (Ren and Zong, 2004). The method is initially based on the fact that the FRF goes through extreme values around the natural frequencies. The frequency at which this extreme value occurs is a good estimate for the frequency of the system. In the context of ambient vibration measurements the FRF is only replaced by the auto spectra of the ambi-

ent outputs. In such a way the natural frequencies are simply determined from the observation of the peaks on the graphs of the averaged normalized power spectral densities (ANPSDs). The ANPSDs are basically obtained by converting the measured accelerations to the frequency domain by a discrete Fourier transform (DFT).

Although the input forces are not measured in ambient vibration testing, this problem has often been circumvented by adopting a derived modal parameter identification technique where the reference sensor (base station) signal is used as an “input” and the FRFs and coherence functions are computed for each measurement point with respect to this reference sensor. It not only helps in the identification of the resonances, but also yields the operational shapes that are not the mode shapes, but almost always correspond to them. The coherence function computed for twosimultaneously recorded output signals has values close to one at the resonance frequencies because of the high signal-to-noise ratio at these frequencies. Consequently inspecting the coherence function may assist to select the frequencies.

In current peak picking method, the components of the mode shapes are determined by the values of the transfer functions at the natural frequencies. Note that in the context of ambient testing, transfer function does not mean the ratio of response over input force, but rather the ratio of response measured by a roving sensor over response measured by a reference sensor. So every transfer function yields a mode shape component relative to the reference sensor. Here it is assumed that the dynamic response at resonance is only dominated by one mode. The validity of this assumption increases as the modes are better separated and as the damping in the structure is lower.

The peak picking is a kind of frequency domain based technique. Frequency domain algorithms are most popular, mainly due to their simplicity and processing speed, and also for historical reasons. These algorithms, however, involve averaging temporal information, thus discarding most of their details. Peak-picking technique has some theoretical drawbacks:

· Picking the peaks is always a subjective task;

· Operational deflection shapes are obtained instead of mode shapes;

· Only real modes or proportionally damped structures can be deduced by the method;

· Damping estimates are unreliable.

In spite of these drawbacks many civil engineering cases exist where the peak-picking technique is successfully applied. The popularity of the method is due to its implementation simplicity and its speed.

3.3.2.2 Eigensystem Realization Algorithm (ERA)

The eigensystem realization algorithm (ERA) is a time domain modal parameter identification technique, which is based on the minimum-order realization theory. The ERA can effectively extract the structural modal parameters from the impulse response data or free vibration data (Xiaodong et al., 2007).

The state space formulation of the motion differential equations of a linear structural system is given by

$$\begin{cases} \dot{x}(t) = Ax(t) + Bu(t) \\ y(t) = Cx(t) \end{cases} \tag{3.1}$$

where $x(t)$ is the state vector, which includes the displacement and velocity vectors; A is the system matrix, which contains the structural system information; B and C are the control and observation matrices, respectively; $u(t)$ and $y(t)$ are the input and output vectors, respectively.

$h_{ij}(k)$ was set as the impulse response function at the k th sampling point, where j and i denote the node numbers of the input and output, respectively. The impulse response function can be obtained from the measurement data. The structural impulse response function matrix $h(k)$, i.e. the Markov parameter matrix, is constructed as $h(k) = \{h_{ij}(k)\}$. The generalized Hankel matrix is formed by the Markov parameter matrices as follows

$$H(k) = \begin{bmatrix} h(k) & h(k+1) & \cdots & h(k+s) \\ h(k+1) & h(k+2) & \cdots & h(k+s+1) \\ \vdots & \vdots & & \vdots \\ h(k+r) & h(k+r+1) & \cdots & h(k+r+1) \end{bmatrix} \tag{3.2}$$

Decomposing the Hankel matrix $H(0)$ by using the singular-value decomposition as follows

$$H(0) = P \begin{bmatrix} D_r & O \\ O & O \end{bmatrix} Q^T \tag{3.3}$$

where D_r =diag $(d_1, d_2, ..., d_r)$, $d_1 \geq d_2 \geq ... \geq d_r > 0$ are the singular values of $H(0)$, and P and Q are the orthonormal matrices. According to the minimum-order realization theory, the system matrix A can be obtained as follows

$$A = D_r^{-1/2} P_r^T H(1) Q_r D_r^{-1/2} \tag{3.4}$$

where P_r and Q_r are the first rth columns of the matrices P and Q, respectively. A singular-value decomposition of the system matrix A is performed

$$\Psi^{-1} A \Psi = Z = \text{diag}\ (z_1, z_2, \cdots, z_i, \cdots, z_n) \tag{3.5}$$

According to the structural dynamic mechanics and the state space theory, the eigenvalue z_i is given by

$$\begin{cases} z_i = \exp(-\zeta_i \omega_i T \pm j\omega_i \sqrt{1-\zeta_i^2}\, T \\ \qquad\qquad s_i = \frac{\ln(z_i)}{T} \end{cases} \tag{3.6}$$

where T is the sampling time interval; $j = \sqrt{-1}; i = 1, 2, ..., n$; and ω_i and ζ_i are the ith modal frequency and damping ratio, respectively. Therefore, ω_i and ζ_i can be obtained as follows

$$\begin{aligned} \omega_i &= \sqrt{[\text{Re}(s_i)]^2 + [\text{Im}(s_i)]^2} \\ \zeta_i &= \frac{\text{Re}(s_i)}{\omega_i} \end{aligned} \tag{3.7}$$

ψ_i, which denotes the column vector of Ψ in Eq. 3.5 , is the ith proportional modal shape vector.

3.3.2.3 Stochastic Subspace Identification (SSI)

Stochastic subspace identification, an advanced technique for performing an operational modal analysis, is an output-only time domain method that directly works with

time data. A structural model can be described by a set of linear second-order differential equations with constant coefficient (Ren and Zong, 2004):

$$M\ddot{U}(t) + C\dot{U}(t) + KU(t) = F(t) \tag{3.8}$$

where M, C and K are the time-invariant mass, damping and stiffness matrices respectively of the structure associated with the n generalized coordinates comprising the vector $U(t)$. $F(t)$ is a time-dependent vector of input forces. Eq. 3.8 can be rewritten as a first-order system of differential equations in a number of ways. One commonly used reformulation in a state-space representation is:

$$\dot{x}(t) = A_c x(t) + B_c u(t) \tag{3.9}$$

where the state vector $x(t) = [U(t), \dot{U}(t)]^T$, the state matrix A_c and the system control influence coefficient matrix B_c are defined by

$$A_c = \begin{bmatrix} 0 & I \\ -M^{-1}K & -M^{-1}C \end{bmatrix}, \quad B_c = \begin{bmatrix} 0 \\ M^{-1}B_2 \end{bmatrix}, \quad F(t) = B_2 u(t) \tag{3.10}$$

Furthermore, the output vector of interest, $y(t)$, can be a part of, or a linear combination of system states, such as

$$y(t) = Cx(t) + Du(t) \tag{3.11}$$

Here C is a real output influence coefficient matrix and D is the out control influence coefficient matrix. Eqs. 3.9 and 3.11 constitute a continuous-time state-space model of a dynamic system. Continuous-time means that the expressions can be evaluated at each time instant. Of course this is not realistic because experimental data are discrete in nature. The sample time and noise are always influencing the measurements. After sampling the continuous-time state-space model looks like

$$\begin{cases} x_{k+1} = Ax_k + Bu_k \\ y_k = Cx_k + Du_k \end{cases} \tag{3.12}$$

where $x_k = x(k\Delta t)$ is the discrete time state vector; $A = \exp(A_c \Delta t)$ is the discrete state matrix; $B = [A - I]\, A_c^{-1} B_c$ is the discrete input matrix. Eq. 3.12 forms a discrete-time state-space model of a dynamic system.

In practice there are always system uncertainties including process and measurement noises. The process noise is due to disturbances and modeling inaccuracies, whereas the measurement noise is due to sensor inaccuracy. If the stochastic components (noise) are included Eq. 3.12 can be extended to consider process noise w_k and measurement noise v_k described as continuous-time stochastic state-space model

$$\begin{cases} x_{k+1} = Ax_k + Bu_k + w_k \\ y_k = Cx_k + Du_k + v_k \end{cases} \tag{3.13}$$

It is difficult to determine accurately the individual process and measurement noise characteristics and thus some assumptions are required. Here the process noise w_k and measurement noise v_k are assumed to be of zero-mean, white and with covariance matrices:

$$E\left[\begin{pmatrix} w_p \\ v_p \end{pmatrix}\begin{pmatrix} w_q^T & v_q^T \end{pmatrix}\right] = \begin{pmatrix} Q & S \\ S^T & R \end{pmatrix}\delta_{pq} \tag{3.14}$$

where E is the expected value operator and δ_{pq} is the Kronecker delta. The sequences w_k and v_k are assumed statistically independent of each other.

In the practical problem of civil engineering structures, the reality is that only the responses of a structure are measured, while the input sequence u_k remains unmeasured. In the case of ambient vibration testing, it is impossible to distinguish the input term u_k from the noise terms w_k, v_k in Eq. 3.13. Modeling the input term u_k by the noise terms w_k, v_k results in a purely stochastic system:

$$\begin{cases} x_{k+1} = Ax_k + w_k \\ y_k = Cx_k + v_k \end{cases} \tag{3.15}$$

The input is now implicitly modelled by the noise terms w_k, v_k. However the white noise assumptions of these noise terms cannot be omitted. The consequence is that if this white noise assumption is violated, for instance if the input contains also some dominant frequency components in addition to white noise, these frequency

components cannot be separated from the eigenfrequencies of the system and they will appear as poles of the state matrix A.

Eq. 3.15 constitutes the basis for the time-domain system identification through ambient vibration measurements. There have been several techniques to realize system identification algorithms based on Eq.3.15. The stochastic subspace identification algorithm is probably the most advanced method known up to date for ambient vibration measurement system identification. The subspace method identifies the state space matrices based on the measurements and by using robust numerical techniques such as QR-factorization, singular value decomposition (SVD) and least squares. Loosely said, the QR results in a significant data reduction, whereas the SVD is used to reject the noise (assumed to be represented by the higher singular values). Once the mathematical description of the structure (the state space model) is found, it is straightforward to determine the modal parameters (by an eigenvalue decomposition): natural frequencies, damping ratios and mode shapes.

The key concept of SSI is the projection of the row space of the future outputs into the row space of the past outputs. The main difference with the proceeding algorithms is that the subspace algorithm is data driven instead of covariance driven so that the explicit formation of the covariance matrix is avoided. It is clear that the stochastic subspace identification is a time domain method that directly works with time data, without the need to convert them to correlations or spectra. Common to all system identification methods for ambient vibration measurements, it is not possible to obtain an absolute scaling of the identified mode shapes (e.g. mass normalization) because the input remains unknown.

3.3.3 Instantaneous identification of nonlinear systems

In the identification of structures characterized by localized nonlinearities, the definition of instantaneous time-frequency estimators (Ceravolo, 2004) may result particularly useful. The information obtained from a nonlinear identification session may both offer a clue in choosing reliable structural models, and forecast the dynamic behavior in non-operational conditions.

The idea underlying time-frequency identification techniques is that, for certain

classes of structural response signals, the availability of a limited number of structural response signals and the availabìlity of a limited number of experimental data can be partially obviated by taking into account the localization in time of the frequency components of the signals.

Time-frequency identification algorithms are usually formulated to find the model parameters that minimize the error between a given time-frequency model, $T(t, f)$, and the time-frequency transform of the measured signal, $T_{x_m}(t, f)$. In principle, a time-frequency model can be identified from the following minimization (Ceravolo et al., 2010):

$$\begin{cases} \varepsilon(\mathbf{p}) = \left\| \tilde{T}(t, f; \mathbf{p}) - T_{x_m}(t, f) \right\| \\ \rightarrow \mathbf{p}_{id} = \arg \left[\min_{\forall \mathbf{p}} \varepsilon(\mathbf{p}) \right] \end{cases} \tag{3.16}$$

where $\mathbf{p}$ is the global vector of the parameters of the time-frequency model and x_m indicates the measured system response (displacement, velocity, or acceleration).

When parameters to be estimated retain a temporal significance (e.g., time-varying systems) it may prove advantageous to perform an instantaneous minimization so as to obtain a punctual estimate of $\mathbf{p}$:

$$\begin{cases} \varepsilon(t, \mathbf{p}) = \left| \int_{-\infty}^{+\infty} \left[\tilde{T}(t, f; \mathbf{p}) - T_{x_m}(t, f) \right] df \right| \\ \rightarrow \mathbf{p}_{id}(\bar{t}) = \arg \left[\min_{\forall \mathbf{p}, t=\bar{t}} \varepsilon(t, \mathbf{p}) \right] \end{cases} \tag{3.17}$$

For every given instant, $\bar{t}$, the minimization leads to an associated optimal $\mathbf{p}_{id}(\bar{t})$. The most convenient minimization form and algorithm will depend on the specific application. In the implementation of Eqs. 3.16 and 3.17, the analytic signal is usually preferred to the measured one, since it avoids cross-term interference between positive and negative frequencies.

A simple way of introducing the time localization of frequency components consists of pre-windowing the signal around a particualr time t, calculating its Fourier transform, and doing that for each time instant t. Accordingly, the 'Short -Time Fourier Transform'- STFT- , of a signal $x(t\prime)$ is defined as:

$$STFT_x^{(\gamma)}(t, f) = \int_{-\infty}^{+\infty} x(t') \gamma^*(t - t') e^{-j2\pi f t'} dt' \tag{3.18}$$

where $\gamma(t)$ is a short-time analysis window centered around t. The superscript * denotes complex conjugation. Such transform as well as its squared magnitude, called 'Spectrogram' (SPEC), is frequently used in many application fields, including modal decoupling, system identification, etc.

3.4 Conclusions

Structural identification is an efficient and accurate way to obtain modal properties of civil engineering structures. However, cable stayed bridges require special attention while designing the structural identification tests due to inherent flexibility and nonlinearity. Output-only techniques with ambient and free vibration tests are very suitable for cable-stayed bridges. A majority of the output-only identification techniques, e.g. ERA and SSI work in the time domain are able to determine modal parameters accurately and efficiently. However, to understand the time dependent behaviour of a structure, vibration reduction systems as well as nonlinearities, the techniques based on time-frequency instantaneous estimators are very helpful.

CHAPTER 4

MODAL IDENTIFICATION OF A LARGE CURVED CABLE-STAYED FOOT-CYCLE BRIDGE

4.1 Introduction

In this chapter, an application is presented. The system identification of a recently built twin deck foot-cycle bridge, i.e. the 'Ponte del Mare' was performed under an Europeon project 'HITUBES'. In detail, the bridge is instrumented in several sensor configurations to obtain its modal properties in a wide range of modes. Ambient and free decay excitations are used. Moreover, the effectiveness of a passive damper system connected to the bridge has been tested too. To understand the complex behaviour of the structure-damper system, the instantaneous estimates of frequency, damping and amplitude is performed. A deck-cable interaction has been detected.

The chapter is organised as follows: the characteristics of the case study are presented in section 4.1, whilst in section 4.3 the dynamic test campaign is described. The ensuing results of the dynamic identification that includes modal frequencies, mode shapes, structural damping and cable identification, are reported in section 4.4, whereas the instantaneous estimates are presented in section 4.5. Finally in section 4.6, the important conclusions are drawn.

4.2 The 'Ponte del Mare' bridge in Pescara

4.2.1 Description of the Structure

The "Ponte del Mare" footbridge is located at the mouth of the Pescara river and is part of a programme for the rehabilitation of the urban area. The footbridge is a cable-stayed structure and it consists of two curved decks sustained by cables connected to a tilted mast, as illustrated in Figure 4.1. The outer deck is dedicated to pedestrians,

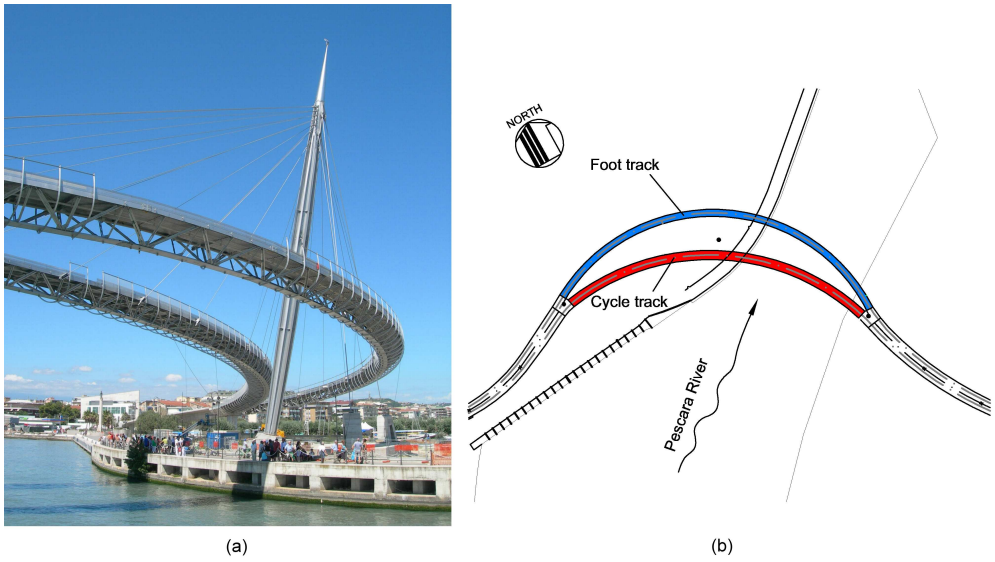

Figure 4.1: The 'Ponte del Mare' footbridge

whilst the inner deck is for cyclists; both decks have constant radius, approximately 80 m and 100 m and their length is 173 m and 148 m, respectively. The two decks are constituted by a spatial steel-concrete composite truss connected to two prestressed concrete access ramps. The two sections of the bridge are reported in Figure 4.2. The mast is made of steel filled with concrete and its inclination is about 11° with respect to the vertical axis. Two anchorage cables connect the top of the mast to the ground in order to reduce the displacements. In sum, the complexity of the structure

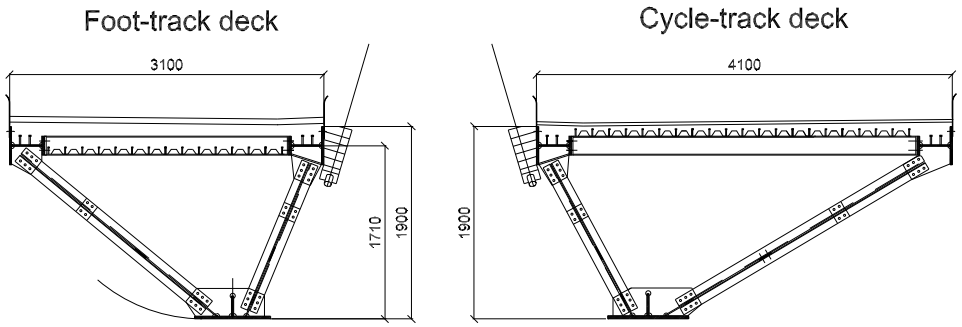

Figure 4.2: Deck cross-sections. Dimensions in mm

is evident. Just note that the bottom chord of the foot-track deck (FTD) is in tension, whilst the chord of the cycle-track deck (CTD) is conversely in compression because of the eccentricity of the cable attachments and of the curve orientation with respect to the mast position.

4.2.2 FE model

A preliminary FE model of the bridge was developed in ANSYS^{TM}, as shown in Figure 4.3. Beam, shell and solid elements were used to accurately model both the main steel decks and the access ramps. The modal characteristics, i.e. the frequencies and mode shapes supplied by the model, were used to design the dynamic tests. In such structures many close modes are typically observed, which in an identification perspective calls for proper testing set-ups. Moreover, the complexity is increased by the high flexural-torsional couplings in each deck and between the two decks. All these issues must be carefully taken into account when designing the structure and the dynamic identification tests. In this case, the investigated frequency range spans from 0 to about 2.5 Hz, because it includes the main natural modes of both the foot- and cycle- track decks, that interact with wind and anthropic actions.

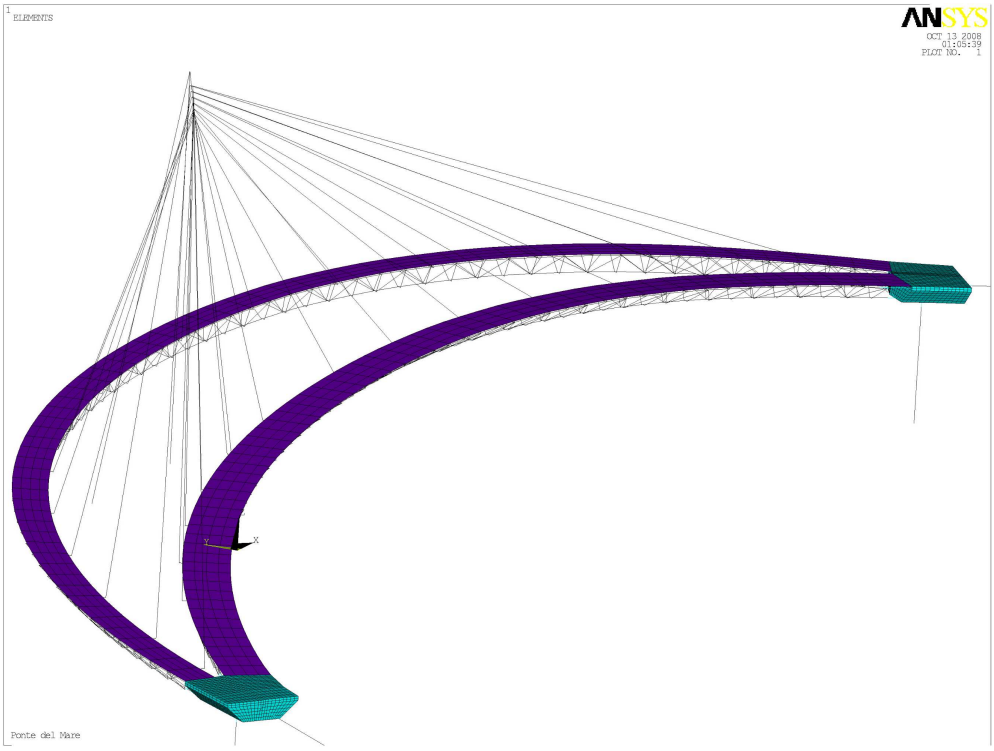

Figure 4.3: 3D FE model of the ’Ponte del Mare’ footbridge

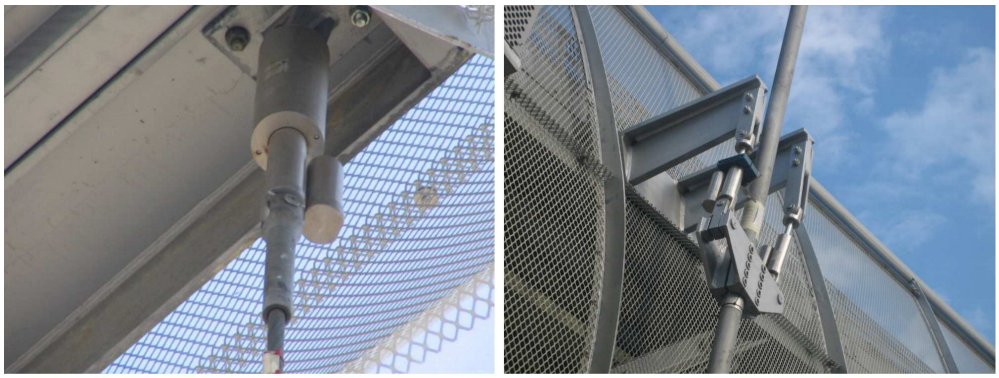

(a) (b)

Figure 4.4: (a) Damper A; (b) Damper C

4.2.3 Description of dampers

The structural high flexibility associated to low damping capabilities, entails higher vulnerability and sensitivity to dynamic phenomena. In fact, a comprehensive wind analysis, that also made use of wind tunnel tests, showed an aeroelastic instability for the first mode related to a galloping phenomenon for a wind speed smaller than the design speed (Tondini et al., 2010). Moreover, even the dynamic pedestrian analysis highlighted discomfort conditions for pedestrians when crossing over the bridge (Tondini et al., 2010). Thus, the introduction of vibration absorption devices was deemed necessary and a passive system was designed by increasing dissipation, while limiting changes in modal frequencies and shapes. The design choice consisted of devices, whose dissipating mechanism was based on viscous fluid damping, i.e. deformation of a viscous elastic fluid. In detail, two dampers - Dampers A, see Figure 4.4(a) - were conceived in order to connect the foot-track deck to the ground, whilst two others - Dampers B - do the same with the cycle-track deck. Eventually, a further couple - Dampers C, see Figure 4.4(b) – were envisaged to link the mast anchorage cables, that act as reaction points, to the foot-track deck. Their location is shown in Figure 4.5, whilst Table 4.1 reports their characteristics provided for by the producer (Industriale, 2009) on the basis of experimental tests. Briefly, a linear force-velocity relationship was requested, and the damping coefficients c_A and c_B were initially cali-

brated in such a way as to prevent aeroelastic instability for the first mode. Then, they were adjusted in order to meet with the comfort requirements expressed in terms

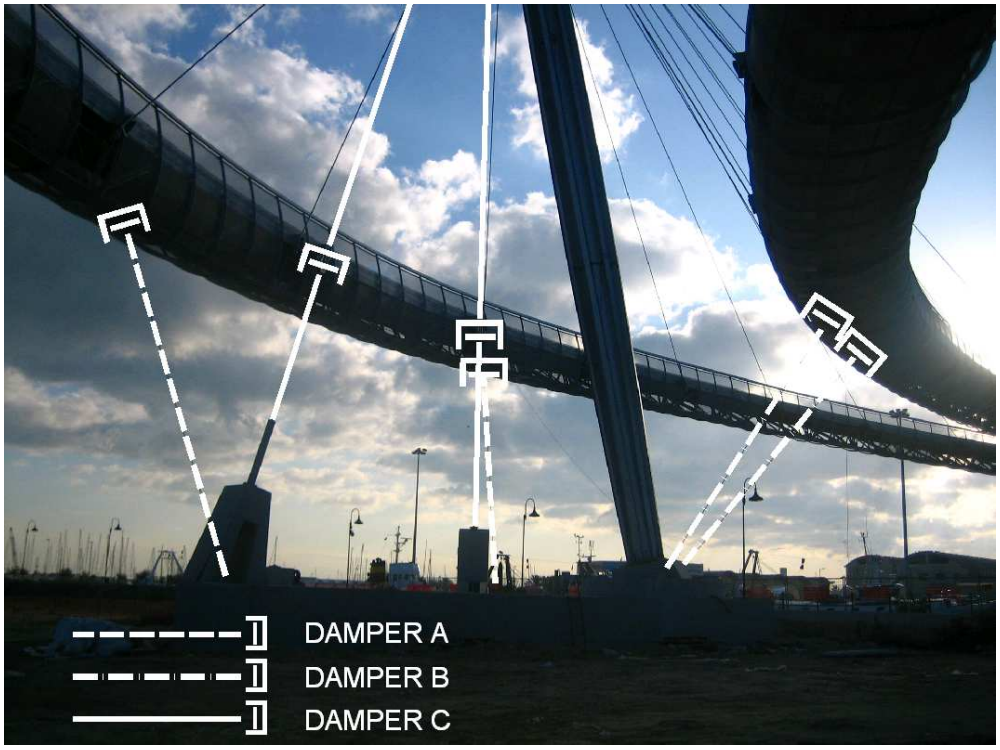

Figure 4.5: Dampers location

of acceleration limits as recommended by the SETRA guidelines (SETRA., 2006), that were developed for the assessment of the vibrational behaviour of footbridges under pedestrian loading. Owing to the architectural constraints, the damper positioning was optimised so as to guarantee effectiveness against the modes relevant for the wind and the pedestrian action. To improve the structure aesthetic appeal, the initial idea of employing rigid tubes for connecting Dampers A and B to the ground was discarded. Thus, slender cables were used, and in order to keep them in traction, Dampers A and B were endowed with a spring, whose stiffness was chosen at the lowest possible value in order to avoid changes in modal frequencies and mode shapes. Conversely, an additional stiffness for Dampers C was not reckoned necessary, since the attachment points were represented by the anchorage cables.

Table 4.1: Damper characteristics

	Damper A	Damper B	Damper C
Producer Typology	FIP/OVE*3.2/140-1.3	FIP/OVE*3.0/140-1.3	FIP/OTP*1.5/80
No. of units	2	2	2+2
Damping constant [kNs/m]	128.0	349.0	794.2
Spring stiffness [kN/m]	127.6 (+-5%)	127.6 (+-5%)	-

4.3 Design of the dynamic tests

4.3.1 Tests set-up

Due to its structural complexity, the dynamic identification test design is crucial. Firstly, the excitation sources have to be chosen. Since the structure is large and the forced vibration techniques were reckoned unsuitable, it was decided to perform output-only tests based on: i) ambient-induced vibrations, and ii) free decay vibrations caused by released masses. If the former test type is associated to low vibration levels, the latter is conversely designed to induce high vibration amplitudes, so that to be allowed to investigate whether the dynamic response of the structure changes according to the oscillation level. In a second stage, on the basis of the dynamic behaviour of the FE model described in subsection 4.2.2, the sensor locations have to be selected in such a way as to allow the discrimination of the experimental modes.

In the tests, sensors consisted of piezoelectric accelerometers connected to a 24-channels acquisition system. During all the tests, 8 accelerometers were kept fixed and were used as reference set-up (Link), as illustrated in Figure 4.6(f). So it was possible to correlate the mode shapes obtained from the various accelerometer configurations, whilst the mode shape construction along the whole structure was hence achieved. The complexity of the bridge led to design the set-ups with the following purposes of: a) uniformly installing the instrumentation on the structure; b) monitoring

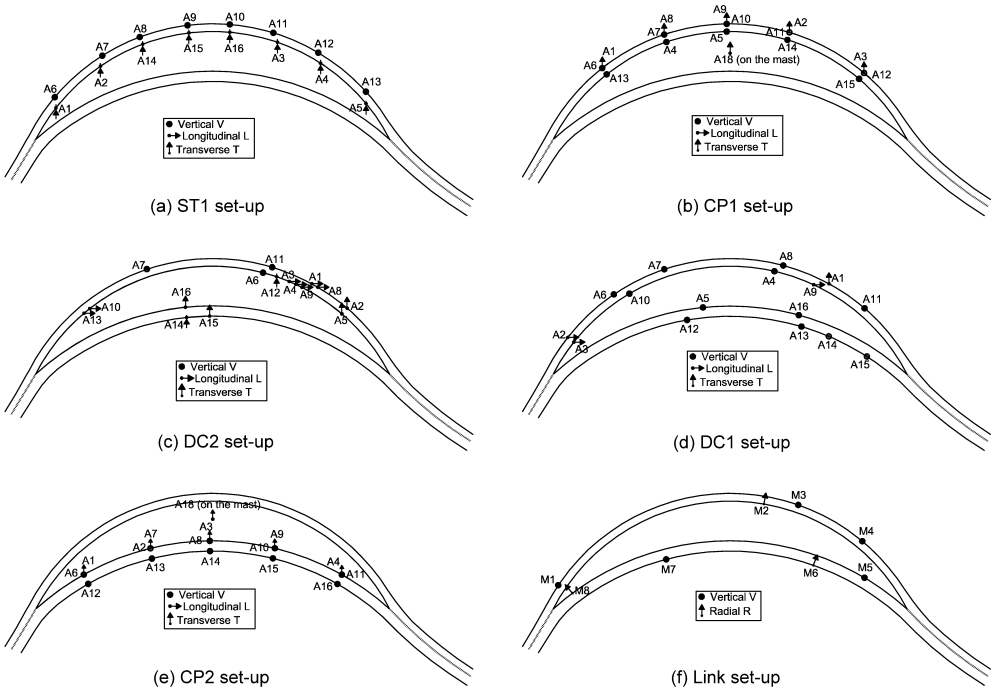

Figure 4.6: Accelerometer set-ups used in the dynamic identification tests

the mast displacement; c) discriminating flexural torsional modes; d) highlighting the flexural deformation of the two decks; e) decoupling specified modes. The sensors belonging to the Link set-up were positioned under the bridge, because it is part of the device system that will be monitoring the whole structure for one year. The accelerometers of the other set-ups were instead attached to the footbridge pavement for more convenience, as illustrated in Figure 4.7(a). The curve internal and external sides of both pavements were properly instrumented so as to appreciate torsional modes as well. Finally, some cables, in particular the longest ones, were also instrumented, see Figure 4.7(b), in order to obtain the modal frequencies. These measurements were very important for the detection of possible deck-cable interactions.

(a) (b)

Figure 4.7: Accelerometer attachments: a) on the deck pavement; b) on a cable

4.3.2 Tests in ambient vibration conditions

For each presented set-up, ambient vibration tests were performed twice: i) with disconnected and ii) with connected dampers, respectively. Since the structure is a footbridge, the wind was the main vibration source. The acquisition was at least 5 minutes long with a sampling frequency of 100 Hz. Figure 4.8 and Figure 4.9 present a few acceleration time-histories related to two set-ups without and with dampers. In Figure 4.8(b) a significant decrease of vibrations with respect to Figure 4.8(a) is

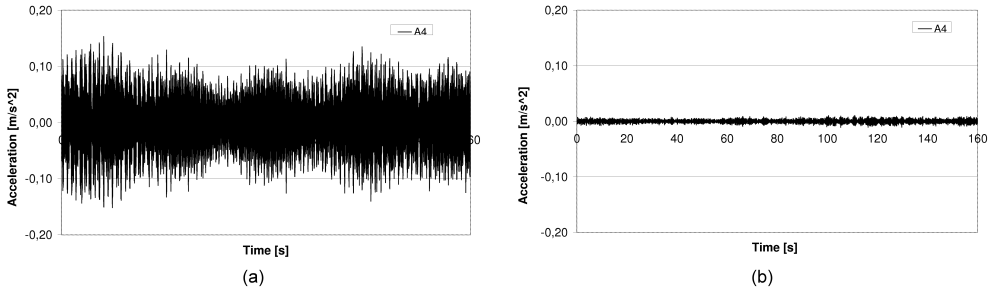

Figure 4.8: Ambient vibration time-histories: a) DC1 w/o dampers relative to position A7 (see Figure 4.6(d)); b)DC1 with dampers relative to position A7 (see Figure 4.6(d))

observed, whilst Figure 4.9(b) shows an opposite behaviour in relationship to Figure 4.9(a). Table 4.2 reports on the relevant wind speed measured by two anemometers

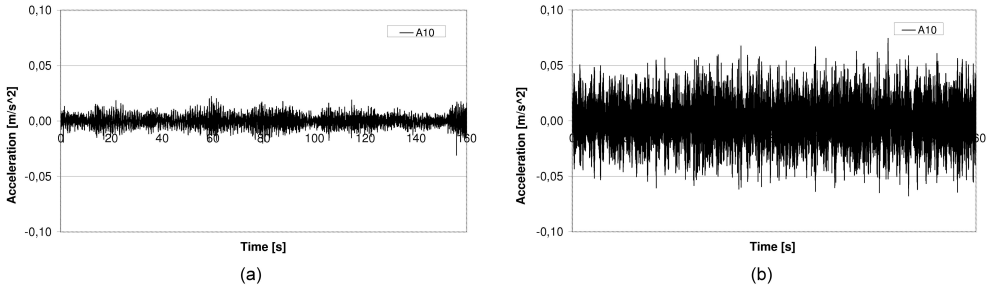

Figure 4.9: Ambient vibration time-histories: a) CP2 w/o dampers relative to position A10 (see Figure 4.6(e)); b)CP2 with dampers relative to position A10 (see Figure 4.6(e))

located at the top of the mast (v1) and below the foot-track deck (v2). Wind data show that, when the dampers were connected, the wind speed (v1) was almost double than the speed measured for the same CP2 set-up but w/o dampers, this being still insufficient to activate the dampers. In other words, there are hints that under ambient noise the vibration control system is basically inactive. In fact, ambient-induced vibrations are associated with low amplitude levels, of the order of millimetres, while dampers activate over a certain threshold. Such finding is confirmed later in section 4.5.

Table 4.2: Wind speed at the time of the acceleration time-histories reported in Fig. 8 and Fig. 9.

day and hour	set-up	v1[m/s]	v2[m/s]
28 Oct 2009-14.10	DC1 w/o dampers	3.81	3.83
29 Oct 2009-18.17	DC1 with dampers	2.12	1.41
28 Oct 2009-18.01	CP2 w/o dampers	1.76	0.82
29 Oct 2009-14.46	CP2 with dampers	3.32	2.83

4.3.3 Tests in free-decay conditions

Tests with released masses, classified as free decay, were also performed. Masses of about 2700 kg were hung at the bottom chord of the decks and then released, so that to intensely excite the bridge, see Figure 4.10. The release points were selected on the basis of the participation of the modes of interest, as predicted by the FE model. In these acquisitions the sampling frequency was set at 1000 Hz. The vibration amplitude observed was of the order of centimetres, high enough to fully activate the dampers when connected to the structure. This is made evident in Figure 4.11 and Figure 4.12, where unlike Figure 4.8 and Figure 4.9, a reduction in vibration levels is observed for both set-ups.

4.4 Output-only identification in time domain

This section reports on the results of a time-domain identification from acceleration signals measured on the structure without and with dampers. In detail, the ambient vibration signals were processed with the SSI method, whilst the free decay data were elaborated by means of the ERA technique. The SSI method was employed as the benchmark to extract all dynamic characteristics.

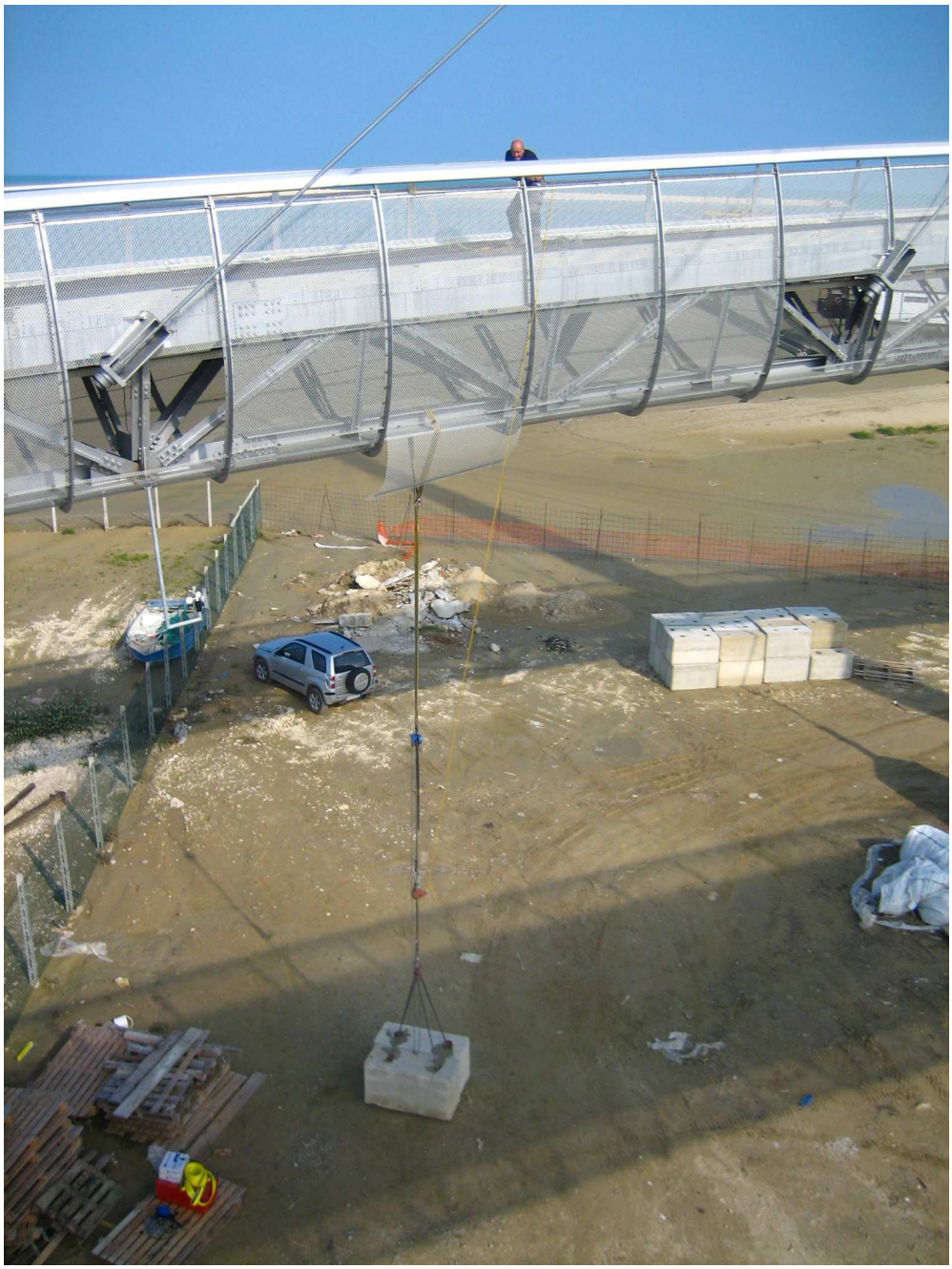

Figure 4.10: Free vibration tests: set-up of the released mass

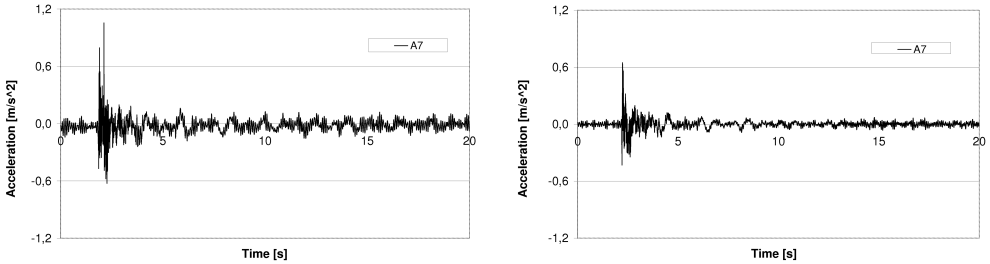

Figure 4.11: Free decay time-histories: a) DC1 w/o dampers relative to position A7 (see Figure 4.6(d)); b)DC1 with dampers relative to position A7 (see Figure 4.6(d))

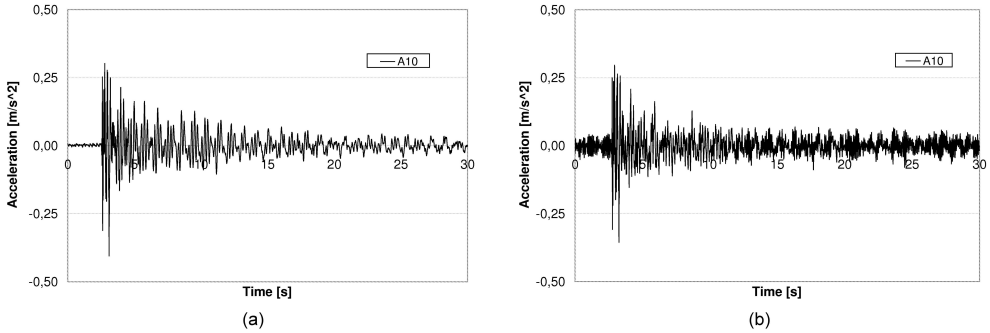

Figure 4.12: Free decay time-histories: a) CP2 w/o dampers relative to position A10 (see Figure 4.6(e)); b)CP2 with dampers relative to position A10 (see Figure 4.6(e))

4.4.1 Modal frequencies

Figure 4.13 compares the identified modal frequencies without and with dampers, respectively. In spite of the fact that the dampers were designed to avoid variations in the dynamics properties, their introduction appears to have produced a significant stiffening effect, because a slight increase of the modal frequencies occurred. In this respect, the first mode was the most sensitive to the damper activation, along with mode 3 and 10. In principle, the increase in damping is expected to depend on the participation of the dampers in single modes. In actual practice, damping is seen to be influenced by modal amplitude, as it will be shown in section 4.5.

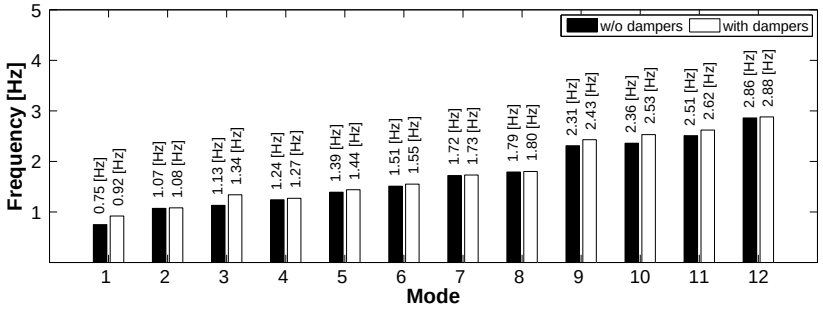

Figure 4.13: Identified modal frequencies w/o and with dampers

4.4.2 Mode shapes

While identified modes are typically complex valued, models currently used in dynamics to date are unable to assimilate frictional or non-linear dissipation phenomena. This makes it difficult to extract useful information from mode phases, which for simplicity are not included in the modal shape representations (Figures 4.14-4.16).

The vertical components of mode shapes for both decks are shown in Figure 4.14, where the structure without and with dampers is considered. MAC (Allemang, 2002) checks were then performed between the experimental mode shapes related to the structure without and with dampers. Table 4.3 summarises the global MAC values for

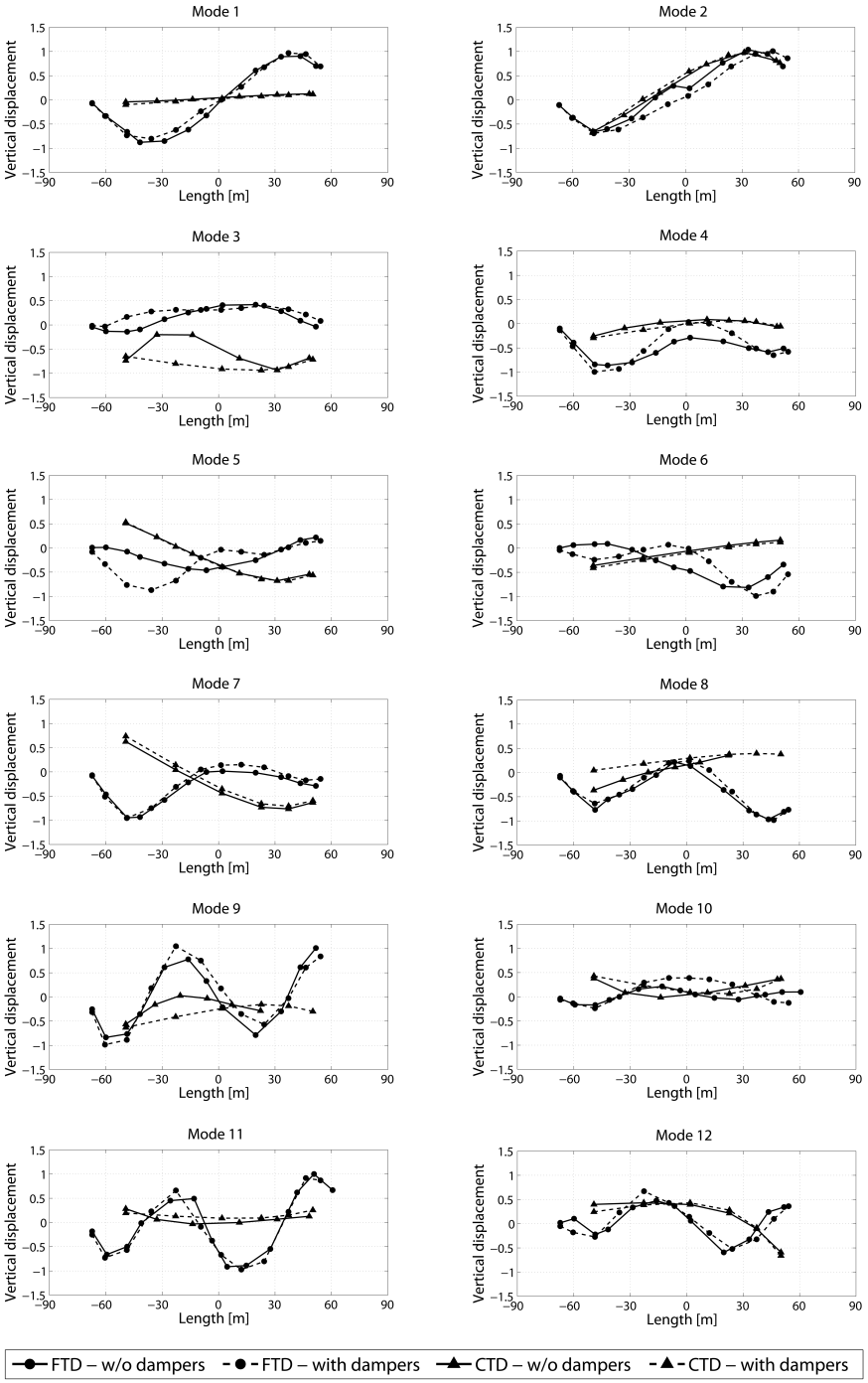

Figure 4.14: Vertical component of the identified mode shapes w/o and with dampers, respectively. For simplicity the mode phases were forced to 0 or π.

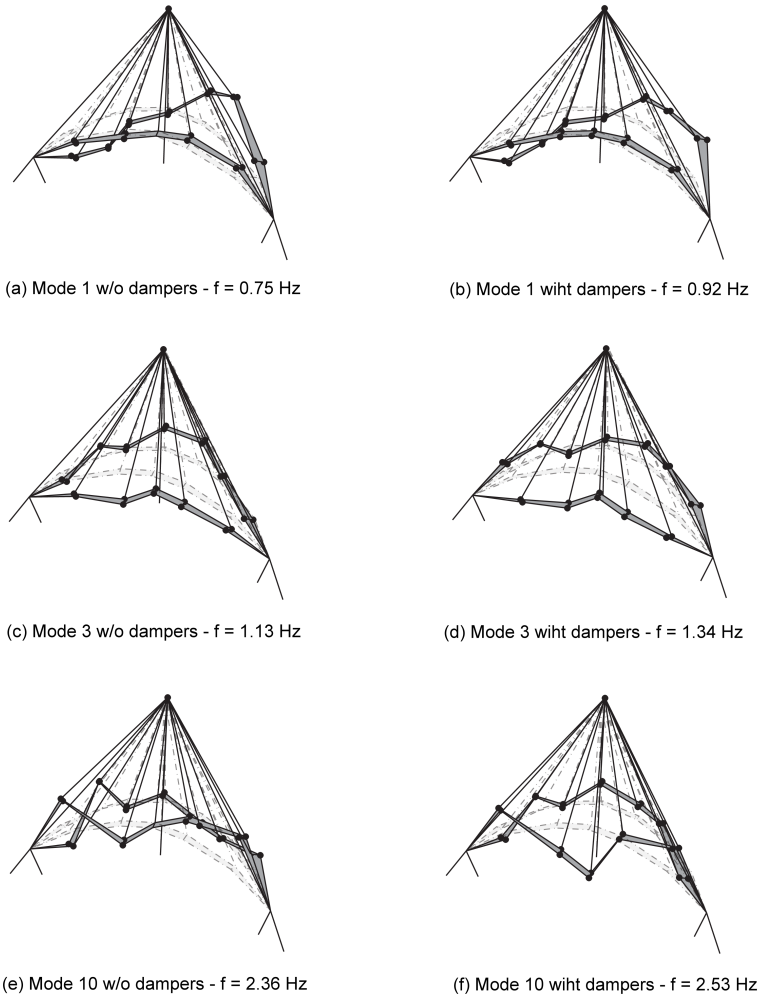

Figure 4.15: 3D views of three of the identified modes w/o and with dampers. For simplicity the mode phases were forced to 0 or π.

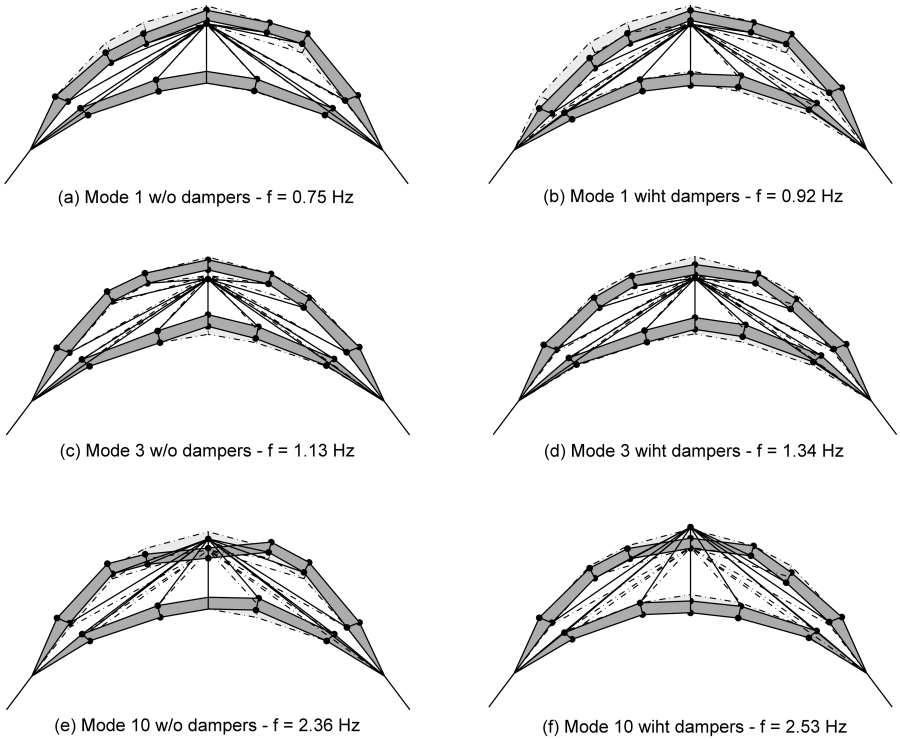

Figure 4.16: In plan views of three of the identified modes w/o and with dampers. For simplicity the mode phases were forced to 0 or π.

the identified modes and shows that dampers strongly affect modes that have relevant displacements at points where dampers are located, that is near the midpoint of the bridge. The outcomes show that the correlation between the modes is basically very good, and they highlight that the dampers affected the mode shapes. Figure 4.15 reports 3D views of some of the modes that experienced important changes, including their lateral component. In particular modes 10 and 11 appear to have been strongly affected also in their lateral component (e.g. see mode 10 in Figure 4.16).

Table 4.3: MAC between experimental mode shapes of the structure w/o and with dampers

		MODES WITH DAMPERS											
		1	**2**	**3**	**4**	**5**	**6**	**7**	**8**	**9**	**10**	**11**	**12**
MODES WITHOUT DAMPERS	**1**	**0.97**	0.33	0.01	0.02	0.06	0.14	0.02	0.01	0.04	0.02	0.05	0.01
	2	0.33	**0.97**	0.01	0.00	0.03	0.01	0.02	0.00	0.06	0.05	0.00	0.01
	3	0.01	0.01	**0.84**	0.04	0.00	0.03	0.00	0.00	0.03	0.13	0.12	0.01
	4	0.02	0.00	0.04	**0.92**	0.08	0.26	0.03	0.09	0.00	0.00	0.01	0.01
	5	0.06	0.03	0.00	0.08	**0.69**	0.10	0.13	0.01	0.03	0.02	0.01	0.01
	6	0.14	0.01	0.03	0.26	0.10	**0.70**	0.08	0.19	0.01	0.00	0.04	0.00
	7	0.02	0.02	0.00	0.03	0.13	0.08	**0.95**	0.05	0.01	0.01	0.01	0.01
	8	0.01	0.00	0.00	0.09	0.01	0.19	0.05	**0.91**	0.01	0.06	0.03	0.01
	9	0.04	0.06	0.03	0.00	0.03	0.01	0.01	0.01	**0.93**	0.06	0.27	0.09
	10	0.02	0.05	0.13	0.00	0.02	0.00	0.01	0.06	0.06	**0.57**	0.11	0.16
	11	0.05	0.00	0.12	0.01	0.01	0.04	0.01	0.03	0.27	0.11	**0.72**	0.08
	12	0.01	0.01	0.01	0.01	0.01	0.00	0.01	0.01	0.09	0.16	0.08	**0.86**

MAC between experimental and FE modes were also calculated. The result was that the model is verified only on lower modes. This finding is due many factors, such as the intrinsic limitations of the model, the modifications that the real structure was subjected to during its construction, the effect of non-structural elements etc.

4.4.3 Modal damping

As above stated, modal damping estimates obtained by applying output-only methods tend to be affected by the inherent non-stationarity of ambient excitation. Moreover, the dampers, as illustrated in subsections 4.3.2 and 4.3.3, seem not to be effective for low vibration levels. The chart given in Figure 4.17(a) confirms these two obser-

vations. In fact, the modal damping of the structure provided for with dampers is for some modes less in relationship with the structure without damping devices, what appears to be in some contrast with the design assumptions.

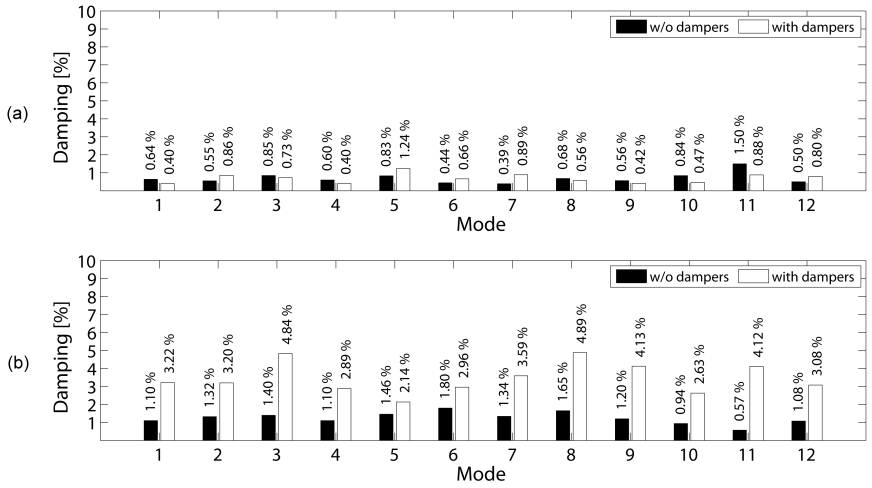

Figure 4.17: Modal damping estimates: a) ambient vibration data (from SSI method); b) free decay data (from ERA method)

The modal damping extracted from free-decay records is reported in Figure 4.17(b) as supplied by the ERA. The installation of the dampers entailed for each mode an increase in dissipation, which for the first and the third modes is seen to increase by a factor of 3. The damping obtained for the first mode, considering the approximations of the aerodynamic and structural models, results to be reliable and sufficient to guarantee the bridge safety with respect to the ultimate limit state related to the wind action. In fact, such value is higher than 2.5%, an amount considered necessary to avoid a galloping phenomenon for the first mode at a wind speed lower than the design speed. Moreover, even the structure without dampers exhibited an increase in modal damping when compared to the values obtained from ambient vibration records through the SSI. This latter finding suggests that the bridge dissipation strongly depends on vibration levels; thus requiring more thorough investigations as presented in section 4.5.

4.4.4 Cable identification

A dynamic identification of bridge cables was also performed. Simple numerical checks indicate that some cables, especially the longest ones, exhibit low natural frequencies that may possibly interact with the structure global modes, as actually reported in section 4.5. In detail, the N8E, N7E, N5E and N4W cables were instrumented under ambient vibrations. Their location is reported in Figure 4.18.

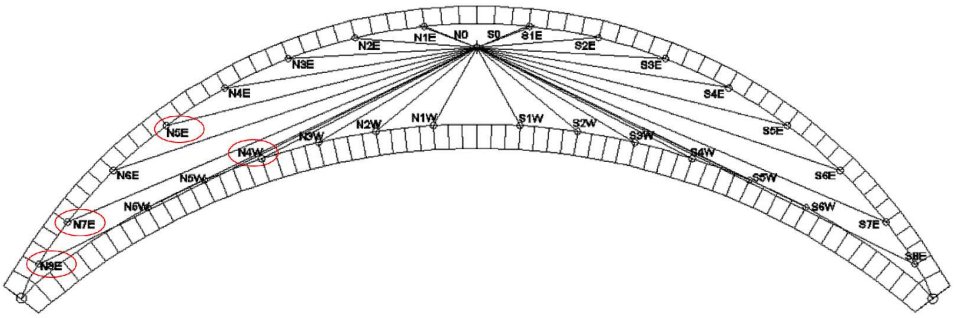

Figure 4.18: Location of instrumented cables

The corresponding frequency spectra in terms of Power Spectral Density (PSD) are presented in Figure 4.19, while the experimental frequencies are reported in Table 4.4. There, each cable is attached with hinges at the ends, L is the cable length, m defines the cable mass per unit length and f_n is the modal frequency of mode n. Each spectrum indicates neat vibrating string multiples of the cable first frequency. Moreover, the first and the second modal frequency of cable N8E are close to the first and fourth modal frequency of the deck. This hints a possible cable-deck interaction as numerically confirmed later on.

Modal estimates, resulting from the application of the SSI method on the same signals, are close to those obtained from peak picking (Table 4.4). For instance, the first frequency of cable N8E was estimated at 0.83 Hz with 0.18% damping, in agreement with literature data (Macdonald and Daniell, 2005).

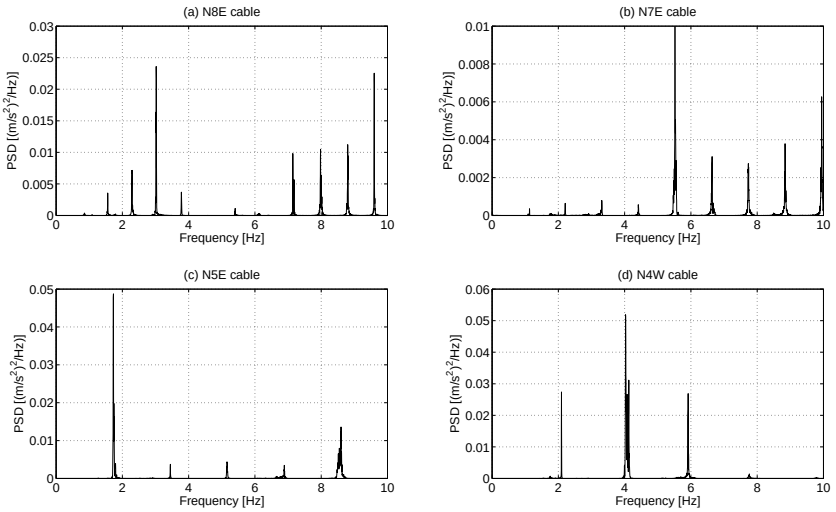

Figure 4.19: Frequency spectra of the cables

Table 4.4: Dynamic identification of the cables obtained from peak picking

Cable	L[m]	m[kg/m]	f1[Hz]	f2[Hz]	f3[Hz]	f4[Hz]	f5[Hz]
N8E	80.0	20.2	0.86	1.56	2.30	3.02	3.78
N7E	73.7	10.7	1.13	2.21	3.31	4.41	5.52
N5E	55.7	10.7	1.72	3.45	5.15	6.89	8.59
N4W	46.9	10.7	2.09	4.04	5.91	7.75	9.80

4.5 Instantaneous identification of the dampers

This section covers time-dependent effects in the bridge response due to the non-stationarity of the excitation source; the dependency of the bridge dynamic characteristics on the vibration amplitude is also discussed. In this respect, time-frequency estimators (Ceravolo, 2004) were used to give an insight into the instantaneous properties of the first vibration mode, as being the most important from a vibration control viewpoint.

4.5.1 Structure without dampers

4.5.1.1 Ambient vibration tests

As a first stage, the study focused on signals measured on the structure with inactive dampers under ambient vibration. For instance, Figure 4.20 reports the time-history of the M3 vertical sensor belonging to the Link set-up located as illustrated in Figure 4.6(f). The signal was acquired according to the ST1 set-up test.

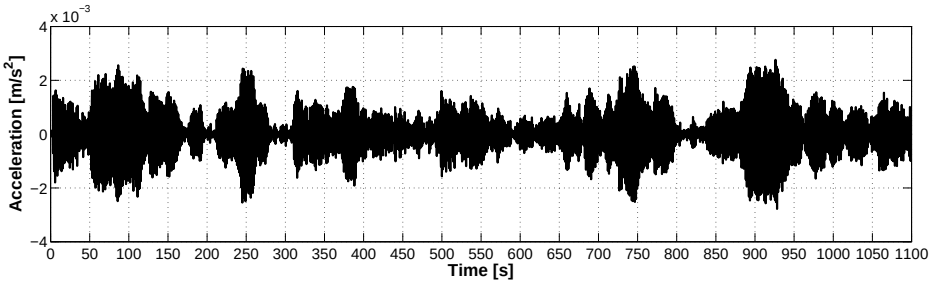

Figure 4.20: Vertical acceleration time-history from ambient vibration (channel M3, ST1 set-up acquisition, structure w/o dampers)

This signal is used to compute the spectrogram depicted in Figure 4.21 that in turn is employed to extract the instantaneous estimates (IE) of frequency, damping and amplitude as shown in Figure 4.22.

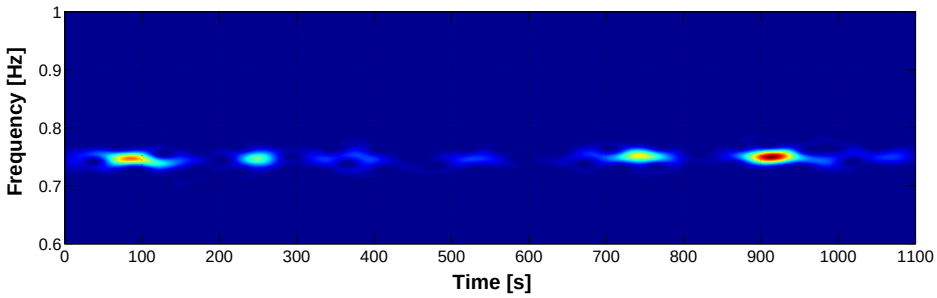

Figure 4.21: Spectrogram obtained from the signal of Figure 4.20

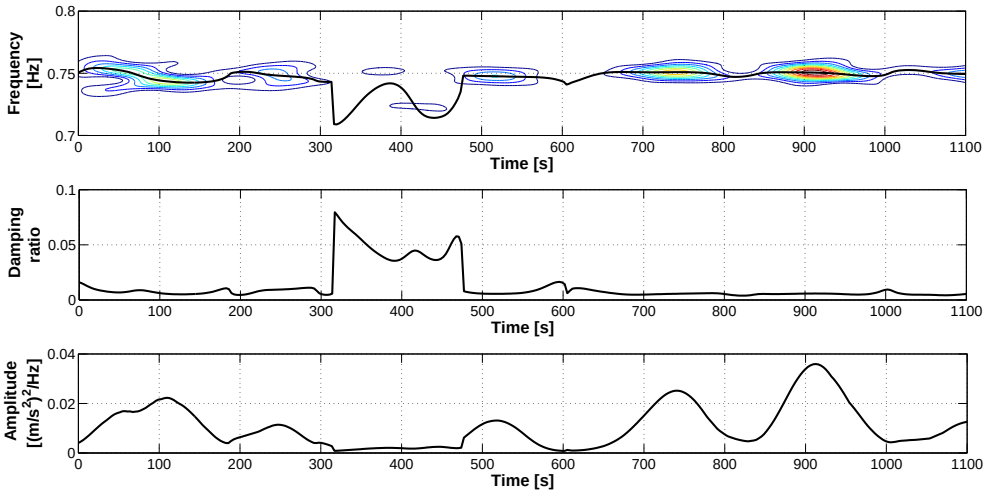

Figure 4.22: Instantaneous estimates of frequency, damping and amplitude of the first mode obtained from ambient vibration tests (channel M3, ST1 set-up acquisition, structure w/o dampers)

The instantaneous frequency and damping are quite stable along the acquisition - apart for a brief time interval - thus highlighting a great consistency. The window length of the spectrogram depends on the de-correlation length of the process (Ceravolo, 2004) and requires the availability of a first estimate for damping. The results of the previous numerical simulations conducted on linear systems in stationary conditions (Ceravolo, 2004) can be approximated by means of the simple rule $H=433\cdot\zeta^{-1.33}$, where H is the windowing length in samples and ζ is the damping. In this case, the value assumed for the damping is that supplied with by time-domain techniques, as reported in subsection 4.4.3.

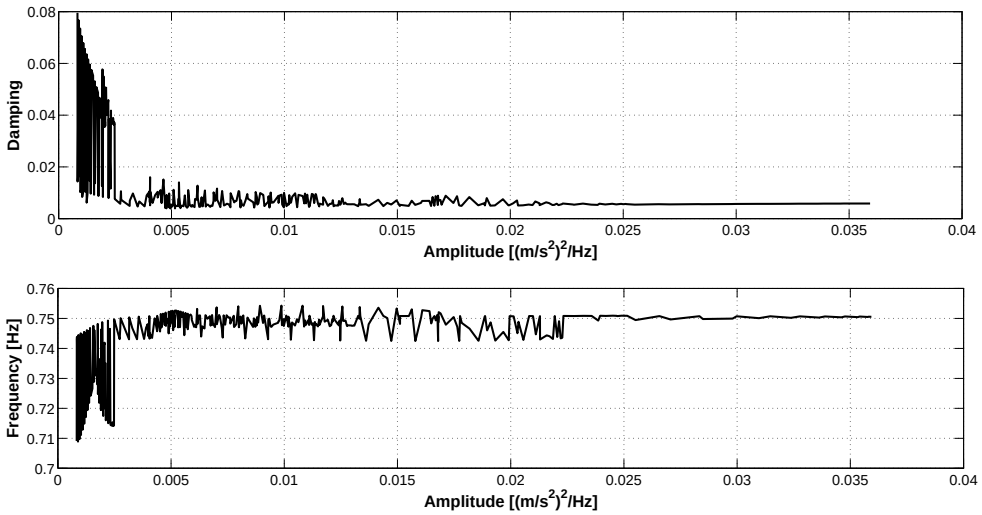

Figure 4.23: Frequency and damping estimates versus instantaneous amplitude from ambient vibration data(channel M3, ST1 set-up, structure w/o dampers)

Then, the frequency and damping estimates are correlated to the instantaneous amplitude as reported in Figure 4.23 and can be noted that for high amplitude values their estimate converges to stable values, as expected (Ceravolo, 2004). In order to confirm the reliability of the identification process, also the stabilisation diagram, resulting from a SSI session performed on the same acquisition record, is plotted relative to the first mode (Figure 4.24). The stabilisation diagram provided the following values: f = 0.75 Hz and ζ = 0.64%.

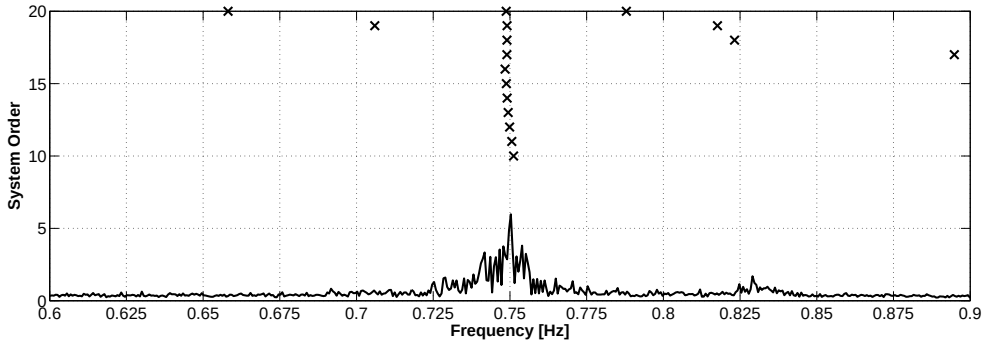

Figure 4.24: Sample stabilisation diagram for ambient vibration record limited to the frequency range of interest(channel M3, ST1 set-up, structure w/o dampers)

4.5.1.2 Free decay tests

Figure 4.25 reports a sample of vertical acceleration time-history caused by free vibrations on the structure with inactive dampers. A preliminary ERA identification provides the following values for the first mode: f = 0.74 Hz and ζ = 0.91%. The frequency value is basically the same as that found through ambient vibration data. Then, the instantaneous estimate of frequency, damping and amplitude was obtained from the spectrogram illustrated in Figure 4.26. The instantaneous estimates depicted in Figure 4.27 show a stable and neat frequency at 0.75 Hz, corresponding to the first mode as previously found, while modal damping appears to slightly increase with vibration amplitude.

4.5.2 Structure provided with dampers

The analyses presented in this section are analogous to those described in subection 4.5.1, but refer to the bridge with dampers.

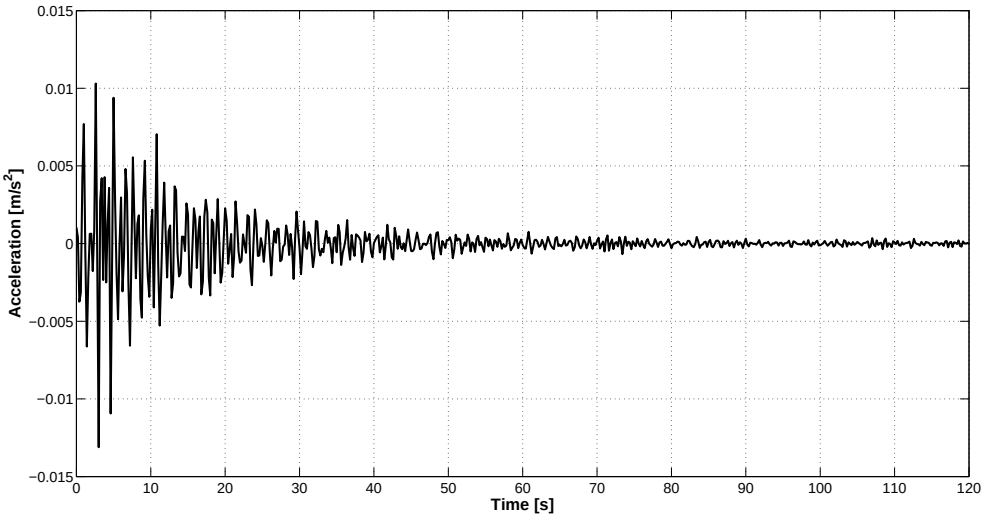

Figure 4.25: Vertical acceleration time-history caused by free vibrations(channel M1, ST1 set-up, disconnected dampers)

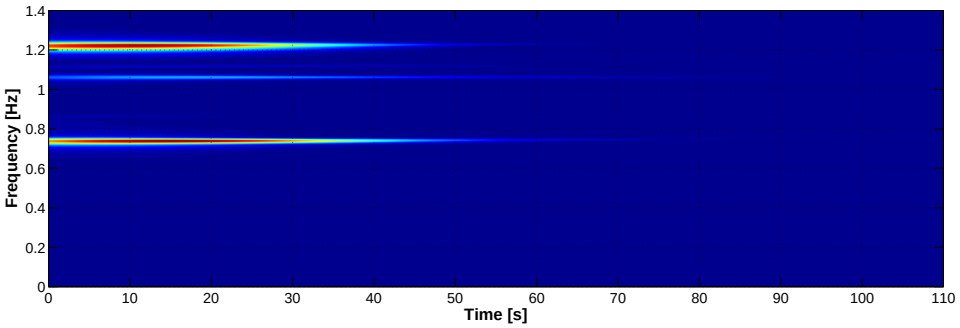

Figure 4.26: Spectrogram obtained from the signal of Figure 4.25

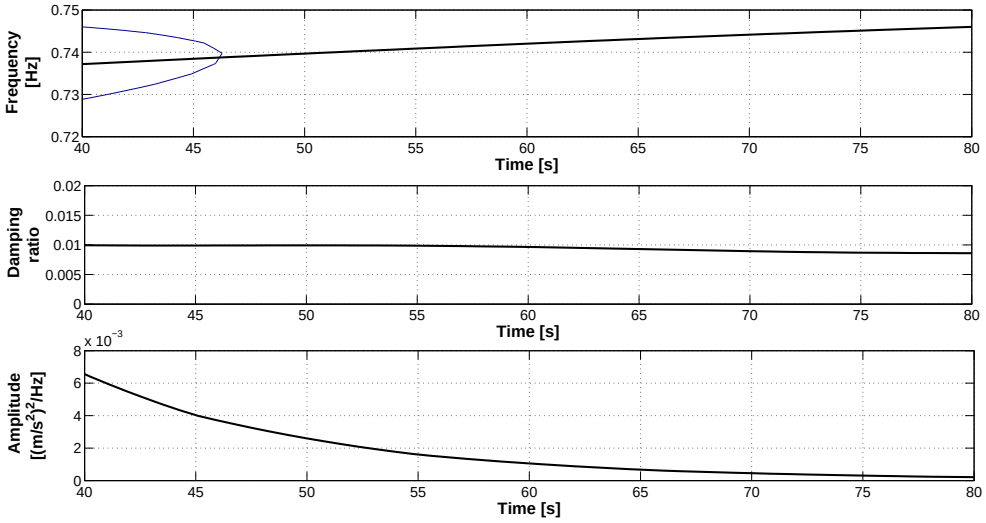

Figure 4.27: Instantaneous estimates of frequency, damping and amplitude of the first mode obtained from free decay tests (channel M1, ST1 set-up, structure w/o dampers)

4.5.2.1 Ambient vibration tests

Figure 4.28 reports the time-history measured by the M3 vertical sensor during ambient vibration tests related to the ST1 set-up, while Figure 4.29 illustrates the associated spectrogram. The latter figure highlights the two following spectral lines that are continuously excited during the entire length of the acquisition: 1) the upper one corresponds to a frequency value of 0.92 Hz, which is the first frequency of the structure with dampers, as identified by the SSI method from ambient vibration data; 2) the lower one corresponds to 0.84 Hz, a value that is very close to the first frequency of the N8E cable, as reported in subsection 4.4.4 .

Due to this interaction between the longest cable and the deck, the instantaneous structural frequency ridge depicted in Figure 4.30 experiences optimisation problems in some time-segments, thus providing thoroughly unreliable estimates. However, if the frequency and damping estimates are correlated to the instantaneous amplitude as reported in Figure 4.31, it can be noted that the values from this single identification session tend to approach those obtained by systematically applying the SSI

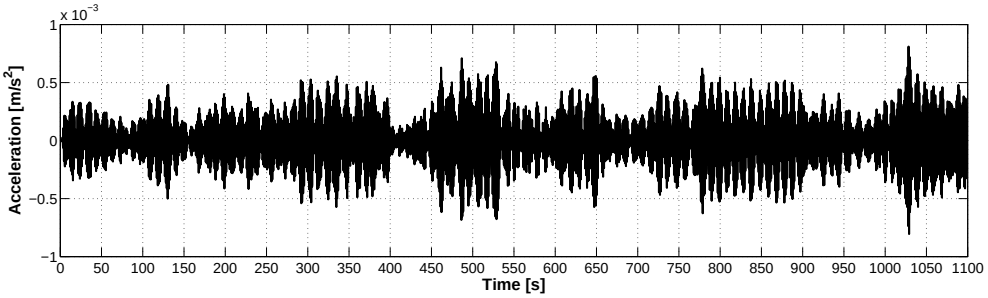

Figure 4.28: Vertical acceleration time-history from ambient excitation(channel M3, ST1 set-up acquisition, structure with dampers)

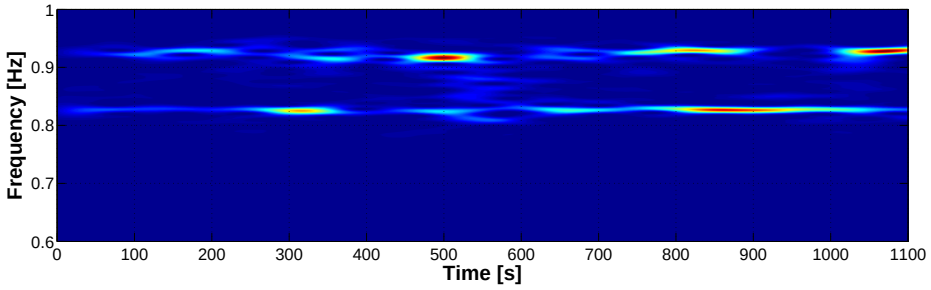

Figure 4.29: Spectrogram obtained from the signal of Figure 4.28

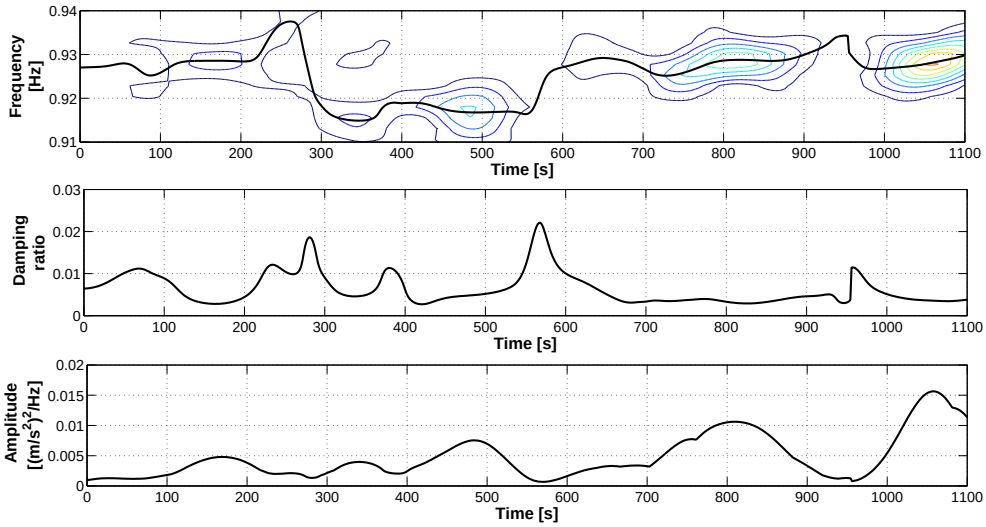

Figure 4.30: Instantaneous estimates of frequency, damping and amplitude of the first mode obtained from ambient vibration tests (channel M3, ST1 set-up acquisition, structure with dampers)

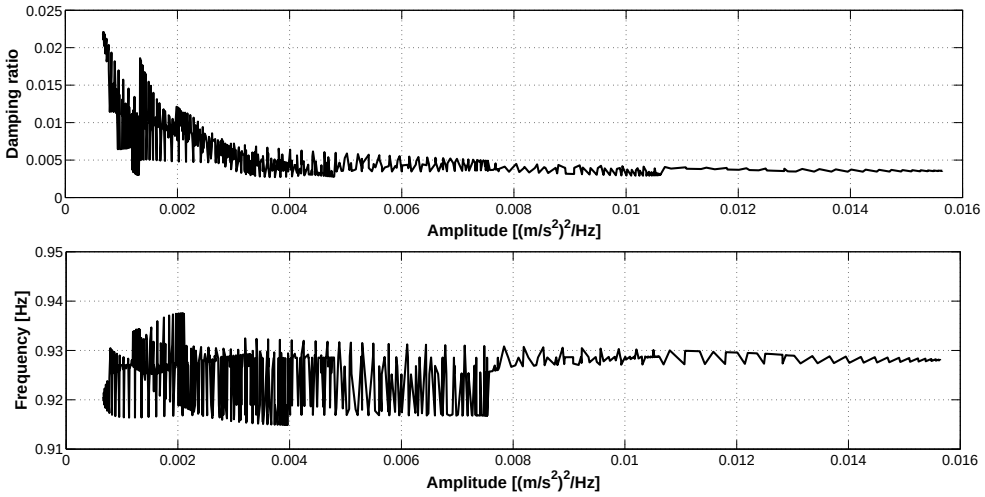

Figure 4.31: Frequency and damping estimates versus instantaneous amplitude from ambient vibration data(channel M3, ST1 set-up, structure with dampers)

technique, i.e. f = 0.93 Hz and ζ = 0.40% (see subsections 4.4.1 and 4.4.2). It is worth pointing out that ambient vibration signals are much longer than the ones of free decay tests and their spectrograms are not affected by boundary effects.

Also in this case, the stabilisation diagram, represented in Figure 4.32, provides a check on the previous findings, showing the first frequency at 0.93 Hz and a further spike in correspondence of the N8E cable frequency. Conversely, the frequency at 0.75 Hz that characterised the first mode of the structure without dampers vanishes.

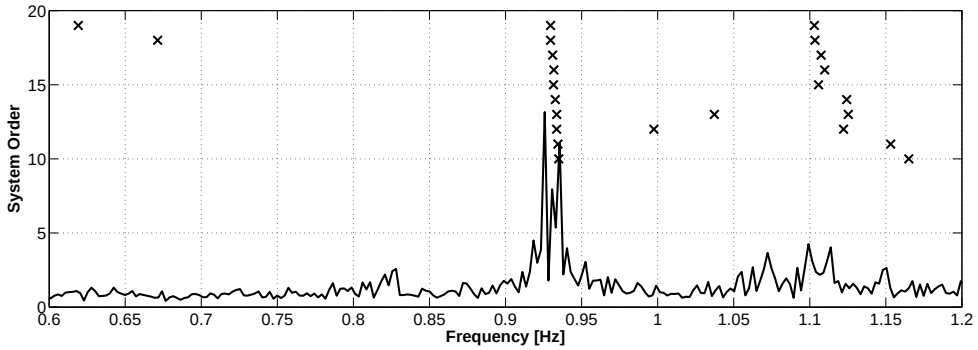

Figure 4.32: Sample stabilisation diagram for ambient vibration record limited to the frequency range of interest(channel M3, ST1 set-up, structure with dampers)

Table 4.5 summarises the modal estimates related to the first mode, as derived from ambient vibration signals, without and with dampers. The results refer to a single record. So they are not directly comparable to the values reported in Figure 4.13 and Figure 4.17.

4.5.2.2 Free decay tests

Figure 4.33 represents a sample free decay signal measured on the bridge with dampers. The associated spectrogram, which is depicted in Figure 4.34, shows an intense component at the start of the acquisition at 0.75 Hz that decreases with time, while is observed a continuous trail at 0.84 Hz, i.e. the N8E cable first frequency. This

Table 4.5: Summary of the modal properties of the first structural mode obtained with different identification techniques from ambient vibration signals (ST1 set-up acquisition)

	w/o dampers (SSI)	w/o dampers (IE)	with dampers (SSI)	with dampers (IE)
Frequency[Hz]	0.75	0.75	0.93	0.93
Damping[%]	0.64	0.59	0.40	0.41

is confirmed by the instantaneous frequency estimate, as shown in Figure 4.35, that sets at 0.75 Hz for high amplitude values.

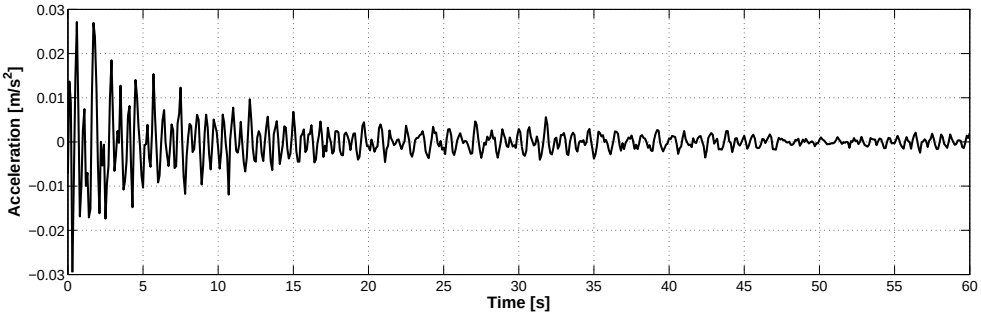

Figure 4.33: Vertical acceleration time-history caused by free vibrations(channel M1, ST1 set-up, structure with dampers)

Then, after about 70 s, it jumps up to 0.92 Hz, namely the first modal frequency obtained from ambient vibration data that corresponds to low oscillation levels. In other words, it seems that the structure with dampers behaves like a threshold system: for high vibration levels the dampers become fully active and, as assumed in the design process, they seem not to affect the bridge stiffness; conversely, at low excitation levels, dampers are not effective, mainly because of friction and connection slacks, and they act as stiffeners. In fact, for small displacements (order of mm) the stiffness introduced by the dampers is expected to be of the same order as that of cables, which is in the range 6500-8000 kN/m. In more detail, stiffness values provided by the producer (Industriale, 2009) induce in the finite element (FE) model used for

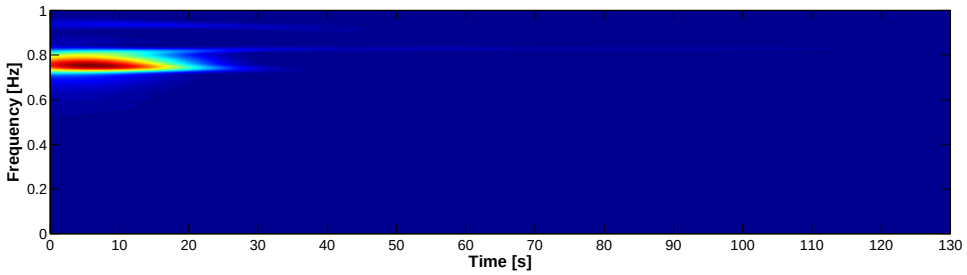

Figure 4.34: Spectrogram obtained from the signal of Figure 4.33

preliminary analyses a 22% increase in the first modal frequency (see Figure 4.36), this being in substantial agreement with the experimental outcomes. Figure 4.36(a) shows the first mode shape when the dampers are fully active, i.e. for high vibrations levels, whilst Figure 4.36(b) illustrates the first mode shape where the dampers are replaced by their inherent stiffness at small displacements. Figure 4.37(a) and Figure 4.37(b) highlight the difference in vertical component of the first mode shape for the two decks.

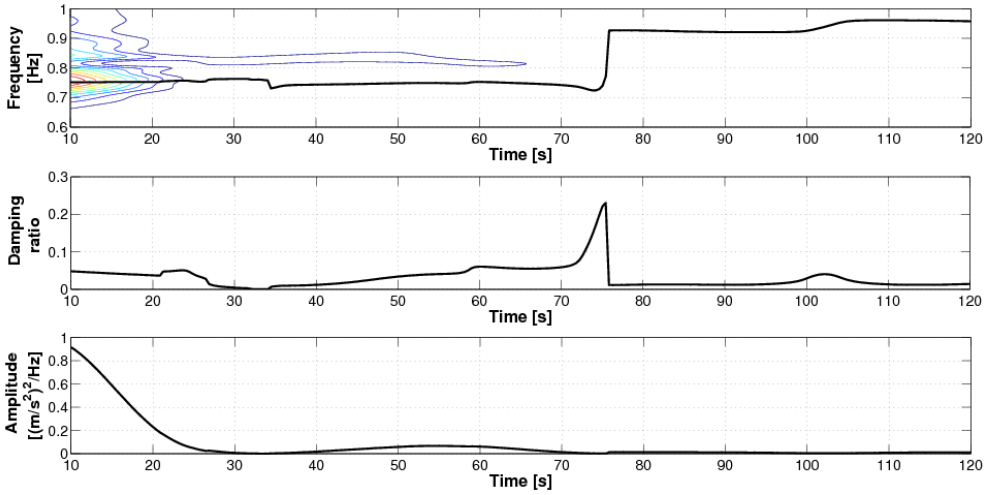

Figure 4.35: Instantaneous estimates of frequency, damping and amplitude of the first mode obtained from free decay tests (channel M1, ST1 set-up acquisition, structure with dampers)

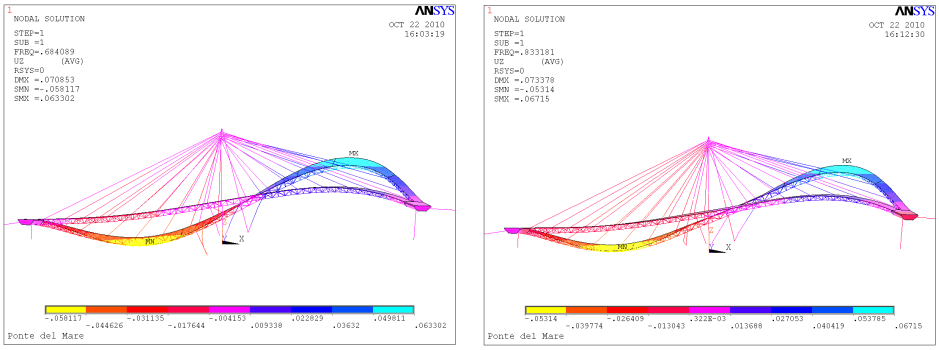

(a) (b)

Figure 4.36: Mode shape 1 as supplied by the preliminary FE model: a) model with fully active dampers; b) FE model where the dampers are replaced by their inherent stiffness at small displacements

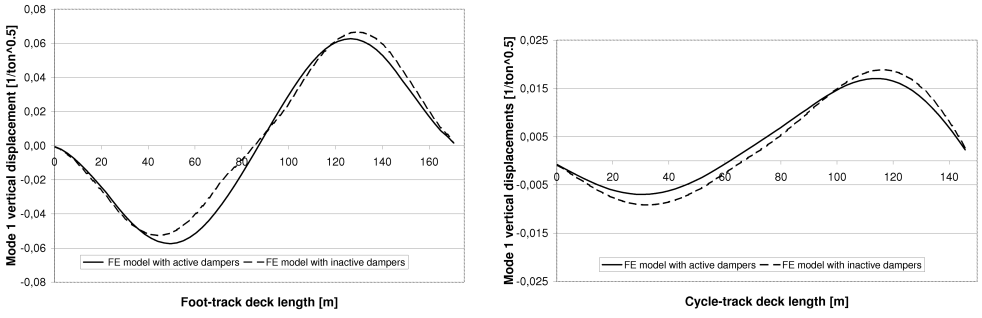

(a) (b)

Figure 4.37: Comparison of FE vertical component of mode shape 1 with active and inactive dampers respectively. a) Foot-track deck and b) cycle-track deck.

It is worth reminding that time-domain techniques applied to the structure with dampers were unable to discriminate the component at 0.75 Hz, as documented by Figure 4.13. Based on the new findings, it was possible to separate this component also with time-domain techniques.

Except for the initial part of the decay, damping estimates tend to be affected by the frequency component of N8E cable. At any rate, instantaneous damping increases with amplitude (Figure 4.38), this being fully consistent with the results supplied by time-domain identification techniques.

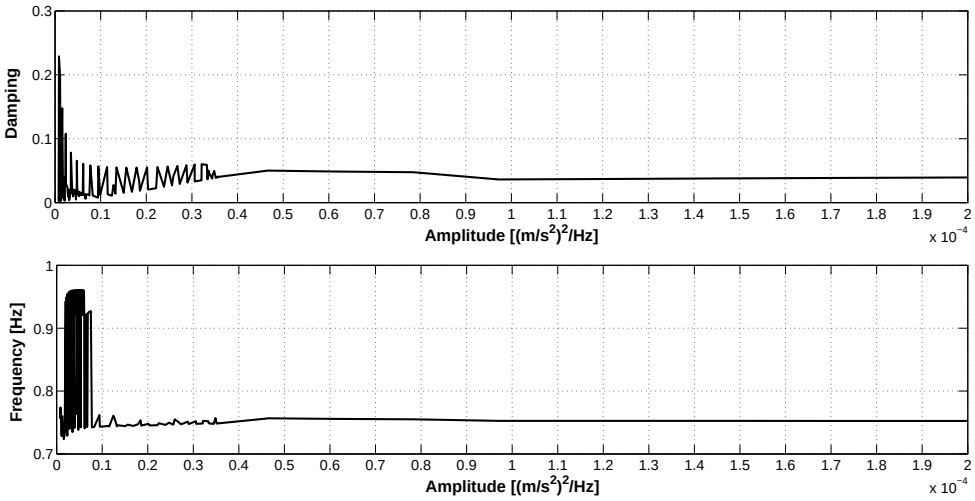

Figure 4.38: Frequency and damping estimates versus instantaneous amplitude from free decay data(channel M1, ST1 set-up, structure with dampers)

4.6 Conclusions

This chapter has presented the effectiveness of the vibration reduction system in a complex cable-stayed footbridge characterised by two curved decks. A passive control system was designed and installed to avoid premature aeroelastic instability

and to control human-induced vibrations. The complex dynamic behaviour and the uncertainties related to the numerical modelling led to a modal testing campaign of the bridge without and with dampers. Output-only ambient vibration tests, associated with low vibration levels, showed that the damping devices were basically inactive, owing to friction and connection slacks. In addition, for such low oscillation amplitudes the dampers caused a stiffening effect that had not been envisaged earlier in the design process. Free decay tests, which were performed by released masses, did produce high vibration levels. In the latter tests, dampers showed a good absorption capacity and the damping doubled or even trebled on some of the modes. In order to clarify these outcomes, modal quantities were instantaneously calculated, based on time-frequency identification techniques. A thorough analysis of dynamic response signals revealed that the structure with dampers actually behaved like a threshold system: i) for low vibration levels the dampers were still, so that they performed as constraints that stiffened the structure; ii) for high vibration levels, the dampers became fully working and, as required at the design stage, they did not significantly affect the main frequencies. Moreover, a deck-cable interaction between one of the longest cables and the first global mode was detected.

CHAPTER 5

MODEL BASED IDENTIFICATION OF A LARGE CURVED CABLE-STAYED FOOT-CYCLE BRIDGE AND UPDATING TECHNIQUES

5.1 Introduction

A preliminary FE model does not represent always the real behaviour of a complex structure, such as in the case of the 'Ponte del mare' footbridge. The reason rests in the limitations of the analytical modelling of all features of a complex structure. Therefore, it is necessary to utilize experimental data obtained during the identification process to improve the FE model. Model updating is a well known and established technique to perform this task. In this chapter, a brief review on model-updating techniques are given. Moreover, the initial FE model of the 'Ponte del mare' footbridge is modeified to better represent changes during construction phase. Then, the same model is updated utilizing the sensitivity-based model updating technique. The result is discussed and important conclusions are derived.

5.2 Model updating techniques

There are two main complementary approaches to the calibration of a model: a model-driven and a data-driven approach. The nature of the problem changes depending on the type of approach which is pursued.

In the case of the model-driven methods the parameters of the model (or at least part of them) are unknown and must be obtained from the measured data. In this case a version of the model is constructed using physical laws based on first principles. Then the model parameters are changed by means of some optimisation techniques to fit the measured data. This procedure is commonly known as Model Updating (MU).

The data-driven approach consists in a forward evaluation and it is treated as a Statistical Pattern Recognition (SPR) problem. Differently from the model-driven methods, in this approach the knowledge of the phenomena ruling the structural behaviour is not derived from physical laws implemented in a model but is extracted directly from data or based on a priori information, if available. In its broader sense pattern recognition consists in the labelling of a sample of measured data according to a series of pre-defined classes.The pattern recognition algorithm is trained to recognise the correspondence between samples of data and type classes (Bonato et al., 1997). Pattern recognition finds applications in several engineering, economic and social fields.

The model updating is a technique that has been developing through the last years. In various fields of engineering, it is frequent to use numerical models to evaluate the behaviour of a physical system. The accurate representation of a system depends on the type of numerical model used to represent the elements of the system and on the properties of this model (e.g. in a structural application: elasticity modulus, boundary conditions, etc). The discrepancies between the behaviour of a numerical model and the real system can be significant as reported by (Zhang et al., 2001) and (Brownjohn et al., 1999).

Inverse methods are commonly used to improve the quality and reliability of a model. They combine an initial (generally finite element) model of the structure -

whose parameters can be derived by specific characterization tests or simply guessed-, and measured data expressed in the form of modal properties or frequency response functions.

5.2.1 Modal reduction and expansion

In comparison between analytic data and experimental data there is a potential problem: the response is measured only at a limited number of points of the structure, and in a limited range of frequencies. Therefore, to compare these different set of data, it is necessary to expand the measured data or to reduce the analytic data.

Modal reduction:

There are different types of modal reduction. The so-called static reduction or Guyan's reduction (Guyan, 1965) allows to calculate a transformation matrix which reduces mass and stiffness matrices to the terms related to the useful degrees of freedom.

The dynamic reduction is an extension of the Guyan's method, accounting of the inertial terms for a particular frequency. In this case is possible to reach higher precision with respect to the static reduction (Zhang, 1995).

An Improved reduction system (IRS) has been introduced by O'Callahan (O'Callahan, 1989) which improves the static reduction method through the introduction of inertial terms as pseudo-static forces.

O'Callahan and others have developed also the System Equivalent Reduction Expansion Process (SEREP) which utilizes the computation of eigenvectors to produce the transformation between master and slave coordinates (O'Callahan et al., 1989).

Modal expansion:

Modal expansion is a procedure strictly related to modal reduction, and it is possible to consider it as an inverse reduction.

The easier way to expand data is to substitute the unknown eigenvector values with the values calculated from the analytical model but using this procedure both analytical and measured modal shapes have to be normalized in the same way.

It is possible to expand data using the stiffness and mass matrices. This procedure is dual to the dynamic reduction (Zhang, 1995).

An alternative method is to use modal data coming from the finite element analysis. The identified modes are treated as a linear combination of the analytical modes and in this way is possible to calculate a transformation matrix. This procedure is strictly linked to the SEREP procedure (O'Callahan et al., 1989).

5.2.2 Direct methods and sensitivity (iterative) methods

Model updating methods may be classified as direct and sensitivity (iterative or parametric) methods. Direct methods try to reproduce the measured data from the structure by applying little changes to the stiffness and mass matrix which are not easily associable to the parameters of the model. Indeed, the main drawback of direct methods is that their results are characterised by a lack in the physical meaning. More details about these methods can be found in (Friswell and Mottershead, 1995; Berman and Nagy, 1983; Caesar, 1986; Baruch and Bar-Itzhack, 1978; Wei, 1990; Minas and Inman, 1988; Gladwell, 1986).

Iterative (or sensitivity-based) methods have seen a larger widespread in comparison to direct methods because of their capability to calibrate the model taking into account the influence of the updating parameters of different structural elements. They offer a wide range of parameters to update that have physical meaning and allow a degree of control over the optimisation process. All these parametric methods rely on the definition of a so-called penalty function which is computed as the quadratic norm of the differences between the measured and the numerical quantities. The discrimination among the methods is based on the choice and the number of parameters to compute the objective function and the optimisation technique used to minimise it. Recently heuristic techniques like Simulated Annealing (Kirkpatrick et al., 1983; Johnson et al., 1989), Genetic Algorithms (Srinivas and Patnaik, 1994) and Evolutionary Strategies (Dack et al., 1991) and probabilistic approaches have supplanted traditional methods to solve non-linear problems like Newton-Raphson. New developments in optimisation techniques consent different approaches to the problem, such an optimisation through all the Pareto set of solution, performing a multi-objective minimization (Christodoulou et al., 2008), and optimisation based on Trust Region such as Powell's Dog-leg method (Molinari et al., 2009; Molinari, 2007).

Due to the fact that the iterative methods are mainly sensitivity based, require the sensitivity matrix **S** to be calculated in every iteration. The sensitivity matrix is a rectangular matrix of order $m \times n$, where m and n are the number of target responses and parameters, respectively (Zivanovic et al., 2007):

$$\mathbf{S} = \left[S_{ij}\right] = \left[\frac{\delta R_i}{\delta P_j}\right] \tag{5.1}$$

S_{ij} is the sensitivity of the target response R_i ($i = 1, 2, ..., m$) to a certain change in parameter P_j ($j = 1, 2, ..., n$). Operator δ presents the variation of the variable. Elements of the sensitivity matrix can be calculated numerically using, for example, the forward finite difference approach:

$$S_{ij} = \frac{R_i(P_j + \Delta P_j) - R_i(P_j)}{(P_j + \Delta P_j) - P_j} \tag{5.2}$$

where $R_i(P_j)$ is the value of the ith response at the current state of the parameter P_j, while $R_i(P_j + \Delta P_j)$ is the value of the same ith response when the parameter P_j is increased by value ΔP_j.

Obviously, for calculation of the sensitivities, the relevant target responses and structural parameters should be selected. The target responses should be chosen between those measured. The responses which are mainly considered in civil engineering applications are natural frequencies, mode shapes and frequency response functions (FRFs), or some combination of these. The choice depends on the measured data available, their quality, and (non)existence of close modes. As a rule, only high-quality measured modal properties should be used as target responses. As natural frequencies are normally measured quite accurately, they are almost always selected. If close modes are present, FRFs might be a better choice for target responses.

Selection of updating parameters is probably the most important step on which the success of the model updating depends. It is recommended to choose uncertain parameters only, and between them to choose those to which the selected target responses are most sensitive. Also, the number of parameters should be kept to an absolute minimum. All this is to avoid numerical problems due to ill-conditioning.

Once relevant (measured) target responses and structural parameters for updating have been selected, the sensitivity matrix can be calculated. Since in the iterative model updating process the updating parameters change at every step, the sensitivity matrix has to be recalculated in each iteration. Let us denote, for a given iteration, the starting parameter and target response vectors as $\mathbf{P}_0$ and $\mathbf{R}_0$, respectively. The vector of updated parameters in the current iteration is $\mathbf{P}_u$, while the target response vector obtained experimentally is $\mathbf{R}_e$. The targeted experimental response vector $\mathbf{R}_e$ can be approximated via vectors $\mathbf{R}_0$, $\mathbf{P}_u$ and $\mathbf{P}_0$ using the linear term in a Taylor's expansion series:

$$\mathbf{R_e} \approx \mathbf{R}_0 + \mathbf{S}(\mathbf{P}_u - \mathbf{P}_0). \tag{5.3}$$

The iterative process is required here because the relationship between target responses and parameters that is mainly nonlinear is approximated by the linear term. This means that updating parameters need to be changed by a small amount in each iterative step until the required minimum difference between the calculated and experimentally measured responses is achieved. Therefore, the finally updated parameters cannot be calculated in a single step.

The task of updating aimed at finding parameter values $\mathbf{P}_u$ in the current iteration can be solved in different ways such as using a pseudo-inverse (least squares) method, weighted least squares or Bayesian method. This depends on whether weighting coefficients for parameters and/or target responses are used as is the case in last two methods. The purpose of these weighting coefficients is to give different significance to numerical parameters and measured target responses depending on the confidence in these data. For example, weighting coefficients for responses take into account the confidence in the measured values, which istypically higher for natural frequencies than for mode shapes. Weighting coefficients for input parameters take into account the degree of uncertainty in them. The more uncertain a parameter is, the lower is the confidence in it, which means that the weighting value is lower too.

From Eq.5.3, the vector of parameter changes $\mathbf{\Delta P}$ reads as:

$$\mathbf{\Delta P} = \mathbf{P}_u - \mathbf{P}_0 = \mathbf{S}^{\dagger} \cdot (\mathbf{R_e} - \mathbf{R}_0) \tag{5.4}$$

where $\mathbf{S}^{\dagger}$is the inverse of the sensitivity matrix $\mathbf{S}$. The inverse is calculated as follows (Brownjohn et al., 2001):

- If $m > n$,

$$\mathbf{S}^{\dagger} = \left(\left(\mathbf{S}^{T} \cdot \mathbf{S} \right)^{-1} \right) \cdot \mathbf{S}^{T} \tag{5.5}$$

- If $m < n$,

$$\mathbf{S}^{\dagger} = \mathbf{S}^{T} \cdot \left(\left(\mathbf{S} \cdot \mathbf{S}^{T} \right)^{-1} \right) \tag{5.6}$$

Every time when calculating the pseudo-inverse of the sensitivity matrix, take caution about condition number (CN) of the $\mathbf{S}$ matrix. The conditioning of the $\mathbf{S}$ can influence the precision in the calculation of the parameter increment and the process of convergence. Besides, CN is influenced by number and type of parameters used in the procedure of model updating. The insensitive parameters that would produce a line of zeros in the $\mathbf{S}$ matrix, get eliminated. The CN of a matrix is defined as the ratio between the largest and the smallest of the singular values.

The suggested limit values in literature to appraise the goodness of the CN are (Molinari, 2007):

- $CN < 10^5$ matrix is well conditioned;
- $10^5 < CN < 10^8$ identified matrix is bad conditioned;
- $CN > 10^8$ indicated matrix is singular.

Bearing all this in mind, the updating procedure can be summarised as follows (Zivanovic et al., 2007):

1. Choose the weighting factors for parameters and target responses.
2. Calculate the sensitivity matrix $\mathbf{S}$ for the given state of parameters $\mathbf{P}_0$ and response $\mathbf{R}_0$.
3. Calculate matrix $\mathbf{S}^{\dagger}$ using either Eq.(5.5) or Eq.(5.6).
4. Using experimental response vector $\mathbf{R_e}$, the updated parameter vector $\mathbf{P}_u$ can be obtained via a re-arranged Eq. (5.4):

$$\mathbf{P}_u = \mathbf{P}_0 + \mathbf{S}^{\dagger} \cdot (\mathbf{R_e} - \mathbf{R}_0) \tag{5.7}$$

5. The new response vector which which corresponds to updated parameters $\mathbf{P}_u$ should then be calculated as a result of modal analysis. This response vector and the vector of updated parameters then become the starting vectors $\mathbf{R}_0$ and $\mathbf{P}_0$ for the next iteration.

The procedure then goes back to step 2 to calculate a new sensitivity matrix (which changes whenever the model is updated between two iterations). Steps 2 to 5 are repeated until a satisfactory convergence of numerical responses to the experimental data is achieved (that is until the error function is minimised to a prespecified tolerance).

5.2.3 Comparison between identified and analytical data MAC and COMAC

The measurement data used to compute the objective function may belong to the frequency or modal domain. Time domain data are generally disregarded because measured time-series are affected by noise and difficulty in handling a large volume of data. Data compression is performed to obtain FRF data, which are less affected by random noise because averaged but suffer little loss of information in the passage from time to frequency domain. Model updating methods based on modal parameters like natural frequencies, mode shapes and damping ratios exploit a further reduction in the number of data points but they have to cope with the reduction of accuracy in the modal parameters estimation. Furthermore, mode shapes are valuable parameters to be implemented in a model updating procedure because they allow to pair the analytical and experimental modes but their precise estimation is difficult to reach and changes due to damage are often smaller than the error bounds on corresponding measurements. In literature, it is possible to find many functional indexes that consent to compare measured and numerical data. Among the most used there is the MAC (Modal Assurance Criterion), defined as:

$$MAC_{jk} = \frac{\left(\{\Phi_m\}_j^T \cdot \{\Phi_a\}_k\right)^2}{\left(\{\Phi_a\}_k^T \cdot \{\Phi_a\}_k\right) \cdot \left(\{\Phi_m\}_j^T \cdot \{\Phi_m\}_j\right)} \tag{5.8}$$

where $\{\Phi_a\}_k$ is the theoretical eigenvalue corresponding to the k^{th} mode, and

$\{\Phi_m\}_j$ is the measured eigenvalue, corresponding to the jth mode. The MAC can vary between 0 and 1, and the comparison could be considered satisfied with a MAC value superior to 0.8.

The COMAC (Co-ordinate MAC) quantifies the correlation between identified and analytical modal shapes referring to a particular degree of freedom:

$$COMAC(j) = \frac{\sum \{\Phi_a\}_{ji}^T \cdot \{\Phi_m\}_{ji}}{\left(\sum \{\Phi_a\}_{ji}^2\right) \cdot \left(\sum \{\Phi_m\}_{ji}^2\right)} \tag{5.9}$$

where i is the i^{th} modal shape and j is the j^{th} degree of freedom.

Many authors use a Weighted MAC (WMAC) which utilises a weight matrix [W]. The weights can depend from the reliability of certain data (due to the distribution or the accuracy of the sensors).

It is useful also to remind the following related terminologies :

- Partial Modal Assurance Criterion (PMAC);
- Modal Assurance Criterion Square Root (MACSR);
- Scaled Modal Assurance Criterion (SMAC);
- Modal Assurance Criterion using Reciprocal Vectors (MACRV);
- Modal Assurance Criterion with Frequency scales (FMAC);
- The Enhanced Coordinate Modal Assurance Criterion (ECOMAC);
- Inverse Modal Assurance Criterion (IMAC);

For a review of all the MAC-derived criteria and a complete bibliography, consult (Allemang, 2002).

Another approach is to compare, instead of the modal shapes, the frequency response functions, with the same principle of the MAC. This comparison is feasible in the case of experimental tests performed with a vibrodina. In this case it is called Frequency Response Assurance Criterion (FRAC).

The Complex Correlation Coefficient (CCC) and the Frequency Domain Assurance Criterion (FDAC) derive from the previous.

5.2.4 Dog-Leg optimisation method

The Dog-Leg (DL) method was implemented for updating of the FE model of the footbridge. It is an iterative method based on the Trust Region (TR) strategy, which works with combinations of the Gauss–Newton (GN) and the Steepest Descent (SD) directions. In detail, the model function L is defined as (Molinari, 2007):

$$L(p) = \frac{1}{2} \cdot \|f(p) + \mathbf{J}(p) \cdot g\|^2 \tag{5.10}$$

where, the objective function (F) and the error function (f) and J are given as follows:

$$F(p) = \frac{1}{2} \sum_{i=1}^{m} f_i^2(p) = f(p)^T . f(p) \tag{5.11}$$

$$f(p) = x_{exp} - x_{num}(p) \tag{5.12}$$

where, x_{exp} is the experimental value and $x_{num}(p)$ is the numerical value of modal properties considered.

$$J = f'(p) = \frac{\partial f_i(p)}{\partial p_j} \tag{5.13}$$

The vector increment h indicates in the direction to search the solution, see Figure 5.1.

$$P_u = P_0 + h_{DL} \tag{5.14}$$

The search direction can be either the GN or the SD, or a linear combination of the two. This choice depends on the fact that the SD method is more efficient further from the minimum point, while the GN operates more reliably close to the minimum.

Given $f : R^n \rightarrow R^m$, at the current iterate p the Gauss-Newton step h_{GN} is the least squares solution to the linear system :

$$\mathbf{J}(p) \cdot h = -f(p) \tag{5.15}$$

It can be computed by solving the normal equations

$$\left(\mathbf{J}(p)^T \cdot \mathbf{J}(p)\right) \cdot h_{GN} = -\mathbf{J}(p)^T \cdot f(p) \tag{5.16}$$

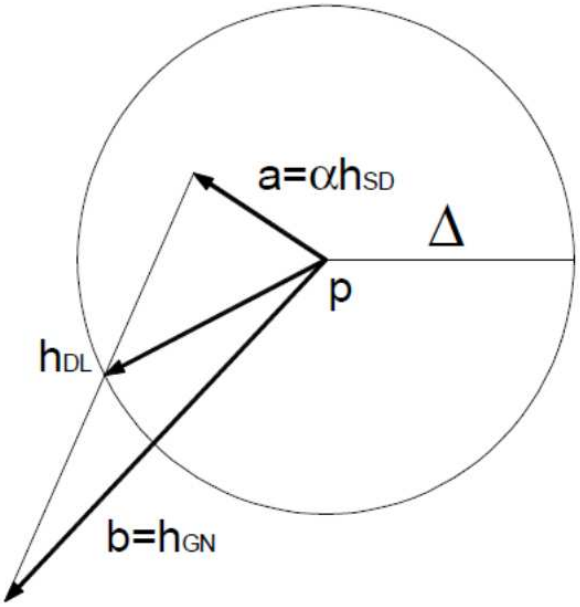

Figure 5.1: Trust-Region and Dog-Leg step

The steepest descent direction is given by

$$h_{SD} = -\mathbf{J}(p)^T \cdot f(p) = -g \tag{5.17}$$

Indicating the radius of the TR with the scalar Δ, the basic strategy of the DL method is:

$$\text{if } \|h_{GN}\| < \Delta \quad \Rightarrow \quad h_{DL} = h_{GN} \tag{5.18}$$

$$\text{if } \|h_{GN}\| \geq \Delta \text{ and } \|\alpha h_{SD}\| \geq \Delta \quad \Rightarrow \quad h_{DL} = \frac{\Delta}{\|h_{SD}\|} h_{SD} \tag{5.19}$$

$$\text{if } \|h_{GN}\| \geq \Delta \text{ and } \|\alpha h_{SD}\| < \Delta \quad \Rightarrow \quad h_{DL} = \alpha h_{SD} + \beta(h_{GN} - \alpha h_{SD}) \tag{5.20}$$

The parameter β is determined imposing that $\|h_{DL}\| = \Delta$. The existence of a finite solution for β can be proved by considering the function ψ, defined as the difference between the radius of the TR and that of the DL step:

$$\psi(\beta) = \|a + \beta \cdot (b - a)\|^2 - \Delta^2 = \|b - a\|^2 \cdot \beta^2 + 2\beta \cdot c + \|a\|^2 - \Delta^2 \tag{5.21}$$

where c is a scalar given as:

$$c = a^T \cdot (b - a) \tag{5.22}$$

It can be verified that:

$$\beta \longrightarrow -\infty \quad \Rightarrow \quad \psi(-\infty) = \infty \tag{5.23}$$

$$\beta \longrightarrow 0 \quad \Rightarrow \quad \psi(0) = \|a\|^2 - \Delta^2 < 0 \tag{5.24}$$

$$\beta \longrightarrow 1 \quad \Rightarrow \quad \psi(1) = \|h_{GN}\|^2 - \Delta^2 > 0 \tag{5.25}$$

So one negative and one positive root exist in the interval]0,1[. The solution depends on the sign of c:

$$\text{if } c \leq 0 \quad \Rightarrow \quad \beta \equiv \frac{-c + \sqrt{c^2 + \|b - a\|^2 \cdot \left(\Delta^2 - \|a\|^2\right)}}{\|b - a\|^2} \tag{5.26}$$

$$\text{if } c > 0 \quad \Rightarrow \quad \beta \equiv \frac{\left(\Delta^2 - \|a\|^2\right)}{c + \sqrt{c^2 + \|b - a\|^2 \cdot \left(\Delta^2 - \|a\|^2\right)}} \tag{5.27}$$

The amplitude of the TR method depends on the quality of the fitting to the objective function of the linear model L. For this purpose, the coefficient ρ is introduced, such that:

$$\rho = \frac{F(p) - F(p + h_{DL})}{L(0) - L(h_{DL})} \tag{5.28}$$

The value of the denominator of ρ depends on the path followed, as illustrated in Figure 5.1. In detail:

$$L(0) - L(h_{DL}) \equiv F(p) \qquad \text{if } h_{DL} = h_{GN} \tag{5.29}$$

$$L(0) - L(h_{DL}) \equiv \frac{\Delta\left(2\left\|g \cdot \alpha\right\| - \Delta\right)}{2\alpha} \qquad \text{if } h_{DL} = \Delta \cdot \frac{g}{\|g\|} \tag{5.30}$$

$$L(0) - L(h_{DL}) \equiv \frac{1}{2}\alpha(1-\beta)^2 \cdot \|g\|^2 + \beta(2-\beta) \cdot F(p) \quad \text{otherwise} \tag{5.31}$$

Values of ρ close to one indicate that the reduction of the error estimated with the model prediction is close to one; so when $\rho > 0.75$, the radius of the TR increases. Values of $\rho < 0.25$ suggest the reduction of the radius of the TR. Steps implying values lower than the tolerance 0.0001 should be rejected.

5.3 Finite Element model of the foot-cycle bridge 'Ponte del Mare' Pescara

5.3.1 Initial FE model

A preliminary linear FE model of the bridge was developed in ANSYS, as shown in Figures 4.3. The design drawing and section details of the bridge are shown in Figures 5.2 and 5.3 respectively. The following element types were used to model the different parts of the bridge.

- BEAM44 - 3D Elastic Tapered Unsymmetrical Beam :- This is a uniaxial element with tension, compression, torsion and bending capabilities. The element has six degrees of freedom at each node: translations in the nodal x,y and z directions

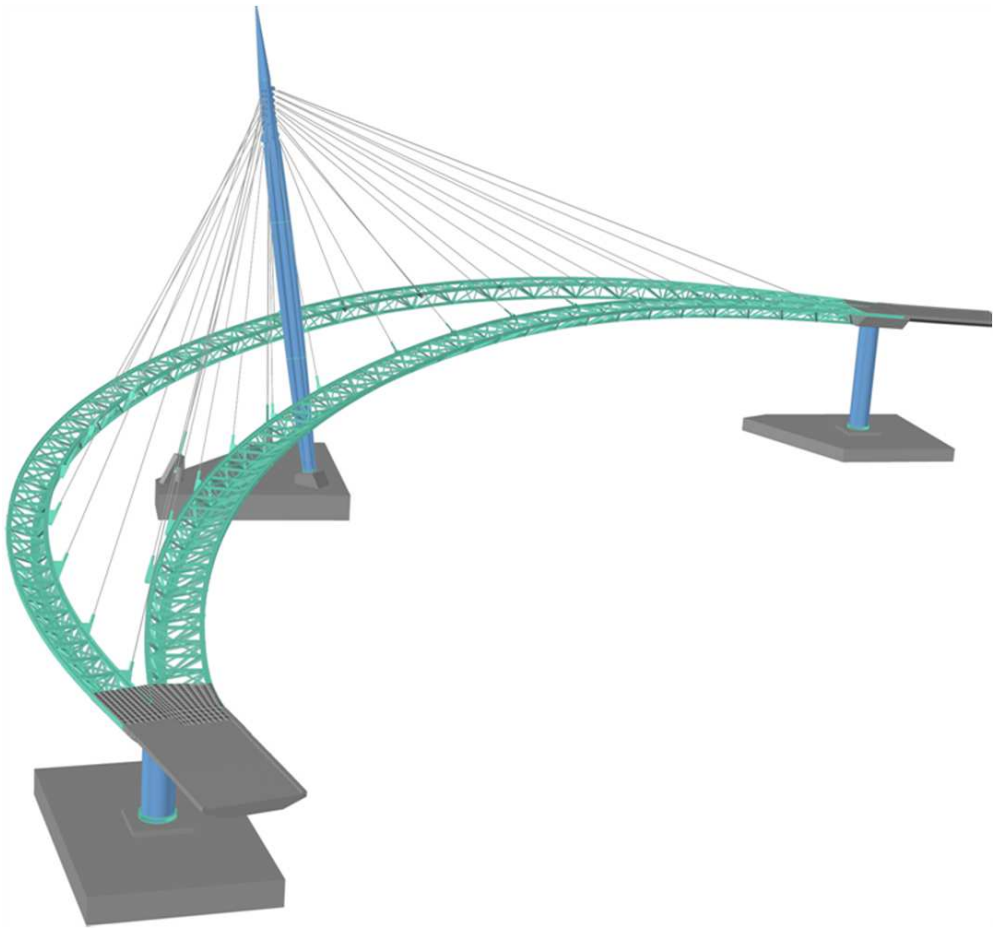

Figure 5.2: 3D drawing of the ‘Ponte del Mare’ footbridge

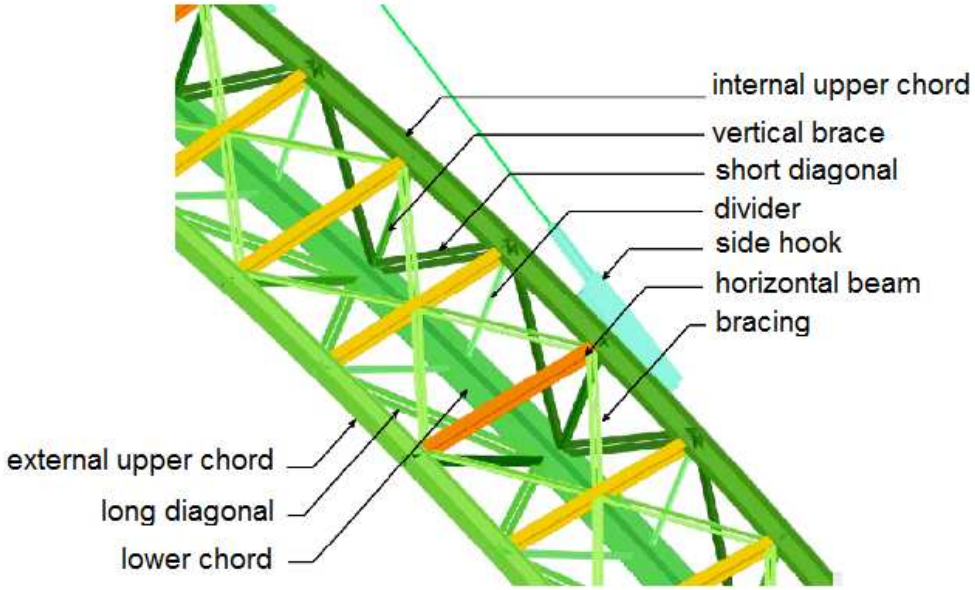

Figure 5.3: Reticular structure of the cycle deck

and rotations about the nodal x,y and z axes. This element allows a different unsymmetrical geometry at each end and permits the end nodes to be offset from the centroidal axis of the beam. This element was used to model all the trusses, rigid connections, piers, ramps and the mast. The section-types of the trusses forming the reticular structure are shown in Figure 5.4 and their geometrical dimensions are given in Tables 5.1 and 5.2. The model considers a fixed connection between trusses and takes into account the eccentricity between their axes. The nodes were assigned a material 100 times more rigid than steel and having zero specific weight. By means of the same element also the connection between slab and horizontal beams and that between cables and the mast were realized. To model plates that realize a connection between cables and chords, we adopted BEAM44 elements having section of unit area and material of rigidity 100 times more than steel. The mast was subdivided into six different parts in order to consider the variability of the section. The BEAM44 element allowed to assign different mechanical properties to the ends that varies linearly along the axis of the mast. The piers P2 and P4, in correspondence to the connections between the cable-stayed bridge and the ramp of access, were realized in a

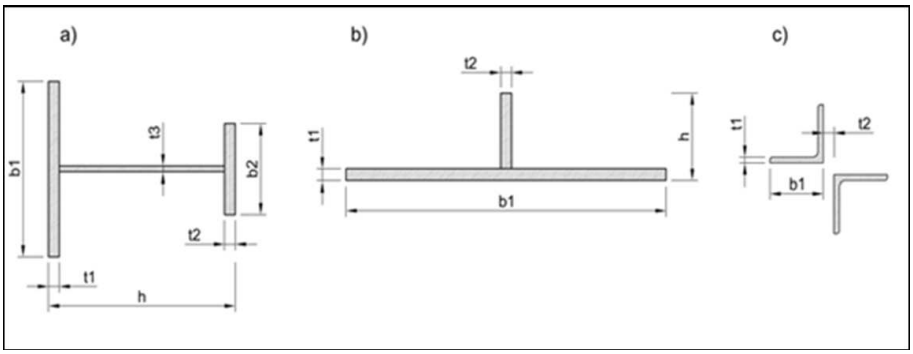

Figure 5.4: Section types of the elements that constitute the beam reticular(a) Upper chord (b) Lower chord (c) diagonals, bracings,vertical braces and dividers.

composite steel-concrete structure, the mechanical properties were homogenised to the steel and the specific weight was increased to consider the presence of concrete.

- LINK8- 3D Spar or Truss :- This is a uniaxial tension-compression element with three degrees of freedom at each node: translations in the nodal x,y and z directions. Stays were modelled with the LINK8 elements and each of them has an initial deformation value, assigned to impose the advisable pretension. Stays were assigned practically a zero mass to avoid modal analysis be influenced by spurious modes due to the large flexibility of these elements.
- SHELL43- 4 Node Plastic Large Strain Shell :- This is well suited to model linear, warped, moderately-thick shell structures. The element has six degrees of freedom at each node: translations in the nodal x,y and z directions and rotations about the nodal x,y and z axes. The deformation shapes are linear in both in-plane directions. For the out-of-plane motion, it uses a mixed interpolation of tensorial components. The element has plasticity, creep, stress stiffening, large deflection, and large strain capabilities. The concrete slab was modelled with SHELL43 elements having a thickness of 55 mm.
- SOLID45- 3D Structural Solid :- This is defined by eight nodes having three degrees of freedom at each node: translations in the nodal x,y and z directions. The element has plasticity, creep, swelling, stress stiffening, large deflection, and large strain capabilities. The concrete block that works as a restraint between deck and piers was modelled with SOLID45.

Table 5.1: Dimension of the section types of the cycle deck

Cycle deck	Element	b1 [mm]	t1 [mm]	b2 [mm]	t2 [mm]	h [mm]	t3 [mm]
external upper chord	C-CSE	380	20	200	20	340	25
internal upper chord	C-CSI-20	380	20	200	20	340	25
	C-CSI-25	380	25	200	25	340	25
lower chord	C-TI-20	800	20		20	240	
	C-TI-30	800	30		20	250	
vertical brace	C-M-80x8-18	80	8	18			
	C-M-100x12-18	100	12	18			
diagonal	C-DC-80x8-18	80	8	18			
	C-DC-110x14-18	110	14	18			
	C-DL-90x9-18	90	9	18			
	C-DL-100x14-18	100	14	18			
bracing	C-CONTR-80x10-18	80	10	18			
divider	C-RL-60x6-18	60	6	18			
horizontal beam	HEA 200						
	HEB 200						

Table 5.2: Dimension of the section types of the pedestrian deck

Pedestrian deck	Element	b1 [mm]	t1 [mm]	b2 [mm]	t2 [mm]	h [mm]	t3 [mm]
external upper chord	P-CSE	380	20	200	20	340	25
internal upper chord	P-CSI	380	20	200	20	340	25
lower chord	P-TI-25	750	25		20	225	
	P-TI-35	750	35		20	235	
	P-TI-40	750	40		20	240	
vertical brace	P-M-80x8-18	80	8	18			
	P-M-100x12-18	100	12	18			
Diagonal	P-DC-100x10-18	100	10	18			
	P-DC-100x14-18	100	14	18			
	P-DL-110x14-18	110	14	18			
bracing	P-CONTR-80x10-18	80	10	18			
divider	P-RL-60x6-18	60	6	18			
horizontal beam	HEA 200						
	HEB 200						

- MASS21- Structural Mass :- This is a point element having up to six degrees of freedom: translations in the nodal x,y and z directions and rotations about the nodal x,y and z axes. A different mass and rotary inertia may be assigned to each coordinate direction. This element was used for assigning the mass due to permanent load.

Table 5.3 reports the properties of the utilised materials in the bridge.

Table 5.3: Properties of the materials used in the FE model

Material	Elastic modulus	Poisson ratio	Density	Coefficient of thermal expansion
reinforce concrete	35000 *MPa*	0.2	2.5 t/m^3	9.9 x 10^{-6} $^0C^{-1}$
structural steel	210000 *MPa*	0.3	7.85 t/m^3	1.17 x 10^{-5} $^0C^{-1}$
steel cable ϕ44	165000 *MPa*	0.3	8.289 t/m^3	1.17 x 10^{-5} $^0C^{-1}$
steel cable ϕ60	165200 *MPa*	0.3	8.32 t/m^3	1.17 x 10^{-5} $^0C^{-1}$
steel cable ϕ75	162800 *MPa*	0.3	8.29 t/m^3	1.17 x 10^{-5} $^0C^{-1}$

Due to the fact that ramp and the piers (beam elements) are bound to a single node of the solid block, surface around the node of the block and the area of the pier were constrained to make rigid. In Figure 5.5 the concrete block and the costraints with the adjacent elements are represented.

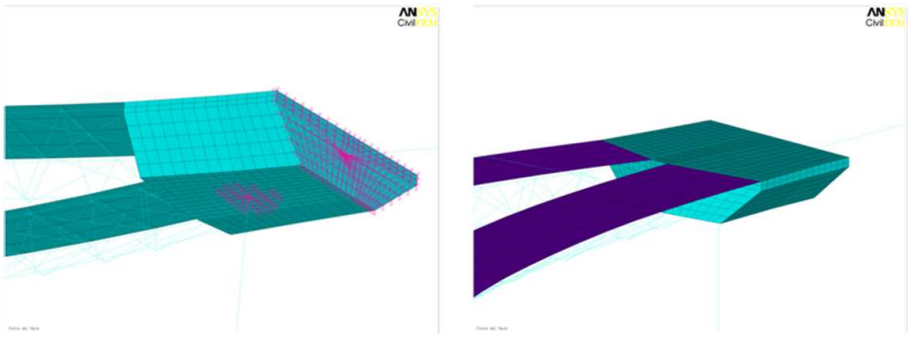

Figure 5.5: Concrete block as the connection between the pedestrian and cycle deck.

The ramps of access have a variable section between 5 m and 7 m, nevertheless, due to the presence of the saddles Gerber, shown in Figure 5.6, their influence is negligible with respect to the dynamics of the cables part. To consider the mass due to permanent carried loads, density of material of the ramps was increased. The connection to the saddle Gerber were obtained through release of some axial actions and of the moments in the vertical and horizontal plane. The blocks in concrete that connect the deck and the top of the piers P2 and P4 were then modelled. Mesh is realized with regular tetrahedral elements and dimension of finite elements was chosen as a compromise between sufficiently refine model in order to pick the structural geometry without excessive deformation of the elements and the speed of calculation.

On the nodes of deck and ramp were added some punctual masses that represent the elements carried after finish and possibly the mass of pedestrians present on the deck. The connections to the ground are all perfectly fixed except the side end of the two ramps that have a connection to roller supports.

In conclusion, the initial FE model comprises:

- 7226 nodes;
- 3037 BEAM44 elements;
- 30 LINK8 elements;
- 496 SHELL43 elements;
- 3920 SOLID45 elements;
- 630 MASS21 elements.

This FE model is very precise from point of view of accuracy of modelling. The justifications for a more precise model essentially are bound to the complexity of the bridge and the objective to pursue, in our case to perform a trial of model updating over a too simplified model would add even more uncertainties and the results obtained will be meaningless.

5.3.2 Modified FE model accounting changes during construction

Due to some changes in the construction phase, the final realized structure diverted from the initial design. Therefore, the initial FE model that was based on the initial design was modified considering the changes during construction.

Figure 5.6: Saddle Gerber between concrete block and ramp of access.

After a check over the cable deck arrived on site, see Figure 5.7, it was realized that the two grounded cables should be of larger diameter to guarantee the structural safety. In order to avoid additional cost and delays to get new cables, already available cables were utilised that realistically caused the changes in the structure of the two decks.

Figure 5.7: Progress of the construction work in site.

Particularly, it was chosen to move the centre of mass of the structure by varying the weight of the concrete slabs between the two decks. It passed from an uniform concrete slab of thickness 55 mm to 5 zones, named as per Figure 5.8, with different sections between them. To increase even more this gap, without exaggerating the thickness of the slab of the pedestrian deck, a lightened concrete was used for all of the zones of the cyclic deck. Such variations in the section made a change in the mass and stiffness of the deck and reflected a change in modal properties of the structure.

The details of the geometrical properties of the sections were calculated using SAP software, for example, two sections are shown in Figures 5.9 and 5.10.

The initial FE model did not consider the contribution of the two side concrete

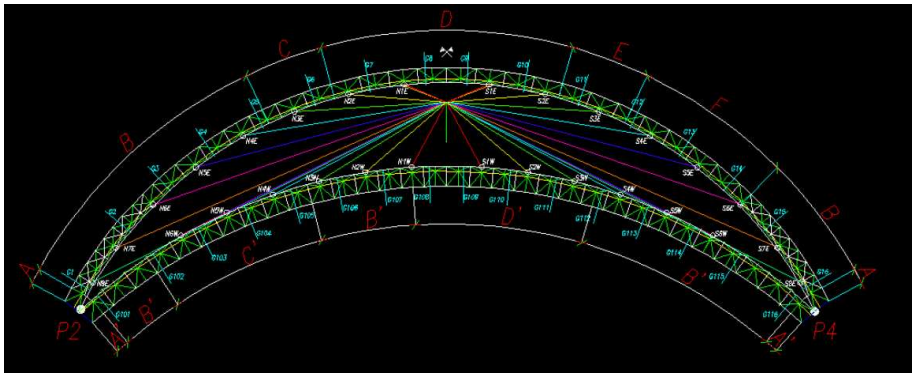

Figure 5.8: Progress of the construction work in site.

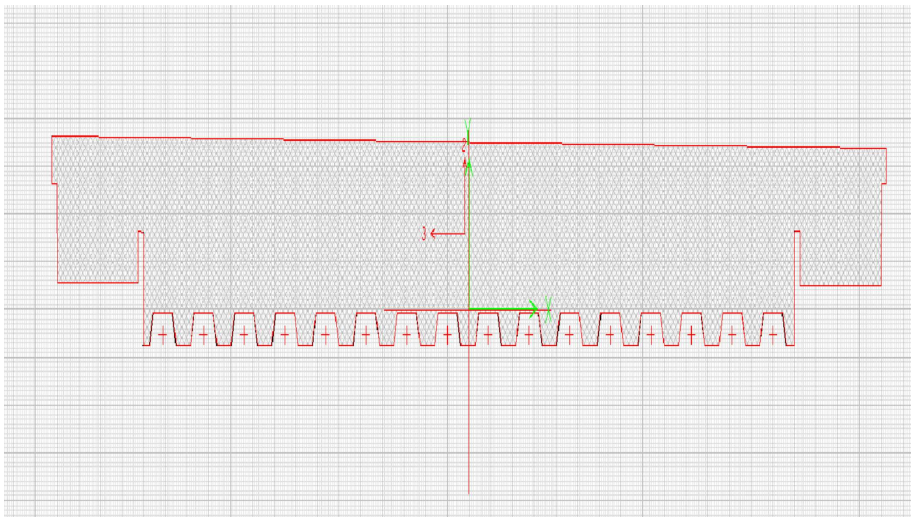

Figure 5.9: Steel-concrete composite secction in zone D of the pedestrian deck.

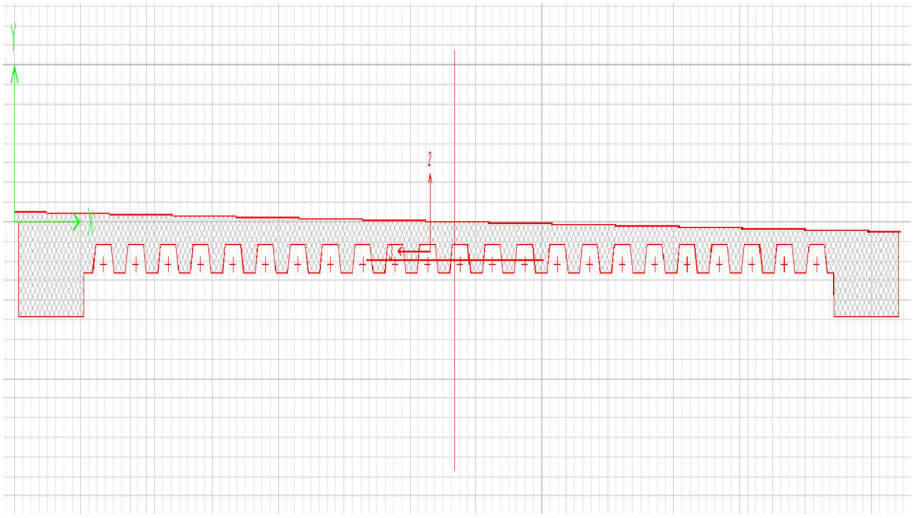

Figure 5.10: Steel-concrete composite secction in zone D' of the cycle deck.

blocks, of the presence of the metal steel sheeting, of the concrete present between outlines of the metal steel sheeting and different thicknesses of the paving. The presence of the metal steel sheeting provides a considerable contribution to the longitudinal bending stiffness, particularly in those sections that have a smaller layer of concrete, Figure 5.10. Therefore once calculated the moment of inertia of the new sections and compared with that of the previous rectangular shell, were obtained various amplifying coefficients C, i.e. a ratio between the moment of inertia of the new and old section.

To note that such a coefficient was multiplied only lengthwise by the elastic modulus of the concrete, transversally in fact the metal steel sheeting does not offer a contribution to the bending stiffness.

Finally, some operations were carried out also on the mast. In the new model the variation of the tubular mast was accounted more precisely, it was held to the different height of the section and of the filling up with concrete, for e.g. see Figure 5.11. The previous Table 5.3 of the materials used in the FE model was modified by adding the lightened concrete used for the cyclic deck, to Table 5.4.

STRUCTURAL STIFFENING WITH DIAGONAL

After some preliminary studies, it was decided to work locally to limit an excessive

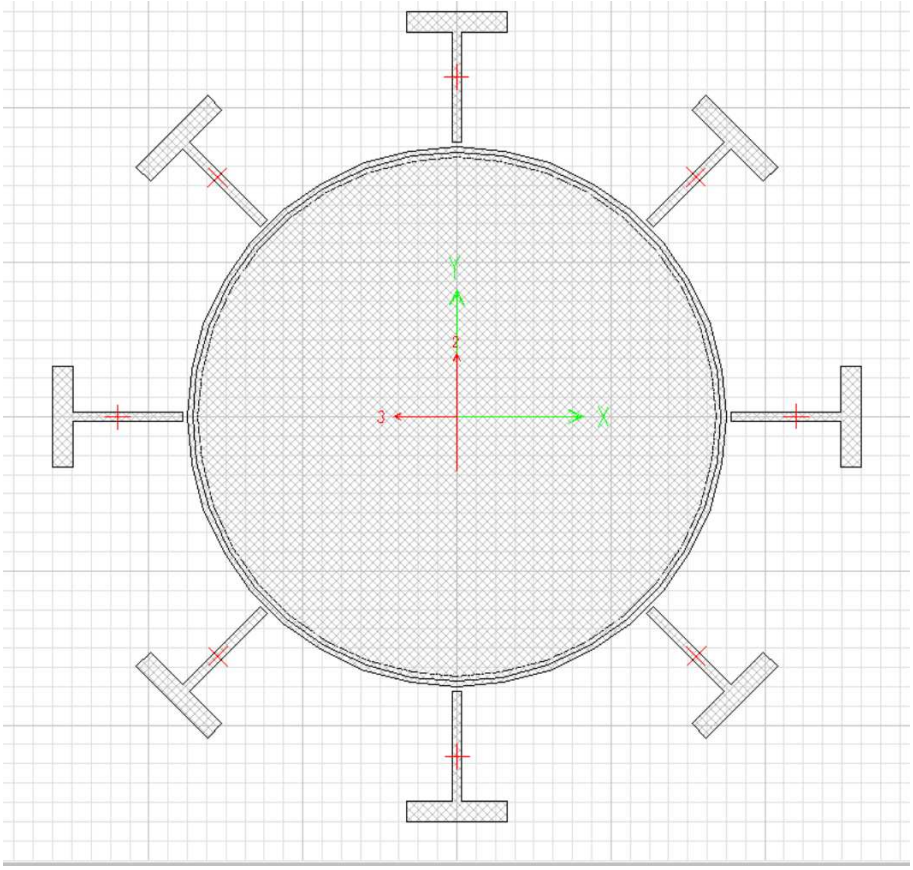

Figure 5.11: Steel-concrete composite secction of the mast.

Table 5.4: Properties of the materials used in the FE model

Material	Elastic Modulus	Poisson ratio	Density	Coefficient of thermal expansion
reinforce concrete	35000 MPa	0.2	2.5 t/m^3	$9.9\times10^{-6}\,{}^\circ C^{-1}$
lightened reinforce concrete	16000 MPa	0.2	1.5 t/m^3	$9.9\times10^{-6}\,{}^\circ C^{-1}$
structural steel	210000 MPa	0.3	7.85 t/m^3	$1.17\times10^{-5}\,{}^\circ C^{-1}$
steel cable ϕ44	165000 MPa	0.3	8.289 t/m^3	$1.17\times10^{-5}\,{}^\circ C^{-1}$
steel cable ϕ60	165200 MPa	0.3	8.32 t/m^3	$1.17\times10^{-5}\,{}^\circ C^{-1}$
steel cable ϕ75	162800 MPa	0.3	8.29 t/m^3	$1.17\times10^{-5}\,{}^\circ C^{-1}$

deformability of some zones of the metallic reticular structure, Figures 5.12 and 5.13. There were added two short diagonals (100x10 mm) on the pedestrian deck, eight long diagonals (100x14 mm), three long diagonals (90x9 mm) and two short diagonals (80x8 mm) on the cycle deck. Lastly, it can be noted that the initial FE model

Figure 5.12: Detail of the diagonals added in different zones of the pedestrian deck.

omitted the metallic plates at junction. The supplementary stiffness data from such plates was not considered but the mass was considered that was spread along the extensions in proximity of same plates.

MODELLING OF THE SUPPORTS WITH RUBBER ARMS

In the initial FE model the connections to a saddle Gerber were obtained through releasing some moments and axial actions in the vertical and horizontal plane. This approximation was refined introducing a spring that accounts for the resistance offered from the two ALGAFLON supports. These supports have rubber arms and are provided of end plates movable in both directions. Once the thickness of the rubber (t_e), the area of the support (A) and the dynamic shear factor G_{din} are known, the equivalent stiffness offered by the support is calculated as:

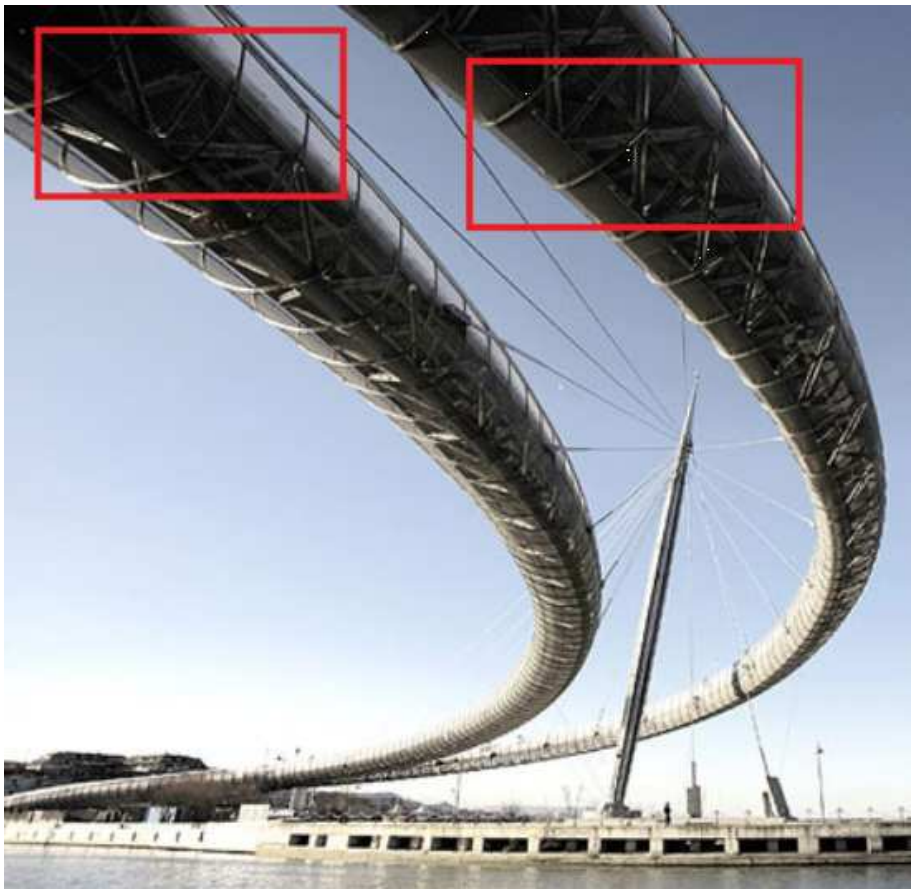

Figure 5.13: Detail of the diagonals added in different zones of the cycle deck.

$$K_{eq} = \frac{G_{din}.A}{t_e} \tag{5.32}$$

This value was then compared with that of the Tables of the ALGAE (Algalink, 2009) society and was chosen a $K_{eq} = 4,220\ kN/mm$.

The effect of rotation was not considered significant because the two supports are aligned, like in Figure 5.14, that limit such rotation also because of the greater rigidity of the sustained decks. Therefore, in the new FE model two COMBIN14 elements were introduced with supply of stiffness K_{eq} and lacking mass. Such elements act as a uniaxial spring once they are defined to the anchored nodes.

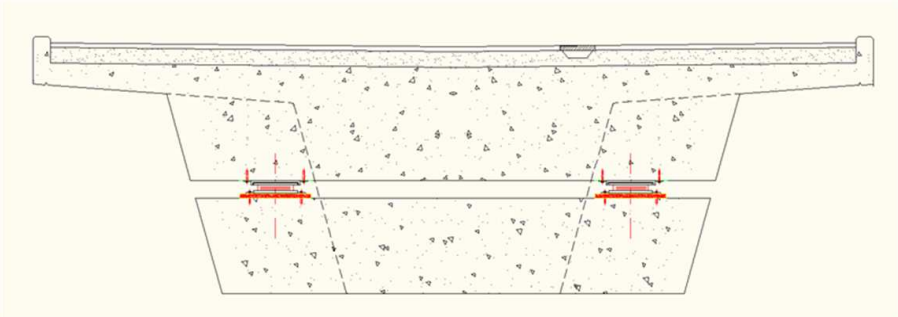

Figure 5.14: Arrangement of ALGAFLON support

The COMBIN14 elements were used to model also fluid viscous dampers, but it will not be treated here as we will concentrate on the model without dampers. In a first step, a model updating without the dampers will be performed in order to exclude eventual complications that could arise due to their application. In a successive step, with the knowledge obtained on the updated FE model, we can pass to the updating of the model provided with dampers.

UPDATING OF THE TENSION IN STAYS

At the conclusion of the construction of the bridge, the Sistral society (SISTRAL, 2009) performed tests to verify the actual value of tension in cables. The test was performed by positioning an accelerometer on a cable and exciting the same one with a mechanical impulse. The frequency relates tension of the cable on the basis of the formula of the taut string, see Eq. 5.33, and of the mechanical properties of the

same cable. The assumptions about this formula are the following (Tinazzi, 2009):

- the cable is perfectly flexible (i.e. sufficiently long to exhibit negligible flexural stiffness) with a hinge connection at each end;
- absence of relative movement of the points of anchorage;
- the cable is inextensible (i.e. slow and small movements do not develop tension).

The n^{th} natural frequency f_n, of a cable is related to the pull T, the length L and the mass per unit length m according to the following formula:

$$fn = \frac{n}{2L} \cdot \sqrt{\frac{T}{m}} \tag{5.33}$$

Equation 5.33 expresses the model of a taut string and involves a logical connection between the frequency f_n and the order n of the mode. It was verified that stays in examination have a dynamic behavior well described from the model of the taut string, and the auto-spectrum of the ambient response characterized the peaks quite distinguished and equidistant. The values of frequency obtained on all the cables and the relevant values of pull are reported in Table 5.5. The values of pull obtained are compared with the theoretical values of the project indicating the relevant differences.

To choose on how to model stays three different models were compared with increasing refinement of the finite elements in a study at University of Trento (Tinazzi, 2009). The interest towards this analysis was born from the observation that the actual values of frequency of some stays fell in the range of that of the bridge, with consequent possible interaction of the cables in a global dynamic analysis of the structure.

In the first model (One element cable system - MEFE) a stay was modelled as a sole element with equivalent elastic modulus, in the second model (Multi Link Model) stays were discretised but the bending stiffness was neglected, finally, in the last model (Multi Beam Model) besides the discretisation also the contribution of the bending stiffness was introduced.

This is rendered in a minimum participation of the transversal movement of a cable to some more distorted flexible modes of the structure, whose geometry is therefore the same one that of the corresponding modal shapes obtained with the MEFE model. It is concluded that the discretisation of cables is significant alone for local analysis

SISTRAL	RILIEVO TIRO EFFETTIVO NELLE FUNI CON METODO ACCELEROMETRICO Ponte del Mare - Pescara								01/12/2009	
Part. N.	Den. Fune	Diam.	Peso	Lunghezza a 20°	Temp Fune	Lunghezza a Temp. Fune	Frequenza Vibrazioni	Tiro Rilevato	Tiro di progetto	Differenza sul tiro di progetto
N.		[mm]	[kg/m]	[m]	[°C]	[m]	[Hz]	[kN]	[kN]	[kN]	%
1	NE8	60	20,2	80,461	14	80,455	0,74	286	385	-99	-26%
2	NE7	44	10,7	73,877	12	73,870	1,06	263	319	-56	-18%
3	NW6	44	10,7	64,377	12	64,371	1,50	398	479	-81	-17%
4	NE6	44	10,7	64,782	12	64,776	1,73	539	603	-64	-11%
5	NW5	44	10,7	55,433	13	55,429	1,56	320	329	-9	-3%
6	NE5	44	10,7	55,602	12	55,596	1,67	368	354	14	4%
7	NW4	44	10,7	46,685	12	46,681	1,93	348	326	22	7%
8	NE4	44	10,7	46,498	13	46,494	2,25	468	449	19	4%
9	NW3	44	10,7	38,393	13	38,390	2,49	392	283	109	39%
10	NE3	44	10,7	37,726	13	37,723	3,18	616	577	39	7%
11	NW2	44	10,7	30,971	13	30,968	2,99	367	235	132	56%
12	NE2	44	10,7	29,741	14	29,739	4,15	652	564	88	16%
13	NW1	44	10,7	25,015	13	25,013	3,72	371	233	138	59%
14	NE1	44	10,7	24,135	13	24,133	4,86	589	619	-30	-5%
15	N1(NE1)	75	32,4	35,695	17	35,694	3,63	2177	1996	181	9%
16	N1(SE1)	75	32,4	35,695	15	35,693	3,57	2105	1996	109	5%
17	SE1	44	10,7	23,087	16	23,086	5,34	651	587	64	11%
18	SW1	44	10,7	24,098	17	24,097	4,09	416	229	187	82%
19	SE2	44	10,7	27,751	17	27,750	4,57	690	510	180	35%
20	SW2	44	10,7	29,12	19	29,120	3,37	411	244	167	69%
21	SE3	44	10,7	35,336	19	35,335	3,28	575	493	82	17%
22	SW3	44	10,7	36,092	22	36,093	2,64	390	279	111	40%
23	SE4	44	10,7	44,07	22	44,071	2,17	392	408	-16	-4%
24	SW4	44	10,7	44,289	21	44,289	2,04	350	324	26	8%
25	SE5	44	10,7	53,308	19	53,307	1,53	284	330	-46	-14%
26	SW5	44	10,7	53,158	19	53,158	1,77	380	333	47	14%
27	SE6	44	10,7	62,697	20	62,697	1,72	500	582	-82	-14%
28	SW6	44	10,7	62,427	21	62,427	1,46	357	405	-48	-12%
29	SE7	44	10,7	71,911	21	71,912	1,11	270	366	-96	-26%
30	SE8	60	20,2	78,231	21	78,232	0,68	232	355	-123	-35%

Table 5.5: Pull in cables compared with the values in project

and that, in point of view of a global dynamic analysis, to neglect their contribution does not contribute significant errors.

Therefore stays were modelled as an equivalent truss; the cable in such approach is treated like a rectilinear truss and the variations of the mechanical property, consequent to the deformed configuration produced from the load applied, keeping in account by means of an reduced elastic modulus being derived from the theory of Dischinger as following (Bruno et al., 2008):

$$E_{sD} = \frac{E_s}{\left(1 + E_s \left(\frac{\gamma^2 \cdot l_1^2}{12 \cdot \sigma_s^3}\right)\right)} \tag{5.34}$$

Stays which are affected more of this reduction of the elastic modulus are clearly those that have a long abscissa about the axis of deck, more height and a smaller effort of traction, Figure 5.15.

Figure 5.15: Arrangements of the cables after final construction

Once the experimental pulls on stays are known, this information can be introduced in the FE model. A LINK8 element, that models the 30 stays of the ‘Ponte del Mare’, requires a value of extension. Therefore, an iterative procedure is created by means

of a written code in Ansys Parametric Design Language (APDL). The objective of the iterative procedures is to determine the variation of extension in the stays and to update such value until that arrives at convergence with the measured pulls of the finished work.

There are mainly two commands of this cycle:

• The command *DOWHILE -that allows the execution of cycle until a condition of exit is verified;

• The static analysis ANTYPE - STATIC -that is carried out at every individual iteration within the *DOWHILE cycle.

The flow chart of the procedure is shown in Figures 5.16. The iterative cycles shown require about 200 iterations before to arrive convergence with the chosen critera and an tolerance (TOL) equal to 1% :

$$\sum_{i=1}^{30} \left(\frac{PULL_{MEASURED_i} - PULL_{ANSYS_i}}{PULL_{MEASURED_i}} \right)^2 < TOL \tag{5.35}$$

The computational burden and the time necessary to arrive at convergence are very high. Therefore a better solution will be to use these files directly after the final step of iterative cycles of model updating.

Table 5.6 shows a comparison of identified and FE model frequency for first 12 modes without connected dampers. It can be noted that the average percentage error reduces after the modification of the initial FE model. However, the modified FE model shows 8.66% error that is quite large and hence the model needs an updating. Table 5.7 and 5.17 show the initial MAC values. The average MAC along the diagonal comes out to 70.59%.

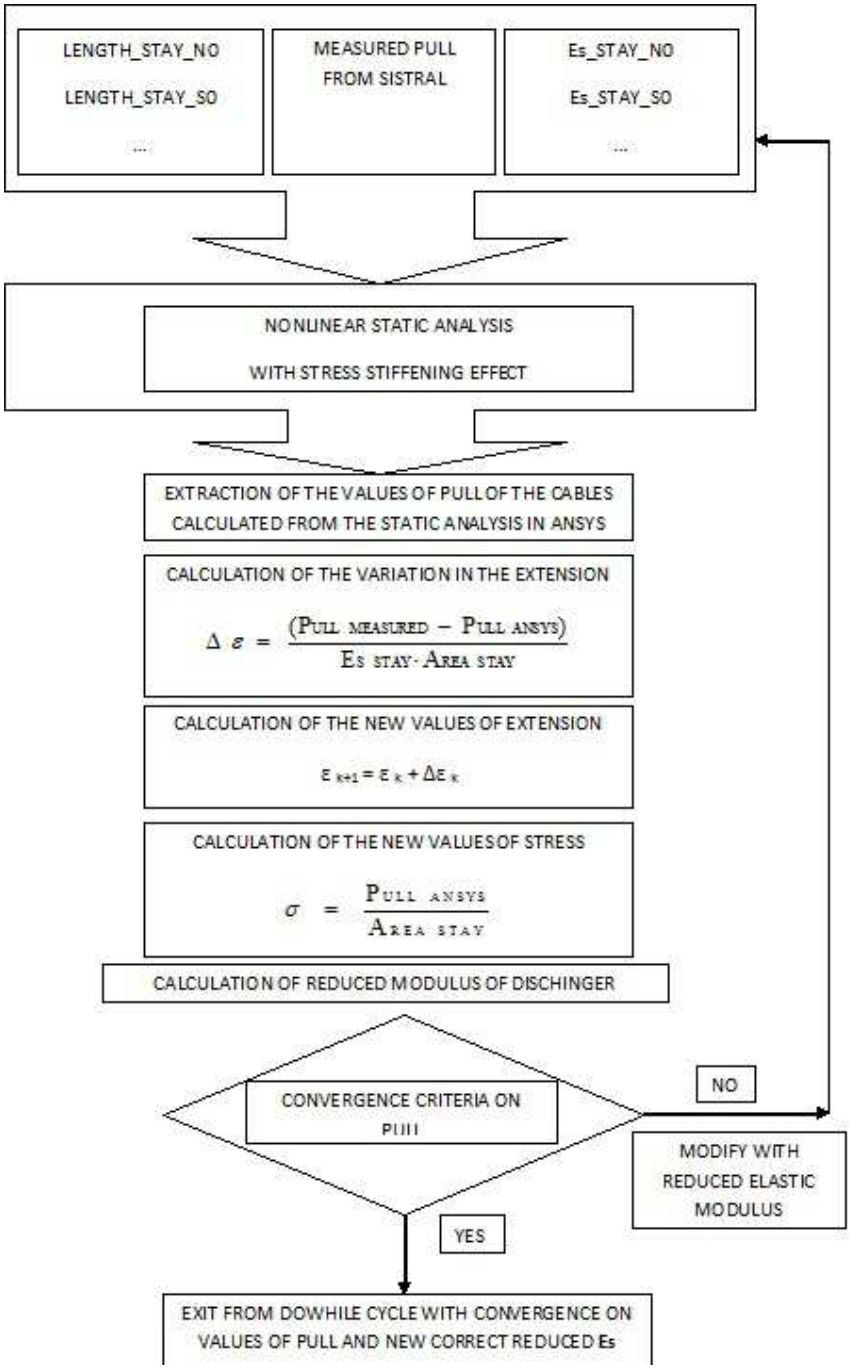

Figure 5.16: Flow chart to calculate the reduced elastic modulus according to Dischinger theory

Table 5.6: Comparison of identified and FE model frequencies

	EMA	Initial FEM	Error %	Modified FEM	Error %
Mode	$f(Hz)$	$f(Hz)$	-	$f(Hz)$	-
1	0.747	0.681	8.8	0.697	6.8
2	1.065	1.003	5.8	1.000	6.1
3	1.126	1.087	3.5	1.059	5.9
4	1.243	1.144	8.0	1.132	8.9
5	1.394	1.369	1.8	1.378	1.1
6	1.510	1.518	-0.5	1.529	-1.3
7	1.716	1.546	9.9	1.565	8.8
8	1.791	1.666	7.0	1.692	5.5
9	2.306	1.702	26.2	1.955	15.2
10	2.364	1.984	16.1	2.079	12.1
11	2.512	2.155	14.2	2.163	13.9
12	2.862	2.299	19.7	2.337	18.34
			10.12		8.66

Table 5.7: Initial MAC values

	1	2	3	4	5	6	8	12	13
1	98.87	1.35	16.63	8.80	7.45	0.83	1.04	11.47	7.27
2	30.77	53.36	25.37	0.61	2.73	6.47	0.97	13.08	2.05
3	0.79	0.26	79.19	4.04	5.48	0.33	0.09	5.59	1.67
4	1.46	11.71	0.01	93.97	14.93	0.61	24.48	0.80	0.01
5	7.54	7.65	4.57	12.98	41.45	2.43	3.39	0.24	5.74
6	13.61	0.91	3.12	10.99	5.17	72.10	2.42	6.77	0.06
7	5.30	4.48	0.76	25.21	1.48	9.92	75.40	0.66	0.00
8	2.17	7.98	10.39	2.17	3.09	2.98	6.05	70.05	6.89
9	5.46	6.69	0.12	0.06	6.58	1.02	1.49	55.14	50.91

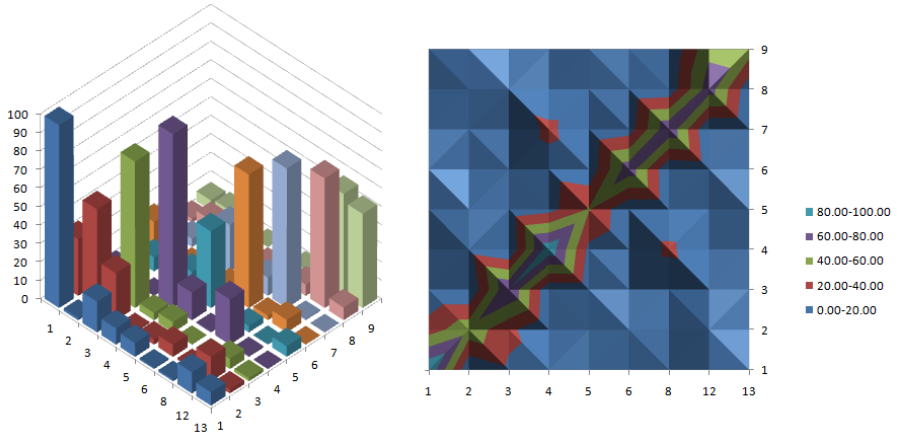

Figure 5.17: Initial MAC in graph

5.4 Model updating of the foot-cycle bridge 'Ponte del Mare' Pescara

5.4.1 Manual updating

This is the so-called phase of manual updating. The primary work in this part is selection of parameters based on engineering judgments and to make sensitivity matrix.

5.4.1.1 Selection of parameters

Observing the 'Ponte del Mare' bridge it appears obvious that a small variation in the elastic modulus of structural steel, steel of stays or of different typologies of concrete used is able to influence the response in a significant manner. Besides, it is observed that the density of concrete used is rarely equal to what verifies in laboratory, the uncertainties in this field are rather large (even more in case of lightened concrete) and since an alteration of the density works on the weight of the deck, it is important to be considered.

The stiffness of the spring that was used to model the support might be able to change the movement of deck in the longitudinal direction and therefore, it was added

as one of the parameters of interest.

Finally, in the set of the parameters of departure, the six *C* coefficients were introduced to take into account of longitudinal stiffening of the different sections in the zones B-C-D-E-F for the pedestrian deck and B' -C' -D' for the cycle deck. To remember that the cycle deck have a uniform section throughout its length. Therefore, only one *C* coefficient was considered for the cycle deck. The shell used to model the deck in the FE model of rectangular plates section, as shown in dark blue in Figure 5.18, were added the features of mass and rigidity of the real section, as shown in red in the same Figure, means the contributions of added mass and the coefficients *C* -that is the ratio between the two different moment of inertia which goes then to multiply the longitudinal elastic modulus of the concrete.

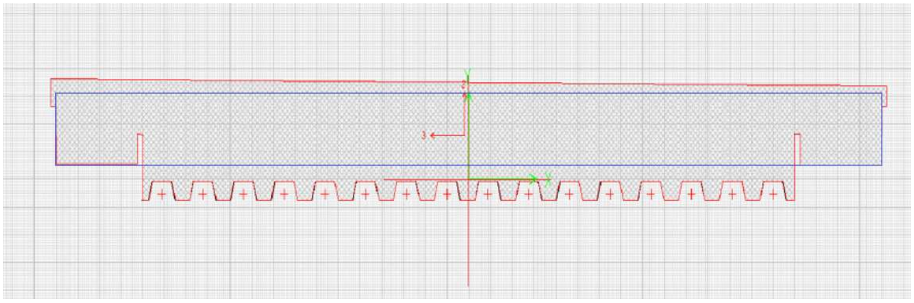

Figure 5.18: Comparison between the real section D and the shell of FE model

Based on the above discussion the initial values of the parameters used to calculate the sensitivity matrix are reported in Table 5.8.

5.4.1.2 Calculation of sensitivity matrix

After choosing the parameters that, according to engineering judgments, could significantly influence the response of the FE model, we proceed to the actual calculation of the sensitivity matrix. The parameters investigated were increased to about 1% to agree a most reasonable approximation necessary for cutting-off the Taylor series.

Moreover, these parameters could not be directly utilised in the calculation of the sensitivity matrix. Recalling the Equation 5.2 for the calculation of *S* looks like, applying merely the formula, the denominator for the line of the matrix that depends on

Table 5.8: Set of the initial parameters for sensitivity check

Parameter number	Parameter	Initial value
$P1$	$Ec1$	35000000 kN/m^2
$P2$	$Ec2$	16000000 kN/m^2
$P3$	Es	210000000 kN/m^2
$P4$	Es_stay_44	165000000 kN/m^2
$P5$	Es_stay_60	165200000 kN/m^2
$P6$	Es_stay_75	162800000 kN/m^2
$P7$	$d1$	1.5 ton/m^3
$P8$	$d2$	2.5 ton/m^3
$P9$	c_cyc	25.40
$P10$	c_ped_B	5.06
$P11$	c_ped_C	1.27
$P12$	c_ped_D	1.15
$P13$	c_ped_E	1.28
$P14$	c_ped_F	7.94
$P15$	k_long	0.00844 kN/m^2

an elastic modulus is $10^7 - 10^8$ times greater than that of the parameters of density. Naturally, all the chosen parameters must have the same unit which is desirable for numerical reasons to obtain a dimensionless sensitivity matrix. Therefore we introduced some dimensionless multiplicative coefficients k (Molinari, 2007) in Eq.(5.2) that will allow to obtain us a correct S:

$$S_{ij} \approx \frac{R_i(K_j + \Delta K_j) - R_i(K_j)}{(K_j + \Delta K_j) - K_j} \tag{5.36}$$

$$P_j^* = P_j \cdot K_j \tag{5.37}$$

where, P_j^* represents a component of the vector of the parameters **P** while **K** is the vector of percentage variation formed from components K_j.

Figures 5.19 and Figure 5.20 show the manual sensitivity matrix based on the frequency.

	S_{i1}	S_{i2}	S_{i3}	S_{i4}	S_{i5}	S_{i6}	S_{i7}	S_{i8}	S_{i9}	S_{i10}	S_{i11}	S_{i12}	S_{i13}	S_{i14}	S_{i15}
S_{1j}	0,04	0,04	0,02	0,04	0,19	0,04	0,21	0,08	0,14	0,15	0,06	0,26	0,07	0,09	0,15
S_{2j}	0,04	0,05	0,02	0,03	0,02	0,02	0,03	0,06	0,12	0,15	0,12	0,09	0,08	0,09	0,07
S_{3j}	0,16	0,17	0,13	0,15	0,11	0,28	0,22	0,28	0,31	0,22	0,51	0,23	0,41	0,70	0,51
S_{4j}	0,03	0,06	0,13	0,21	0,06	0,31	0,16	0,29	0,09	0,16	0,13	0,07	0,27	0,27	0,15
S_{5j}	0,01	0,02	0,04	0,01	0,00	0,00	0,00	0,00	0,00	0,00	0,00	0,00	0,02	0,00	0,00
S_{6j}	0,00	0,01	0,05	0,04	0,00	0,00	0,00	0,01	0,00	0,01	0,01	0,01	0,03	0,00	0,00
S_{7j}	-0,04	-0,08	-0,08	-0,04	-0,06	-0,09	-0,07	-0,12	-0,14	-0,13	-0,16	-0,10	-0,13	-0,28	-0,12
S_{8j}	-0,09	-0,08	-0,09	-0,17	-0,39	-0,19	-0,36	-0,16	-0,27	-0,29	-0,16	-0,63	-0,18	-0,10	-0,35
S_{9j}	0,01	0,02	0,01	0,02	0,01	0,01	0,01	0,02	0,06	0,11	0,09	0,08	0,05	0,07	0,04
S_{10j}	0,02	0,02	0,01	0,01	0,00	0,01	0,02	0,03	0,03	0,03	0,03	0,01	0,02	0,01	0,03
S_{11j}	0,01	0,01	0,00	0,00	0,00	0,00	0,00	0,00	0,00	0,01	0,00	0,00	0,01	0,00	0,01
S_{12j}	0,01	0,01	0,00	0,02	0,00	0,01	0,01	0,04	0,05	0,03	0,01	0,00	0,02	0,01	0,02
S_{13j}	0,01	0,01	0,00	0,00	0,00	0,00	0,00	0,00	0,00	0,01	0,00	0,00	0,01	0,00	0,01
S_{14j}	0,01	0,01	0,00	0,01	0,00	0,00	0,00	0,01	0,02	0,01	0,00	0,00	0,02	0,01	0,01
S_{15j}	0,00	0,00	0,00	0,00	0,00	0,00	0,00	0,00	0,00	0,00	0,00	0,00	0,00	0,00	0,00

Figure 5.19: Manual sensitivity matrix

Observing the sensitivity matrix we can make some consideration:

• to an increment of 1% of the parameters it is noted that only the density of the concrete lowers the frequency response while all the other parameters stiffen the structure;

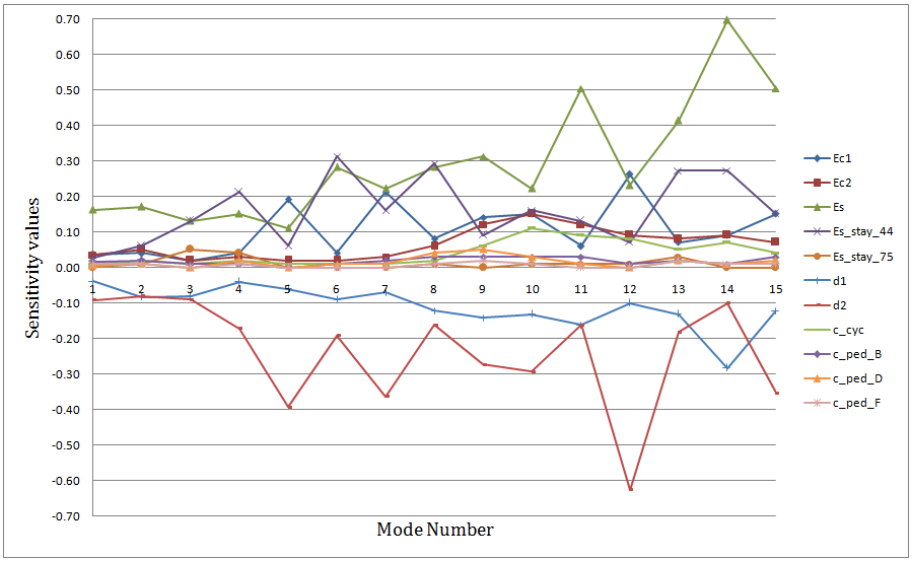

Figure 5.20: Graphical view of the sensitivity matrix

• the inffluence of the moment of inertia or the *C* coefficient is more significant whereas the sections of the deck have smaller thicknesses of concrete, that is comparable looking at the *c_cyc*;

• the elastic modulus of the stays with diameter 60 mm and 75 mm influence the structural response lesser than those with diameter 44 mm, essentially because smaller in number;

• the elastic modulus of the structural steel is by far the most sensitive parameter of the structure and this was imaginable as the bridge is mainly composed of steel.

On the basis of the above considerations we can exclude the less sensitive parameters. Therefore, the parameters *k_long* that identifies the rigidity of the ALGAFLON supports, the elastic modulus of cables *Es_stay_*60 and *Es_stay_*75 and some the *C* coefficents of the pedestrian deck, that give relatively low contribution to the sensitivity matrix, were excluded.

Generally, it is worth to use the condition number (CN) of the matrix **S** of departure and later to see how the CN varies after removing the lines of the less sensitive parameters. The CN must not surpass the threshold of the CN equal to 10^5, already discussed in Section 5.2.

This analysis was performed as a check on the manual sensitivity matrix, because we did not find a simpler manner to implement the QR method in APDL language, that meant a tie in the selection of the number of the parameters from updating. In fact if we don't utilise the QR method there remain two alternatives to invert S: the inverse of a square matrix or the pseudo-inverse of Moore-Penrose (MP) for a rectangular one.

Nevertheless, in an automatic updating procedure it calculates a different sensitivity matrix to every iteration and it is possible that at a given iteration it surpasses the CN limit and therefore the pseudo-inverse calculated with QR or MP will not be correct. Therefore, for simplicity, computational efficiency and in order not to run in mistakes, 9 chosen frequencies will be updated by means of 9 parameters. To choose the 9 most sensitive parameters simply the RMS (Root Mean Square) value was used. Later, it was found that these 9 parameters verify a CN of about 300 that is obviously less than the threshold of 10^5. The parameters used for the updating and the relevant vector $\mathbf{K}_9$ are shown in Table 5.9.

Table 5.9: Set of parameters used in model updating

Parameter	K_9
*Ec*1	*k*1
*Ec*2	*k*2
Es	*k*3
*Es_stay_*44	*k*4
*d*1	*k*5
*d*2	*k*6
c_cyc	*k*7
c_ped_B	*k*8
c_ped_D	*k*9

5.4.2 Automatic updating: implementation of the method

We implemented the whole MU procedure in the APDL language. APDL is a scripting language that you can use to automate common tasks or even build your model in terms of parameters (variables). While all Ansys commands can be used as part of the scripting language, the APDL commands are the true scripting commands and encompass a wide range of other features such as repeating a command, macros, if-then-else branching, do-loops, and scalar, vector and matrix operations. While APDL is the foundation for sophisticated features such as design optimisation and adaptive meshing, it also offers many conveniences that you can use in your day-to-day analyses. This presents a large advantage because if any detail on the FE model is modified the same procedure itself obtains directly the results without obliged to pass through other programs. To implement a mathematical subroutine that is not present in the ANSYS library can be recalled in any mathematics program, like for example MATLAB, with the help of a simple string.

All the methodologies of updating that will be treated later on have in common the first and the last part. In the first part two kind of analyses will be made - the nonlinear static analysis under gravitational loads and - the modal analysis for the first 13 modes. These two solutions will be used on other n occasions inside the methods to calculate each component of the sensitivity matrix, where n is the number of the components of the vector $\mathbf{K}$. The APDL code is written as follows.

```
!Nonlinear static analysis
/SOLU
OUTPR,ALL,LAST
    !Command that controls the solution printout for all the elements.
OUTRES,ALL,LAST
    !Controls the solution data written to the database file.
ANTYPE,STATIC
    !Performs nonlinear static analysis under gravitational loads.
NLGEOM,ON
    !Includes large-deflection effects in the analysis.
SSTIF,ON
```

!Activates stress stiffness effects in a nonlinear analysis.

EMATWRITE,YES

!Forces the writing of all the element matrices to file.emat.

ALLSEL

!Selects all entities with a single command.

ACEL,0,0,9.81

!Specifies the linear acceleration of the structure in the global Cartesian X, Y, and Z axis directions, respectively.

FINISH

!Nonlinear modal analysis

/SOLU

ANTYPE,MODAL

!Performs modal analysis.

SSTIF,ON

!Activates stress stiffness effects in a nonlinear analysis.

MODOPT,LANB,13

!Specifies the mode extraction method to be used for the modal analysis: Block Lanczos.

MXPAND,13

!Specifies the number of modes to expand and write for a modal analysis.

PSOLVE,EIGLANB

!Calculates the eigenvalues and eigenvectors using Block Lanczos.

EXPASS,ON

!Specifies an expansion pass of an analysis.

PSOLVE,EIGEXP

!Expands the eigenvector solution.

FINISH

In the last part the results of the analysis will be extracted through postprocessor, i.e. the vector $\mathbf{K}_9$ in the case of 9 frequencies. For example, the following code represents a case of 9 frequencies where a vector of size 9x1 is assembled with the components of the parameters *ki* then to export it in a text file in the desired format.

/POST1

*CFOPEN,RESULTS_ITER_9,txt

!Opens a ”command” file.

*DIM,P0,,9,1

!Defines a vector of parameters and dimensions.

*VFILL,P0(1),DATA,k1

...

*VFILL,P0(11),DATA,k9

!Fills a vector of parameters.

*VWRITE,P0

(19(f20.5,5x))

!Writes data to a file in a formatted sequence.

*CFCLOSE

!Closes a ”command” file.

FINISH

Also the selection of the convergence criterion is identical for all of the MU methods taken into consideration. Between the varied possible criteria it has been chosen to use the direct comparison of error (DELTAR) with a fixed tolerance (TOL) not on the vector but on the individual components. Such comparison is carried out in every cycle using the command IF-THEN and until every component does not respect this condition, the cycle continues according to the DOWHILE command:

KK=1

!Name of the parameter rise used as indicator of the loop.

*DOWHILE,KK

!Cycle repeats untill meets the order *ENDDO.

...

*DIM,Rexp,,9,1

...

*DIM,R0,,9,1

...

*DIM,DELTAR,,9,1

*VOPER,DELTAR,Rexp,SUB,R0

!Operation between two vectors.

```
*DIM,TOL,,9,1
*DO,i,1,9,1
    !Command that defines the start of a cycle of DO.
*VFILL,TOL(i),DATA,0.05
*ENDDO
    !Closes the cycle DO.
*IF,DELTAR,LT,TOL,THEN
    !Condition imposed on command *IF. LT: lower than (for VAL1<VAL2).
KK=0
*ENDIF
    !Ends the 'IF-THEN-ELSE'.
*ENDDO
    !Ends the action of DOWHILE cycle.
```

Finally, limits on the variation of the parameters were imposed. The bound problem will have surely more difficulty to converge with respect to the unbound one, but this will allow us to obtain some more realistic physical values.

To implement this choice in APDL we used the IF-THEN-ELSEIF-ELSE construction. An example is shown for the case of the elastic modulus of steel E_s that varies to every iteration through $k3$:

```
*IF,Pu(3),GT,1.05,THEN
k3=1.05
*ELSEIF,Pu(3),LE,1.05,AND,Pu(3),GE,0.95
k3=Pu(3)
*ELSE
k3=0.95
*ENDIF
```

The new parameter is retained physically valid only in the case in which 199500000 kN/m^2 $< E_s <$ 220500000 kN/m^2, that is within a range of $\pm$5%, while if surpassed the thresholds, it would be restored automatically to the limit value of the range.

For the elastic modulus of steel, we choose a rather limited range due to the accuracy in the production of these materials. Greater uncertainties instead were used for the elastic modulus and the density of the two concrete types, as is known, depend

on the quality of labor and the conditions on site. Particularly, the density fluctuates from 2.1 to 2.2 ton/m^3 but it is necessary to add a further $12 - 16\%$ variation due to the contribution of other uncertainties and alterations in the run of work. In the FE model, in fact the permanent loads carried by handrails, centerings, concrete layer of the slopes, steel nets and paving were parameterised in function of the density associated to the respective sections.

Finally, analysing the *C* coefficents, i.e. a ratio between the moment of inertia of the section of the FE model and of the section calculated with the Section Designer of SAP would not need a wide range of variation. $\pm$15% finds besides verification in article on the MU of the pedestrian bridges (Zivanovic et al., 2007), in fact in that case the layer of asphalt contributed largely to stiffen the structure. The variability associated to every parameter is shown in Table 5.10.

Table 5.10: Range of the admissibility of the parameters

Parameter	Initial value	Range ”physical”
*Ec*1	35000000 kN/m^2	$\pm$15%
*Ec*2	16000000 kN/m^2	$\pm$15%
Es	210000000 kN/m^2	$\pm$5%
*Es_stay_*44	165000000 kN/m^2	$\pm$5%
*d*1	1.5 ton/m^3	$\pm$30%
*d*2	2.5 ton/m^3	$\pm$30%
c_cyc	25.40	$\pm$15%
c_ped_B	5.06	$\pm$15%
c_ped_D	1.15	$\pm$15%

5.5 Results and discussion

5.5.1 The final result

The value of the radius, $\Delta_{initial}$ of the Trust-Region is assigned manually for trials. Starting from a unit value, it is increased one by one the radius of departure till 6. From the six values, $\Delta_{initial} = 2$ offered the lowest average percentage error. After 9 iterations is obtained the set of parameters that minimizes the difference between the frequencies, shown in Table 5.11, but it is necessary to keep into consideration that the pull of the stays is remained unchanged inside the cycle.

Table 5.11: Set of parameters that minimize the difference with the experimental frequency

Parameter	$\underline{K_9}$
*Ec*1	1.0957
*Ec*2	0.8500
Es	1.0500
*Es_stay_*44	0.9500
*d*1	0.7613
*d*2	0.7000
c_cyc	1.0999
c_ped_B	1.0413
c_ped_D	0.9957

The set $\mathbf{K}_9$ was therefore introduced in the file for the calculation of the elongation of the stays. Table 5.12 presents the updated frequencies. It is notable that the average percentage error between the absolute values is equal to 2.89%, on 9 frequencies examined decrease of about 30% with respect to the non-updated model.

Table 5.13 shows the MAC values of the updated FE model, and Figures 5.21 and 5.22 shows the MAC values between the experimental and updated FE model. The

Table 5.12: Frequencies obtained at the end of model updating and mean percentage error comes 2.89%

EMA		FEM		|Error%|
*Rxp*1	0.7476*Hz*	*Rans*1	0.7380*Hz*	1.28%
*Rxp*2	1.0653*Hz*	*Rans*2	1.0475*Hz*	1.67%
*Rxp*3	1.1257*Hz*	*Rans*3	1.0994*Hz*	2.33%
*Rxp*4	1.2430*Hz*	*Rans*4	1.1793*Hz*	5.12%
*Rxp*5	1.3939*Hz*	*Rans*5	1.4372*Hz*	3.11%
*Rxp*6	1.5098*Hz*	*Rans*6	1.6081*Hz*	6.51%
*Rxp*7	1.7165*Hz*	*Rans*8	1.7609*Hz*	2.58%
*Rxp*10	2.3639*Hz*	*Rans*12	2.4345*Hz*	2.98%
*Rxp*11	2.5119*Hz*	*Rans*13	2.5024*Hz*	0.38%

Table 5.13: Updated MAC values

	1	2	3	4	5	6	8	12	13
1	98.61	0.06	15.84	8.23	8.08	8.18	1.24	7.70	7.00
2	32.53	42.47	29.75	0.45	4.12	6.91	0.64	11.07	2.92
3	0.81	0.89	76.81	3.72	5.95	0.24	0.72	10.01	0.54
4	1.47	11.29	0.45	94.77	16.63	1.89	23.11	0.56	0.11
5	7.50	7.24	4.19	12.15	37.96	0.03	9.21	1.90	3.54
6	13.91	0.07	3.39	10.85	11.46	88.32	0.26	10.33	0.07
7	5.49	6.63	0.27	26.52	1.38	14.81	72.89	0.46	0.06
8	2.19	6.88	10.82	2.25	2.66	0.02	4.16	60.37	10.10
9	5.49	6.65	0.24	0.02	6.47	0.60	0.75	26.79	48.73

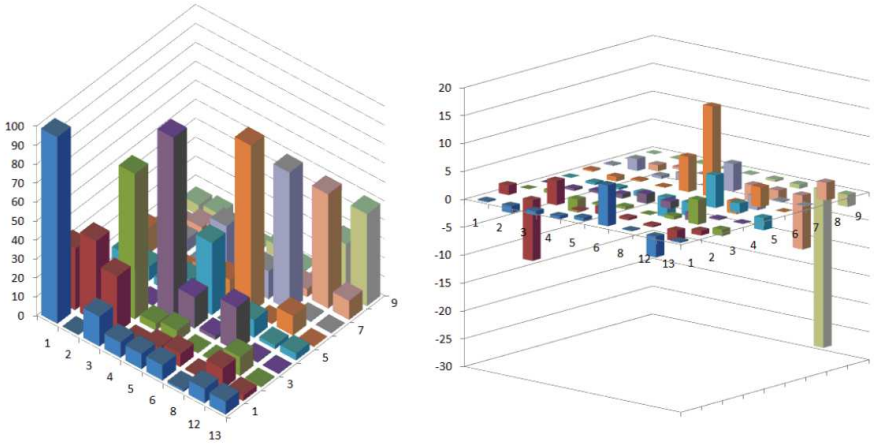

Figure 5.21: At left a classical view of MAC and at the right difference in MAC values

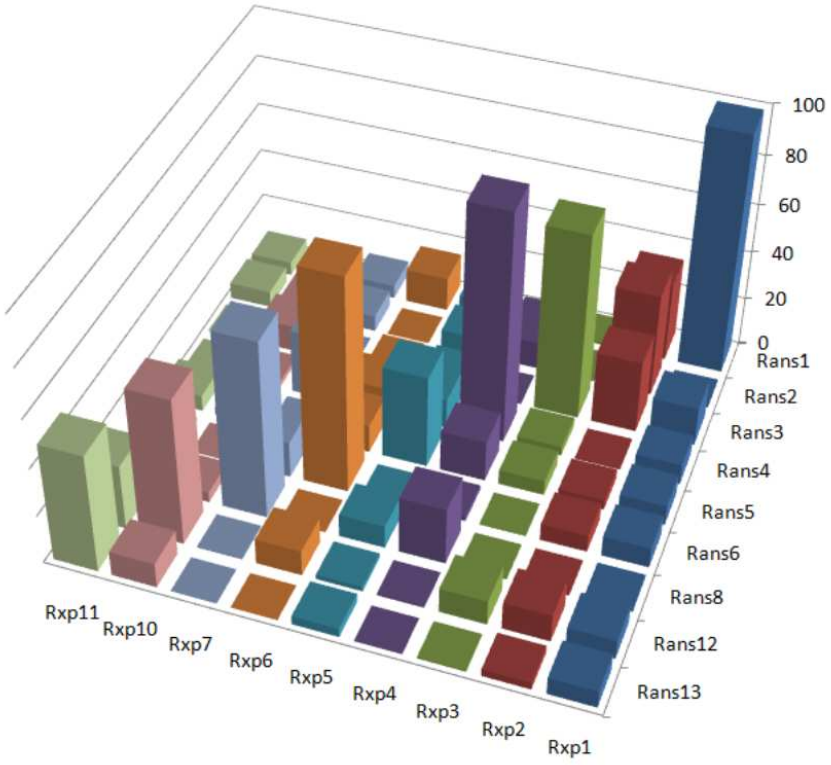

Figure 5.22: MAC, xp- experimental & ans- ANSYS

following important points can be considered:

• the average value of the diagonal of the MAC matrix decreases by about 1%, i.e. from 70.59% to 68.99%, however, beating down the values outside the diagonal;

• the correlation between the modes $2-2$ falls about 10%, negative red bar in ΔMAC;

• the correlation between the modes $6-6$ increases about 16%, positive orange bar in ΔMAC;

• the correlation between the modes $10-12$ falls about 10%, negative pink bar in ΔMAC; nevertheless, the correlation between $11-12$ falls about 28% removing the sole present uncertainty.

Therefore, one can see that the updating on the frequency with the Dog Leg method carried to a physically acceptable set of parameters, produced two negative and two positive effects in the MAC matrix. Nevertheless, the diagonal maintains a high percentage of correlation between modes. These results persuade to affirm that this is a feasible compromise between mode shape and frequency.

After the Modal Assurance Criterion, we carried a visual comparison on the modal shapes, see Figures 5.23-5.64. Particularly, it confirms with the lower values of MAC found in Figures 5.28, 5.50 and 5.60.

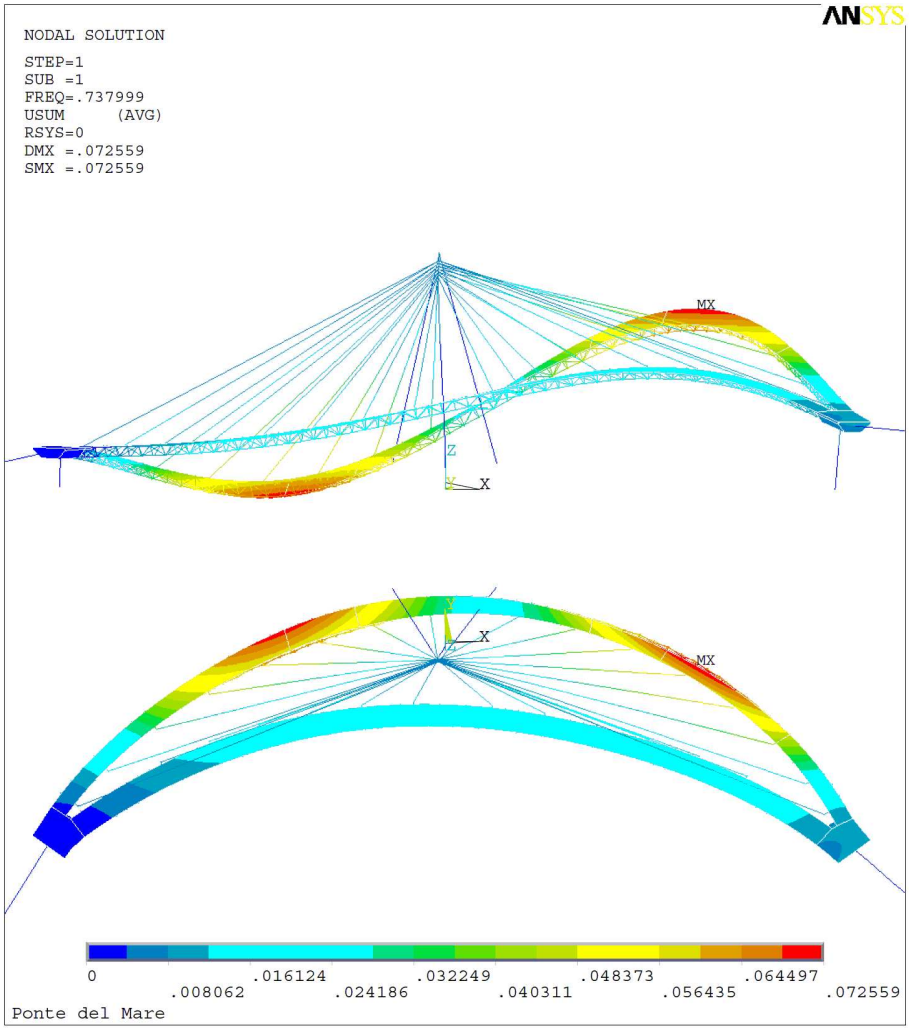

Figure 5.23: 1st mode of ANSYS correlated with 1st mode of experiment with MAC=98.6

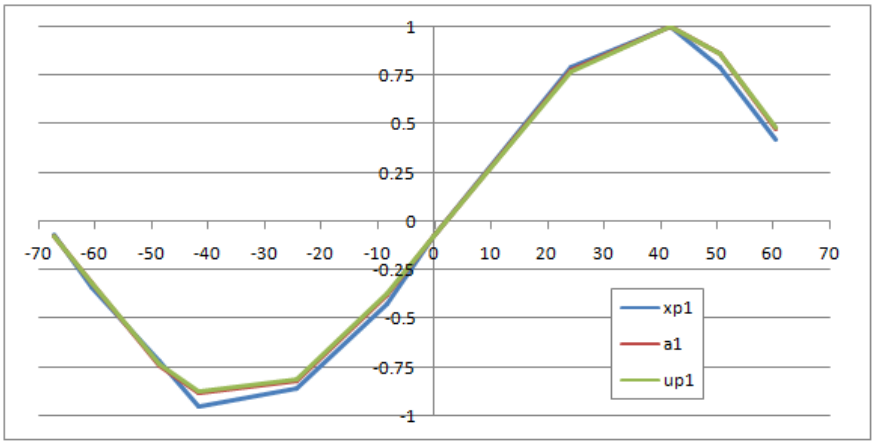

Figure 5.24: Normalized vertical autovector of the pedestrian deck

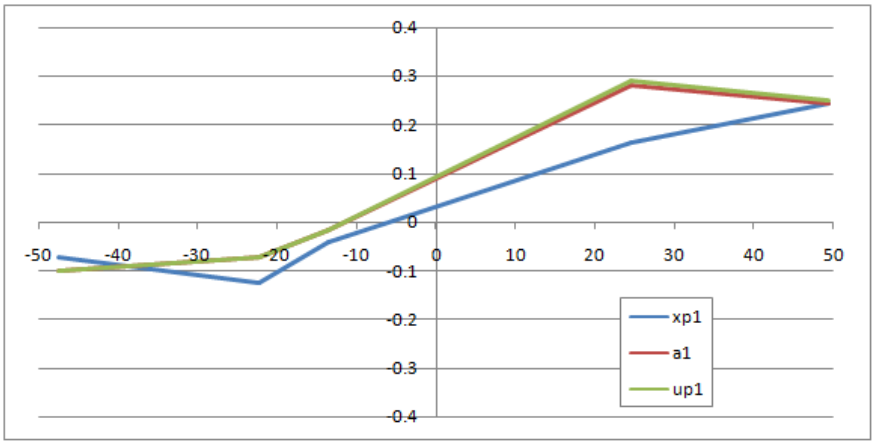

Figure 5.25: Normalized vertical autovector of the cycle deck

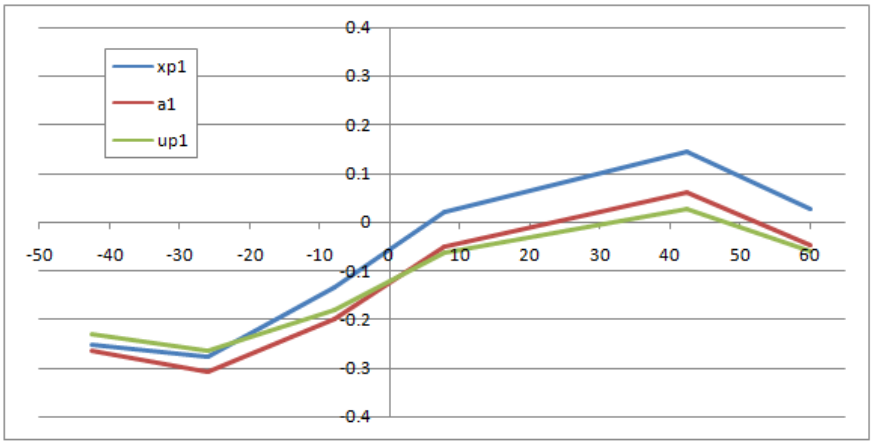

Figure 5.26: Normalized radial autovector of the pedestrian deck

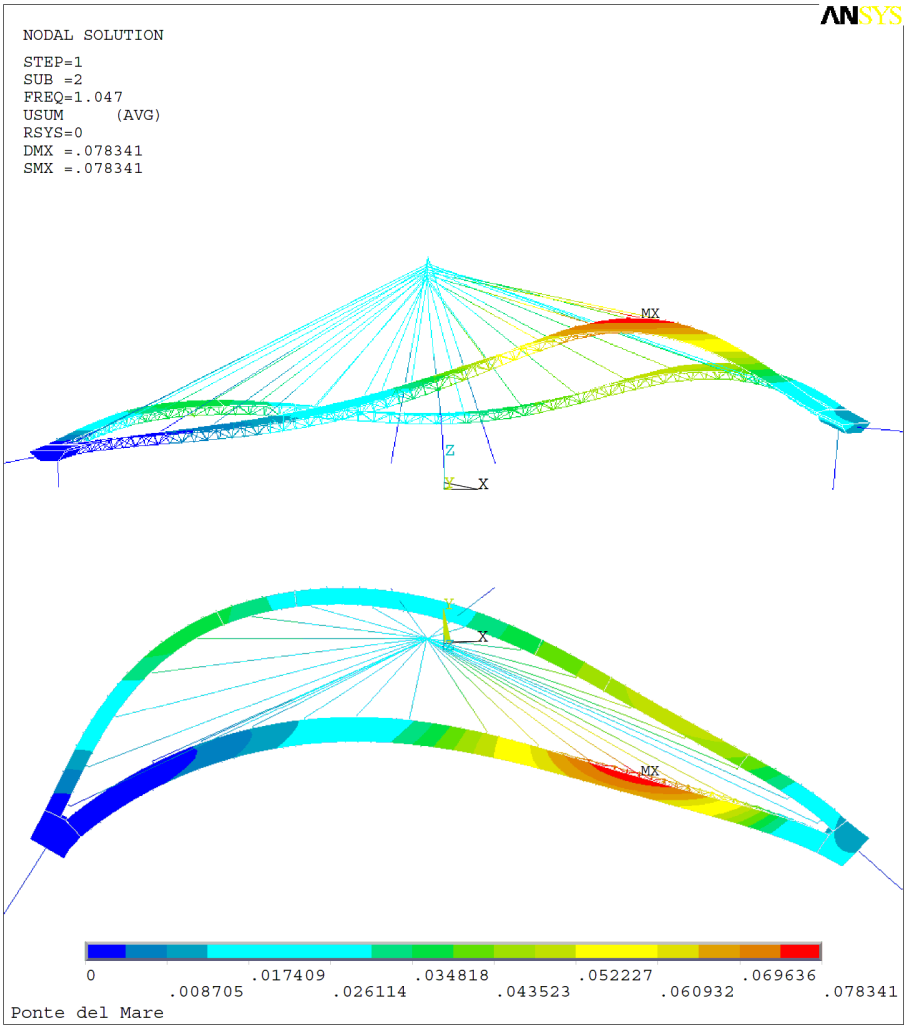

Figure 5.27: 2nd mode of ANSYS correlated with 2nd mode of experiment with MAC=42.5

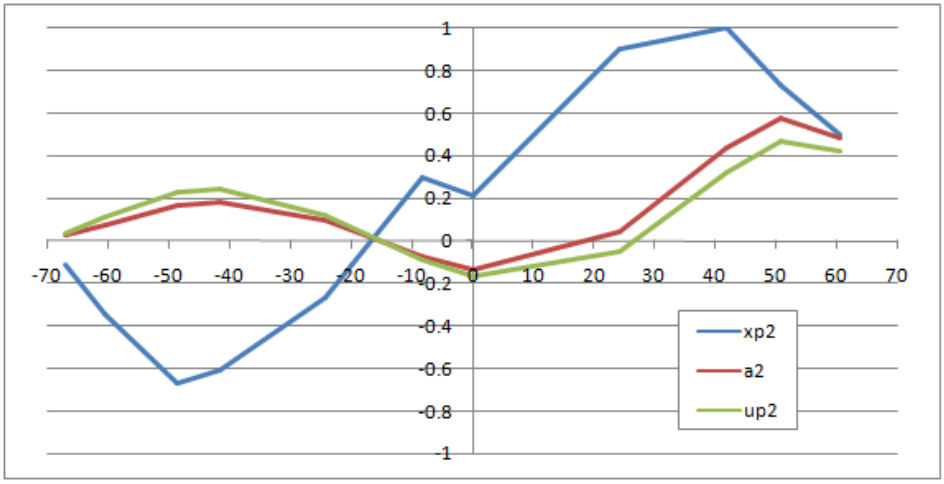

Figure 5.28: Normalized vertical autovector of the pedestrian deck

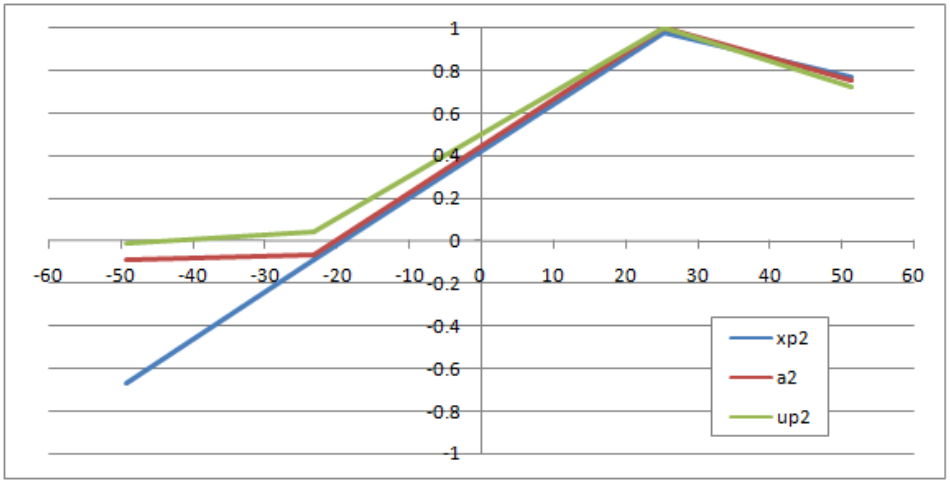

Figure 5.29: Normalized vertical autovector of the cycle deck

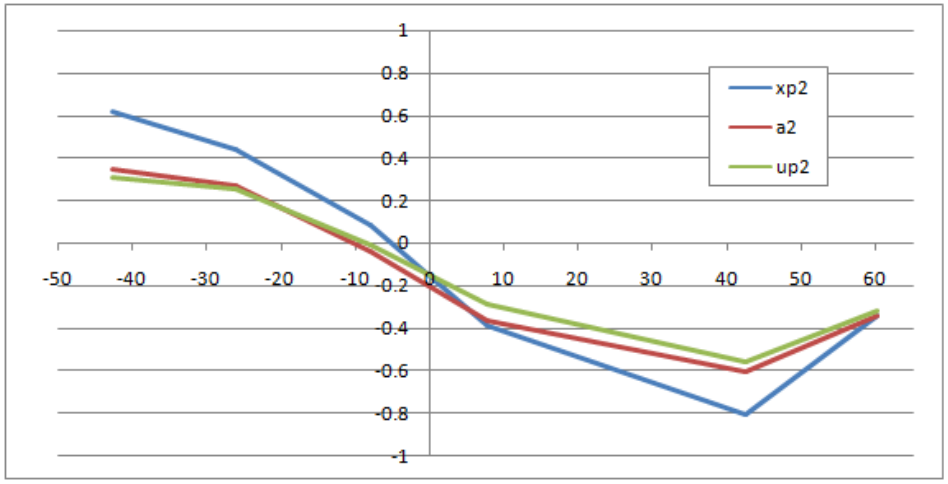

Figure 5.30: Normalized radial autovector of the pedestrian deck

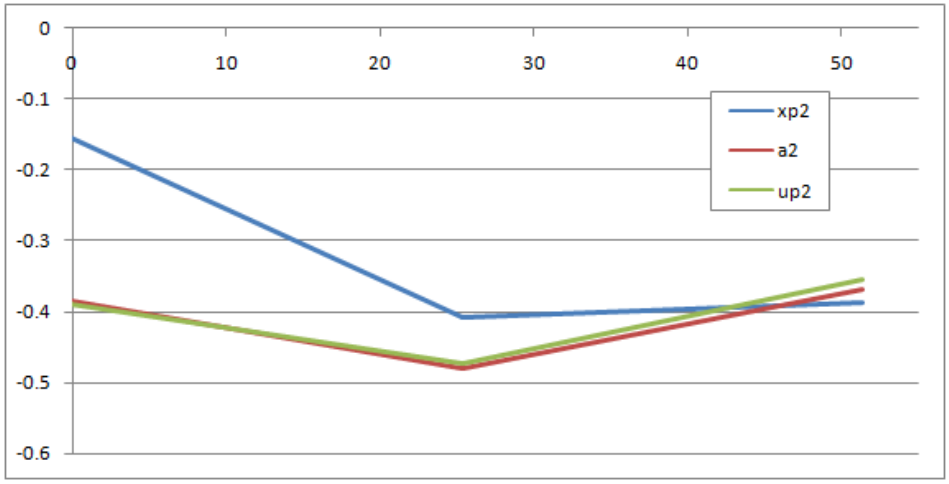

Figure 5.31: Normalized radial autovector of the cycle deck

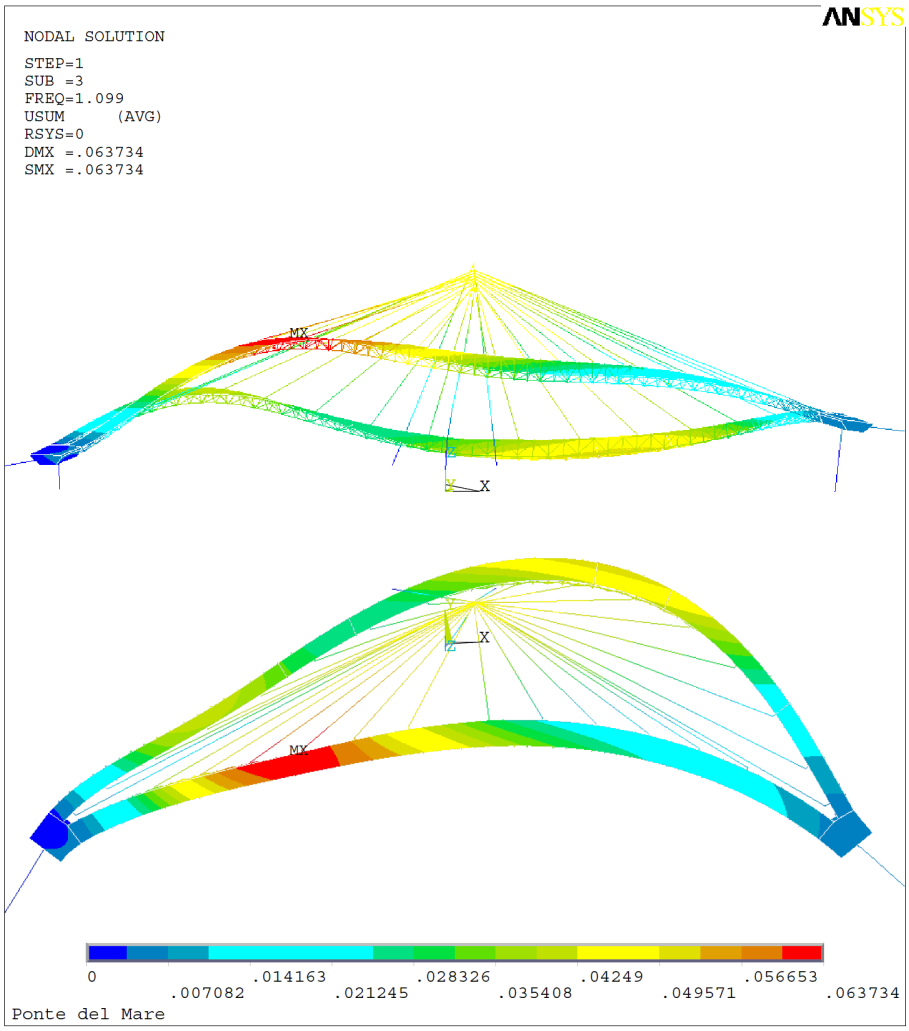

Figure 5.32: 3rd mode of ANSYS correlated with 3rd mode of experiment with MAC=76.8

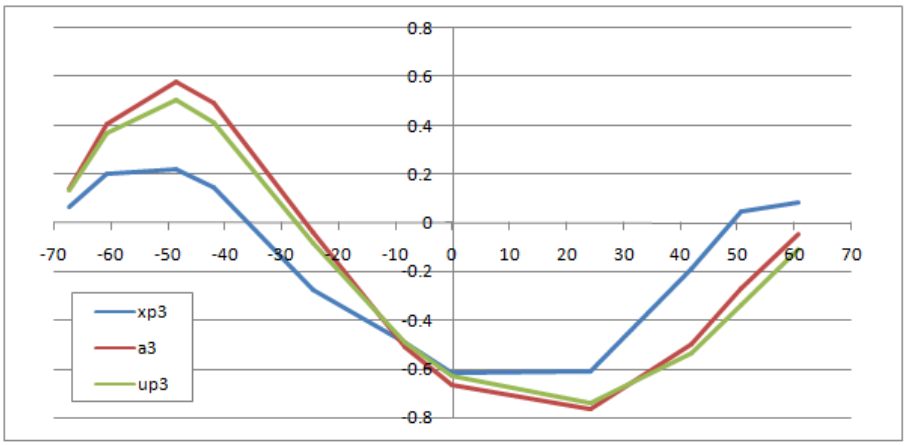

Figure 5.33: Normalized vertical autovector of the pedestrian deck

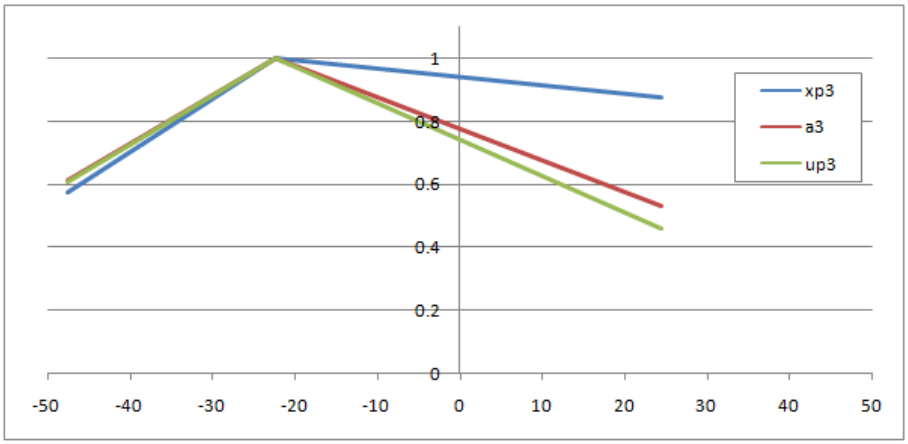

Figure 5.34: Normalized vertical autovector of the cycle deck

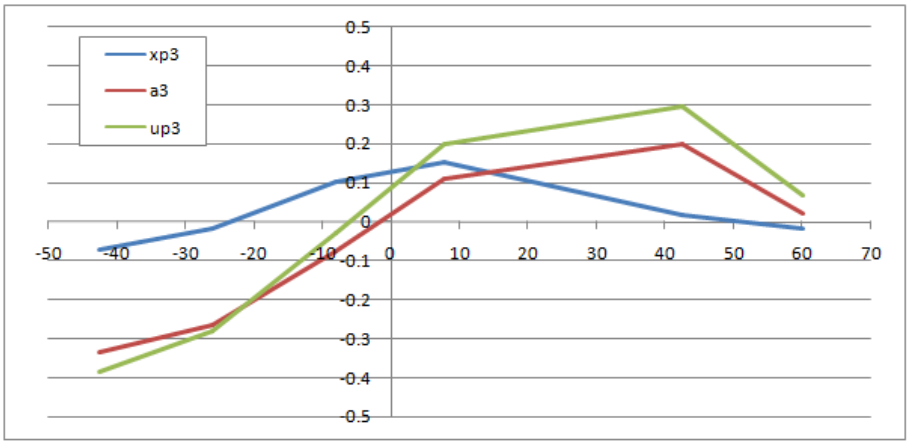

Figure 5.35: Normalized radial autovector of the pedestrian deck

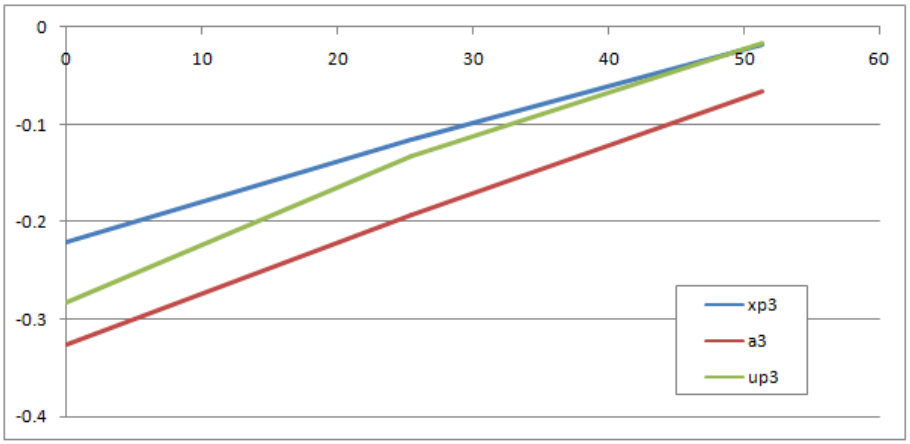

Figure 5.36: Normalized radial autovector of the cycle deck

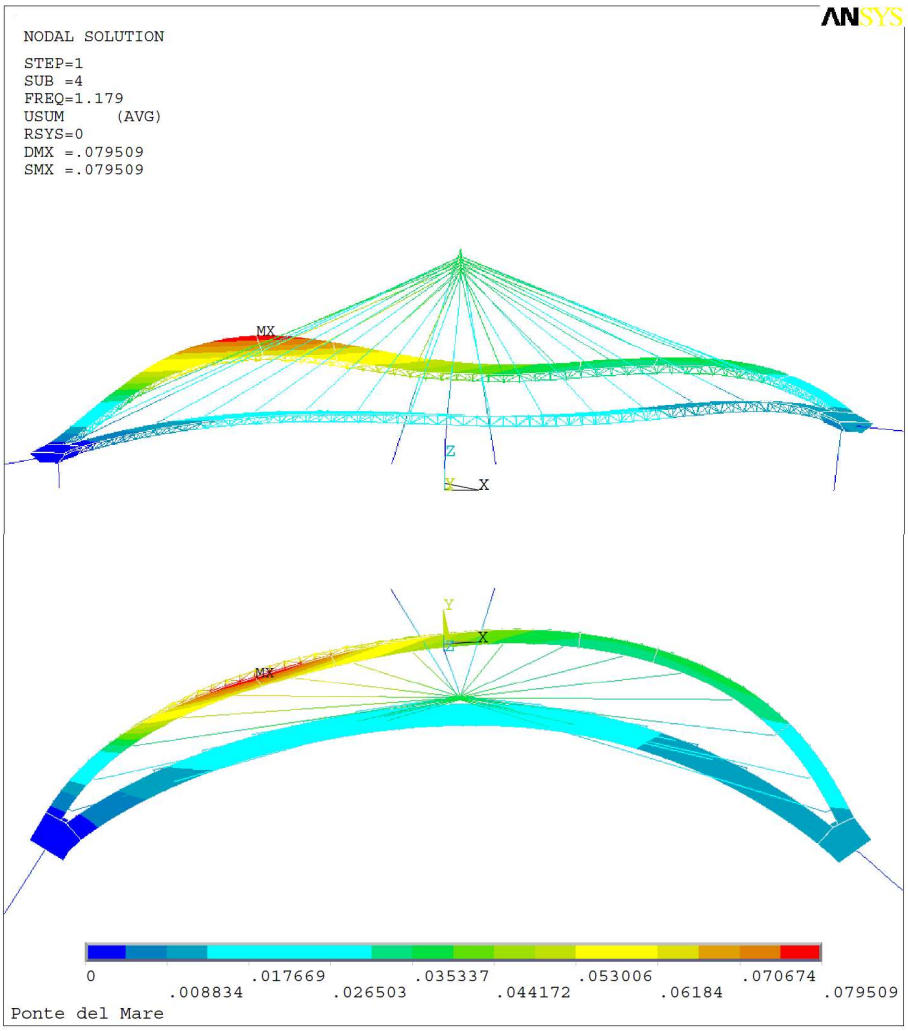

Figure 5.37: 4th mode of ANSYS correlated with 4th mode of experiment with MAC=94.8

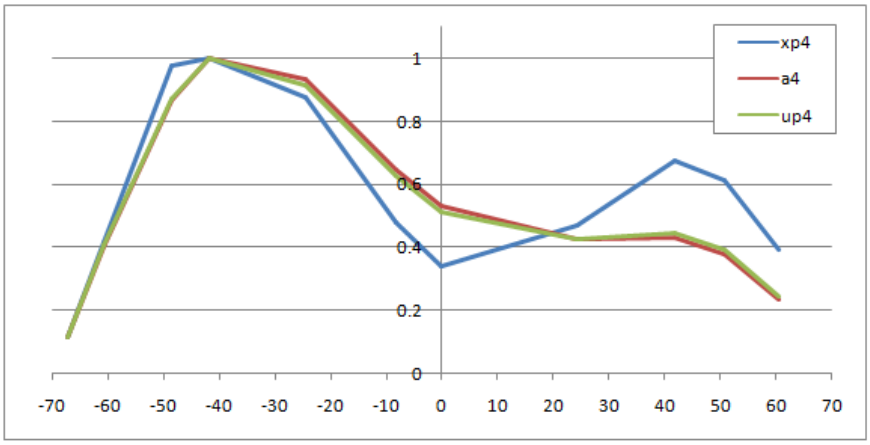

Figure 5.38: Normalized vertical autovector of the pedestrian deck

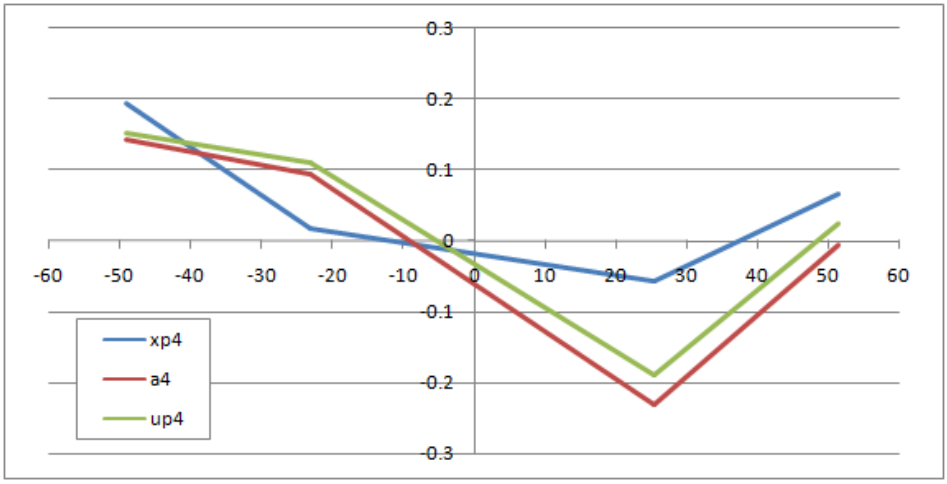

Figure 5.39: Normalized vertical autovector of the cycle deck

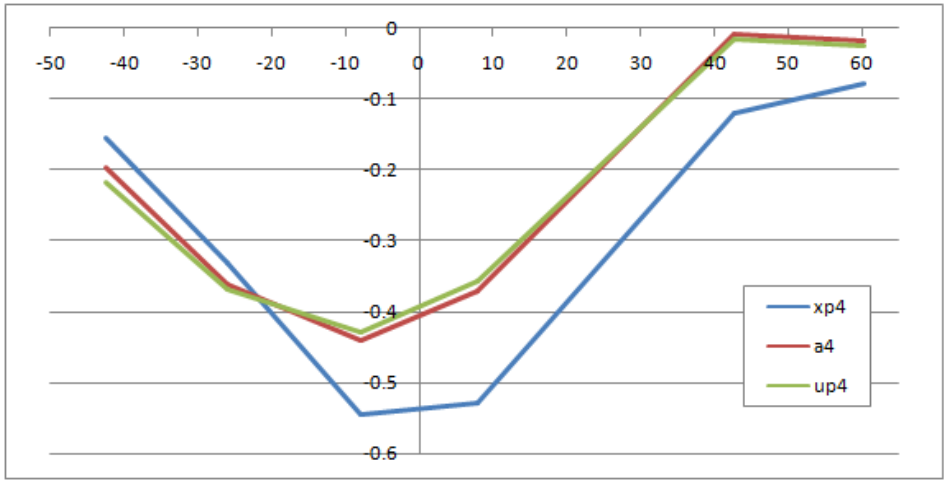

Figure 5.40: Normalized radial autovector of the pedestrian deck

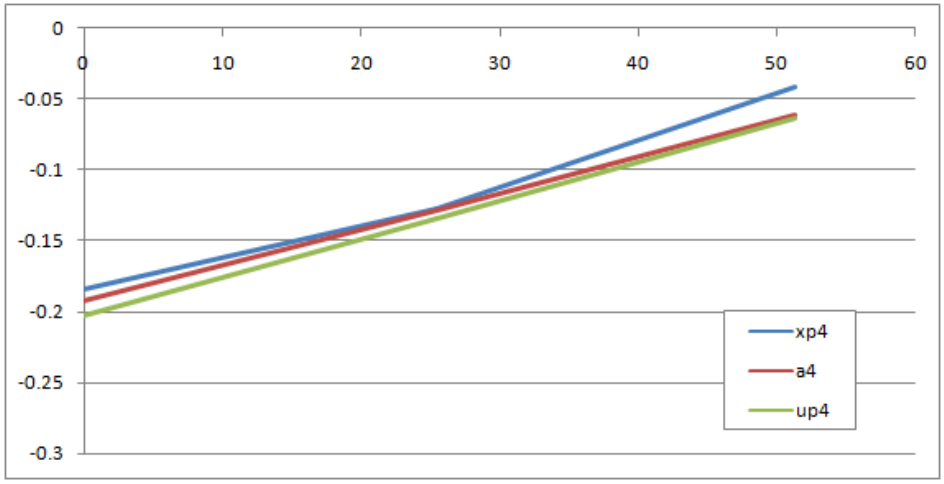

Figure 5.41: Normalized radial autovector of the cycle deck

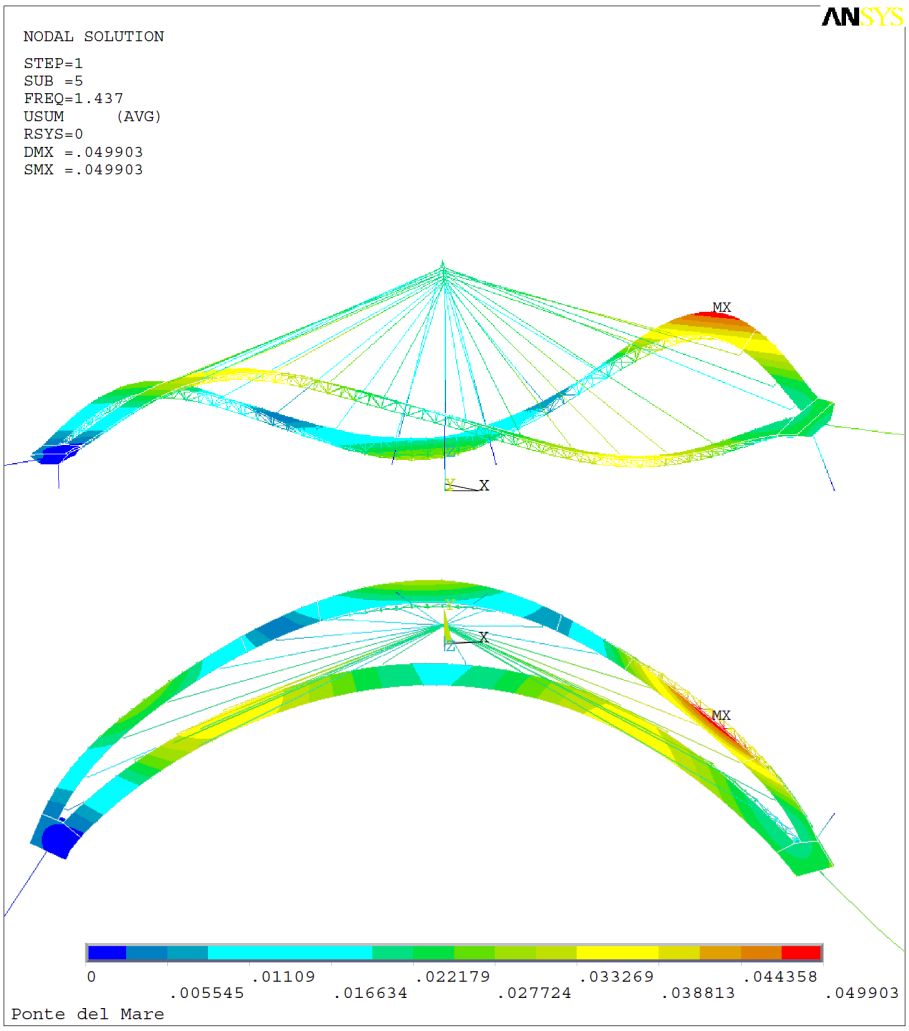

Figure 5.42: 5th mode of ANSYS correlated with 5th mode of experiment with MAC=38.0

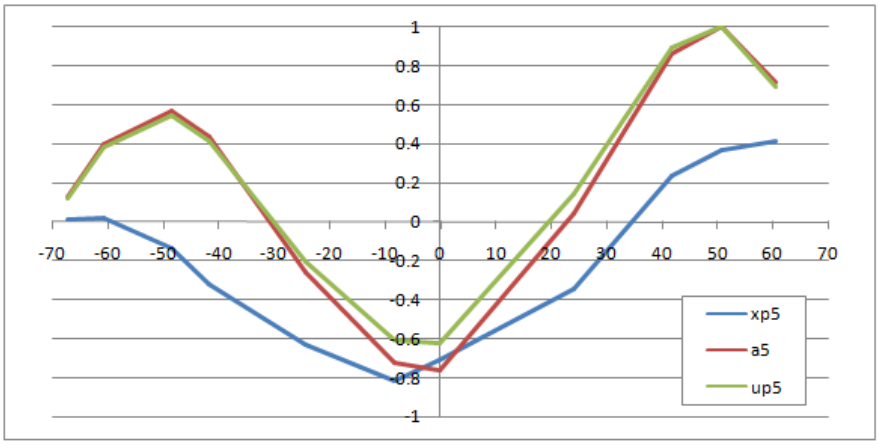

Figure 5.43: Normalized vertical autovector of the pedestrian deck

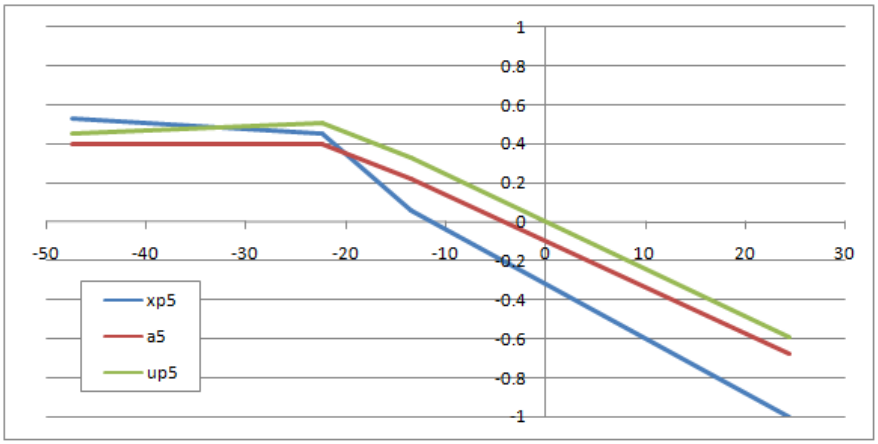

Figure 5.44: Normalized vertical autovector of the cycle deck

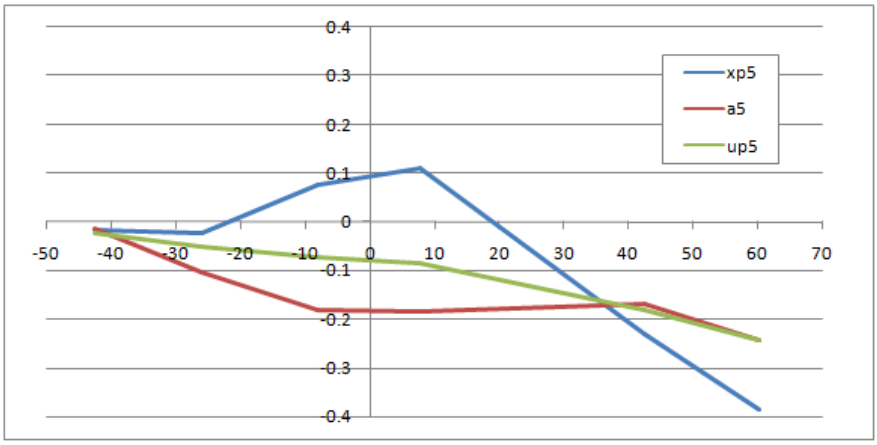

Figure 5.45: Normalized radial autovector of the pedestrian deck

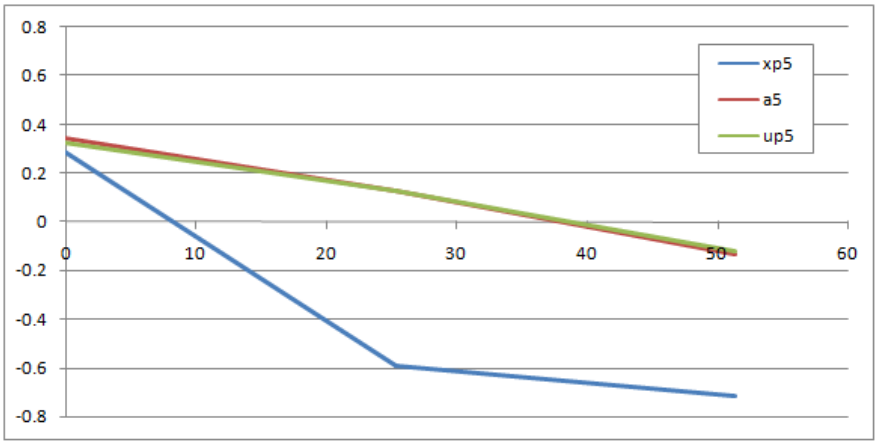

Figure 5.46: Normalized radial autovector of the cycle deck

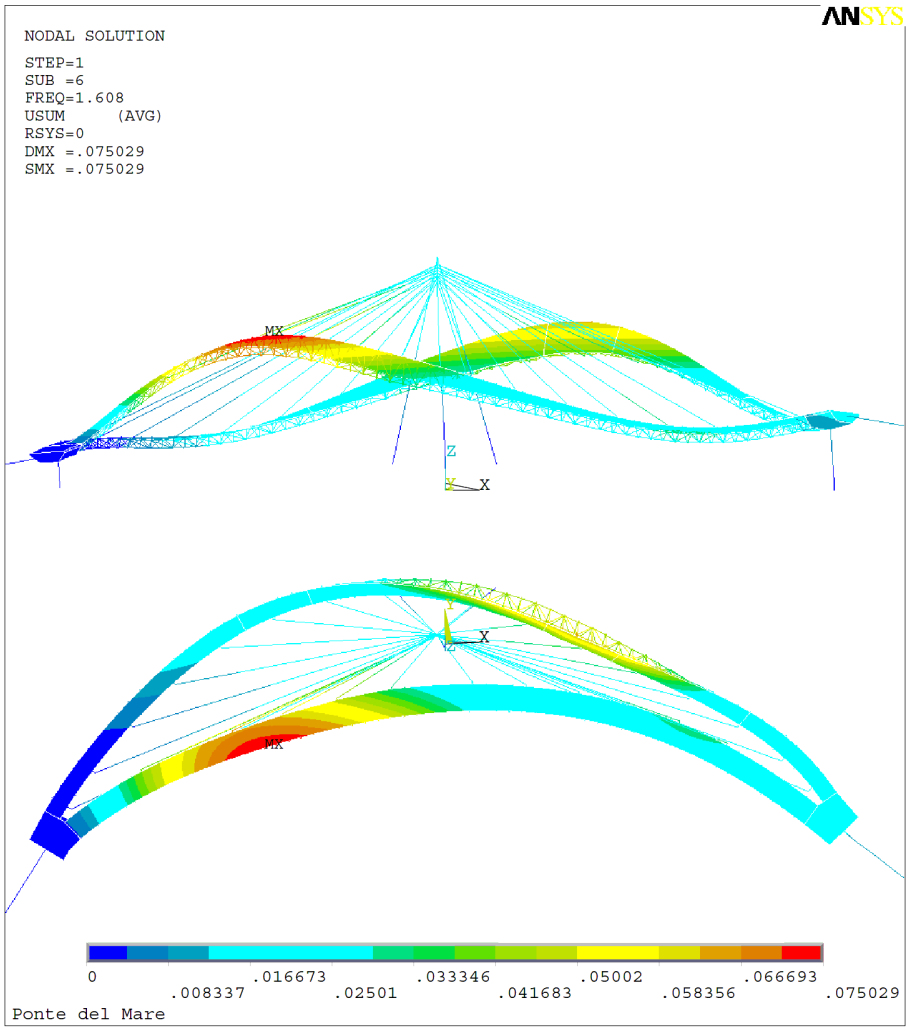

Figure 5.47: 6th mode of ANSYS correlated with 6th mode of experiment with MAC=88.3

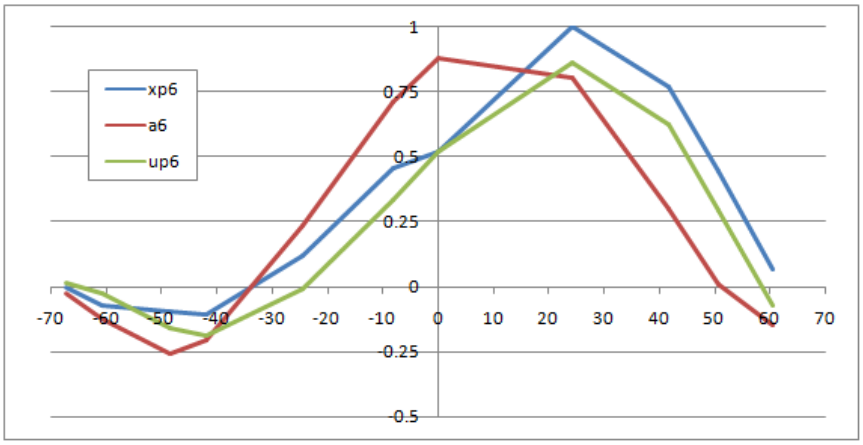

Figure 5.48: Normalized vertical autovector of the pedestrian deck

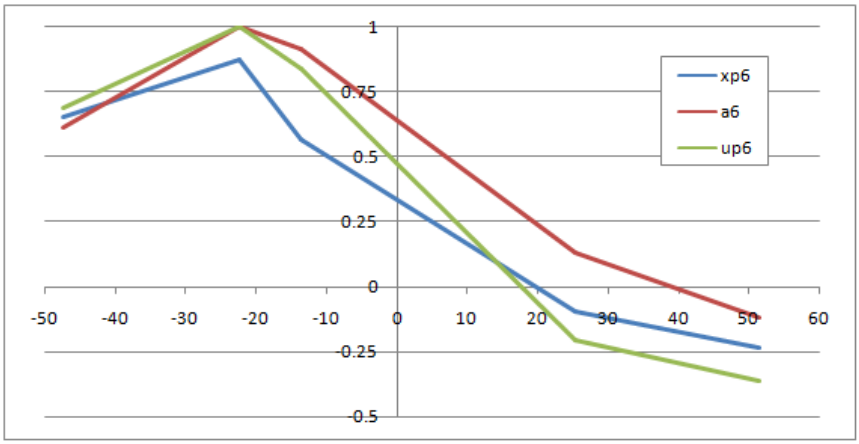

Figure 5.49: Normalized vertical autovector of the cycle deck

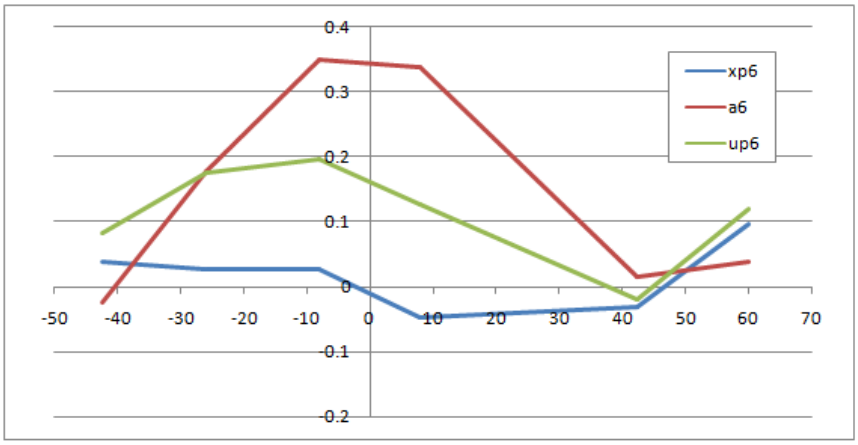

Figure 5.50: Normalized radial autovector of the pedestrian deck

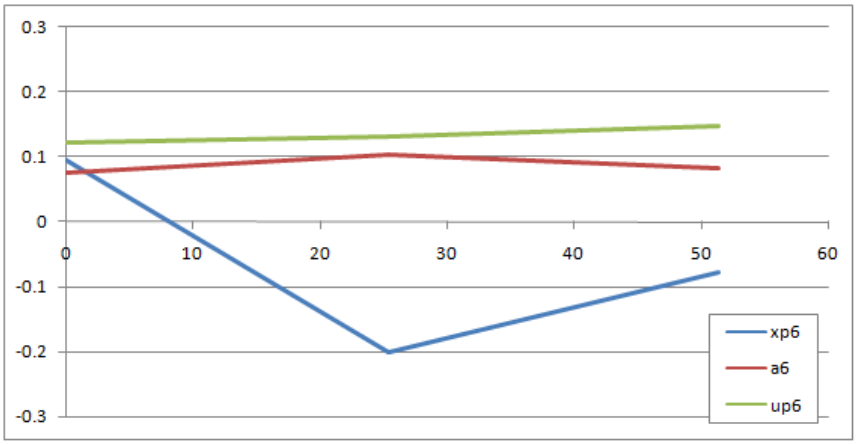

Figure 5.51: Normalized radial autovector of the cycle deck

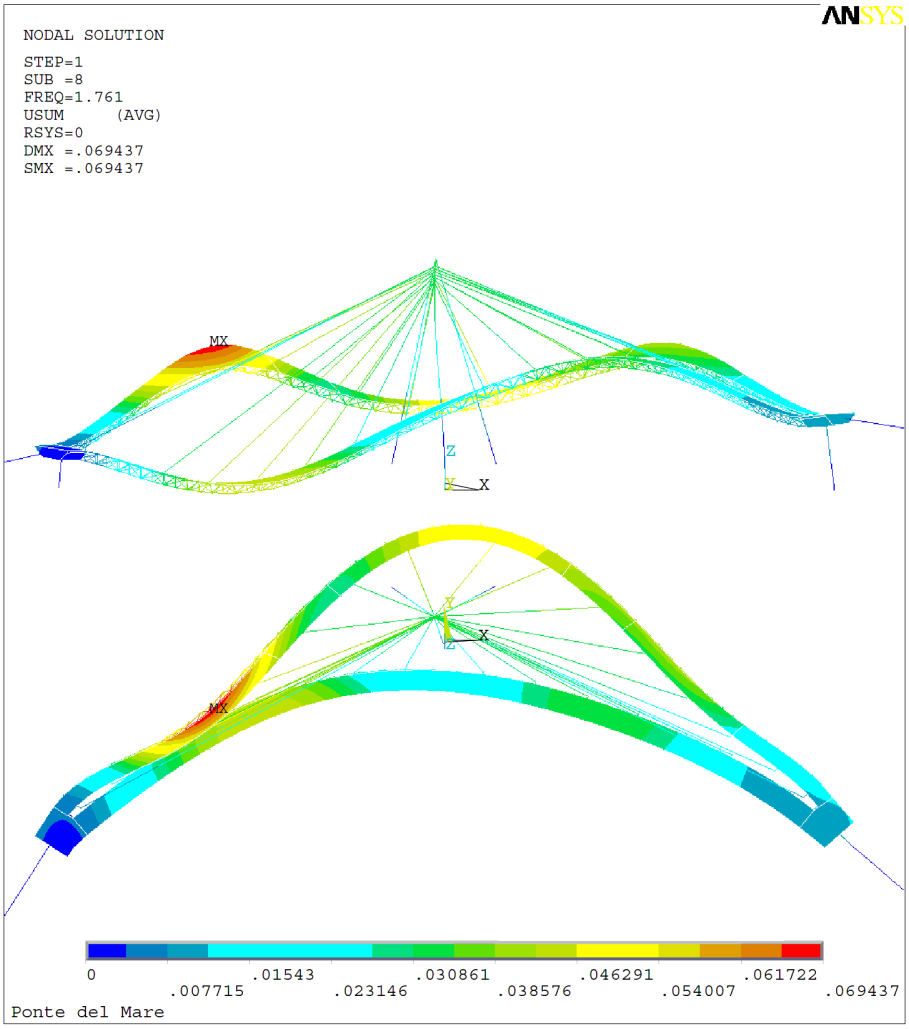

Figure 5.52: 8th mode of ANSYS correlated with 7th mode of experiment with MAC=72.9

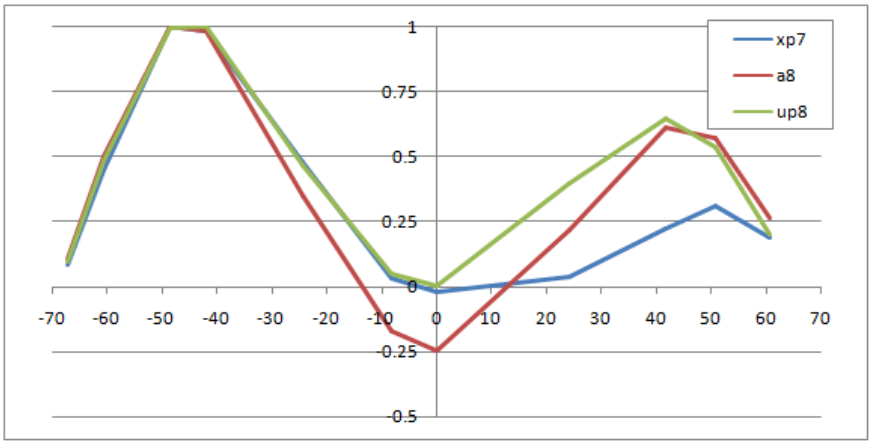

Figure 5.53: Normalized vertical autovector of the pedestrian deck

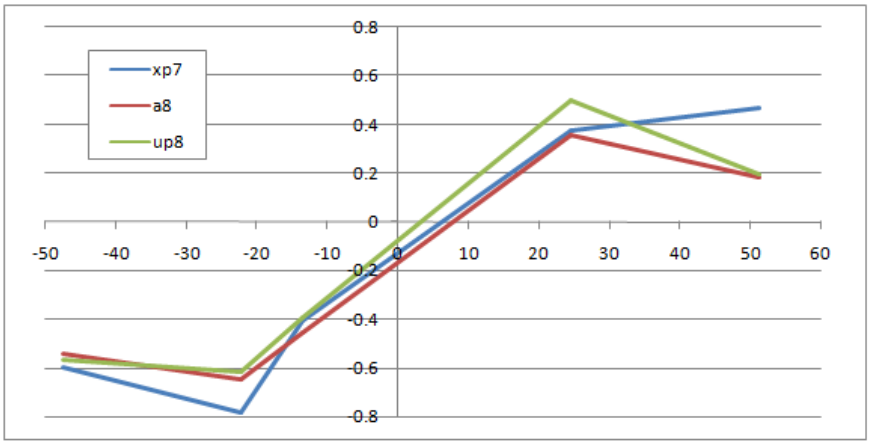

Figure 5.54: Normalized vertical autovector of the cycle deck

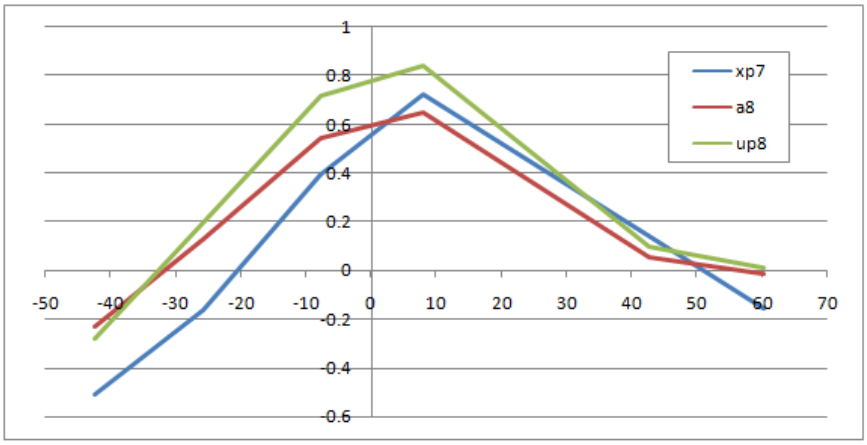

Figure 5.55: Normalized radial autovector of the pedestrian deck

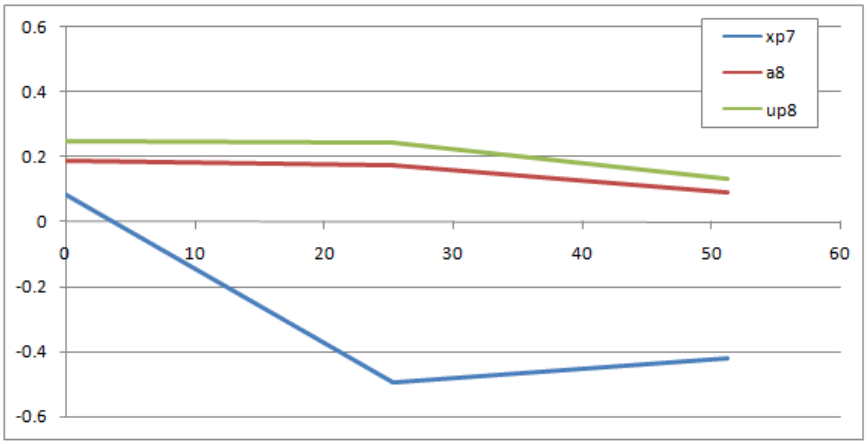

Figure 5.56: Normalized radial autovector of the cycle deck

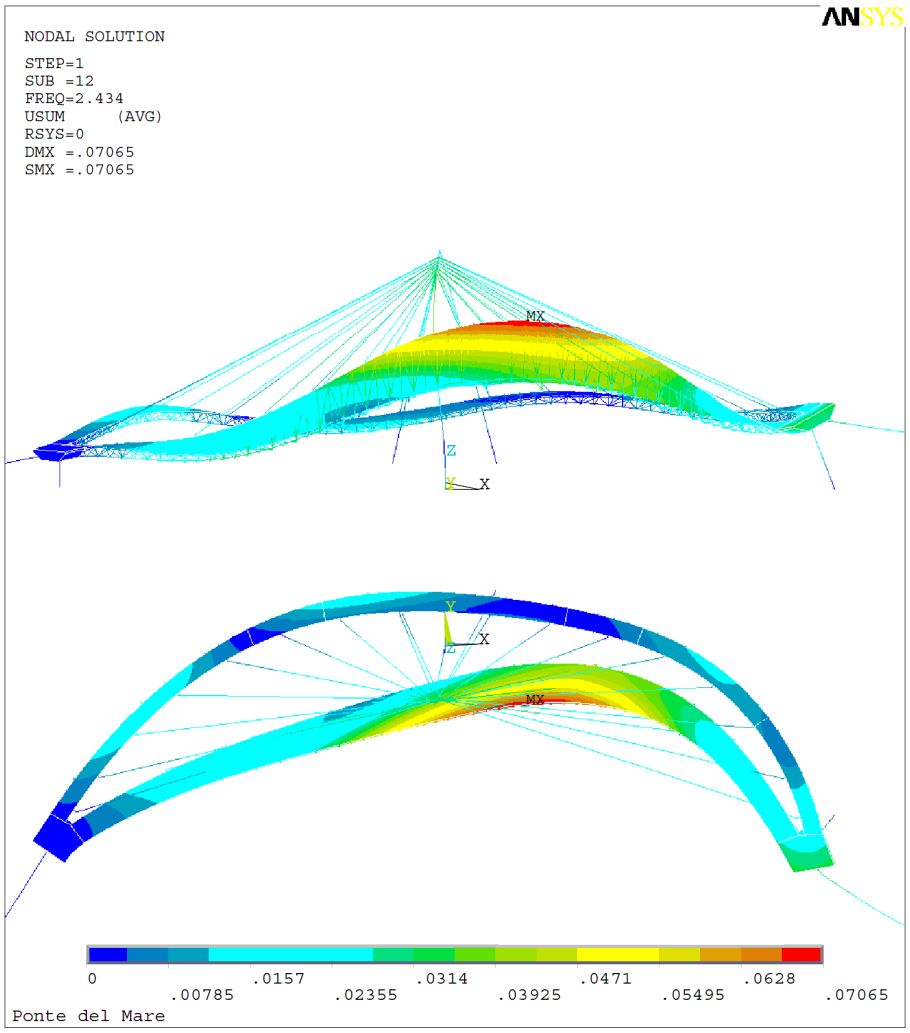

Figure 5.57: 12th mode of ANSYS correlated with 10th mode of experiment with MAC=60.4

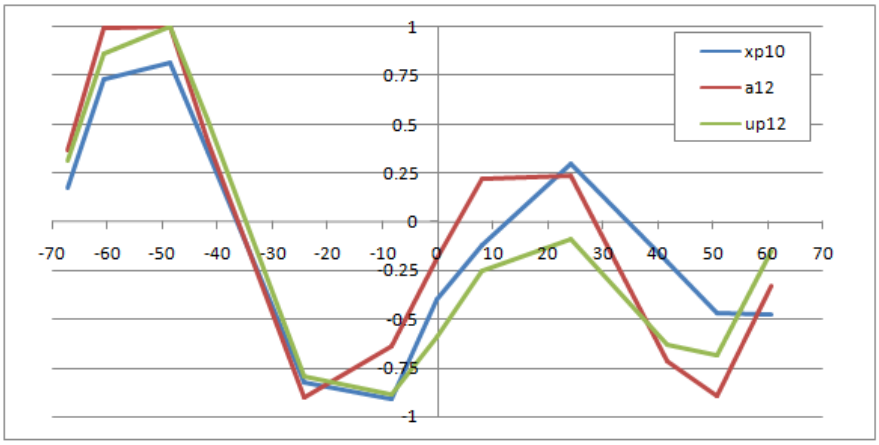

Figure 5.58: Normalized vertical autovector of the pedestrian deck

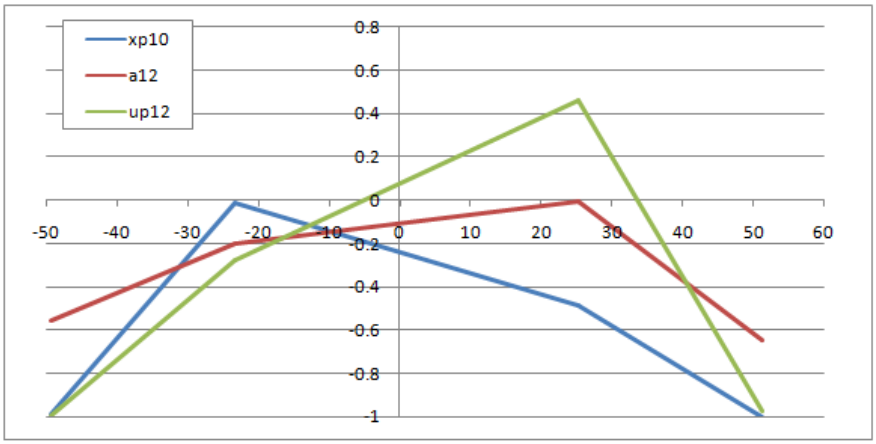

Figure 5.59: Normalized vertical autovector of the cycle deck

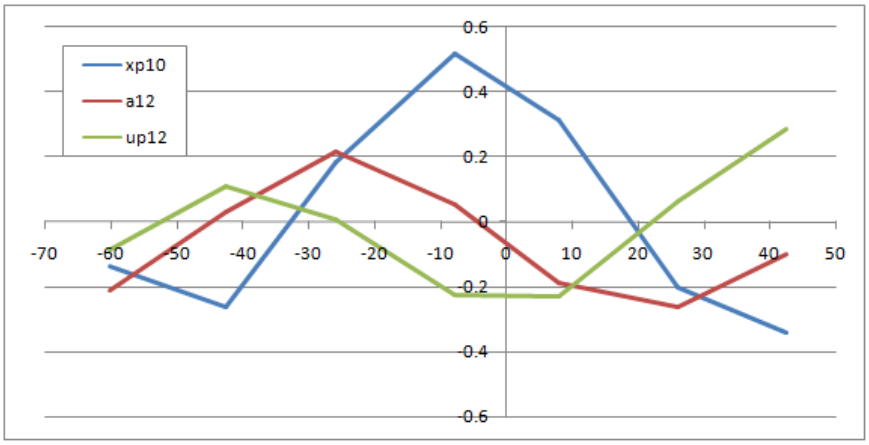

Figure 5.60: Normalized radial autovector of the pedestrian deck

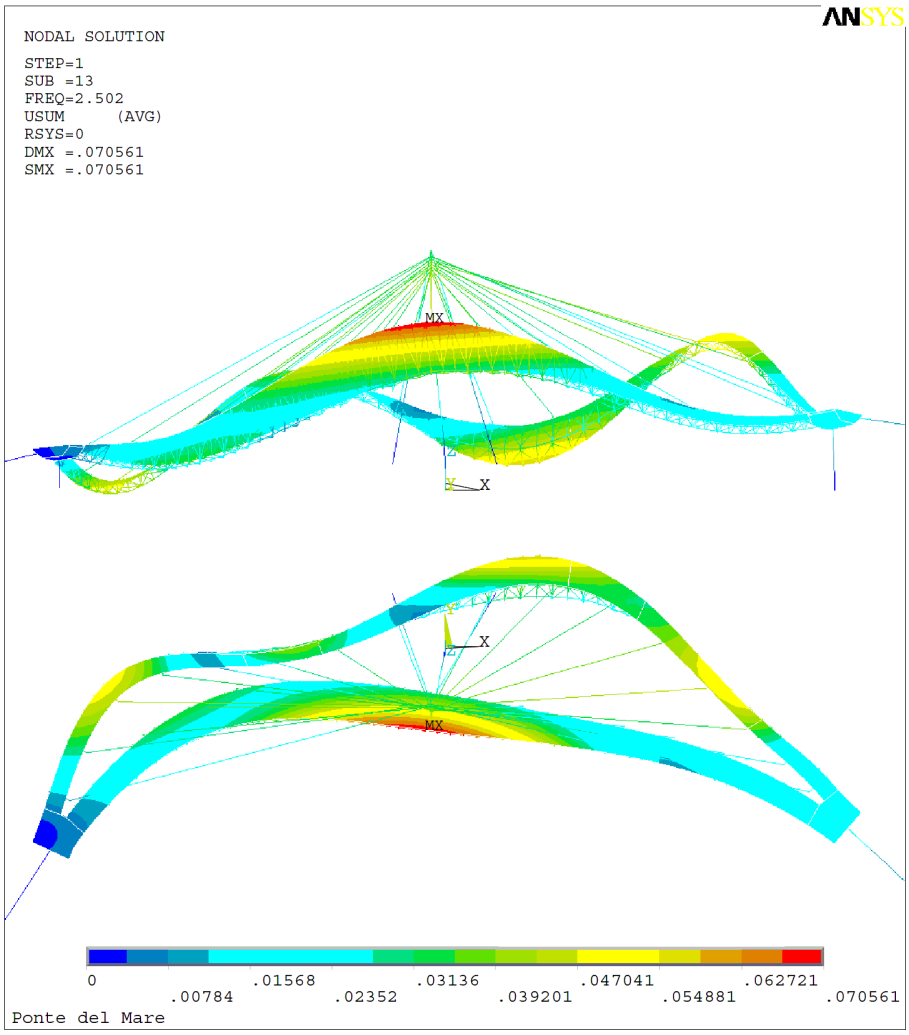

Figure 5.61: 13th mode of ANSYS correlated with 11th mode of experiment with MAC=48.7

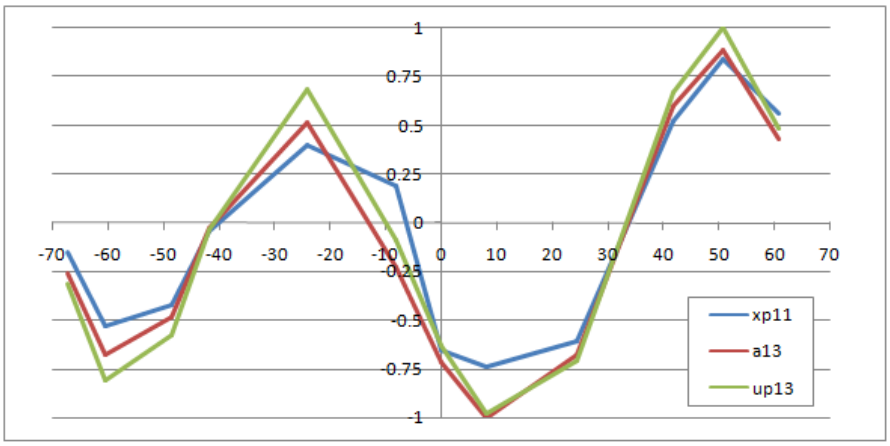

Figure 5.62: Normalized vertical autovector of the pedestrian deck

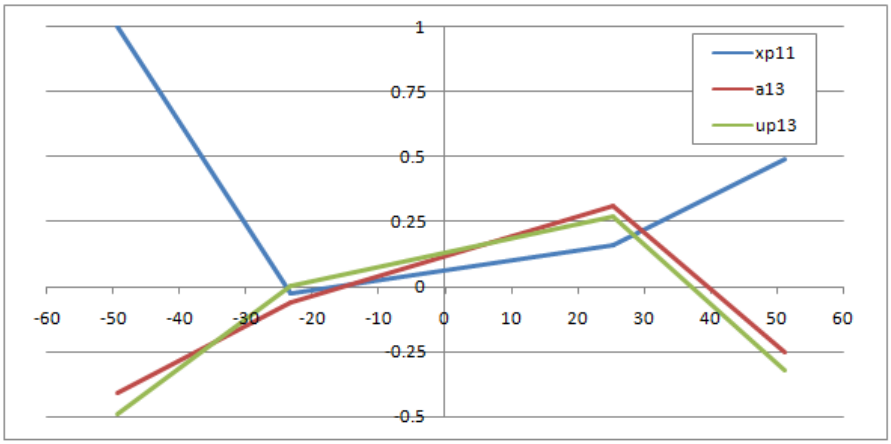

Figure 5.63: Normalized vertical autovector of the cycle deck

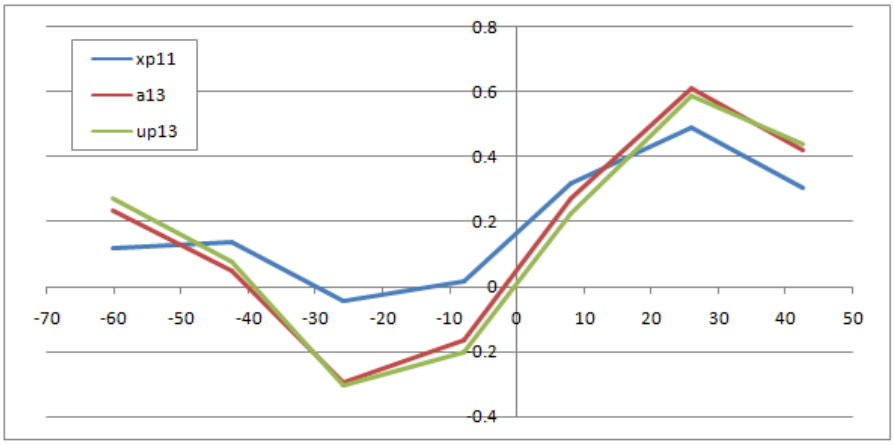

Figure 5.64: Normalized radial autovector of the pedestrian deck

5.5.2 Applicability of the updated model

After the updating of the FE model with the 9 parameters, the same was considered to use to reproduce the acceleration response under the actual wind loading to check the applicability of the model. The 'Ponte del mare' bridge is under monitoring with 8 accelerometers, arrangement shown in Figure 4.6(f), since December 2009. An especially intense wind recorded on $25/12/2009$ during $12:49$ - $12:59$ is chosen. The mean wind speed near the deck was considered 16.19 m/s, i.e. an average of the measurement obtained from the two anemometers, see Figure 5.65 and 5.66. Besides, the wind introduced inside the model was changed with the multiplicative coefficient that allows to take into account the maximum and the minimum variation with respect to the mean speed.

To underline that the updated model is the one without the dampers, however, the acceleration data recorded by the 8 accelerometers belong to the actual structure that is connecccted with the dampers, see Figure 4.5 and Table 4.1. Though it is not logical to compare the two situations, however, we intend to see if the model picks merely the order of the the acceleration magnitudes. Certainly, a more complete model updating is possible considering parameters sensitive to the presence of the dampers.

(a) (b)

Figure 5.65: Position of the two anemometers, (a) below the pedestrian deck, (b) at the top of the mast

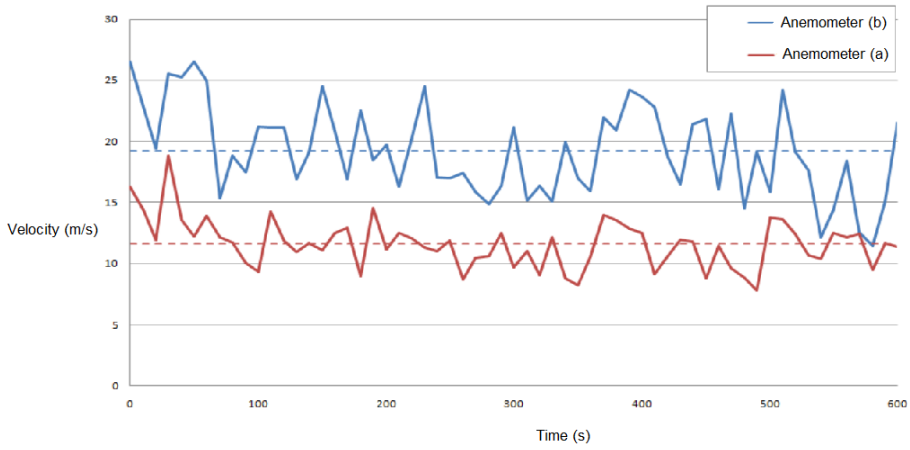

Figure 5.66: The wind speed from the two annemometers

Therefore a transient time history analysis is carried out in the ANSYS software, preceded by a static analysis logically necessary to define the distortion of the structure subject to permanent loads. The method used for the integration of the equations of the motion is that of Newmark, with parameters β = 0.25 and γ = 0.5 chosen specially to avoid the presence of the numerical damping.

Figures 5.67 and 5.68 present the acceleration response obtained after the execution of the analysis on the model without the dampers while that with the connected dampers is shown in Figures 5.69 and 5.70. The damping values were used from Table 4.1. It can be noticed that the trend of the accelerations and the maximum values for the node corresponding to the accelerometer M1 are approachable to the records of the same accelerometer.

This behavior, as appears good, is checked also for the M5, nevertheless, that happens mainly because the values of acceleration in M1 and M5 are very low because they are positioned in the proximity of the ramp of access to the deck. In fact, all the other comparisons are like that of M3 in Figure 5.70 and to check simply the order of magnitude by calculating the root-mean-square (RMS) values presents large percentage difference, as shown in Table 5.14.

The results obtained emphasized that the model provided with or without dampers, in both the cases, underestimate the accelerations measured from the sensors. There could be the following possible reasons:

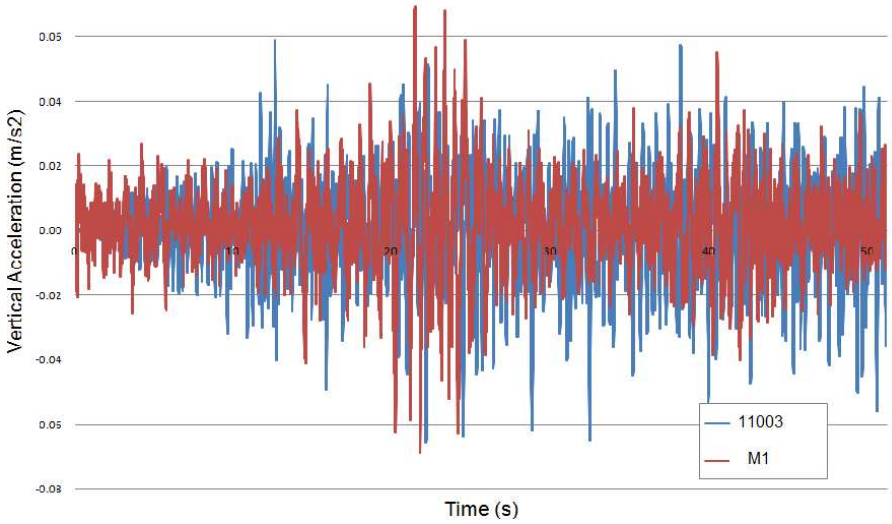

Figure 5.67: comparison between the acceleration recorded at M1 with the vertical acceleration at node 11003 of ANSYS model without dampers

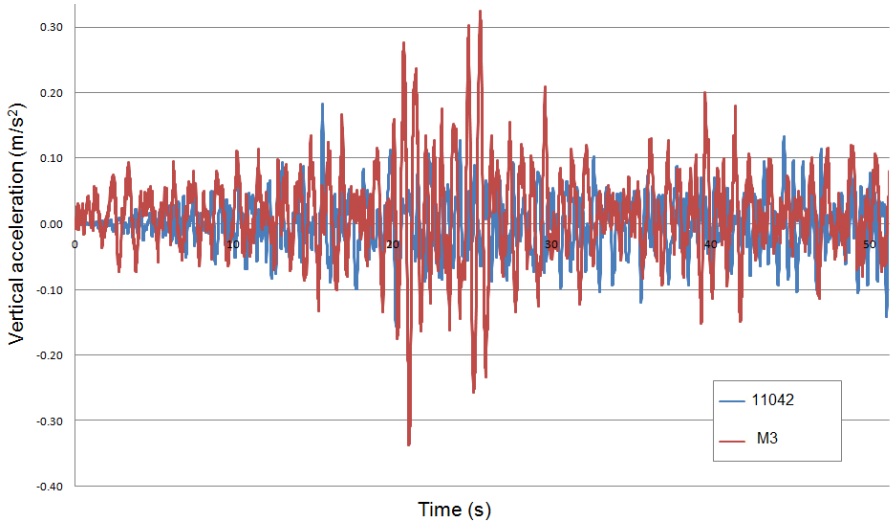

Figure 5.68: comparison between the acceleration recorded at M3 with the vertical acceleration at node 11042 of ANSYS model without dampers

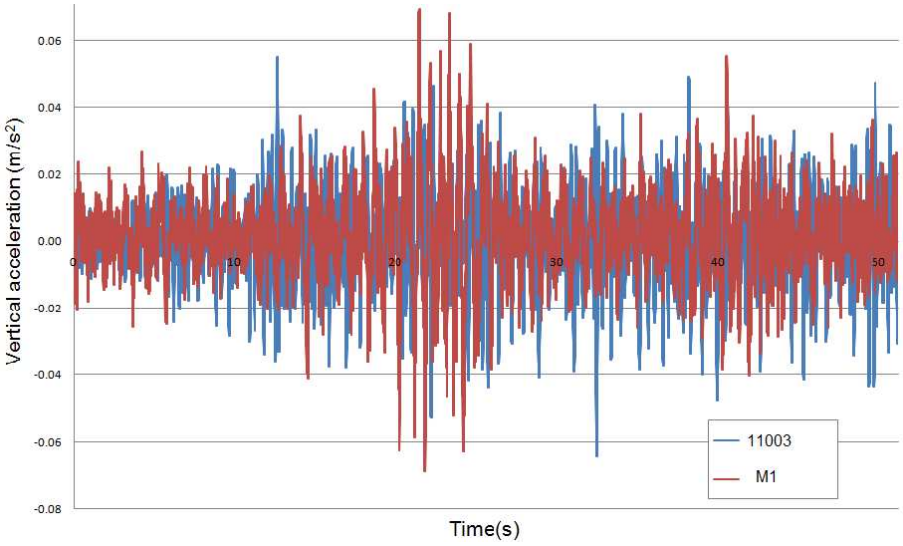

Figure 5.69: comparison between the acceleration recorded at M1 with the vertical acceleration at node 11003 of ANSYS model with dampers

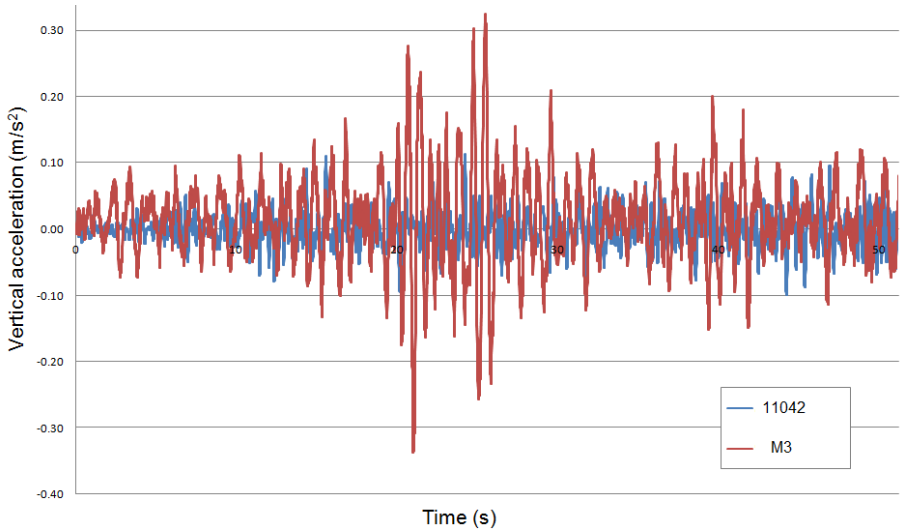

Figure 5.70: comparison between the acceleration recorded at M3 with the vertical acceleration at node 11042 of ANSYS model with dampers

Table 5.14: Difference in acceleration RMS values recorded and from FE model with and without dampers

	$RMS_{recorded}$	$RMS_{AnsysDamper}$	$\lvert Error\% \rvert$	$RMS_{AnsysNoDamper}$	$\lvert Error\% \rvert$
$M1$	0.014 m/s^2	0.015 m/s^2	7.8%	0.017 m/s^2	25.1%
$M2$	0.060 m/s^2	0.020 m/s^2	66.2%	0.027 m/s^2	54.6%
$M3$	0.069 m/s^2	0.027 m/s^2	60.9%	0.041 m/s^2	40.9%
$M4$	0.086 m/s^2	0.031 m/s^2	64.1%	0.043 m/s^2	49.3%
$M5$	0.037 m/s^2	0.020 m/s^2	46.6%	0.024 m/s^2	35.5%
$M6$	0.043 m/s^2	0.018 m/s^2	57.9%	0.021 m/s^2	49.8%
$M7$	0.061 m/s^2	0.026 m/s^2	58.2%	0.042 m/s^2	31.4%
$M8$	0.016 m/s^2	0.007 m/s^2	53.0%	0.009 m/s^2	44.7%

- a possibility of sustained pedestrian crossing around noon of the $25/12/2009$, when the measurements were recorded;

- an incorrect evaluation of some of the aerodynamic coefficients i.e. C_M, C_L or C_D (Zasso et al., 2009);

- the chosen wind history for the simulation may not be close to the reality;

- the necessity to carry out a MU on the model with dampers and not only on the eigenvalues but also on the eigenvectors.

The possible improvements in the next stage of the development of the model could be achieved considering the above points, however, it is obvious that the wind in prompt analysis of the deck flows at low frequency, typically involving the first two modes, and to re-analyse the mode shapes of prime suspect is the second mode due to its low correlation with the experimental data.

5.6 Conclusions

The initial FE model was updated in the light of the experimental data obtained from the identification of the bridge. The sensitivity based model updating techniques and Powell's Dog-Leg method of optimisation based on the Trust-Region approach were used. The sensitivity matrix was calculated and the 9 most sensitive parameters were selected. The final updated model showed a considerable reduction of errors relevant to frequencies. The updated model reproduced the response of the footbridge under an actual wind loading condition. Moreover, it underestimated the acceleration response with respect to the one obtained from measurements. From the practical point of view the second mode needs a better correlation to the experimental reality.

CHAPTER 6

IDENTIFICATION OF WEAK NONLINEARITIES IN CABLES OF CABLE-STAYED FOOTBRIDGES

6.1 Introduction

A cable-stayed bridge consists of three main structural components: deck or girder, cables and mast. It was proven experimentally as well as analytically that the response of cable-stayed bridges is highly nonlinear owing to its inherent flexible nature (Nazmy and Abdel-Ghaffar, 1990; Abdel-Ghaffar and Nazmy, 1991; Ali and Abdel-Ghaffar, 1995). Large displacements associated with cable-stayed bridges, especially during dynamic actions, lead to geometric nonlinearities in the structural response. Cable sag and stiffening effects impart nonlinearity to the bridge under gravity loads. Moreover, the interaction of the response between stiffening girders and various other components -cable-deck or cable-cable-, gives rise to additional geometric nonlinearities. Figure 6.1 shows the typical nonlinear response of cable-stay bridges, which is different from the response of conventional structures because in cable-supported structures, the stiffness increases as the load increases, i.e. a hardening behaviour(Nazmy and Abdel-Ghaffar, 1990; Abdel-Ghaffar and Khalifa, 1991; Abdel-Ghaffar and Nazmy, 1991; Ali and Abdel-Ghaffar, 1995). An analysis of cable-stayed bridges should accurately capture these nonlinearities to represent the real state of the structure. Eventually, the dynamic responses of a cable-stayed bridge are the combination of interactions between the motions of the bridge deck and the pylons as well as those of the stay cables (Cheng and Lau, 2002).

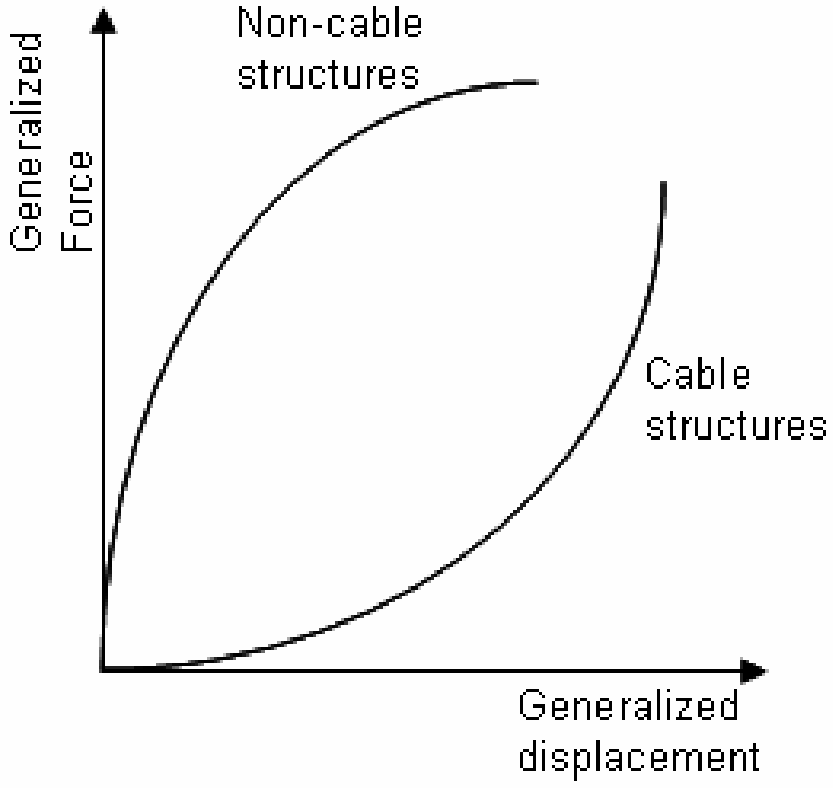

Figure 6.1: Typical response of cable-stay bridges after (Abdel-Ghaffar and Nazmy, 1991)

Due to their overall flexibility and low energy dissipation capacity, cables are susceptible to large-amplitude vibration that may eventually degrade their performance(Yu and Xu, 1999). Under the conditions of heavy traffic loads or unfavorable weather conditions of wind accompanied by rain, the amplitude of a stay cable vibration can be large (Cheng and Lau, 2002). The observation of significant rain-wind-induced cable vibration was first reported by Hikami (Hikami, 1986) during the construction of the Meiko-Nishi cable-stayed bridge in Japan, with a maximum amplitude of 0.55 m. However, peak-to-peak vibration amplitude up to 6 ft (about 2 m) have been reported with typical values of around 2 ft (about 0.6 m), primarily in the lower cable modes, with frequencies ranging approximately from 1 to 3 Hz (Kumarasena et al., 2005). One of the most intensive cable vibrations were registered on the Oresund Bridge, linking Denmark and Sweden during severe snow storms. The registered amplitude of cable vibrations approached 3 m, the cable kept on vibrating for over an hour (Malanka et al., 2007). Large displacements associated with stay cables, especially during dynamic actions lead to geometric nonlinearity in the structural response. Dynamic non-linearities occurring in large-amplitude vibration of a cable mainly arise from the quadratic and cubic nonlinear terms in the equations of motion (Takahashi and Konishi, 1987; Warnitchai et al., 1995; Rega, 2004a). These non-linear terms come up due to the stretching of the cable associated with the large-amplitude vibration (Takahashi and Konishi, 1987). The existence of the quadratic and cubic nonlinear terms makes the in-plane cable motion couple with the out-of-plane cable motion and induces modal interaction (Yu and Xu, 1999). The interaction between cables vibration and deck vibrations can have significant influence on the response of a bridge (Caetano et al., 2000). A model of the deck-cable interaction should consider the quadratic and cubic nonlinear terms in the equation of motion of both the deck and the cable (Gattulli et al., 2002). For structures characterized by nonlinear behaviour even for low-energy excitation, the assumption of linear behaviour could not be sufficient to reach a reliable characterization of its dynamic behaviour (Demarie et al., 2005b). Hence, a linear model may not be the best alternative and a nonlinear model is needed for the analysis of cable behaviour (Carrin-Viramontes et al., 2008).

Nonlinear system identification entails the modelling of the dynamics of a nonlinear system from measured input and output data. In detail, nonlinear model consists

of more parameters due to higher order terms involved in the equations of motion. Therefore, the correctness of a model depends on right estimate of these parameters. Dynamic system identification is a major tool to retrieve suitable description of the system and its parameters from experimental observations of the input and output variables. In other words, an identification procedure allows a mapping of available experimental data into a model. Moreover, identification of a nonlinear system requires special attention. While all methods have their individual merits, they also have some weaknesses and it is wise to say that no single technique offers a solution to all problems (Worden et al., 2007). A comprehensive book is available by Worden and Tomlinson on this topic (Worden and Tomlinson, 2001). A classification of nonlinear identification methods is given in Figure 6.2 . In various available methods the non-parametric methods based on Volterra series and polynomial expressions have certain advantages over other methods. These methods were successfully used for instantaneous identification of nonlinear systems having (assuming) quadratic and cubic terms in their equations of motion (Demarie et al., 2005a,b, 2010; Bursi et al., 2010). Because both the quadratic and the cubic type of nonlinearities are present in the cable dynamics, we can use the polynomial expression method with a polynomial of order three. In general, to identify the higher order terms, a system is tested with a relatively high level excitation, since most continuous nonlinearities have a greater influence on the behaviour of the system as the level is increased. Discontinuous nonlinearities, such as friction, often have the opposite effect, although if they are to be approximated by a polynomial, a high level of excitation is again appropriate (Storer, 1991).

In absence of experimental data, response data were generated by means of ANSYS software by modelling a cable element. A simple model of a cable with in-plane motion is considered, and it is reduced to a Single-Degree-of-Freedom (SDoF) system by harmonic excitation in its first mode (Rega, 2004a). The data are used to find the applicability of the non-parametric methods to nonlinear identification of cable vibration in the MATLAB environment. Nevertheless, nonlinear system identification could provide additional knowledge. Of course, the SDoF model is in some sense a fairly poor idealization of the actual infinite-dimensional system. Nevertheless, it allows us to understand several basic features of its nonlinear dynamics, in order to

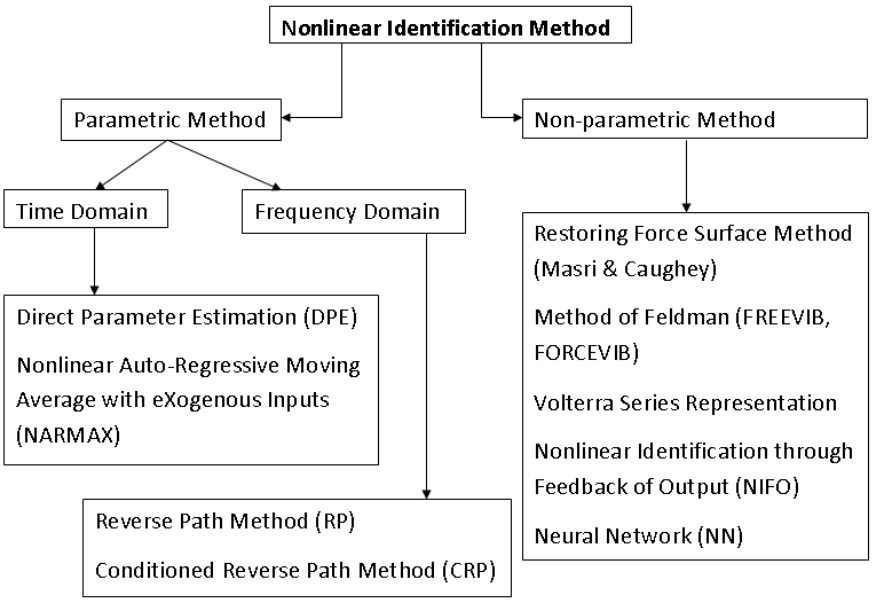

Figure 6.2: Classification of the nonlinear identification methods

compare different approaches and, more generally, to enter smoothly the rather involved issue of complex dynamics (Rega, 2004b). Along this line, we assume that the system is weakly nonlinear and that most of the energy is in the primary resonance associated to the first mode. Consequently, data are forced to fit the model of a weakly nonlinear SDoF system. In this way, distortions due to the discrepancy between the assumed model and the real system are perceived as noise in the optimisation procedure.

Initially, section 6.2 provides a brief idea about the presence of nonlinearity in cable vibration and the formulation of the equation of motion of the reduced simplified model. The next section 6.3 presents the higher order frequency response functions and the theory behind Volterra series. Then, section 6.4 describes the theory behind the time-frequency techniques and the instantaneous identification. Then, section 6.5 describes the FE model used to model the cable element and the formulation of the problem. Afterwards, results are presented and discussed in section 6.6. Finally, main conclusions are drawn.

Cables are very efficient structural members and hence have been widely used in many applications including cable-stayed bridges. Since cables are light, very flexible and lightly damped, structures utilizing cables, i.e. cable-structure systems, usually have various dynamic problems. Dynamic non-linearity occurring in large-amplitude vibration of a cable mainly arises from the quadratic and cubic non-linear terms in its equations of motion (Yu and Xu, 1999). Several efforts in the past were made to model the behaviour of the sag suspended cable, progressing from the basic model of the taut strings, both linear and nonlinear models were formulated (Rega, 2004a). A heavy cable suspended between two supports at the same level a distance *l* apart is shown in Figure 6.3.

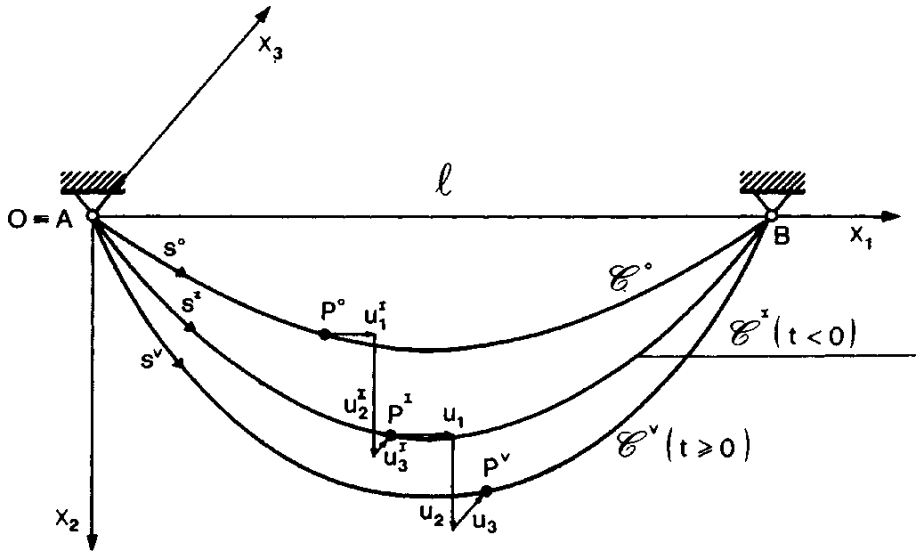

Figure 6.3: Cable configurations and displacement components in a global reference system, after (Rega, 2004a)

The reader can refer to the review article of Rega (Rega, 2004a) that presents a collection of works on the modeling of nonlinear dynamics of cable. We can start with

the following equation (Benedettini et al., 1995):

$$\begin{cases} EA[u' + y'v' + (1/2)(v'^2 + w'^2)]' - \mu_u \dot{u} + p_u = m\ddot{u} \\ \left\{Hv' + EA(y' + v')[u' + y'v' + (1/2)(v'^2 + w'^2)]\right\}' - \mu_v \dot{v} + p_v = m\ddot{v} \\ \left\{Hw' + EAw'[u' + y'v' + (1/2)(v'^2 + w'^2)]\right\}' - \mu_w \dot{w} + p_w = m\ddot{w} \end{cases} \tag{6.1}$$

Eq. 6.1 presents the displacement components (u, v, w) of the suspended cable in (x, y, z) coordinates. However, it assumes that: i) the initial static configuration described through the parabola $y = 4d[x/l - (x/l)^2]$ with mid-span sag d (a valid approximation for $d/l \leq 1/8$),ii) the initial strain negligible with respect to unity, which also entails $H/EA \ll 1$,and iii) the gradient of the longitudinal displacement (u) component negligible with respect to unity, which corresponds to moderately large rotations in the cable motion. H is horizontal component of the initial tension, A is cross-sectional area, E is material elastic modulus, m is mass per unit length.

In the absence of external actions in the longitudinal direction, and neglecting the corresponding inertia and viscous forces, the u displacement component can be obtained from the first of Eqs. 6.1 through a static condensation procedure (Kauderer, 1958). Thus, Eqs.6.1 are reduced to two partial integro-differential equations in the planar v and nonplanar w displacement components

$$\begin{cases} \{Hv' + (EA/l)(y' + v')e(t)\}' - \mu_v \dot{v} + p_v = m\ddot{v} \\ \{Hw' + (EA/l)w'e(t)\}' - \mu_w \dot{w} + p_w = m\ddot{w} \end{cases} \tag{6.2}$$

where

$$e(t) = \int_l [y'v' + (1/2)(v'^2 + w'^2)]dx \tag{6.3}$$

with $h(t) = EAe(t)$ representing the spatially uniform additional (dynamic) cable tension. Such equations (which can be suitably nondimensionalized) are accurate for studying the low-frequency nonlinear forced dynamics of suspended cables for which $H/EA = O[(d/l)^2]$ and the dynamic displacement components u, v, and w are, respectively, $u = O[\varepsilon d^2/l]$, v and $w = O[\varepsilon d]$, ε herein denoting a small parameter of the order of the amplitude. In technical applications, such situations occur for sag-to-span ratios up to about $1/20$.

6.2.1 Linearized dynamics of small-sag continuous cable

The in-plane linear mode of a (shallow) cable in the noncondensed formulation always combines transverse and longitudinal motion. However, transverse (elastic) modes are those which involve substantial transverse/vertical (tangential/longitudinal) motion (Burgess and Triantafyllou, 1988), the behavior of cables at low frequency being dominated by transverse modes, while that at high frequencies involving meaningful elastic modes. Since we are dealing with low-frequency nonlinear dynamics, we report only on the corresponding transverse modes (Irvine and Caughey, 1974), whereas elastic modes of high-frequency are dealt with in (Burgess and Triantafyllou, 1988). The effect of axial stretching on the linear frequencies of arbitrarily sagged cables is accounted for in (Shih and Tadjbakhsh, 1984) and in the numerical model of Srinil et al (Srinil et al., 2004), who also investigate the nonlinear interaction effects of low-frequency elastic modes occurring for highly extensible cables (Srinil et al., 2003). In turn, accounting for the longitudinal inertia within a wavelet- Galerkin procedure has allowed Al-Qassab and Nair (Al-Qassab and Nair, 2003, 2004) to highlight the occurrence of high-order modes with horizontal components larger than the vertical ones, called reverting partially swapping modes.

Upon eliminating the longitudinal displacement component u from the linearized version of Eqs. 6.1 through the condensation procedure, the equations for linearized undamped free dynamics of a parabolic cable in global coordinates are obtained from Eqs. 6.2 by considering that $H = const$. and by neglecting second-order terms:

$$\begin{cases} Hv'' + hy'' = m\ddot{v} \\ Hw'' = m\ddot{w} \end{cases} \tag{6.4}$$

In Eqs. 6.4, $h(t) = EAe(t)$ represents the first-order part of the spatially uniform dynamic tension (see Eq. 6.3).

The horizontal out-of-plane motion w is uncoupled from the vertical in-plane motion v because, to first order, it involves no additional cable tension. The solutions of the inplane and out-of-plane eigenvalue problems provide the relevant natural frequencies and linear normal modes (Irvine and Caughey, 1974).

6.2.1.1 Out-of-plane vibration

The eigenvalue problem for the out-of-plane horizontal motion is identical to that of a taut string and admits the eigenmodes

$$w_i(x) = A_{wi} \sin(i\pi x/l), \qquad i = 1, 2, 3, ... \tag{6.5}$$

and the associated natural frequencies

$$\omega_i = \frac{i\pi}{l}\sqrt{\frac{H}{m}}, \quad i = 1, 2, 3, ... \tag{6.6}$$

The frequency of the first (symmetric) out-of-plane horizontal mode is the lowest natural frequency of any given parabolic cable.

6.2.1.2 In-plane vibration

Antisymmetric and symmetric modes with respect to cable midspan must be distinguished. The former (the latter) consist of antisymmetric (symmetric) vertical components and symmetric (antisymmetric) longitudinal components. No additional cable tension $h(t)$ is induced by the motion in the antisymmetric modes, to first order, whereas additional cable tension is induced in the symmetric modes (Irvine and Griffin, 1976).

The natural frequencies of the antisymmetric modes are given by

$$\omega_i = \frac{2i\pi}{l}\sqrt{\frac{H}{m}}, \quad i = 1, 2, 3, ... \tag{6.7}$$

and are the same as of taut string modes (Routh, 1955). The corresponding vertical modal components read

$$v_i(x) = A_{vi} \sin(2i\pi x/l), \qquad i = 1, 2, 3, ... \tag{6.8}$$

The vertical component of the ith-symmetric mode is given by

$$v_i(x) = \frac{C_{vi}}{(\beta_i l)^2}\left\{1 - \tan(1/2\beta_i l)\sin\beta_i x - \cos\beta_i x\right\}, \qquad i = 1, 3, 5, ... \tag{6.9}$$

where C_{vi} is an arbitrary constant and $\beta_i = \omega_i(m/H)^{1/2}$, ω_i being the corresponding natural frequency. The value of $\beta_i l$ follows from the transcendental equation

$$\tan(1/2\beta l) = (1/2\beta l) - (4/\lambda^2)(1/2\beta l)^3 \tag{6.10}$$

where

$$\lambda^2 = 64(EA/H)(d/l)^2 = 512(EA/mgl)(d/l)^3 = v_l^2/(v_t^2)3 \tag{6.11}$$

is a nondimensional parameter which accounts for the elastic and geometric cable properties, and governs the nature of the roots of the equation.

6.2.2 Discrete models of continuous cable for analysis of reduced problems

Discretised versions of the equations of motion of a continuous cable in global coordinates are obtained in the framework of the search for a solution for the unknown displacement components u_i through separate variables:

$$u_i(x,t) = \sum_{j=1}^{\infty} f_{ij}(x)q_{ij}(t), \qquad i = 1, 2, 3, ... \tag{6.12}$$

Then, one assumes the spatial functions, $f_{ij}(x)$, space discretisation, or the temporal functions, $q_{ij}(t)$, time discretisation. With time discretisation, the $q_{ij}(t)$ are usually taken to be harmonic and the method of harmonic balance is used to obtain an infinite set of nonlinear boundary-value problems for the $f_{ij}(x)$. With space discretisation, the $f_{ij}(x)$—and thus the spatial dependence—are assumed a priori (assumed mode technique) and are considered constant during the motion. If the boundary conditions are homogeneous, the $f_{ij}(x)$ are usually taken to be the eigenfunctions of the linearized problem. The method of weighted residuals or variational principles are then used to determine an infinite set of nonlinear ordinary differential equations governing the $q_{ij}(t)$. Nearly all of the cable discrete models developed in the literature have been formulated in the context of a space discretisation approach through the Galerkin procedure. Moreover, the summation in Eq. 6.12 is usually truncated to a finite integer n.

Accordingly, one main aspect is concerned with the number of discretising terms to be considered in an approximate finite-degree-of-freedom model. It depends on the features of the original continuum problem we are trying to preserve and on the method we will apply to get the solution of the discrete system. Low-order models must be considered when searching for a solution through analytical or semianalytical methods, which often allow to highlight basic dynamical features of the nonlinear problem.

The selection of proper degree-of-freedom (dof) to be taken into account for the elastic cable depends on whether the attention is devoted to system 2D (planar) or 3D (spatial) dynamics, on possible nearness to conditions of internal resonance involving system natural frequencies, and on the dynamical features of the external actions. In the following subsection, reduced model for 2D finite dynamics is presented as it is relevant to the study presented in this chapter. For 3D reduced models and details reader is suggested to refer Rega (Rega, 2004a).

6.2.2.1 Reduced models for 2D dynamics

To study the cable monofrequent planar response to a harmonic forcing of frequency Ω with given spatial distribution $\varphi(x)$,namely $p(x,t) = \varphi(x)P\cos\Omega t$,reference is made to the simple single-degree-freedom (SDF) model obtained by describing the displacement $v(x,t)$ through one eigenfunction of the linearized equation of free motion: $v(x,t) = f(x)q(t)$. By applying the Galerkin method to Eq.6.2(a) (with $w = 0$), one dimensionless ordinary differential equation is obtained (Luongo et al., 1984; Benedettini and Rega, 1987):

$$\ddot{q} + \mu\dot{q} + q + c_2 q^2 + c_3 q^3 = P\cos\Omega t \tag{6.13}$$

The coefficient of the linear term in Eq. 6.13 is equal to unity since time is nondimensionalized with respect to a cable linear frequency, and the other coefficients depend on cable properties and on the assumed shape functions. Eq. 6.13 corresponds to a Helmholtz-Duffing oscillator in the theory of dynamical systems. It contains all of the main features of the original planar continuum model, namely the quadratic (Helmholtz) and cubic (Duffing) nonlinearities associated with the initial cur-

vature and stretching of the cable axis, respectively. In case of zero sag-to-span ratio (equilibrium curvature), the quadratic nonlinearity term c_2 vanishes (Rega, 2004a).

The relevant coefficients, c_2 and c_3 , account for cable properties just through the same unique elastogeometric parameter λ^2 (Eq.6.11) that governs the linear dynamics, when the displacement is nondimensionalized with respect to the sag (Luongo et al., 1984). In contrast, they depend separately on the mechanical and geometrical cable properties, when the displacement is nondimensionalized with respect to the span. This is, however, a more suitable assumption for the effective description of resonant motions of cables with only different sag-to-span ratios.

With proper choice of the cable vertical eigenfunction, Eq. 6.13 can be used for studying either symmetric or antisymmetric cable planar response under the corresponding harmonically varying distributed forces. It is worth noticing that the quadratic nonlinearity in Eq. 6.13 vanishes if the assumed mode is antisymmetric.

6.3 Higher order dynamic response functions

6.3.1 Time domain- IRF

For a general linear system, the input-output map can be expressed by Duhamel's integral (Billings and Tsang, 1989a),

$$x(t) = \int_{-\infty}^{+\infty} h(\tau)u(t-\tau)d\tau \tag{6.14}$$

Equation 6.14 is manifestly linear and therefore cannot hold for arbitrary nonlinear systems. However, it admits a generalisation. The extended form of equation 6.14 was obtained by Volterra (Volterra, 1959). It takes the form of an infinite series,

$$x(t) = x_1(t) + x_2(t) + x_3(t) + ... \tag{6.15}$$

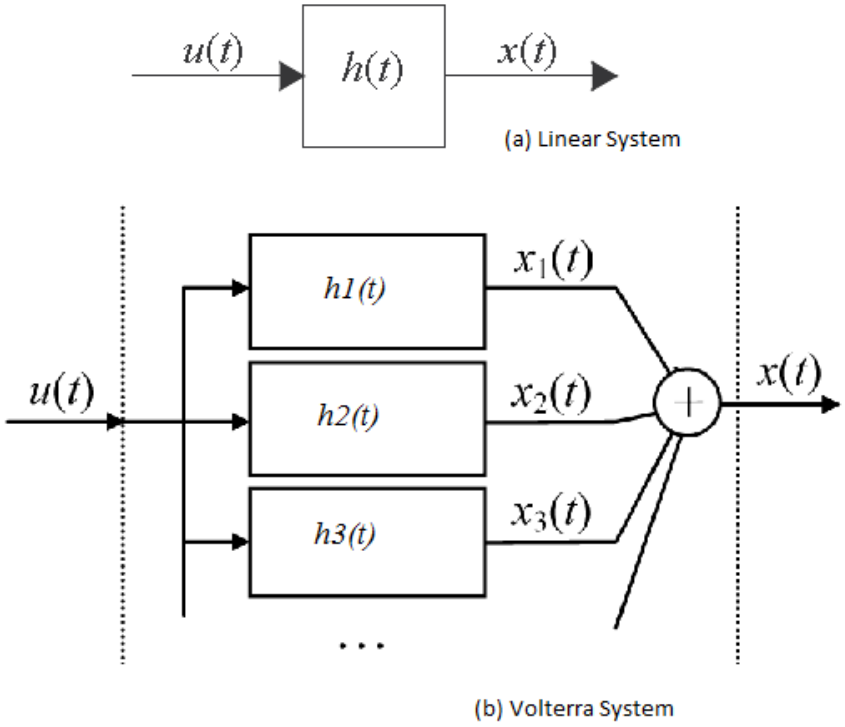

Figure 6.4: Input-output diagram

where,

$$x_1(t) = \int_{-\infty}^{+\infty} h_1(\tau_1)u(t-\tau_1)d\tau_1 \quad (6.16)$$

$$x_2(t) = \int_{-\infty}^{+\infty}\int_{-\infty}^{+\infty} h_2(\tau_1,\tau_2)u(t-\tau_1)u(t-\tau_2)d\tau_1 d\tau_2 \quad (6.17)$$

$$x_3(t) = \int_{-\infty}^{+\infty}\int_{-\infty}^{+\infty}\int_{-\infty}^{+\infty} h_3(\tau_1,\tau_{2,}\tau_3)u(t-\tau_1)u(t-\tau_2)u(t-\tau_3)d\tau_1 d\tau_2 d\tau_3 \quad (6.18)$$

The form of the general term is obvious from the above. The functions $h_1(\tau)$, $h_2(\tau_1,\tau_2)$, $h_3(\tau_1,\tau_{2,}\tau_3)$ and $h_n(\tau_1,...\tau_n)$, . . . are generalisations of the linear impulse response function and are usually referred to as Volterra kernels. The expression 6.14 simply represents the lowest order truncation which is of course exact only for linear systems. The input-output relation of linear and Volterra system are compared graphically in Figure 6.4.There are many practical issues associated with the existence and convergence of the Volterra series and a good summary can be found in (Palm and Poggio, 1977).

6.3.2 Frequency domain- FRF

There exists a dual frequency-domain representation for nonlinear systems. The higher order FRF's or Volterra kernel transforms $H_n(\omega_1,...,\omega_n)$, $n = 1,...,\infty$ are defined as the multi-dimensional Fourier transforms of the kernels, i.e.,

$$H_n(\omega_1,...,\omega_n) = \int_{-\infty}^{+\infty}...\int_{-\infty}^{+\infty} h_n(\tau_1,...,\tau_n)e^{-i(\omega_1\tau_1+...+\omega_n\tau_n)}d\tau_1...d\tau_n \quad (6.19)$$

It is a straightforward matter to obtain the frequency-domain dual of the expression 6.15,

$$X(\omega) = X_1(\omega) + X_2(\omega) + X_3(\omega) + ... \quad (6.20)$$

where,

$$X_1(\omega) = H_1(\omega)U(\omega) \tag{6.21}$$

$$X_2(\omega) = \frac{1}{2\pi}\int_{-\infty}^{+\infty} H_2(\omega_1, \omega-\omega_1)\ U(\omega_1)\ U(\omega-\omega_1)d\omega_1 \tag{6.22}$$

$$X_3(\omega) = \frac{1}{(2\pi)^2}\int_{-\infty}^{+\infty}\int_{-\infty}^{+\infty} H_3(\omega_1, \omega_2, \omega-\omega_1-\omega_2)\ U(\omega_1)U(\omega_2)U(\omega-\omega_1-\omega_2)d\omega_1 d\omega_2 \tag{6.23}$$

One use of the Volterra series is the construction of analytic approximations to various quantities of interest in experimental structural analysis. Approximations to the FRFs of SDOF and MDOF systems with cubic nonlinearities and excited by Gaussian white noise can be found in the work of Worden and Manson (Worden and Manson, 1998, 1999).

There are various methods for efficiently determining the higher order FRF's for a system, for e.g. Time-Delay Neural Network (TDNN) (Wray and Green, 1994), harmonic testing (Storer and Tomlinson, 1991) and impulse testing (Liu et al., 1987). More work on identification of nonlinear systems via the Volterra kernels and kernel transforms can be found in Khan and Vyas (Khan and Vyas, 1999), Chatterjee and Vyas (Chatterjee and Vyas, 2003) and Tawfiq and Vihn (Tawfiq and Vihn, 2003).

If one knows the equation of motion of a system, an alternative approach can be used which yields exact expressions for the higher order FRF's. The method of harmonic probing was introduced by Bedrossan and Rice specifically for systems with continuous-time equations of motion (Bedrossan and Ricand, 1971). The method was extended to discrete-time systems by Billings and Tsang (Billings and Tsang, 1989a,b). An alternative, recursive approach to probing is presented in Peyton Jones and Billings (Peyton Jones and Billings, 1989).

6.4 Non-parametric methods for instantaneous identification of nonlinear systems

In the identification of structures characterized by localized nonlinearities, the definition of instantaneous time-frequency estimators (Ceravolo, 2004) may result partic-

ularly useful: more specifically, its extension to nonlinear systems, whose input/output relationship can be depicted as a Volterra series (Volterra, 1959). The information obtained from a nonlinear identification session may both offer a clue in choosing reliable structural models, and forecast the dynamic behavior in non-operational conditions (Ceravolo, 2004). A state-of art is already presented on instantaneous identification of nonlinear systems in section 3.2.

The formulation of parametric methods requires the adoption of an appropriate form for the model, which should accurately describe the dynamic behaviour of the real structures under investigation. Sometimes, however, it may prove very difficult to meet this requirement: this is what prompted the development of non-parametric methods whose formulation does not require any a priori knowledge of the restoring force of a structure. A list of nonlinear identification methods, both parametric and non-parametric, is given in Figure 6.2.

6.4.1 Identification of Volterra series forms

Within the framework of the Volterra series representation of the input/output relationship of a nonlinear dynamic system, the identification process is based on the experimental determination of the higher order frequency response functions or, alternatively, the kernels in the time domain. If the system is subjected to a stochastic load, the identification reduces to the determination of the second and higher order spectral moments of the excitation and system response (i.e., (Tick, 1961; Kim and Powers, 1993)) or, in the time domain, through the estimate of higher order cumulant function (i.e., (Koukoulas and Kalouptsidis, 2000)). A consistent evaluation of the statistical characteristics of order > 2 hinges on the availability of a great quantity of experimental data, greater than is necessary in linear system identification: in structural engineering applications, this requirement cannot be easily met, especially when the measurements are performed in situ.

Let us consider a time-invariant nonlinear dynamic system with a single degree of freedom as described by the following equation of motion (Worden and Tomlinson, 2001):

$$m\ddot{x} + f_d(\dot{x}) + f_s(x) = u(t) \tag{6.24}$$

where m is the mass, $f_d(x)$, is the nonlinear damping term and $f_s(x)$ is the nonlinear elastic restoring force, $u(t)$ and $x(t)$ are the system's excitation and response. Let us assume that the input/output relationship can be approximated through a Volterra series, Eq. 6.15 can be written as:

$$\begin{cases} x(t) = x_1(t) + x_2(t) + x_3(t) + ... \\ = \int_{-\infty}^{+\infty} h_1(\tau_1)u(t-\tau_1)d\tau_1 + \int_{-\infty}^{+\infty}\int_{-\infty}^{+\infty} h_2(\tau_1,\tau_2)u(t-\tau_1)u(t-\tau_2)d\tau_1 d\tau_2 + \\ + \int_{-\infty}^{+\infty}\int_{-\infty}^{+\infty}\int_{-\infty}^{+\infty} h_3(\tau_1,\tau_{2,}\tau_3)u(t-\tau_1)u(t-\tau_2)u(t-\tau_3)d\tau_1 d\tau_2 d\tau_3 + ... \end{cases} \tag{6.25}$$

where $h_1(\tau_1)$, $h_2(\tau_1,\tau_2)$, $h_3(\tau_1,\tau_{2,}\tau_3)$ are respectively the system's linear, quadratic and cubic impulse response functions, $x_1(t)$, $x_2(t)$ and $x_3(t)$ are respectively the linear, quadratic and cubic contributions to the system response. Without losing in generality, let us consider a system with a symmetric behaviour (the laws $f_d(x)$ and $f_s(x)$ are odd functions, all the even contributions in the series are identically zero) and apply to the previous expression the definition of the Short-Time Fourier Transform (Cohen, 1995):

$$\begin{cases} D(t,f) = \int_{-\infty}^{+\infty} x(\tau)w(\tau-t)e^{i2\pi f\tau}d\tau = \int_{-\infty}^{+\infty}(x_1(\tau)+x_3(\tau)+...)w(\tau-t)e^{i2\pi f\tau}d\tau \\ = \int_{-\infty}^{+\infty}(\int_{-\infty}^{+\infty} h_1(\tau_1)u(\tau-\tau_1)d\tau_1)w(\tau-t)e^{i2\pi f\tau}d\tau + \\ + \int_{-\infty}^{+\infty}(\int_{-\infty}^{+\infty}\int_{-\infty}^{+\infty}\int_{-\infty}^{+\infty} h_3(\tau_1,\tau_{2,}\tau_3)u(\tau-\tau_1)u(\tau-\tau_2)u(\tau-\tau_3)d\tau_1 d\tau_2 d\tau_3)w(\tau-t)e^{i2\pi f\tau}d\tau + ... \end{cases} \tag{6.26}$$

where $D(t,f)$ is the system's Short-Time Fourier Transform (STFT) and $w(t)$ is a "window" function defined in the time domain, such that it leaves more or less unaltered the signal unaltered around the time t but suppresses the signal for times distant from the time of interest.ies representation of the input/output relationship (Eq. 6.25), we can work out the form of $D(t,f)$ directly from Eq. 6.26, which requires the knowledge of the form of the impulse response functions.

Let us assume to have measured the system response in N instants and let **p** be the vector of the parameters expressing the functionals of $f_d(x)$ and $f_s(x)$ in Eq. 6.24: the following instantaneous objective function can be introduced:

$$F_{ob}(n^*,\mathbf{p}) = \left| \sum_{m=0}^{N-1} \left[|D(n^*, m)|^2 - |D_s(n^*, m)|^2 \right] \right| \tag{6.27}$$

where:

n^* : discrete instant at which the objective function is evaluated;

$D(n^*, m)$: STFT transform of system response (measured);

$D_s(n^*, m)$: STFT transform of the system response corresponding to a given configuration of parameters **p**.

Eq. 6.27 describes the difference between the instantaneous energies respectively of the signal at time $t^* = n^*\Delta t$ and of a signal corresponding to a given configuration of the unknown parameters **p**,approximated via a truncated Volterra series: the number of terms to be included is function of the energy and characteristics of the input. Each term of the summation can be obtained via different methods, i.e. solving the associated linear equations (Vazquez Feijoo et al., 2004). Thus, by resorting to classical optimisation procedures, it proves possible to determine instant by instant the minimum of the $F_{ob}(n^*,\mathbf{p})$ function through which the vector of the instantaneous estimators $\mathbf{p}(t)$ of the mechanical properties of the system can be defined.

6.4.2 Identification of polynomial forms

Within non-parametric identification techniques, this procedure assumes that the restoring force $f_s(x)$ can be expressed through a polynomial approximation, characterized by time-varying coefficients. The papers (Bursi et al, 2009; Ceravolo et al., 2010) proposed already a general method capable of capturing the non-linear behaviour of a dynamic system, based on the concept of instantaneous identification, performed in the time-frequency domain as defined by Ceravolo (Ceravolo, 2004, 2009). It might be known or intuitively obvious, for example, that the non-linearity is in the stiffness function rather than in the damping, and correspondingly the higher order damping terms could be omitted from the model (Storer, 1991). Eq. 6.24 can be expresses as follows:

$$m\ddot{x} + c\dot{x} + (k_1 x + k_2 x^2 + k_3 x^3 + ...) = u(t) \tag{6.28}$$

The choice of the degree of the polynomial depends on the behaviour of the system to identify: the more complex is the constitutive behaviour of the system, the higher is the degree of the polynomial approximation needed and, consequently, the number of coefficients to be determined. This drawback is well known when a polynomial is used to fit a general curve and can be overcome by resorting to a basis of orthogonal functions (i.e. Chebyshev polynomials). On the other hand, Eq. 6.28 is required to approximate the response on a short time interval; hence a low-degree polynomial approximation is expected to be suitable for most applications. From the practical viewpoint, a suitable choice can be made performing the identification with different polynomials, progressively increasing the degree, and selecting a posteriori the one that gives the best results in representing the system response.

The polynomial form implies some advantages: i) the polynomial expression allows to identify the structural responses without assuming any a priori constitutive model for the system, nevertheless, a-priori information can be used to simplify the polynomial model before proceeding to the parameter identification stage; ii) within the range of validity of the approximation adopted, Eq. 6.28 is characterized by a smooth non-linearity, which makes it particularly suited for a non-parametric instantaneous approach (Ceravolo et al., 2010).

A discrete form of time-frequency identification algorithms based on spectrogram are formulated to find the model parameters which minimize the error between a given time-frequency model and the time-frequency transform of the measured or numerical signal (Ceravolo, 2004, 2009).

Let us suppose that the system response $x_n(t)$ - displacement, velocity or acceleration - is known, either from measurement or from numerical simulation. Then, if also the excitation $u(t)$ is known, a possible choice for the time-frequency model is represented by the time-frequency transform of the response $x_n(t)$, that for a given configuration of parameters $\mathbf{p}$ can be computed via a Runge-Kutta method. Accordingly, a time-frequency model can be identified from the following minimization:

$$\begin{cases} \varepsilon(j,\mathbf{p}) = \left| \sum_{j=0}^{N-1} \left[SPEC_{x}^{(\gamma)}[j,k;\mathbf{p}] - SPEC_{x_n}^{(\gamma)}[j,k] \right] \right| \\ \rightarrow \mathbf{p}_{id}(\bar{t} = \bar{j}\Delta t) = \arg\left[\min_{\forall \mathbf{p}, j=\bar{j}} \varepsilon(j,\mathbf{p}) \right] \end{cases} \tag{6.29}$$

where $\mathbf{p} = \{c\ k_1\ k_2\ k_3\}$ is the vector of parameters describing the dynamic properties of the polynomial system. $SPEC_{x_n}^{(\gamma)}[j,k]$ and $SPEC_{x}^{(\gamma)}[j,k;\mathbf{p}]$ are the values of the spectrogram- SPEC- at a discrete time instant $j \cdot \Delta t$ and frequency $k \cdot \Delta f$ of the system response, measured and associated with the model, respectively. The parameter ε gives the modulus of the difference between the instantaneous energy of the measured response and that of the system output corresponding to a given configuration of the unknown parameter vector $\mathbf{p}$. By resorting to classical optimisation procedures, one can determine the minimum of $\varepsilon\left(j = \overline{j}, \mathbf{p}\right)$ at every instant $\overline{t} = \overline{j} \cdot \Delta t$, through which the vector of the instantaneous polynomial coefficients can be defined. It is worth remarking that an instantaneous optimisation is possible through the temporal localization of frequency components, i.e. the time-frequency representation. Despite the procedure leads to instantaneous or time-varying parameters, see for instance (Wu and Smyth, 2008), a time-frequency method cannot be strictly defined a real-time approach. In fact, the time-frequency uncertainty principle does not allow for an on-line implementation. For a comprehensive discussion on this matter see (Ceravolo et al., 2010).

The direct identification of the parameters $\mathbf{p}$ of the model, without passing through the polynomial coefficients, is possible too and c, k_1, k_2 and k_3 would be computed by time-averaging of the identified instantaneous values. However, it can be proven that this direct procedure is computationally more expensive. Moreover, it would be justified only when the true structural behaviour is close to that of the chosen model. Conversely, the polynomial approximation used here is always suited, since it can be intended as non-parametric, in the sense that its coefficients do not need to retain a definite meaning.

6.5 Nonlinear identification of cables

6.5.1 A numerical example

A cable element, shown in Figure 6.5, with zero-sag (pretensioned) was modelled in ANSYS. The material and geometrical properties are presented in Table 6.1. The cable was divided in 10 elements. LINK1-Truss element was used. The 2-D spar (Truss) element is a uniaxial tension-compression element with two degrees of freedom at each node: translations in the nodal x and y directions. The element is defined by two nodes, the cross-sectional area, an initial strain, and the material properties.

The result of the modal analysis is shown in Table 6.2 and the modal vector ϕ from the FE model of the cable are given in Eq. 6.30..

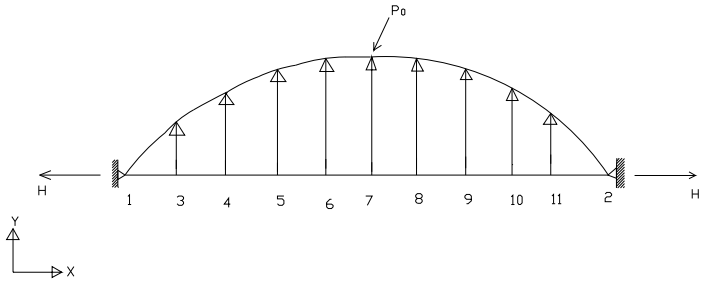

Figure 6.5: Cable element of example

Table 6.1: Properties of the cable

Parameter	Value
Length	73.73 m
Area	0.001303 m^2
Elastic modulus	165x10^9 N/m^2
Density	8289 kg/m^3
Poisson's ratio	0.3
Pre-strain	0.0016

Table 6.2: Modal frequencies

Mode No.	Freqency (Hz)
1	1.2162
2	2.4625
3	3.7692
4	5.1662
5	6.6778
6	8.3091
7	10.014
8	11.639
9	12.880

$$\phi = \begin{pmatrix} 0.0156 & 0.0305 & -0.0437 & 0.0544 & 0.0614 & 0.0635 & -0.0591 & 0.0468 & 0.0262 \\ 0.0297 & 0.0493 & -0.0514 & 0.0336 & 0 & -0.0393 & 0.0695 & -0.0757 & -0.0499 \\ 0.0409 & 0.0493 & -0.0167 & -0.0336 & -0.0614 & -0.0393 & -0.0226 & 0.0757 & 0.0686 \\ 0.0481 & 0.0305 & 0.0317 & -0.0544 & 0 & 0.0635 & -0.0430 & -0.0468 & -0.0807 \\ 0.0506 & 0 & 0.0540 & 0 & 0.0614 & 0 & -0.0731 & 0 & 0.0848 \\ 0.0481 & -0.0305 & 0.0317 & 0.0544 & 0 & -0.0635 & -0.0430 & 0.0468 & -0.0807 \\ 0.0409 & -0.0493 & -0.0167 & 0.0336 & -0.0614 & 0.0393 & -0.0226 & -0.0757 & 0.0686 \\ 0.0297 & -0.0493 & -0.0514 & -0.0336 & 0 & 0.0393 & 0.0695 & 0.0757 & -0.0499 \\ 0.0156 & -0.0305 & -0.0437 & -0.0544 & 0.0614 & -0.0635 & -0.0591 & -0.0468 & 0.0262 \end{pmatrix} \tag{6.30}$$

The cable vibration represents a multi-degree of freedom system. In order to simplify the study it was decided to work with a single degree of freedom system especially in the first mode. To exite the cable truly in its first mode, a harmonic load, frequency 1.2162 *Hz*, was applied with the load magnitude varying according to the first mode shape, Eq.6.31 .

$$\phi_1 = \begin{pmatrix} 0.31 \\ 0.59 \\ 0.81 \\ 0.95 \\ 1.00 \\ 0.95 \\ 0.81 \\ 0.59 \\ 0.31 \end{pmatrix} \tag{6.31}$$

To study the cable monofrequent planar response to a harmonic forcing of frequency Ω with given spatial distribution ϕ, namely $p(t) = \phi P_0 \sin \Omega t$ was applied (Rega, 2004a). In Section 6.4, it was discussed that the polynomial method, we will apply for identification purpose, has the advantage that the polynomial expression allows to identify the structural responses without assuming any a priori constitutive model

for the system. Nevertheless, as already described in section 6.2, quadratic and cubic nonlinearities are relevant to the cable vibration, we assume that the equation of motion for the first mode of nonlinear vibration can be written in the form of Eq. 6.32.

$$M_1 \ddot{q}_1 + C \dot{q}_1 + K_1 q_1 + K_2 q_1^2 + K_3 q_1^3 = \phi_1^T \phi_1 P_0 \sin \Omega t \tag{6.32}$$

Putting M_1 = 1.0 and the product $\phi_1^T \phi_1$ = 0.0128, Eq. 6.32 results as follows:

$$\ddot{q}_1 + C \dot{q}_1 + K_1 q_1 + K_2 q_1^2 + K_3 q_1^3 = 0.0128 \cdot P_0 \sin \Omega t \tag{6.33}$$

One can notice in Eq. 6.33 that for a known excitation value of P_0 the system has four parameters, i.e. C, K_1, K_2 and K_3. The parameter K_1 is related to the linear natural frequency of the system, therefore it's variation will show, indirectly, the change of the frequency. As already said in section 6.2 quadratic term of the nonlinearity vanishes in case of zero sag-to-span ratio, we keep the parameter K_2 for the verification. C is the damping parameter and as the high level of uncertainty is involved in damping estimation, this parameter will be processed for identification.

6.6 Results and discussion

In order to get an initial estimate of the type of nonlinearity present in the cable element, a load, amplitude increasing linearly upto 100 *kN* in the middle (node 7) and distributed along the cable according to the first mode, was applied. The force-displacement curve is plotted in Figure 6.6, fitted with the following relation:

$$P = 4857 \cdot u + 0 \cdot u^2 + 1478 \cdot u^3 \tag{6.34}$$

Eq. 6.34 reveals an absence of the quadratic nonlinear term.

Several values of P_0 from lower to higher, i.e., 0.5 *kN*, 5 *kN*, 20 *kN*, 50 *kN*, 200 *kN*, 300 *kN*, 400 *kN* and 500 *kN*, were chosen , in order to identify the parameters in a wide

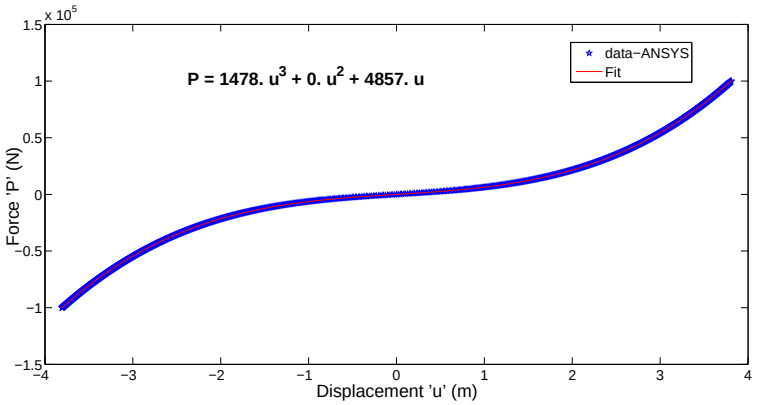

Figure 6.6: Force-displacement relation

range of loads. The results are presented in Figures 6.7-6.29 and Tables 6.3-6.4, respectively. Here, it can be recalled that in a real application for cable-stayed bridges, typical amplitude of the cable vibration reported approaches 1 m (Kumarasena et al., 2005), similar to the response values obtained at P_0 = 0.5 *kN*. In this respect, see Figure 6.8. However, for the purpose of study and with the fact that to see clearly the higher order nonlinear effects the system must be excited at higher amplitude (Storer, 1991), higher loads were considered.

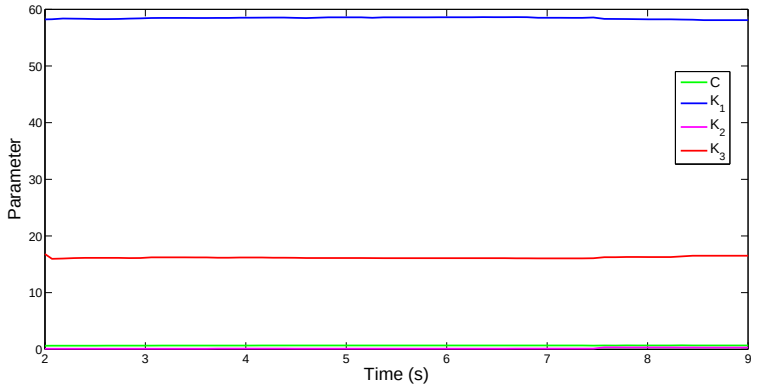

Figure 6.7: Time variation of the parameters for P_0 = 0.5 *kN*

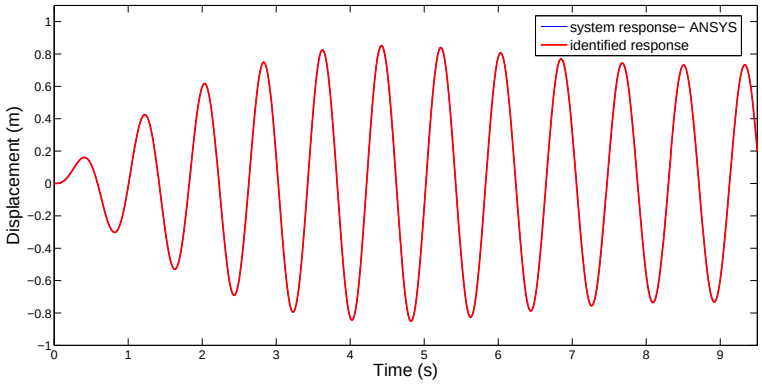

Figure 6.8: Displacement response for P_0 = 0.5 *kN*

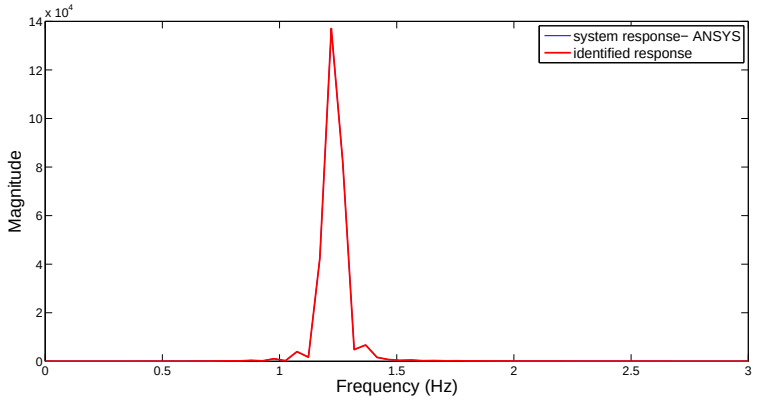

Figure 6.9: FFT of the displacement response, P_0 = 0.5 *kN*

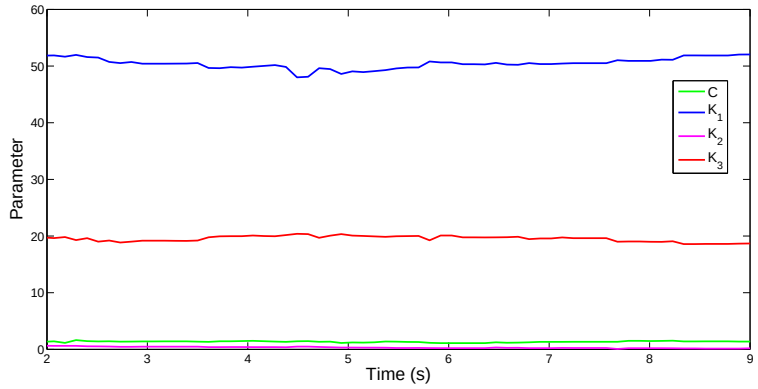

Figure 6.10: Time variation of the parameters for P_0 = 5 *kN*

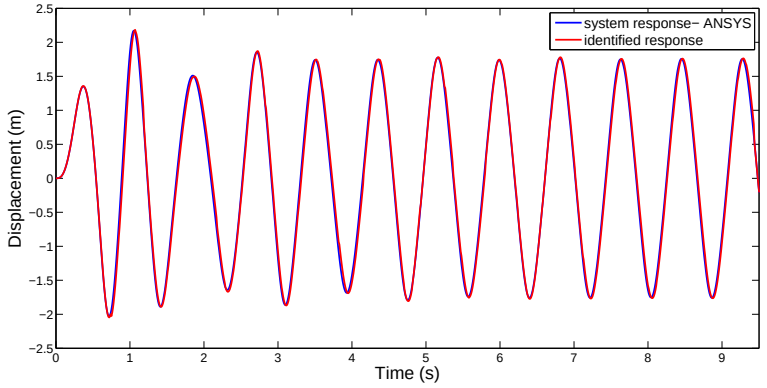

Figure 6.11: Displacement response for P_0 = 5 *kN*

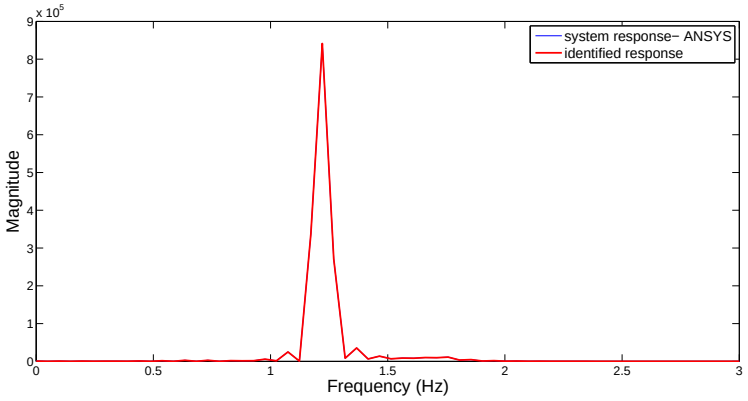

Figure 6.12: FFT of the displacement response, P_0 = 5 *kN*

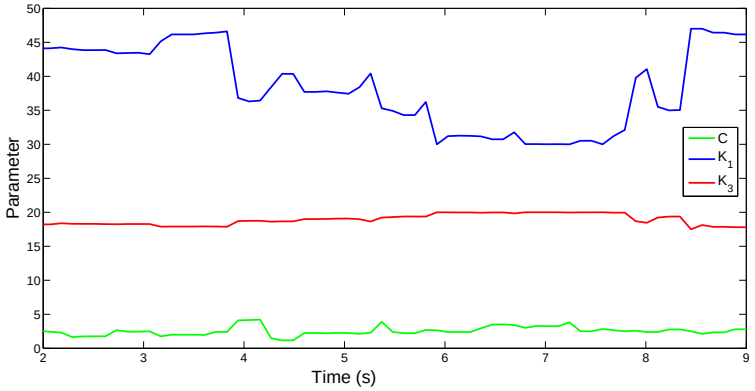

Figure 6.13: Time variation of the parameters for P_0 = 20 *kN*

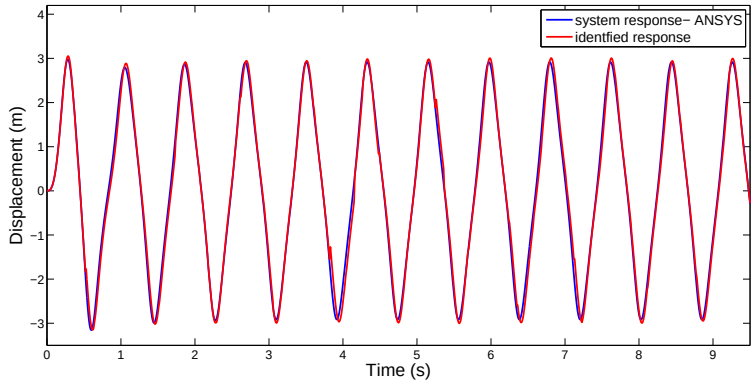

Figure 6.14: Displacement response for P_0 = 20 *kN*

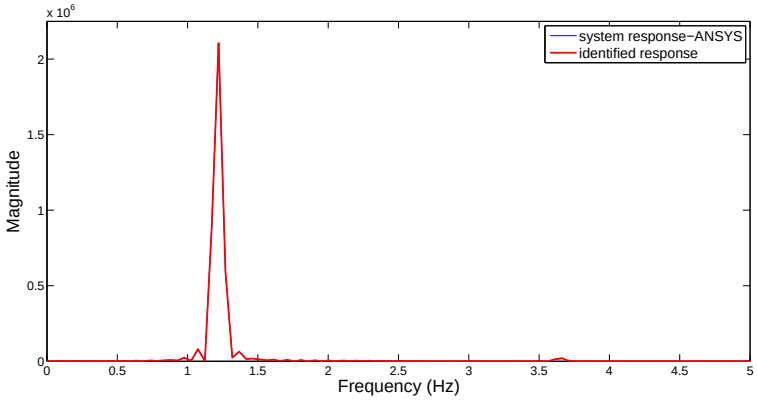

Figure 6.15: FFT of the displacement response, P_0 = 20 *kN*

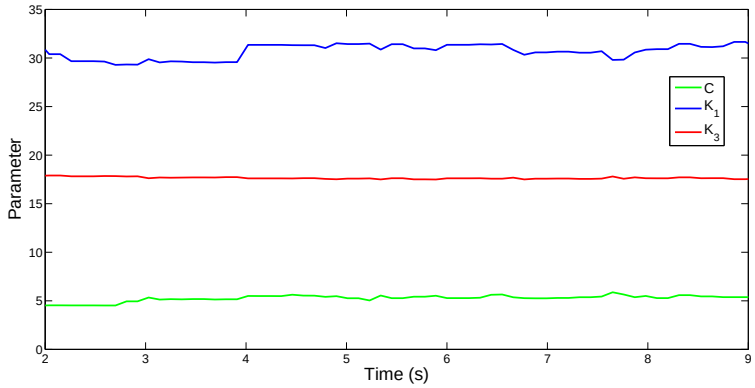

Figure 6.16: Time variation of the parameters for P_0 = 50 *kN*

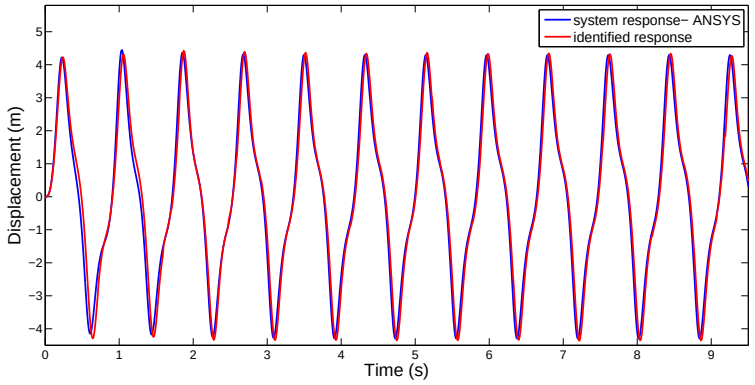

Figure 6.17: Displacement response for P_0 = 50 *kN*

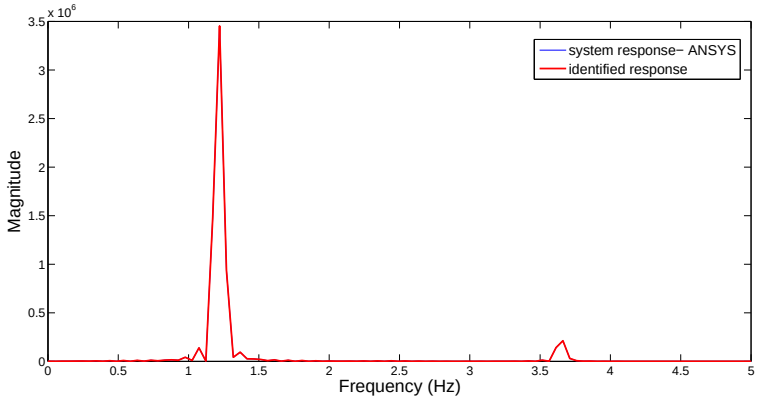

Figure 6.18: FFT of the displacement response, P_0 = 50 *kN*

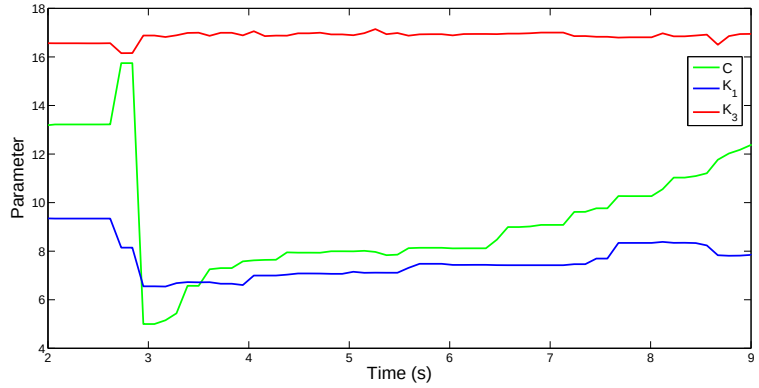

Figure 6.19: Time variation of the parameters for P_0 = 200 *kN*

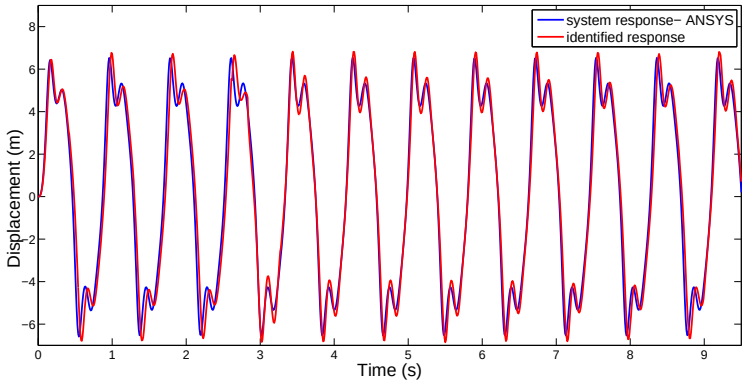

Figure 6.20: Displacement response for P_0 = 200 *kN*

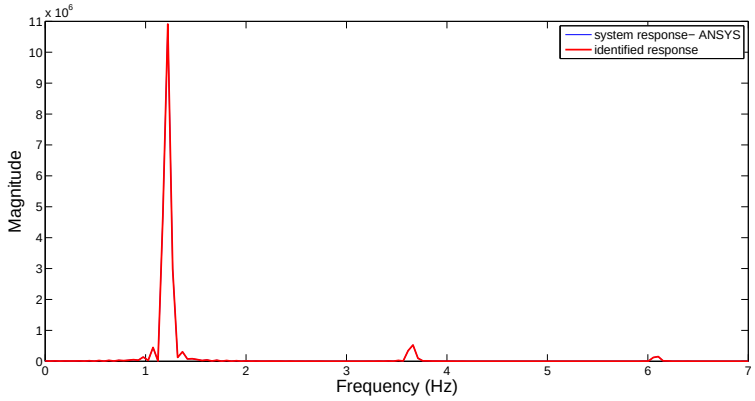

Figure 6.21: FFT of the displacement response, P_0 = 200 *kN*

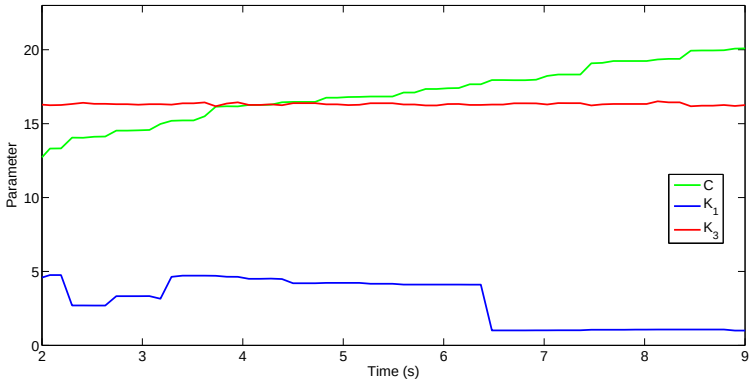

Figure 6.22: Time variation of the parameters for P_0 = 300 *kN*

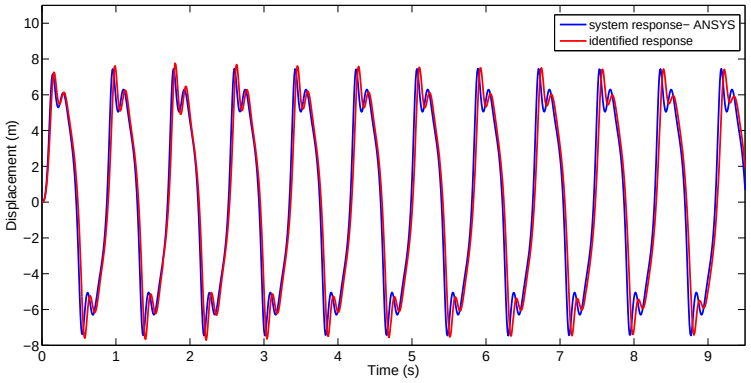

Figure 6.23: Displacement response for P_0 = 300 *kN*

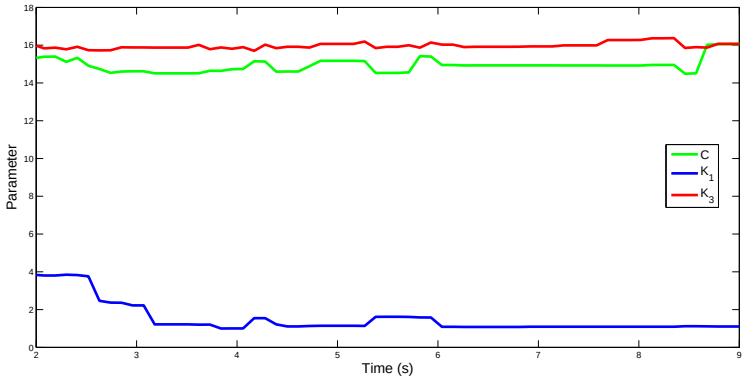

Figure 6.24: Time variation of the parameters for P_0 = 400 *kN*

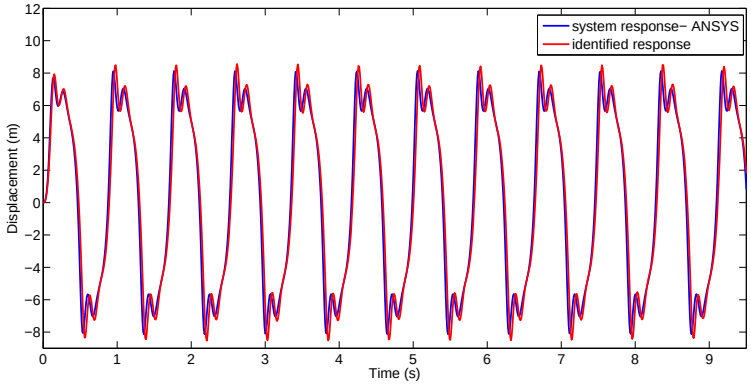

Figure 6.25: Displacement response for P_0 = 400 *kN*

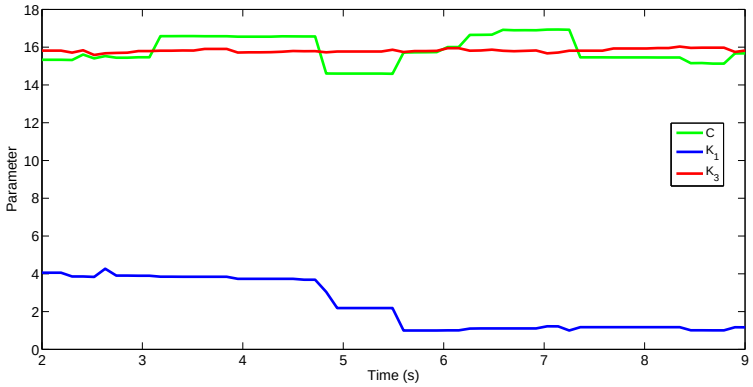

Figure 6.26: Time variation of the parameters for P_0 = 500 *kN*

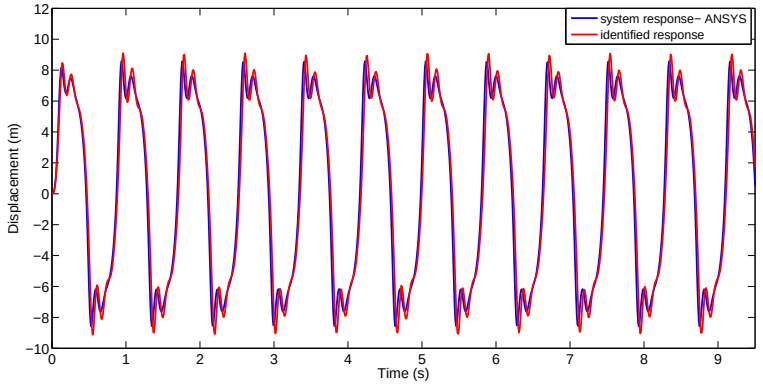

Figure 6.27: Displacement response for P_0 = 500 *kN*

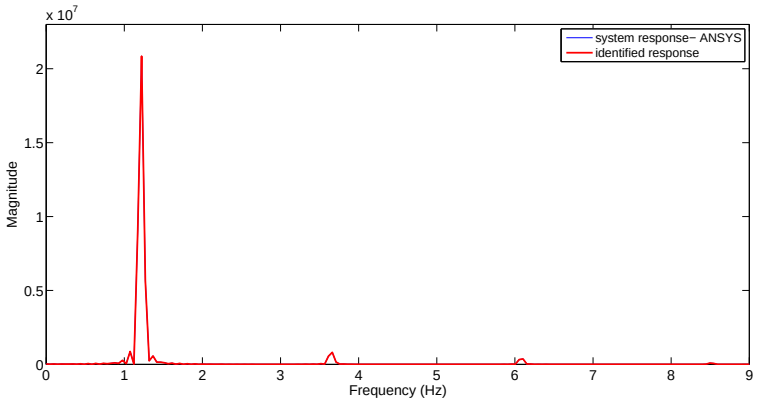

Figure 6.28: FFT of the displacement response, P_0 = 500 *kN*

Table 6.3: Identified parameters: mean value, standard deviation (sd) and coefficient of variation (cv %)

P_0 (*kN*)	C	K_1	K_3	sd-C	sd-K_1	sd-K_3	cv-C	cv-K_1	cv-K_3
0.5	0.65	58.38	16.24	0.03	0.21	0.42	4.2	0.4	2.6
5	1.31	50.57	19.47	0.15	1.6	0.48	11.6	3.2	2.4
20	2.56	39.49	18.75	0.6	5.54	0.74	23.5	14.0	4.0
50	5.27	30.68	17.64	0.31	0.75	0.10	5.9	2.4	0.6
200	13.67	9.76	16.37	1.65	0.67	0.28	12.1	6.8	1.7
300	17	2.99	16.3	2.18	1.56	0.1	12.8	52.1	0.6
400	15.13	2.04	15.96	0.49	1.3	0.15	3.21	63.4	0.96
500	15.69	2.54	15.84	0.81	1.37	0.13	5.18	53.96	0.83

The aforementioned results disclose that the applied time-frequency technique is capable to identify the system parameters of the cable element from numerical response data. The correctness of the procedure is justified by the good fitting of the identified displacement response to the system response obtained from ANSYS. Moreover, the following observations can be made:

(i) only a cubic type of nonlinearity, i.e. K_3 is present in all load cases; the quadratic nonlinearity, i.e. K_2 is nearly zero in all the load cases, due to the zero initial curvature

Table 6.4: Frequencies obtained from the FFT of the response

P_0 (kN)	Frequency (Hz)
0.5	1.221
5	1.221
20	1.221, 3.662
50	1.221, 3.662
200	1.221, 3.662, 6.104
300	1.221, 3.662, 6.104, 8.545
400	1.221, 3.662, 6.104, 8.545
500	1.221, 3.662, 6.104, 8.545

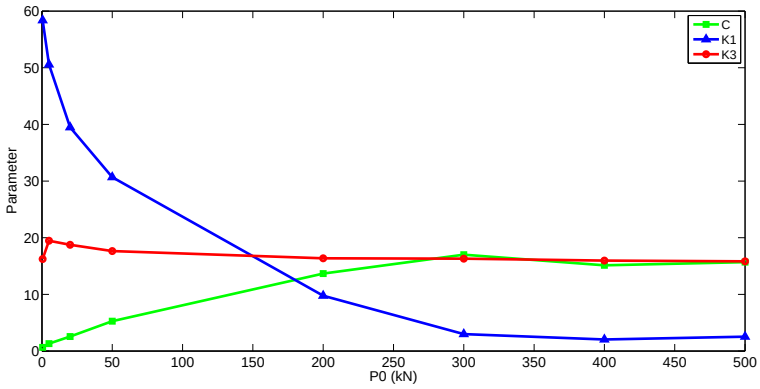

Figure 6.29: Variation of mean values of parameters vs. P_0

or sag (Rega, 2004a).

(ii) Damping parameter C increases whereas linear-frequency parameter K_1 decreases with the load amplitude. However, the cubic parameter K_3 remains almost constant from lower to higher load amplitudes, as shown in Figure 6.29.

(iii) All the three parameters approach constant values at higher loads. This shows that the identification procedure works more efficiently at higher loads.

(iv) From Table 6.4, it can be noticed that as the magnitude of the load increases more frequencies of higher order appear in the response. The higher frequencies are in exact odd multiple (3-, 5-, 7- times) of the primary frequency. This represents a typical behaviour of a nonlinear system subject to a harmonic excitation, when there is a leakage of energy to frequencies other than the linear natural frequencies, although the response remains essentially harmonic (Nayfeh and Mook, 1995; Zheng et al., 2002). The 3rd, 5th and 7th order super-harmonics are excited, and none of the sub-harmonics are present.

(v) Figures 6.13 and 6.19 show large fluctuation in K_1 and C, respectively. These trends however depends on the optimisation process, after a while the estimate converges to constant values.

6.7 Conclusions

A time-frequency identification technique for the nonlinear identification of a cable element was proposed in this chapter. A polynomial form of non-parametric method was used. A simple 2D cable model was reduced to a SDoF system. A good fitting of the identified and numerical data were obtained. Some interesting phenomena were observed. In particular, only a cubic type of nonlinearity was identified, whilst the quadratic type of nonlinearity was not present owing to zero initial-curvature or sag. Moreover, an increase of the parameter related to damping and a decrease of the parameter relevant to linear-frequency were observed versus the loading amplitude. However, the values of the parameters stabilised at higher load amplitudes. Super-

harmonics were present in the response at higher loading amplitudes. Therefore, the identification procedure was more effective at higher load amplitudes.

In conclusion, the time-frequency technique proposed here exhibited a good capability in the nonlinear identification of cables. Nonetheless, some major challenges remain for a more powerful application of the proposed identification method. In detail: (i) the choice of a complete initial polynomial approximation; (ii) the computational burden related to the calculation both of the solution of the polynomial equation and the STFT at each instant of time.

CHAPTER 7

FOOTBRIDGE-PEDESTRIAN INTERACTION

7.1 Introduction

The aesthetic demand of human beings and advances in material technology have enabled the design and construction of light and slender structures, like footbridges, stairways, stadium etc. On one hand, these structures may very well satisfy the design strength criteria; on the other hand, they become more prone to the vibration serviceability problems due to human induced dynamic loads (Wood, 1948; Jones and Eyre, 1981; Bachmann and Ammann, 1987; Pimentel et al., 1999). The sensitivity of human beings to vibration levels as low as 0.001 mm triggers the vibration serviceability problem much before the damage of the structure due to large vibration (Pretlove and Rainer, 1995). The large lateral vibrations of the London Millenium Bridge (a steel suspension bridge) on its opening day have highlighted the criticality of the human-structure vibration serviceability problem (Dallard et al., 2001a). Several cable-stayed footbridges have also shown this phenomenon (Fujino et al., 1993; Nakamura and Fujino, 2002). The interpretation of this pedestrians-structure interaction as a synchronization phenomenon have been further studied and experimentally confirmed by several researchers (Dallard et al., 2001a; Newland, 2003; Roberts, 2005; Strogatz et al., 2005; Nakamura and Kawasaki, 2006; Eckhardt et al., 2007; Bodgi et al., 2007; Piccardo and Tubino, 2008). Several efforts have been made to find a model to reproduce the phenomenon of pedestrians-structure interaction. In a few of these articles, i.e. (Newland, 2003; Roberts, 2005; Macdonald, 2008), a

pedestrian has been modelled as a single degree of freedom oscillator with different definitions of the restoring force. Following the same approach a pedestrian is modelled as a self-sustained oscillator based on a modified hybrid Van der Pol/Rayleigh (MHVR) model in (Erlicher et al., 2010). This model has been studied for the walking of a pedestrian on a rigid floor (Erlicher et al., 2010; Trovato et al., 2008, 2009). We extend this MHVR model to represent a pedestrian walking on an oscillating floor. The amplitude, stability and phase of the entrained response of the MHVR model is analyzed. The main study is theoretical. The comparison with experimental data concerning pedestrian structure interaction mainly has an illustrative purpose.

After the Introduction, the MHVR model is presented in section 7.2. Section 7.3 concerns the determination of the response amplitude equation for the MHVR oscillator using the harmonic balance method. Then, the stability analysis is carried out in section 7.4. Section 7.5 represents the application of the model to find the number of synchronized pedestrians on a given floor vibration. Then, the phase analysis is carried out in section 7.6. Section 7.7 investigates the effect of variation of the floor parameters on the phase and amplitude of the oscillator. Section 7.8 compares the simulation results with some experimental results available in the literature for an illustrative purpose. The conclusion gives a summary of the main findings of the work.

7.2 A modified hybrid Van der Pol/Rayleigh (MHVR) oscillator for modelling the lateral pedestrian force on a moving floor

It is assumed that a pedestrian can be represented by a Single-Degree-of-Freedom oscillator. Only the lateral motion is analyzed. The mass is supposed equal to that of the pedestrian. In order to define the restoring force of such an oscillator, the *self-sustained* nature of the walking phenomenon is accounted for, i.e. the fact that a pedestrian produces by itself the energy spent to preserve its motion. In the nonlinear dynamics literature, the so-called self-sustained oscillators are well-known and they possess some properties that seem to be well suited for a pertinent and sim-

plified modelling of the pedestrian behavior. One of the most important properties of non-autonomous self-sustained oscillators is that they may have an *entrained* response (Pikowski et al., 2001), i.e. a response characterized by the same frequency as that of the excitation.

Actually, an entrained response represents a pedestrian *synchronized* with the moving floor, even if its natural frequency is different. With a less precise terminology, it can be said that the walker *synchronizes* its frequency with that of the floor. The term synchronization should be used when two of more coupled self-sustained oscillators with different natural frequencies move at the same frequency, while the entrainment concerns an oscillator that assumes the same frequency than that of an *external agency*. Both terms will be used here indifferently, as it is usually done in the applications concerning the pedestrian-floor interaction. The particular case of a *harmonic excitation* is considered because, on one hand, it is the natural assumption required to apply the *harmonic balance method* and, on the other hand, because a floor lateral motion at constant frequency and amplitude is a simple experimental condition, easy to obtain when pedestrians walk on a treadmill placed on a shake table, see e.g. (Nakamura et al., 2008; Sun and Yuan, 2008).

7.2.1 Pedestrian on a rigid floor

In recent papers (Erlicher et al., 2010; Trovato et al., 2008, 2009), Erlicher et al. proposed an approach to represent the lateral oscillations of pedestrians during walking on a rigid floor, based on a modified hybrid Van der Pol/Rayleigh (MHVR) oscillator :

$$\frac{d^2u_y}{dt^2} - 2\mu\omega_0\frac{du_y}{dt}\left(1 - \beta u_y^2 - \frac{\gamma}{\omega_0}\frac{du_y}{dt}u_y - \frac{\delta}{\omega_0^2}\left(\frac{du_y}{dt}\right)^2\right) + \omega_0^2 u_y = 0 \tag{7.1}$$

where u_y is the lateral displacement of the center of mass of the pedestrian; ω_0 is the angular frequency of the underlying linear oscillator, μ, β, γ and δ are coefficients associated with the nonlinear damping term, which allows the self-sustaining mechanism responsible of perpetual periodic oscillations in the autonomous case. The oscillator (7.1) is *self-sustained*, viz. it has a stable limit cycle, when $\mu > 0$ and $\beta + 3\delta > 0$. The parameter identification made in (Erlicher et al., 2010) has been performed by imposing the stronger conditions $\beta > 0$ and $\delta \geq 0$ or $\beta \geq 0$ and $\delta > 0$.

By means of this assumption, a very good fitting of experimental results in the rigid floor regime has been obtained (Erlicher et al., 2010). In the limit of small μ values, the amplitude of the limit cycle reads $u_{y,\max} \simeq 2/\sqrt{\beta + 3\delta}$, while the natural frequency is

$$\omega_1 \simeq \omega_0 \left(1 + \frac{\mu\gamma}{\beta + 3\delta}\right)$$

The details about this oscillator and its application in the modelling of the lateral pedestrian oscillations on a rigid floor are discussed in (Erlicher et al., 2010).

7.2.2 Pedestrian on a moving floor

The main aim of the present work is to study the response of the MHVR oscillator (7.1) *under a harmonic external force*, representing a periodic floor motion, with an amplitude small enough to avoid the loss of the lateral stability of the walker. If the mode shape effect is neglected, the coupling between this oscillator and one of the lateral modes of a structure is represented by the following system (see also Figure 7.1a):

$$\begin{cases} \frac{d^2U_y}{dt^2} + 2\xi_s\omega_s \frac{dU_y}{dt} + \omega_s^2 U_y = \frac{1}{M} F_y\left(u_y, \frac{du_y}{dt}\right) \\ m\frac{d^2u_y}{dt^2} + F_y\left(u_y, \frac{du_y}{dt}\right) = -m\frac{d^2U_y}{dt^2} \end{cases} \tag{7.2}$$

where

$$F_y\left(u_y, \frac{du_y}{dt}\right) = m\left(-2\mu\omega_0\frac{du_y}{dt}\left(1 - \beta u_y^2 - \frac{\gamma}{\omega_0}u_y\frac{du_y}{dt} - \frac{\delta}{\omega_0^2}\left(\frac{du_y}{dt}\right)^2\right) + \omega_0^2 u_y\right) \tag{7.3}$$

is the restoring force of the MHVR oscillator; U_y is the floor (structure) displacement; M is the modal mass of the structure for the lateral mode under exam; ξ_s and ω_s are the modal damping and circular frequency, respectively; u_y is the lateral displacement of the center of mass of the pedestrian *with respect to the structure*; m is the pedestrian mass; ω_0 is the frequency of the underlying linear system associated with the MHVR oscillator, $\mu > 0$, β, γ and δ are coefficients associated with the *nonlinear damping term*, which is at the origin of the self-sustained oscillations in the autonomous case.

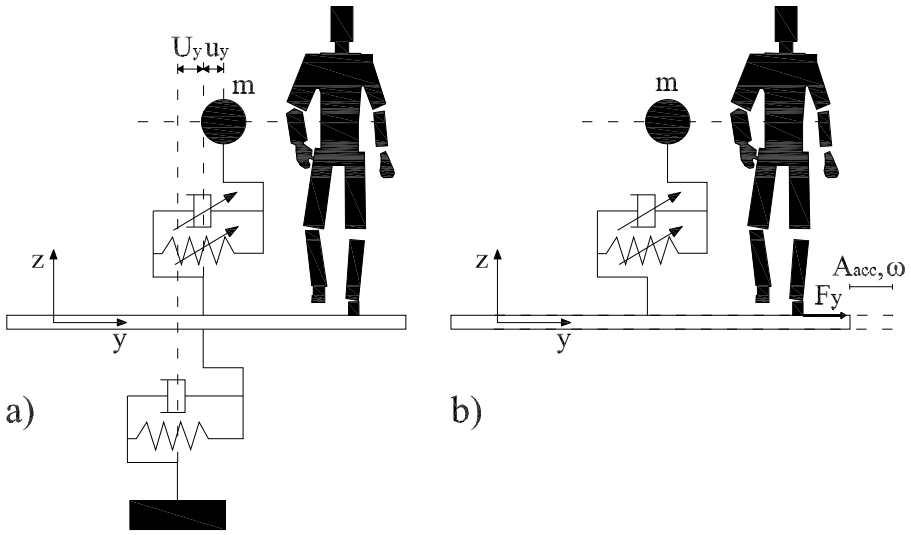

Figure 7.1: (a) Scheme of the Two-DoF system representing the coupled lateral motion of a pedestrian and the deck of a footbridge. (b) Single-DoF oscillator representing a pedestrian on a floor undergoing a harmonic motion.

The coupled pedestrian-structure behaviour modelled by the system (7.2) is not considered. A simpler situation is rather analyzed, where the floor lateral motion is supposed known and harmonic with displacement amplitude $A_d > 0$ and with frequency ω:

$$U_y(t) = A_d \cos(\omega t) \quad \longrightarrow \quad \frac{d^2 U_y(t)}{dt^2} = -A_{acc} \cos(\omega t) \tag{7.4}$$

where $A_{acc} := A_d \omega^2$ is the floor acceleration amplitude. Hence the second equation in (7.2) becomes

$$\frac{d^2 u_y(t)}{dt^2} - 2\mu\omega_0 \frac{du_y(t)}{dt}\left(1 - \beta u_y^2(t) - \frac{\gamma}{\omega_0}\frac{du_y(t)}{dt}u_y(t) - \frac{\delta}{\omega_0^2}\left(\frac{du_y(t)}{dt}\right)^2\right) + \omega_0^2 u_y(t) = A_{acc}\cos(\omega t) \tag{7.5}$$

Eq. (7.5) represents a pedestrian walking on a floor undergoing lateral harmonic oscillations; see also Figure 7.1b. This condition can be easily obtained in a laboratory test, asking pedestrians to walk on a treadmill placed on a shake table (Nakamura et al., 2008).

7.3 Analytical solution: the harmonic balance method

In this Section, the analysis of the periodic solutions of Eq. (7.5) having frequency equal to that of the excitation, is presented. Actually, the non-autonomous MHVR oscillator (7.5) is quite general: if β=γ = 0 the Rayleigh oscillator is retrieved, while γ=δ = 0 leads to the standard Van der Pol oscillator. The non-autonomous Van der Pol and Rayleigh oscillators have been studied in textbooks (e.g. (Jordan and Smith, 2007; Guckenheimer and Holmes, 1983)). A more complex analysis of the Rayleigh model is presented in (Chedjou et al., 2006), where an external force with *two* periodic components is considered. One also observes that the term depending on γ is analogous to the *inertia hardening* term mentioned in (Hamdan and Shabaneh, 1997; Al-Qaisia and Hamdan, 1999, 2002). However, in the oscillator discussed by those authors, this nonlinear term is always accompanied by a second one: it is not possible to distinguish the contributions of each one, as it should be done for our purposes.

A stationary solution of the form

$$u_y(t) = R\cos(\omega t+\theta) \tag{7.6}$$

is postulated. Eq. (7.6) indicates that the oscillator/pedestrian has the same frequency as the moving floor, where R is the amplitude of the displacement measured with respect to the structure and θ is the phase difference between this displacement and $-\frac{d^2U_y}{dt^2}$, i.e. minus the acceleration of the floor.

The research of an approximated solution of the form (7.6) corresponds to solve Eq. (7.5) by using the Harmonic Balance (HB) method with expansion limited to the first harmonic (Al-Qaisia and Hamdan, 2002). The advantages and drawbacks of this method, in particular in comparison with the multiple scales method, are discussed e.g. in (Al-Qaisia and Hamdan, 1999; Hassan and Burton, 1995). A more sophisticated theoretical analysis without any approximation is possible, but this is beyond the purposes of the work. Instead of directly solving Eq. (7.5) with the assumption (7.6), the new time-scale

$$\tau=\omega_0 t \tag{7.7}$$

is introduced. By replacing Eq. (7.7) in Eq. (7.5), one obtains

$$\ddot{w}(\tau) - \epsilon\dot{w}(\tau)\left(1 - \beta w(\tau)^2 - \gamma\dot{w}(\tau)\, w(\tau) - \delta(\dot{w}(\tau))^2\right) + w(\tau) = \frac{A_{acc}}{\omega_0^2}\cos(\tilde{\omega}\tau) = A_d\tilde{\omega}^2\cos(\tilde{\omega}\tau) \tag{7.8}$$

where the dot indicates the differentiation with respect to the time-scale τ and

$$w(\tau) := u_y\left(\frac{\tau}{\omega_0}\right), \qquad \tilde{\omega} := \frac{\omega}{\omega_0}, \qquad \epsilon = 2\mu \tag{7.9}$$

Analogously, the periodic solution (7.6) becomes

$$w(\tau) = R\cos(\tilde{\omega}\tau + \theta) \tag{7.10}$$

According to the HB method, the expression (7.10) is replaced into Eq. (7.8). After some trigonometric simplifications, one has:

$$\begin{aligned}
&\left(-\tilde{\omega}^2 R + R + \tfrac{\gamma}{4}\epsilon\tilde{\omega}^2 R^3\right)\cos(\tilde{\omega}\tau + \theta) + \left(\epsilon\tilde{\omega}R - \epsilon\tilde{\omega}R^3\tfrac{1}{4}\left(\beta + 3\delta\tilde{\omega}^2\right)\right)\sin(\tilde{\omega}\tau + \theta) \\
&-\tfrac{1}{4}\epsilon\tilde{\omega}R^3\left(\beta - \delta\tilde{\omega}^2\right)\sin(3\tilde{\omega}\tau + 3\theta) - \tfrac{1}{4}\epsilon\tilde{\omega}R^3\gamma\tilde{\omega}\cos(3\tilde{\omega}\tau + 3\theta) \\
&= \left(A_d\tilde{\omega}^2\cos(\theta)\right)\cos(\tilde{\omega}\tau + \theta) + \left(A_d\tilde{\omega}^2\sin(\theta)\right)\sin(\tilde{\omega}\tau + \theta)
\end{aligned}$$

Neglecting third order harmonic components and equating to zero both sinus and cosinus terms, one obtains the following algebraic equations:

$$\begin{cases}
\epsilon\tilde{\omega}\left(-\frac{\tilde{\omega}^2 - 1}{\epsilon\tilde{\omega}}R + \frac{\gamma}{4}\tilde{\omega}R^3\right) = A_d\tilde{\omega}^2\cos(\theta) \\
\epsilon\tilde{\omega}\left(R - R^3\tfrac{1}{4}\left(\beta + 3\delta\tilde{\omega}^2\right)\right) = A_d\tilde{\omega}^2\sin(\theta)
\end{cases} \tag{7.11}$$

Due to the assumptions on the sign of parameters discussed above, one has $\beta + 3\delta > 0$. Moreover, $\tilde{\omega}$ is supposed close enough to 1, in order to have $\beta + 3\delta\tilde{\omega}^2 > 0$. Therefore, by introducing the following quantities

$$R_0 = \frac{2}{\sqrt{\beta + 3\delta\tilde{\omega}^2}}, \quad \alpha = \frac{\gamma\tilde{\omega}}{\beta + 3\delta\tilde{\omega}^2} \tag{7.12}$$

where R_0 has the meaning of reference response amplitude and α is a normalized form of the parameter γ, three normalized variables can be defined:

$$r = \frac{R}{R_0}, \qquad \lambda = \frac{A_d\tilde{\omega}}{R_0\epsilon} = \frac{A_{acc}}{\omega_0^2}\frac{1}{R_0\epsilon\tilde{\omega}}, \qquad \nu = \frac{\tilde{\omega}^2 - 1}{\epsilon\tilde{\omega}} \tag{7.13}$$

r is a non-dimensional response amplitude, λ is a non-dimensional external acceleration amplitude and ν is a non-dimensional difference (detuning) between the floor

frequency ω and the frequency ω_0 of the underlying linear system associated with the MHVR oscillator. By substituting Eqs. (7.12) and (7.13) into Eq. (7.11), one gets

$$\begin{cases} r\left(-\nu+\alpha r^2\right) = \lambda\cos(\theta) \\ r\left(1-r^2\right) = \lambda\sin(\theta) \end{cases} \tag{7.14}$$

By solving these equations for $\cos(\theta)$ and $\sin(\theta)$ and then using the identity $\sin^2(\theta) + \cos^2(\theta) = 1$, one easily obtains

$$r^2\left(1-r^2\right)^2 + r^2\left(\nu-\alpha r^2\right)^2 - \lambda^2 = 0 \tag{7.15}$$

Eq. (7.15) states that the squared normalized amplitude $z = r^2$ is a root of a polynomial of order 3, provided that ν, λ and α are fixed. Once r^2 is known, the value of θ can be determined by means of the expression

$$\tan(\theta) = \frac{1-r^2}{-\nu+\alpha r^2} \tag{7.16}$$

obtained from (7.14). One notices that both the standard Van der Pol and Rayleigh oscillators are represented by Eqs. (7.15)-(7.16) with $\alpha = 0$. The additional term associated α, which is in turn related to the coefficient γ, introduces a *non-isochronous* behaviour (Pikowski et al., 2001). Eq. (7.15) can also be thought as the steady-state solution of the following complex-valued equation depending on the three non-dimensional parameters ν, α and λ:

$$\frac{da}{d\zeta} = (1 + i\nu)\,a - (1 + i\alpha)\,|a|^2\,a + \lambda \tag{7.17}$$

where $a = re^{i\theta}$ and ζ is a generic normalized time-variable, equal to $\frac{\epsilon}{2}\tau$ in the specific case considered here (see also (Pikowski et al., 2001)). A similar expression is analyzed in (Glendinning and Proctor, 1986):

$$\frac{da}{d\zeta} = (\xi + i\nu)\,a - (1 + i\alpha)\,|a|^2\,a + 1 \tag{7.18}$$

There are still three non-dimensional parameters, but one of them is different from those used in Eq. (7.17). Another analogous expression is investigated in (Levina and Nepomnyaschiy, 1986):

$$\frac{da}{d\zeta} = (\xi \pm i)\,a - (1 \pm i\alpha)\,|a|^2\,a + \lambda \tag{7.19}$$

where the normalization is still different. The analyses of the steady solutions of (7.18) and (7.19) presented in (Glendinning and Proctor, 1986) and (Levina and

Nepomnyaschiy, 1986), respectively, are somehow complementary, due to the different choice of the normalized parameters. Eq. (7.17) represents a third complementary viewpoint on the same equation, and, to the authors' knowledge, very few analyses of it can be found in the literature. For this reason, and without forgetting the final application to the pedestrian modelling, a detailed study of Eq. (7.15), giving the amplitude of the steady solutions of Eq. (7.17), is presented hereinafter.

7.3.1 Response curves $\nu - r^2$

Eq. (7.15) involves four quantities: the normalized amplitude r of the steady response of the non-autonomous self-sustained oscillator (7.5) and three non-dimensional parameters ν, λ and α. It follows that the system response may be represented in several ways, for instance in a bidimensional plot $\nu - r^2$, with fixed α and λ values, or by assuming constant values of α and ν and plotting r vs. λ, etc.

In this Subsection, the $\nu - r^2$ representation is analyzed. It generalizes analogous well-known plots concerning the standard Van der Pol and Rayleigh models; see e.g. (Jordan and Smith, 2007). In order to simplify the notation, Eq. (7.15) and (7.16) are rewritten by using the variable $z = r^2$:

$$p_{\nu,\alpha,\lambda}(z) := \left(1 + \alpha^2\right) z^3 - 2\left(1 + \nu\alpha\right) z^2 + \left(1 + \nu^2\right) z - \lambda^2 = 0 \tag{7.20}$$

$$\tan(\theta) = \frac{1-z}{-\nu+\alpha z} \tag{7.21}$$

Due to the definition of z, only *real* and *positive* roots of $p_{\nu,\alpha,\lambda}(z)$ are admissible. Two examples of response curves $\nu - z$ plotted using Eq. (7.20) are shown in Fig. 7.2. Fig. 7.2a concerns the *isochronous* case $\alpha = 0$, associated with the classical models of Van der Pol and Rayleigh, while Fig. 7.2b illustrates a particular *non-isochronous* case, with $\alpha = 2$.

In both Figures, one observes that for given ν and λ values, either one or three real and positive roots of $p_{\nu,\alpha,\lambda}(z)$ may exist. In more detail, using the Descartes' sign rule, it can be proven that if the second coefficient of the polynomial (7.20) is null, i.e. if $1+\nu\alpha = 0$, then $p_{\nu,\alpha,\lambda}(z)$ has one real positive root and two complex conjugate roots

for any λ value. Fig. 7.2b illustrates the vertical line corresponding to $1 + \nu\alpha = 0$, for the case $\alpha = 2$. If $1 + \nu\alpha < 0$, there is one real positive root for all λ, while the two other roots are either negative or complex conjugate. One can conclude that when $1 + \nu\alpha \leq 0$, there is only one admissible (i.e. real and positive) root of the polynomial $p_{\nu,\alpha,\lambda}(z)$. Conversely, when

$$1 + \nu\alpha > 0 \tag{7.22}$$

the situation is more difficult. The polynomial (7.20) admits either three real positive roots or one real positive and two complex conjugate roots. The transition between these two situations occurs when there is one real positive root plus another real positive root with multiplicity equal to two. This threshold corresponds to the locus of points where the derivative of $p_{\nu,\alpha,\lambda}(z)$ is equal to zero (Rand, 2005):

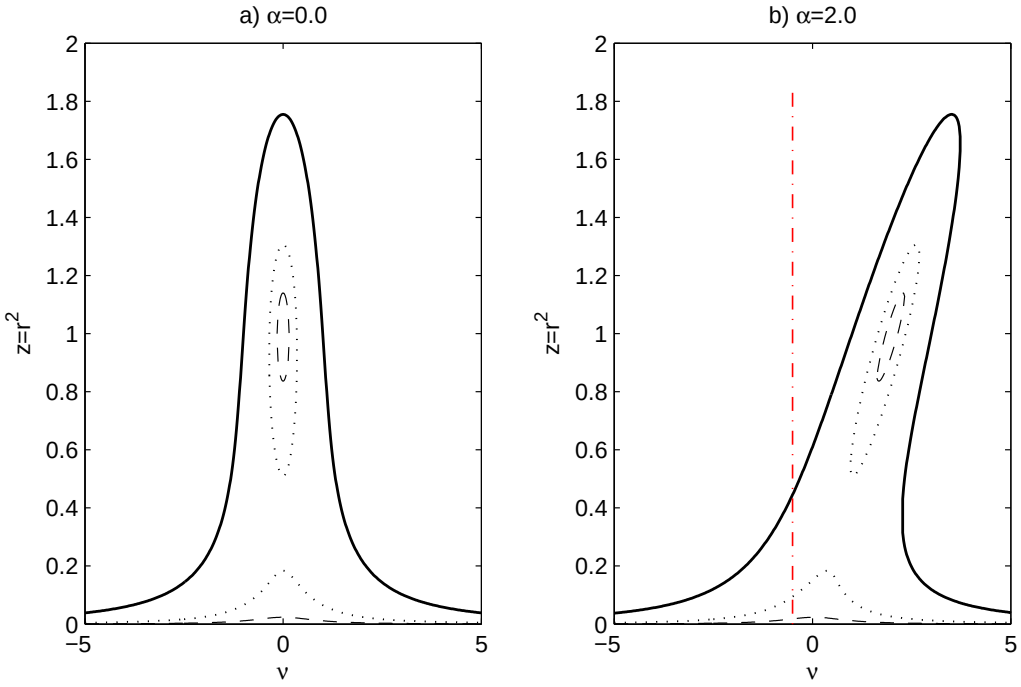

Figure 7.2: Response curves of the MHVR oscillator: (a) isochronous case (α = 0) and (b) non-isochronous case (example with α = 2). The curves show the real and positive solutions of Eq. (7.15). Dashed line: λ =0.15 , dotted line: λ=0.35 , solid line: λ=1.0 .

$$\frac{dp_{\nu,\alpha}(z)}{dz} = 3z^2\left(1+\alpha^2\right) - 4z\left(1+\nu\alpha\right) + 1 + \nu^2 = 0 \tag{7.23}$$

For a given α value, Eq. (7.23) represents a *conic* in the $\nu - z$ half-plane ($z > 0$) independent from the external excitation parameter λ.

Let us consider the general expression of a conic, that reads

$$c_1 z^2 + c_2 z\nu + c_3\nu^2 + c_4 z + c_5\nu + c_6 = 0 \tag{7.24}$$

with at least one of the coefficients c_1, c_2 and c_3 different from zero. By comparing Eqs. (7.23) and (7.24), one has $c_1 = 3\left(1+\alpha^2\right)$, $c_2 = -4\alpha$, $c_3 = 1$, $c_4 = -4$, $c_5 = 0$, $c_6 = 1$. It is evident that the nature of this conic change with the value of α**.** Three cases may occur:

(i) $c_2^2 - 4c_1c_3 < 0 \Longleftrightarrow |\alpha| < \sqrt{3}$. Eqs. (7.23)-(7.24) represent an ellipse;

(ii) $c_2^2 - 4c_1c_3 > 0 \Longleftrightarrow |\alpha| > \sqrt{3}$. Eqs. (7.23)-(7.24) represent a hyperbola;

(iii) $c_2^2 - 4c_1c_3 = 0 \iff \alpha = \pm\sqrt{3}$. Eqs. (7.23)-(7.24) represent a parabola.

These three cases are schematically illustrated in Fig. 7.3 b,d,c, respectively. In addition, Fig. 7.3a concerns the simple isochronous case $\alpha = 0$. The other lines plotted in the same figure are related to the nature (nodes, spirals, etc.) and stability of the equilibrium points. These points will be discussed in the next Section.

An illustration of the meaning of Eq. (7.23) and how it is related to the multiplicity of the roots of $p_{\nu,\alpha,\lambda}(z)$ is given in Figs. 7.4 and 7.5. The polynomial $p_{\nu,\alpha,\lambda}(z)$ is represented for $\alpha = \overline{\alpha} = 1$ and $\nu = \overline{\nu} = 1.4492$, and for five different values of λ, $\lambda' < \lambda_Q < \lambda'' < \lambda_P < \lambda'''$, indicated in the figures. Notice that the modification of λ induces vertical translations of the curve in Fig. 7.4, but it does not affect the abscissas z_P and z_Q of the points of zero-slope, where Eq. (7.23) is fulfilled. With reference to the numerical values of the Figure, Eq. (7.23) leads to $z_P \simeq 0.42934$ and $z_Q \simeq 1.2035$. The corresponding points P and Q, belonging to the conic defined by Eq. (7.23), are indicated in Fig. 7.5.

When $\lambda = \lambda'$, $p_{\overline{\nu},\overline{\alpha},\lambda'}(z)$ has *one* real positive root, $z_{1'} < z_P$ (see Fig. 7.4). The corresponding point $1'$ in Fig. 7.5, having coordinates $(\overline{\nu}, z_{1'})$, is outside the region bounded by the conic (7.23). When $\lambda = \lambda''$, there are *three* real positive roots of

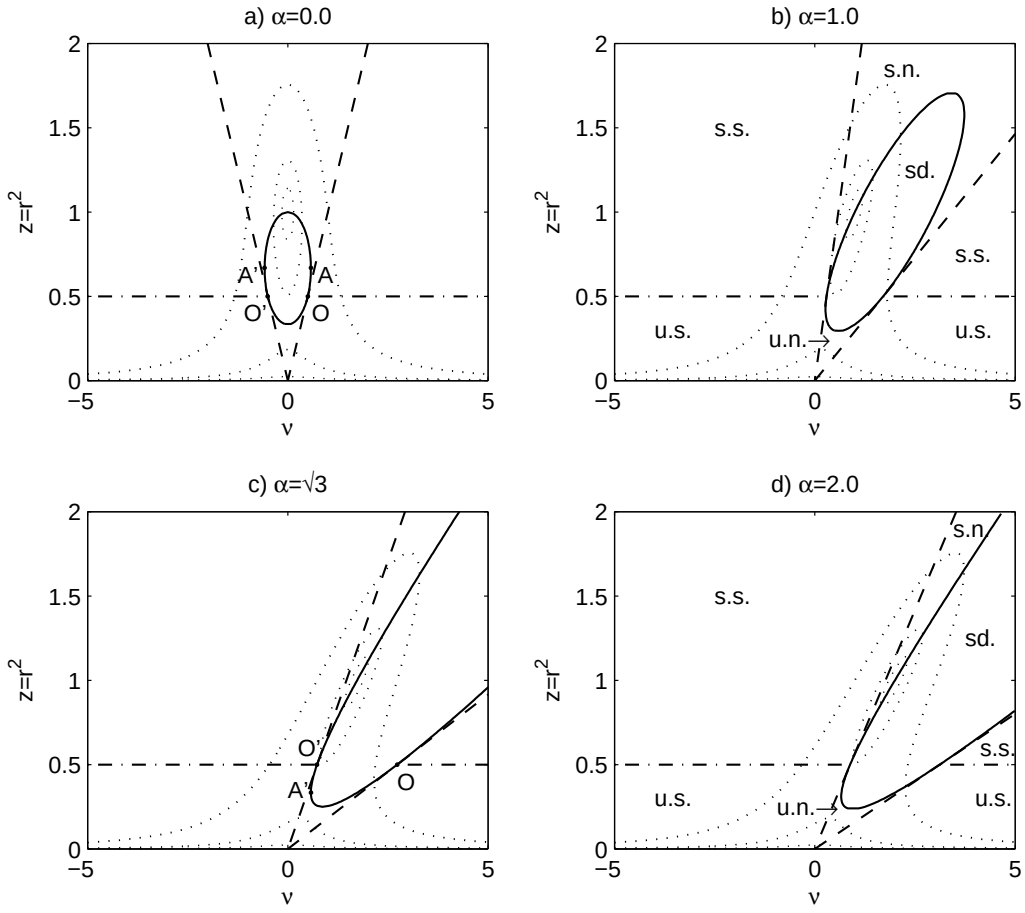

Figure 7.3: Response curves and stability regions of the MHVR oscillator. Dotted lines: response amplitude curves associated with Eq. (7.20). Continuous lines: conic associated with the saddle-node bifurcation (7.44). Dashed-dotted lines: Hopf bifurcation (7.45). Dashed lines: nodes-spirals bifurcation (7.46).

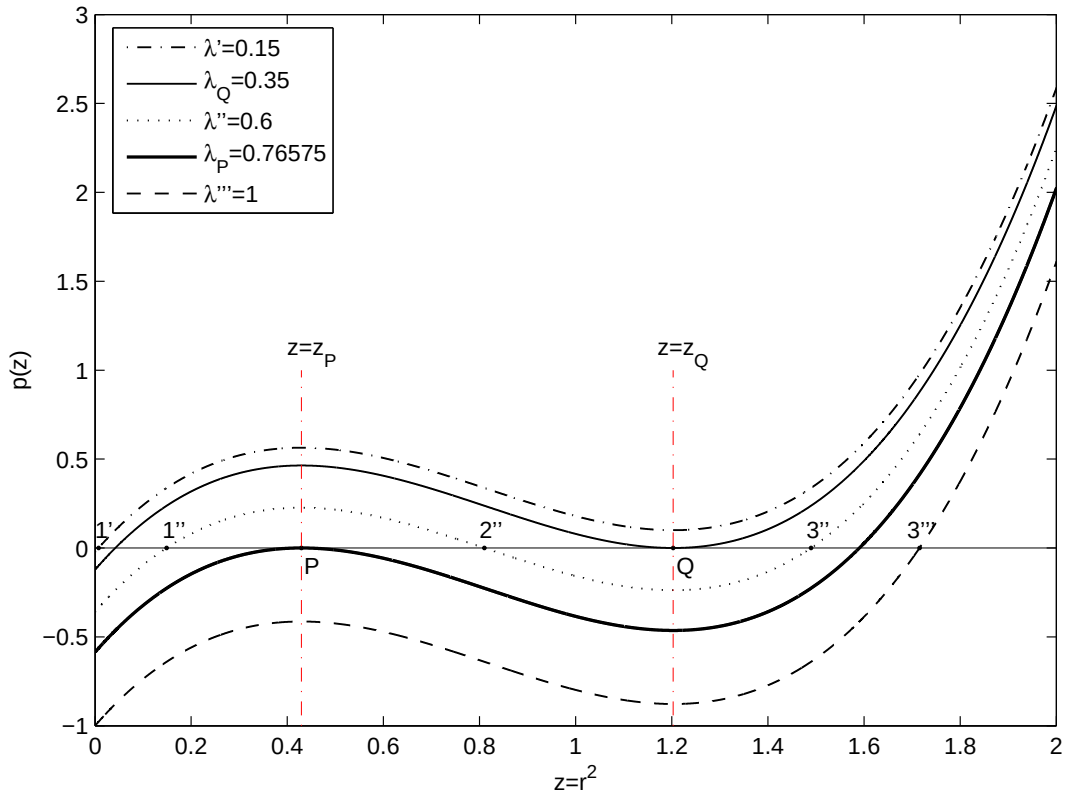

Figure 7.4: Plot of the polynomial $p(z)$, Eq. (7.20), for $\alpha = 1$, $\nu = 1.4492$ and five λ-values.

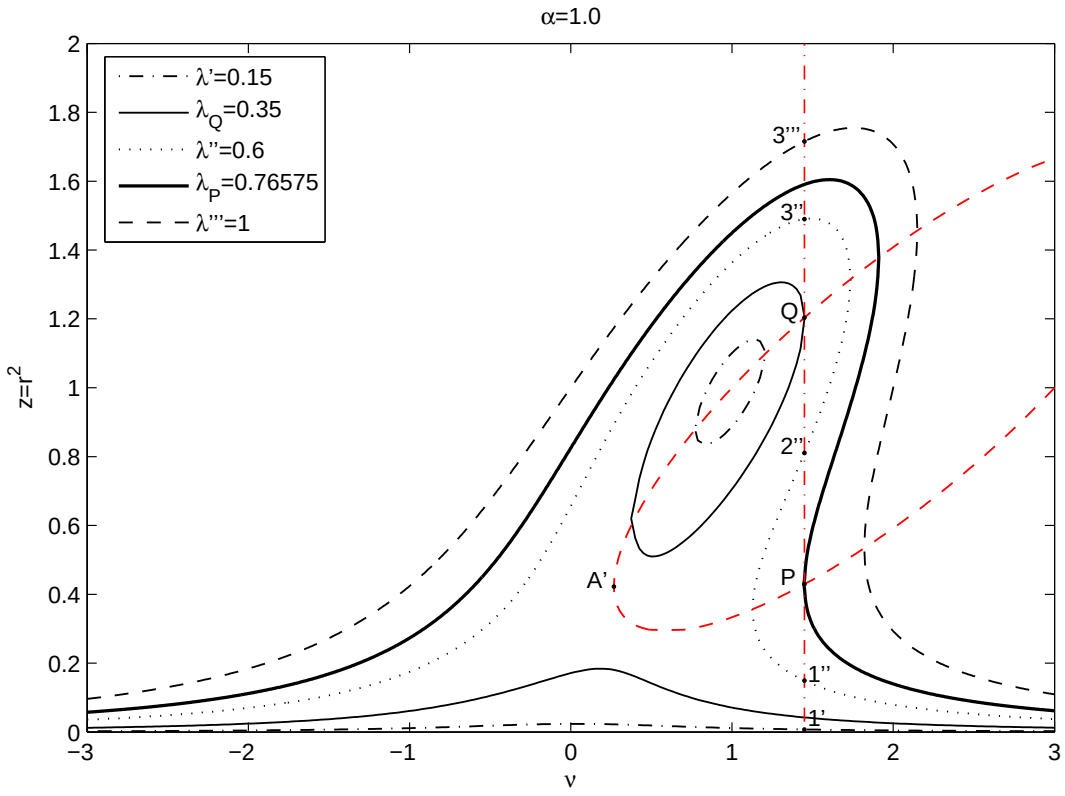

Figure 7.5: Response curves of the MHVR oscillator (Eq. (7.15)) for α = 1 and with five different λ-values. The vertical line corresponds to ν = 1.4492, while the dashed ellipse is associated with the condition (7.23).

$p_{\bar{\nu},\bar{\alpha},\lambda''}(z)$, associated with the points $1'', 2''$ and $3''$ indicated in Fig. 7.4. One is inside the conic, while the others are outside. In the intermediate case $\lambda = \lambda_Q$, the polynomial (7.20) has *three* real positive roots and two of them coincide and are equal to $z = z_Q$. The value $\lambda_Q \simeq 0.35$ used in Figs. 7.4-7.5 has been found by replacing the numerical value of $z_Q, \bar{\alpha}$ and $\bar{\nu}$ in Eq. (7.20). When $\lambda = \lambda'''$, $p_{\bar{\nu},\bar{\alpha},\lambda'''}(z)$ has *one* real positive root $z_{3'''} > z_Q$. When $\lambda = \lambda_P$, the situation is analogous to that of the case $\lambda = \lambda_Q$. In summary, for given α and ν values, the polynomial (7.20) has three real and distinct positive solutions when

$$\lambda_Q(\nu, \alpha) < \lambda < \lambda_P(\nu, \alpha) \tag{7.25}$$

On the boundaries of this interval two of the three real positive solutions coincide, while outside the interval there is only one real positive solution.

Looking at Figs. 7.3 and 7.5, one notices that there is one (or two) special point(s) where the tangent to the conic (7.23) is vertical, i.e. where P and Q degenerate into a single point. If the conic is an ellipse, there are two points, called A' and A. There is only one point in the other cases. The coordinates of A and/or A' can be computed by imposing that the polynomial (7.20) has three real repeated roots (Rand, 2005):

$$\frac{d^2 p_{\nu,\alpha}(z)}{dz^2} = 6z\left(\alpha^2 + 1\right) - 4\nu\alpha - 4 = 0 \tag{7.26}$$

This leads to

$$z = \frac{2}{3}\frac{1 + \nu\alpha}{1 + \alpha^2} \tag{7.27}$$

Then, in order to impose that the points belong to the conic, Eq. (7.27) is replaced into (7.23):

$$\left(\alpha^2 - 3\right)\nu^2 + 8\alpha\,\nu + \left(1 - 3\alpha^2\right) = 0 \tag{7.28}$$

The solution of Eq. (7.28) is found considering the cases (i), (ii) and (iii) defined above:

(i) $|\alpha| < \sqrt{3}$. The polynomial (7.28) has a couple of real roots

$$\nu_{A'} = \frac{\sqrt{3}\alpha - 1}{\alpha + \sqrt{3}} < \nu_A = \frac{\sqrt{3}\alpha + 1}{\sqrt{3} - \alpha} \tag{7.29}$$

Both values of ν in (7.29) satisfy the inequality (7.22), i.e. $1 + \nu_{A'}\,\alpha > 0$ and $1 + \nu_A\,\alpha > 0$. It means that both solutions are admissible and this is consistent

with the fact that the conic is an ellipse. The coordinates $z_{A'}$ and z_A can be computed by replacing (7.29) into Eq. (7.27). Finally, the corresponding values of λ are obtained from (7.20) (see Table 7.2).

(ii) $|\alpha| > \sqrt{3}$. The polynomial (7.28) still has the couple of real roots

$$\nu_A = \frac{\sqrt{3}\alpha + 1}{\sqrt{3} - \alpha} < \nu_{A'} = \frac{\sqrt{3}\alpha + 1}{\sqrt{3} - \alpha} \tag{7.30}$$

However, in this case the sign of the inequality between ν_A and $\nu_{A'}$ is inverted and only one of the ν values in (7.30) fulfils (7.22), depending on the sign of α. The other one must be discarded. This is consistent with the hyperbolic shape of the conic. The final coordinates are collected in Table 7.2.

(iii) $\alpha = \pm\sqrt{3}$. Eq. (7.28) becomes of first order in the variable ν and the solutions read

$$\begin{aligned} &\alpha = \sqrt{3} \quad \Longrightarrow \nu_{A'} = \tfrac{\sqrt{3}}{3}, \;\; z_{A'} = \tfrac{1}{3}, \;\; \lambda_{A'} = \tfrac{2}{3\sqrt{3}} \\ &\alpha = -\sqrt{3} \quad \Longrightarrow \nu_A = -\tfrac{\sqrt{3}}{3}, \;\; z_A = \tfrac{1}{3}, \;\; \lambda_A = \tfrac{2}{3\sqrt{3}} \end{aligned}$$

where $z_{A'}, z_A$ have been calculated from (7.27) and then $\lambda_{A'}, \lambda_A$ from (7.20). For a given value of α, only one solution exists and this means that only one limit point exists. This is consistent with the fact that the conic is a parabola (recall Fig. 7.3c). In both cases ($\alpha = \pm\sqrt{3}$), the inequality (7.22) is fulfilled.

The coordinates of A and A' can be also found by an alternative procedure, related to a different representation of the conic (7.23), obtained by replacing Eq. (7.23) into (7.20) and eliminating the variable z:

$$27\left(1+\alpha^2\right)^2\lambda^4 + \lambda^2\left(-4 + \left(60\alpha\nu - 36\alpha^2 - 36\nu^2\right)(1+\nu\alpha) - 4\alpha^3\nu^3\right) + 4(\alpha-\nu)^2\left(1+\nu^2\right)^2 = 0 \tag{7.31}$$

A detailed analysis of this expression is made in the next Section.

7.3.2 Analytical vs. numerical results

A comparison between numerical simulation results and analytical response amplitudes predicted by Eq. (7.15) or, equivalently, by Eq. (7.20) is reported in Fig. 7.6.

The points associated with the numerical solution are plotted for the cases where the entrained periodic response exists, i.e. it is stable. It has been obtained by solving Eq. (7.5) by means of the solver ODE45 implemented in Matlab and then computing the amplitude of the first harmonic of the periodic response. The numerical simulations have been performed with the parameters ω_0 = 1 rad/s, $\epsilon = 2\mu$ = 0.05, β = 1 m^{-2}, δ = 1 m^{-2}. The non-dimensional parameter α is constant (α = 1), while three values of λ are considered (λ = 0.35, λ = 1.5, λ = 2.5). As a result, for each fixed ν value, the remaining parameters ω, A_{acc} and γ needed for numerical integration of Eq. (7.5) are computed using (7.9) and (7.13) and the identity $A_{acc} = \omega^2 A_d$. Fig. 7.6 shows that there is a good agreement between numerical and analytical results. Actually, the good approximation obtained in this example concerns values of $z = r^2$ less than 2.5, while λ is less than 2.5 and μ is small. The accuracy of analytical predictions diminishes for higher values of these quantities and of the modulus of α.

7.4 Stability analysis

7.4.1 Local stability of the entrained steady response

In this section, we analyze the *local* stability of the solution (7.10) of Eq. (7.8) by considering a small perturbation $v(\tau)$, according to a procedure similar to that presented in (Al-Qaisia and Hamdan, 1999). The perturbed solution reads

$$w(\tau) = R\cos(\tilde{\omega}\tau + \theta) + v(\tau) \tag{7.32}$$

Only the "first type" of stability is investigated (Al-Qaisia and Hamdan, 1999). This corresponds to assume that the perturbation $v(\tau)$ can be approximated by a harmonic expression with the same fundamental frequency and truncated at the same order than the assumed response (7.10):

$$v(\tau) = B_{1c}(\tau)\cos(\tilde{\omega}\tau + \theta) + B_{1s}(\tau)\sin(\tilde{\omega}\tau + \theta) \tag{7.33}$$

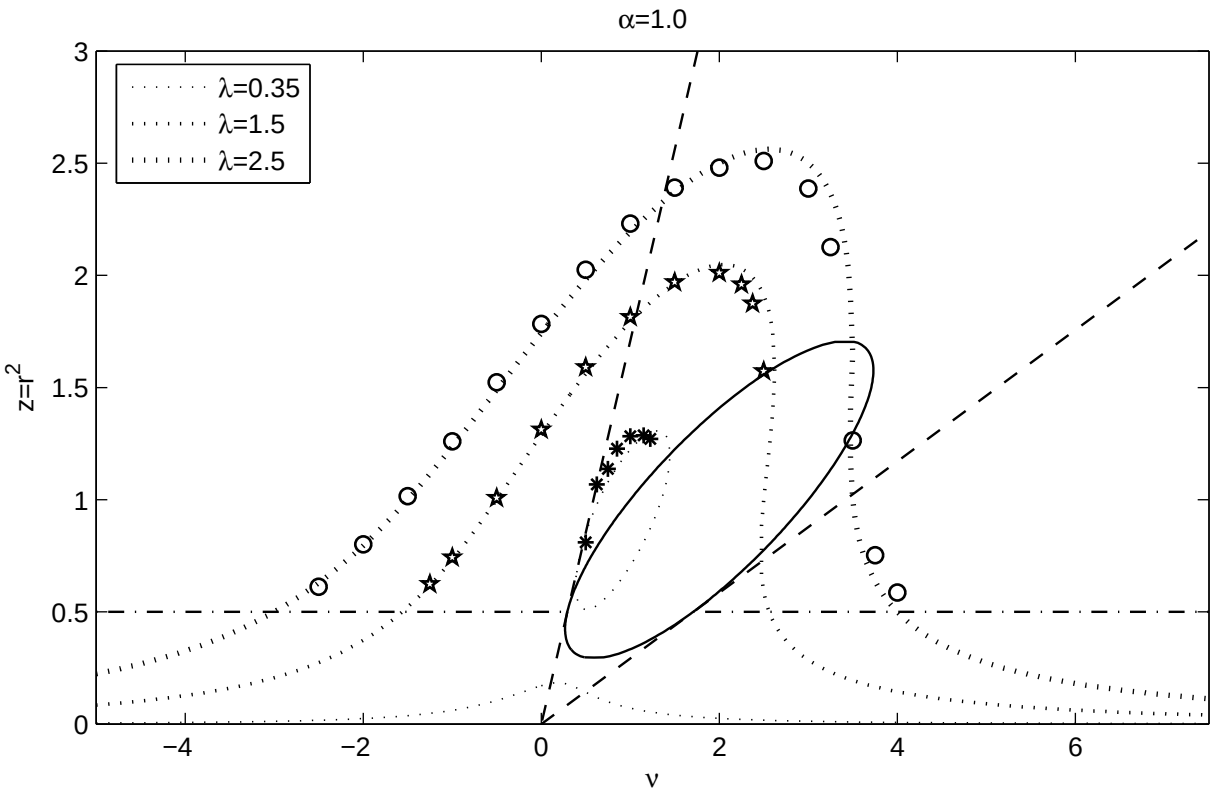

Figure 7.6: Response curves of the MHVR oscillator (Eq.(7.15)) for α = 1. Comparison between numerical and analytical results for three different λ-values.

By inserting the expression (7.32) of the perturbed solution into the equation (7.8), one obtains

$$
\begin{aligned}
&\ddot{\mathrm{v}}(\tau)+\mathrm{v}(\tau)\\
&-\epsilon\dot{\mathrm{v}}(\tau)\begin{pmatrix}
1-\beta\left(R^2\left(\frac{1}{2}+\frac{1}{2}\cos\left(2\tilde{\omega}\tau+2\theta\right)\right)+\mathrm{v}^2(\tau)+2\mathrm{v}(\tau)R\cos\left(\tilde{\omega}\tau+\theta\right)\right)\\
-\gamma\left(-R^2\tilde{\omega}\frac{1}{2}\sin\left(2\tilde{\omega}\tau+2\theta\right)-R\tilde{\omega}\sin\left(\tilde{\omega}\tau+\theta\right)\mathrm{v}(\tau)\right)\\
-\gamma\left(R\cos\left(\tilde{\omega}\tau+\theta\right)\dot{\mathrm{v}}(\tau)+\mathrm{v}(\tau)\dot{\mathrm{v}}(\tau)\right)\\
-\delta\left(R^2\tilde{\omega}^2\left(\frac{1}{2}-\frac{1}{2}\cos\left(2\tilde{\omega}\tau+2\theta\right)\right)+\dot{\mathrm{v}}^2(\tau)-2\dot{\mathrm{v}}(\tau)R\tilde{\omega}\sin\left(\tilde{\omega}\tau+\theta\right)\right)
\end{pmatrix}\\
&+\epsilon R\tilde{\omega}\begin{pmatrix}
-\beta\left(2R\frac{1}{2}\sin\left(2\tilde{\omega}\tau+2\theta\right)\mathrm{v}(\tau)+\sin\left(\tilde{\omega}\tau+\theta\right)\mathrm{v}(\tau)^2\right)\\
-\gamma\left(-R\tilde{\omega}\left(\frac{1}{2}-\frac{1}{2}\cos\left(2\tilde{\omega}\tau+2\theta\right)\right)\mathrm{v}(\tau)+R\frac{1}{2}\sin\left(2\tilde{\omega}\tau+2\theta\right)\dot{\mathrm{v}}(\tau)\right)\\
-\gamma\left(\sin\left(\tilde{\omega}\tau+\theta\right)\dot{\mathrm{v}}(\tau)\mathrm{v}(\tau)\right)\\
-\delta\left(-2R\tilde{\omega}\left(\frac{1}{2}-\frac{1}{2}\cos\left(2\tilde{\omega}\tau+2\theta\right)\right)\dot{\mathrm{v}}(\tau)+\sin\left(\tilde{\omega}\tau+\theta\right)\dot{\mathrm{v}}(\tau)^2\right)
\end{pmatrix}\\
&=0
\end{aligned}
\tag{7.34}
$$

The external excitation term related to A_{acc} does not appear in Eq. (7.34), since it cancels out together with the terms fulfilling the equilibrium equations (7.11). The third order harmonics have also been neglected, according to the harmonic balance method and to the assumption (7.33). The *linearization* of (7.34) leads to

$$
\begin{aligned}
&\ddot{\mathrm{v}}(\tau)+\mathrm{v}(\tau)\left(1-\epsilon\beta R^2\tilde{\omega}\sin\left(2\tilde{\omega}\tau+2\theta\right)+\gamma\epsilon R^2\tilde{\omega}^2\left(\frac{1}{2}-\frac{1}{2}\cos\left(2\tilde{\omega}\tau+2\theta\right)\right)\right)\\
&-\epsilon\dot{\mathrm{v}}(\tau)\left(1-\beta R^2\left(\frac{1}{2}+\frac{1}{2}\cos\left(2\tilde{\omega}\tau+2\theta\right)\right)+\gamma R^2\tilde{\omega}\sin\left(2\tilde{\omega}\tau+2\theta\right)\right)\\
&-\epsilon\dot{\mathrm{v}}(\tau)\left(-3\delta R^2\tilde{\omega}^2\left(\frac{1}{2}-\frac{1}{2}\cos\left(2\tilde{\omega}\tau+2\theta\right)\right)\right)\\
&=0
\end{aligned}
\tag{7.35}
$$

We recall the definition (7.33) and make a Van der Pol transformation between the variables $(\mathrm{v},\dot{\mathrm{v}})$ and (B_{1c},B_{1s}):

$$
\begin{cases}
\mathrm{v}(\tau)=B_{1c}\cos\left(\tilde{\omega}\tau+\theta\right)+B_{1s}\sin\left(\tilde{\omega}\tau+\theta\right)\\
\dot{\mathrm{v}}(\tau)=-B_{1c}\tilde{\omega}\sin\left(\tilde{\omega}\tau+\theta\right)+\tilde{\omega}B_{1s}\cos\left(\tilde{\omega}\tau+\theta\right)
\end{cases}
\tag{7.36}
$$

with the compatibility condition

$$
\dot{B}_{1s}\sin\left(\tilde{\omega}\tau+\theta\right)=-\dot{B}_{1c}\cos\left(\tilde{\omega}\tau+\theta\right)
\tag{7.37}
$$

This identity is obtained imposing that the velocity defined in $(7.36)_2$ is equal to the velocity computed by differentiating Eq. $(7.36)_1$. The acceleration, obtained by differentiating $(7.36)_2$, reads:

$$
\ddot{\mathrm{v}}(\tau)=-B_{1s}\tilde{\omega}^2\sin\left(\tilde{\omega}\tau+\theta\right)-B_{1c}\tilde{\omega}^2\cos\left(\tilde{\omega}\tau+\theta\right)+\tilde{\omega}\dot{B}_{1s}\cos\left(\tilde{\omega}\tau+\theta\right)-\dot{B}_{1c}\tilde{\omega}\sin\left(\tilde{\omega}\tau+\theta\right)
$$

(7.38)

By replacing (7.36) and (7.38) in Eq. (7.35) and after some trigonometric development, one has

$$
\begin{aligned}
&-B_{1s}\tilde{\omega}^2\sin(\tilde{\omega}\tau+\theta)-B_{1c}\tilde{\omega}^2\cos(\tilde{\omega}\tau+\theta)+\tilde{\omega}\dot{B}_{1s}\cos(\tilde{\omega}\tau+\theta)-\dot{B}_{1c}\tilde{\omega}\sin(\tilde{\omega}\tau+\theta)\\
&+B_{1s}\left(\sin(\tilde{\omega}\tau+\theta)-\epsilon\beta R^2\tilde{\omega}\tfrac{1}{2}\cos(\tilde{\omega}\tau+\theta)+\gamma\epsilon R^2\tilde{\omega}^2\left(\tfrac{1}{2}\sin(\tilde{\omega}\tau+\theta)+\tfrac{1}{4}\sin(\tilde{\omega}\tau+\theta)\right)\right)\\
&+B_{1c}\left(\cos(\tilde{\omega}\tau+\theta)-\epsilon\beta R^2\tilde{\omega}\tfrac{1}{2}\sin(\tilde{\omega}\tau+\theta)+\gamma\epsilon R^2\tilde{\omega}^2\tfrac{1}{4}\cos(\tilde{\omega}\tau+\theta)\right)\\
&-\epsilon\tilde{\omega}B_{1s}\left(\cos(\tilde{\omega}\tau+\theta)-\beta R^2\tfrac{3}{4}\cos(\tilde{\omega}\tau+\theta)+\gamma R^2\tilde{\omega}\tfrac{1}{2}\sin(\tilde{\omega}\tau+\theta)-\tfrac{3}{4}\delta R^2\tilde{\omega}^2\cos(\tilde{\omega}\tau+\theta)\right)\\
&+\epsilon B_{1c}\tilde{\omega}\left(\sin(\tilde{\omega}\tau+\theta)-\beta R^2\tfrac{1}{4}\sin(\tilde{\omega}\tau+\theta)+\gamma R^2\tilde{\omega}\tfrac{1}{2}\cos(\tilde{\omega}\tau+\theta)-\tfrac{9}{4}\delta R^2\tilde{\omega}^2\sin(\tilde{\omega}\tau+\theta)\right)\\
&=0
\end{aligned}
$$

where the third harmonic components have been neglected like in the previous expressions. This equation and the compatibility condition (7.37) constitute a system of two first order equations which can be rewritten, after some developments, as follows:

$$
\begin{cases}
-2\tilde{\omega}\dot{B}_{1s}=B_{1s}\left(\epsilon\beta R^2\tilde{\omega}\tfrac{1}{4}-\epsilon\tilde{\omega}+\epsilon\tilde{\omega}\delta R^2\tilde{\omega}^2\tfrac{3}{4}\right)+B_{1c}\left(-\left(\tilde{\omega}^2-1\right)+\gamma\epsilon R^2\tilde{\omega}^2\tfrac{3}{4}\right)\\
2\tilde{\omega}\dot{B}_{1c}=B_{1s}\left(-\left(\tilde{\omega}^2-1\right)+\gamma\epsilon R^2\tilde{\omega}^2\tfrac{1}{4}\right)+B_{1c}\left(\epsilon\tilde{\omega}-\epsilon\tilde{\omega}\beta R^2\tfrac{3}{4}-\tfrac{9}{4}\epsilon\tilde{\omega}R^2\tilde{\omega}^2\delta\right)
\end{cases}
$$

The even superharmonics have been neglected. By using the normalized parameters and variables defined by (7.12) and (7.13), one obtains the equivalent system:

$$
\begin{cases}
2\dot{B}_{1s}=\epsilon\left(1-r^2\right)B_{1s}+\epsilon\left(\nu-3\alpha r^2\right)B_{1c}\\
2\dot{B}_{1c}=\epsilon\left(-\nu+\alpha r^2\right)B_{1s}+\epsilon\left(1-3r^2\right)B_{1c}
\end{cases}
\tag{7.39}
$$

The corresponding matrix form is given in (7.40).

$$
\dot{\mathbf{B}}=\mathbf{M}\,\mathbf{B}\quad\text{with}\quad\mathbf{B}=\begin{bmatrix}B_{1s}\\B_{1c}\end{bmatrix}\quad\text{and}\quad\mathbf{M}=\frac{\epsilon}{2}\begin{bmatrix}1-r^2&\nu-3\alpha r^2\\-\nu+\alpha r^2&1-3r^2\end{bmatrix}
\tag{7.40}
$$

By setting

$$
B_{1s}(\tau)=b_{1s}e^{\kappa\tau},\quad B_{1c}(\tau)=b_{1c}e^{\kappa\tau}
$$

where b_{1c} and b_{1s} are constant, the eigenproblem $(\mathbf{M}-\kappa\mathbf{I})\,\mathbf{b}=\mathbf{0}$ is derived. According the standard procedure (Jordan and Smith, 2007), the stability is related to the eigenvalues $\kappa_{1,2}$ of the matrix **M**, which are solutions of the characteristic equation $\kappa^2-\kappa\,\mathrm{tr}(\mathbf{M})+\det\mathbf{M}=0$, where "tr" and "det" are the trace and determinant operators. The stability requires that the real part of the eigenvalues is negative. This means that the

two following conditions must hold:

$$q = \det \mathbf{M} = \frac{\epsilon^2}{4}\left(3r^4\left(1+\alpha^2\right) - 4r^2(1+\nu\alpha) + 1 + \nu^2\right) > 0 \tag{7.41}$$

$$p = \mathrm{tr}\mathbf{M} = \epsilon\left(1 - 2r^2\right) < 0 \tag{7.42}$$

The negative determinant characterizes saddles, for all values of p. When the determinant is positive, the fixed points may be stable or unstable, according to the sign of the trace p and they are nodes or spirals, according to the sign of the discriminant

$$\Delta = p^2 - 4q = \epsilon^2\left(\left(1-3\alpha^2\right)r^4 + 4\nu\alpha\, r^2 - \nu^2\right) \tag{7.43}$$

The conditions $q = 0$, $p = 0$ and $\Delta = 0$ define curves associated with a change of stability and/or nature of the fixed points, i.e. the steady solutions. It is possible to represent these transition curves in the $\nu - r^2$ plane and in the $\nu - \lambda$ plane. In the next two Subsections, both approaches are considered.

7.4.2 Representation in the $\nu - r^2$ plane

Let us begin with the condition $q = 0$. By using the definition of q given in (7.41) and setting $z = r^2$, one has:

$$B_S : q = 0 \quad \longrightarrow \quad 3z^2\left(1+\alpha^2\right) - 4z(1+\nu\alpha) + 1 + \nu^2 = 0 \tag{7.44}$$

It can be easily proven that (7.44) is identical to the condition $\frac{dp_{\nu,\alpha,\lambda}(z)}{dz} = 0$ where $p_{\nu,\alpha,\lambda}(z)$ is the polynomial given in Eq. (7.20). This condition defines the *conic* in the $\nu - z$ plane where $p_{\nu,\alpha,\lambda}(z)$ has three real positive roots and two of them are repeated. In the previous section, it has been shown that this conic can be an ellipse ($|\alpha| < \sqrt{3}$), a parabola ($\alpha = \pm\sqrt{3}$) or a hyperbola ($|\alpha| > \sqrt{3}$); see also Figure 7.3. The points in the ($\nu - z$) plane inside the conic correspond to $q < 0$. Therefore, they are saddles. The equilibrium points outside the conic ($q > 0$) and having the discriminant $\Delta > 0$ are nodes. For this reason, the conic is called saddle-node bifurcation B_S. Moreover, one has

$$B_H : p = 0 \quad \longrightarrow \quad z = \frac{1}{2} \tag{7.45}$$

i.e. the condition $p = \mathrm{tr}\mathbf{M} = 0$ defines a horizontal line in the $\nu - z$ plane. This line intersects the conic B_S. However, since inside the conic the equilibria are saddles

independently from the sign of p, the part of this line lying inside B_S does not change the nature of equilibria and it can be canceled out. Conversely, outside B_S the sign of p affects the stability of the fixed points: the two horizontal half-lines associated with (7.45) separate stable from unstable fixed points and define the so-called Hopf bifurcation B_H. The stable region ($p < 0$) corresponds to $z > \frac{1}{2}$ (Fig. 7.3).

The transition between nodes and spirals is defined by the condition $\Delta = 0$ (Eq. (7.43)). Four cases are distinguished, according to the α value. For each case, the transition is defined by a couple of half-lines B_N issuing from the origin of the $\nu - z$ plane (recall that $z \geq 0$):

$$
(B_N): \quad
\begin{array}{ll}
|\alpha| < \frac{1}{\sqrt{3}} \longrightarrow & \left\{ \begin{array}{l} \nu = \nu_1(z) = \left(2\alpha - \sqrt{\alpha^2+1}\right) z \\ \nu = \nu_2(z) = \left(2\alpha + \sqrt{\alpha^2+1}\right) z \end{array} \right. \\
|\alpha| > \frac{1}{\sqrt{3}} \longrightarrow & \left\{ \begin{array}{l} \nu = \nu_1(z) = \left(2\alpha + \sqrt{\alpha^2+1}\right) z \\ \nu = \nu_2(z) = \left(2\alpha - \sqrt{\alpha^2+1}\right) z \end{array} \right. \\
\alpha = \frac{1}{\sqrt{3}} \longrightarrow & \left\{ \begin{array}{l} \nu = \nu_1 = 0, \forall z \\ \nu = \nu_2(z) = \frac{4}{\sqrt{3}} z \end{array} \right. \\
\alpha = -\frac{1}{\sqrt{3}} \longrightarrow & \left\{ \begin{array}{l} \nu = \nu_1(z) = -\frac{4}{\sqrt{3}} z \\ \nu = \nu_2 = 0, \forall z \end{array} \right.
\end{array}
\tag{7.46}
$$

The condition $\Delta < 0$, associated with spirals, is fulfilled for $\nu < \nu_1$ and $\nu > \nu_2$ (see Figure 7.3). The intersections between B_S, B_H and B_N define the points O and O'. By solving a system formed by Eqs. (7.44) and (7.45), one has the (ν, z) coordinates of these points; see Table 7.1. It is easy to check that B_N also passes through the same points. Then, the corresponding λ values are determined inserting (ν, z) into Eq. (7.20). Other important points are those where the tangent to the conic B_S is vertical, like the points A and A' of Fig. 7.3. Instead of studying these points in the $\nu - z$ plane, like it has been made in the previous Section, the alternative $\nu - \lambda$ representation is preferred. The details are reported in the following Subsection.

7.4.3 Representation in the $\nu - \lambda$ plane

In this section, a representation of the curves B_S, B_H and B_N in the $\nu - \lambda$ plane is considered. The expression of each curve is obtained by replacing the corresponding

Table 7.1: Coordinates (z, ν, λ) of the points O and O', at the intersection of B_S, B_H and B_N.

	$z = r^2$	ν	$\lambda\,(>0)$
O'	$\frac{1}{2}$	$\alpha - \frac{1}{2}\sqrt{\alpha^2+1}$	$\frac{1}{2\sqrt{2}}\sqrt{1+\left(\alpha-\sqrt{\alpha^2+1}\right)^2}$
O	$\frac{1}{2}$	$\alpha + \frac{1}{2}\sqrt{\alpha^2+1}$	$\frac{1}{2\sqrt{2}}\sqrt{1+\left(\alpha+\sqrt{\alpha^2+1}\right)^2}$

definition, i.e. (7.44), (7.45) or (7.46), into Eq. (7.20) and eliminating the variable z. By this procedure, the expression associated with B_S reads:

$$27\left(1+\alpha^2\right)^2\lambda^4+\lambda^2\left(-4+\left(60\alpha\nu-36\alpha^2-36\nu^2\right)(1+\nu\alpha)-4\alpha^3\nu^3\right)+4(\alpha-\nu)^2\left(1+\nu^2\right)^2=0 \tag{7.47}$$

Observe that Eq. (7.47) can be rewritten under the form of the second order polynomial $a_1x^2 + a_2x + a_3 = 0$ in the variable $x = \lambda^2$, having the coefficients

$$\begin{aligned} a_1 &= a_1(\alpha) = 27\left(1+\alpha^2\right)^2 \\ a_2 &= a_2(\nu,\alpha) = -4+\left(60\alpha\nu-36\alpha^2-36\nu^2\right)(1+\nu\alpha)-4\alpha^3\nu^3 \\ a_3 &= a_3(\nu,\alpha) = 4(\alpha-\nu)^2\left(1+\nu^2\right)^2 \end{aligned}$$

The two real and positive roots are indicated by $\lambda_Q^2(\nu,\alpha)$ and $\lambda_P^2(\nu,\alpha)$. Their square roots read:

$$\begin{aligned} \lambda_Q(\nu,\alpha) &= \sqrt{\tfrac{1}{2a_1(\alpha)}\left(-a_2(\nu,\alpha)-\sqrt{a_2^2(\nu,\alpha)-4a_1(\alpha)a_3(\nu,\alpha)}\right)} > 0 \\ \lambda_P(\nu,\alpha) &= \sqrt{\tfrac{1}{2a_1(\alpha)}\left(-a_2(\nu,\alpha)+\sqrt{a_2^2(\nu,\alpha)-4a_1(\alpha)a_3(\nu,\alpha)}\right)} > 0 \end{aligned} \tag{7.48}$$

According to (7.48), for a given α one has $\lambda_Q(\nu,\alpha) < \lambda_P(\nu,\alpha)$. The plot of λ_P and λ_Q as functions of ν, for fixed α, gives the upper and bottom branches of the saddle-node bifurcation, respectively (see Figs. 7.7, 7.8, 7.9 and 7.10). The ν-values associated with the *cusps* A and A' at a given α derive from the condition $a_2^2 = 4a_1a_3$ (see Table 7.2). Moreover, at these points one has $\lambda_Q^2 = \lambda_P^2 = -a_2(\nu,\alpha)/(2a_1(\alpha))$ and this leads to the coordinates λ of the cusps reported in the last column of Table 7.2. The corresponding amplitudes $z = r^2$ are finally derived by using Eq. (7.44).

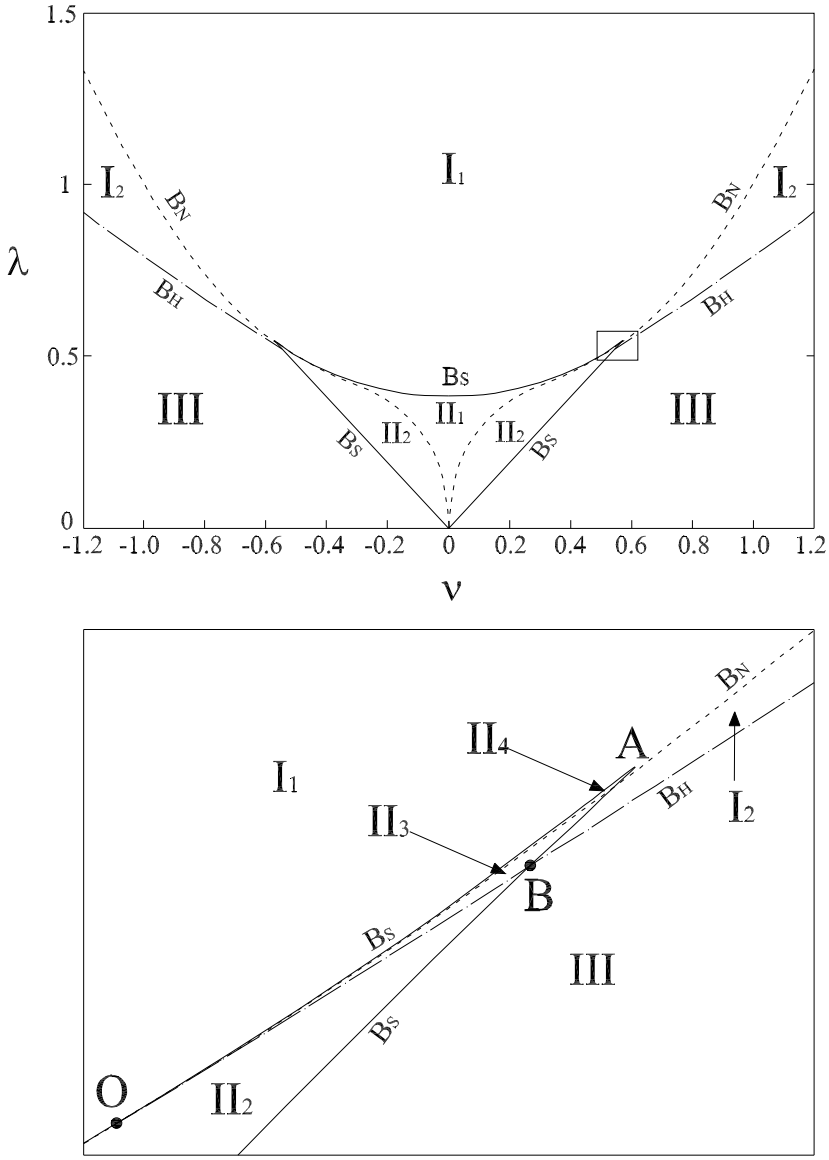

Figure 7.7: Bifurcations portraits of the MHVR oscillator in the parameter plane (ν,λ). Case α = 0. Global view and detail of the zone around the right cusp *A* of the saddle-node bifurcation B_S.

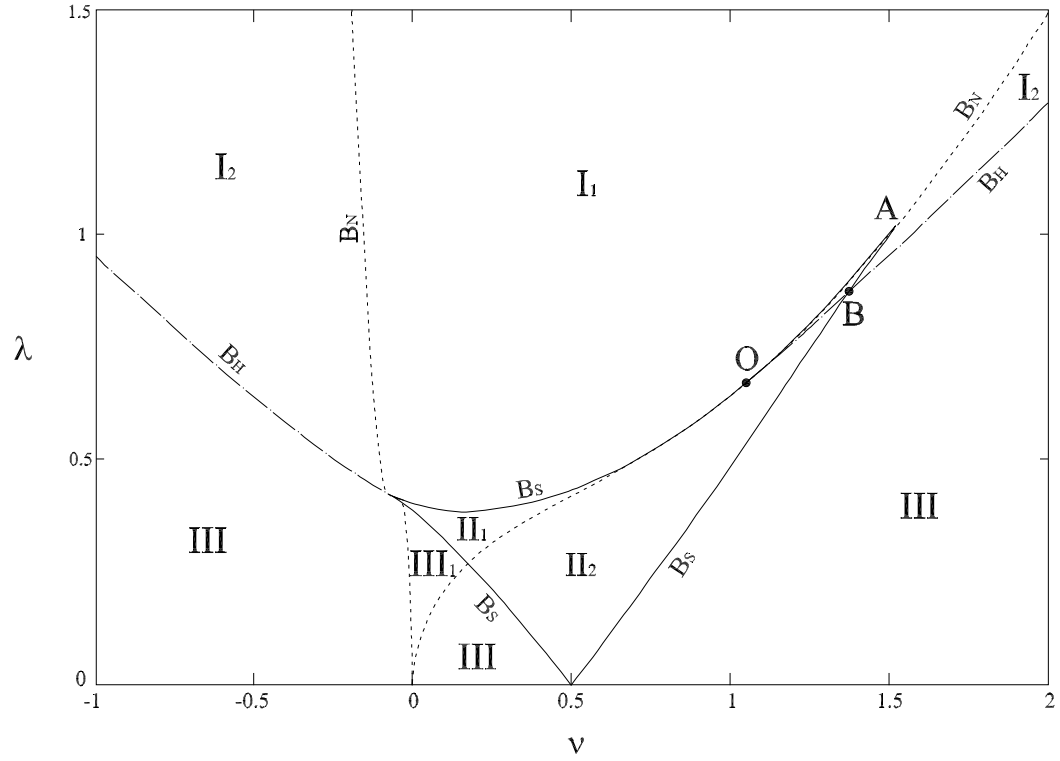

Figure 7.8: Bifurcations portraits of the MHVR oscillator in the parameter plane (ν,λ). Case α = 0.5.

Table 7.2: Coordinates z and (ν, λ) of the cusp points of the saddle-node bifurcation B_S.

		$z = r^2$	ν	$\lambda\,(>0)$
$\alpha < -\sqrt{3}$,	A :	$\frac{2}{3-\sqrt{3}\alpha}$	$\frac{1+\sqrt{3}\alpha}{\sqrt{3}-\alpha}$	$\sqrt{\frac{8\sqrt{3}}{9}\frac{\alpha^2+1}{(\sqrt{3}-\alpha)^3}}$
$\alpha = -\sqrt{3}$,	A :	$\frac{1}{3}$	$-\frac{\sqrt{3}}{3}$	$\frac{2}{3\sqrt{3}}$
$\lvert\alpha\rvert < \sqrt{3}$,	A' :	$\frac{2}{3+\sqrt{3}\alpha}$	$\frac{\sqrt{3}\alpha-1}{\alpha+\sqrt{3}}$	$\sqrt{\frac{8\sqrt{3}}{9}\frac{\alpha^2+1}{(\alpha+\sqrt{3})^3}}$
	A :	$\frac{2}{3-\sqrt{3}\alpha}$	$\frac{\sqrt{3}\alpha+1}{\sqrt{3}-\alpha}$	$\sqrt{\frac{8\sqrt{3}}{9}\frac{\alpha^2+1}{(\sqrt{3}-\alpha)^3}}$
$\alpha = \sqrt{3}$,	A' :	$\frac{1}{3}$	$\frac{\sqrt{3}}{3}$	$\frac{2}{3\sqrt{3}}$
$\alpha > \sqrt{3}$,	A' :	$\frac{2}{3+\sqrt{3}\alpha}$	$\frac{-1+\sqrt{3}\alpha}{\alpha+\sqrt{3}}$	$\sqrt{\frac{8\sqrt{3}}{9}\frac{\alpha^2+1}{(\alpha+\sqrt{3})^3}}$

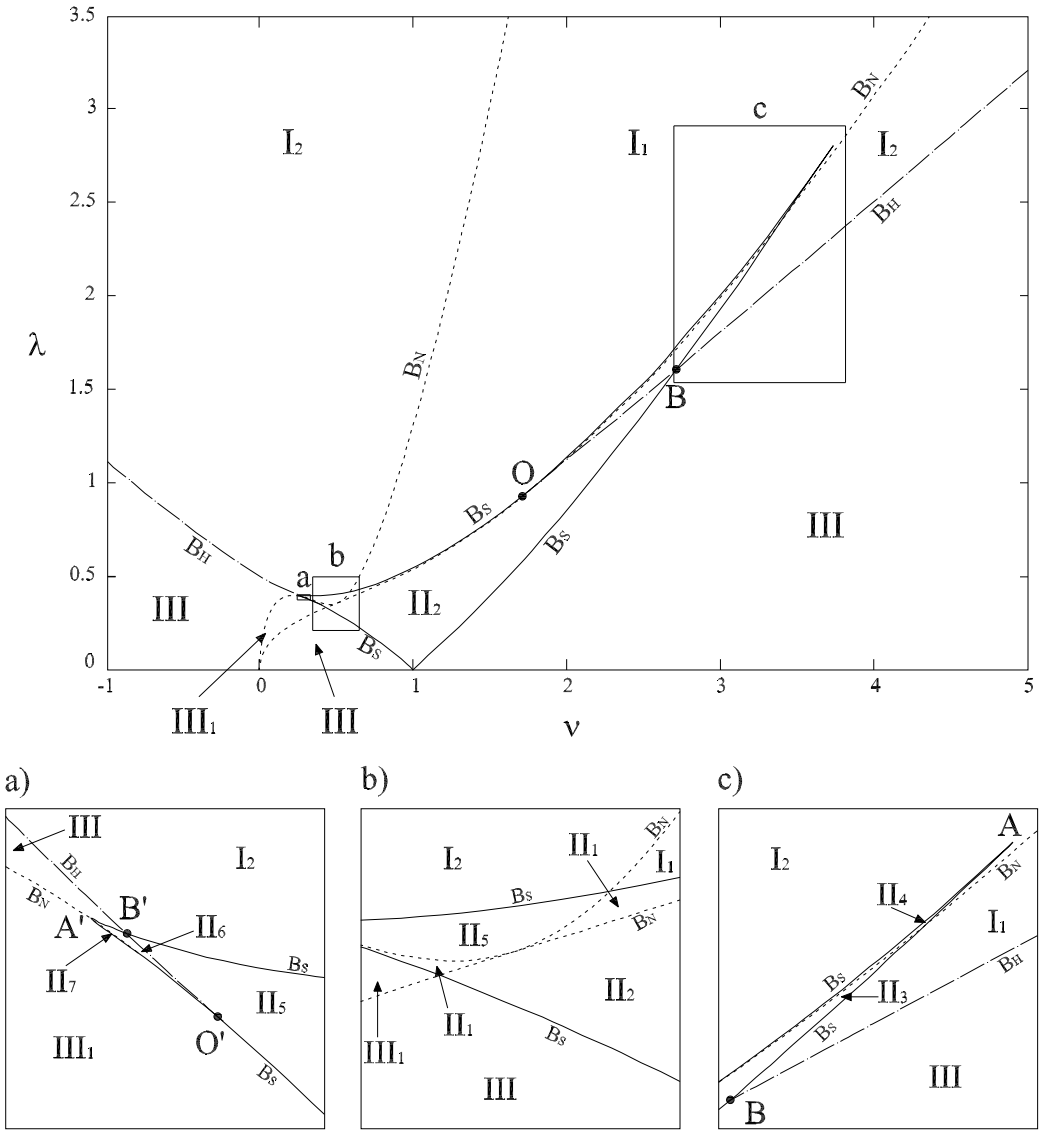

Figure 7.9: Bifurcations portraits of the MHVR oscillator in the parameter plane (ν,λ). Case α = 1. Global view and (a) detail of the zone around the left cusp of B_S; (b) detail of the zone inside B_S where the branches of the node-spiral bifurcation B_N intersect; (c) detail of the zone around the right cusp of B_S.

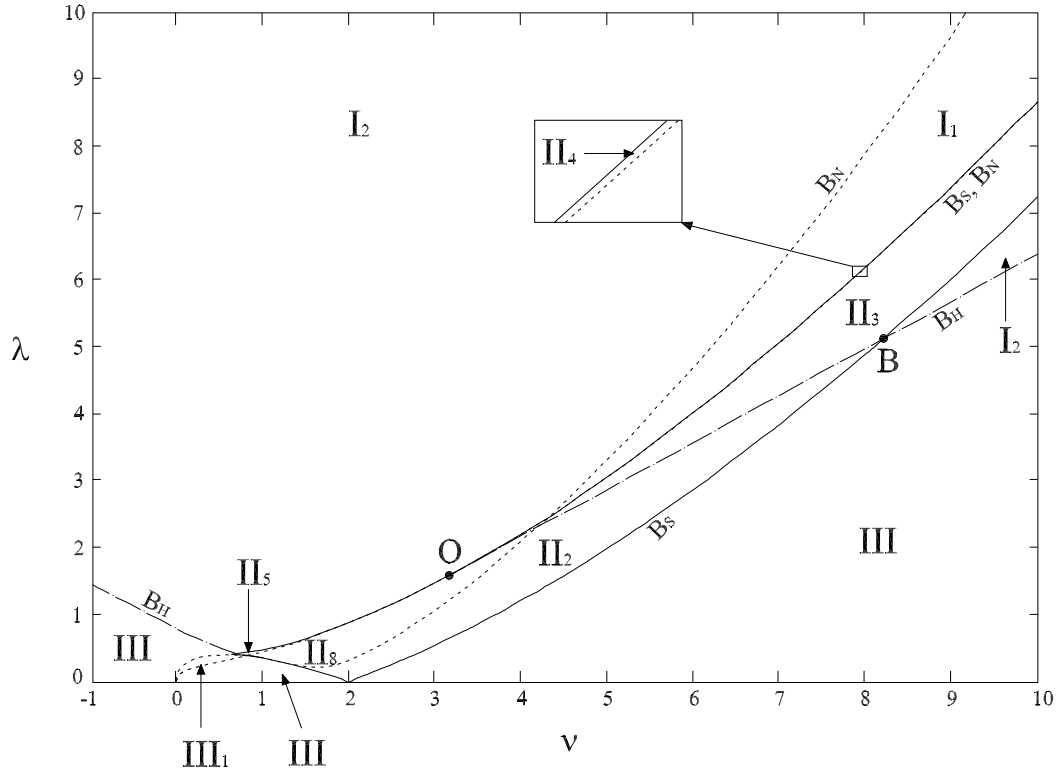

Figure 7.10: Bifurcations portraits of the MHVR oscillator in the parameter plane (ν,λ). Case α = 2.

The $\nu - \lambda$ representation of the Hopf bifurcation B_H is obtained by replacing Eq. (7.45) into Eq. (7.20). This leads to:

$$\lambda_H(\nu, \alpha) = \sqrt{\frac{1}{8} + \frac{1}{2}\left(\nu - \frac{1}{2}\alpha\right)^2} \quad \text{with } \nu < \nu_{O'} \text{ or } \nu > \nu_O \tag{7.49}$$

Moreover, by replacing Eq. (7.46) in Eq. (7.20), one obtains the node-spiral bifurcations B_N. The explicit expressions are not reported for brevity.

In the $\nu - z$ plane, there are two common points between the Hopf bifurcation B_H and the saddle-node bifurcation B_S, viz. O and/or O' (see Fig. 7.3). In the $\nu - \lambda$ plane, the curves B_H and B_S are tangent at the same points (Figs. 7.7, 7.8, 7.9 and 7.10). Moreover, in this plane B_H and B_S intersect at two other points, B and B'. In order to find their coordinates, one needs to replace Eq. (7.49) into (7.47). This leads to the following equation:

$$\frac{1}{64}\left(3\alpha^2 - 8\alpha\nu + 4\nu^2 - 1\right)^2\left(3\alpha^4 - 8\alpha^3\nu + 14\alpha^2 - 40\alpha\nu + 16\nu^2 - 5\right) = 0 \tag{7.50}$$

The first factor is null when $\nu = \alpha \pm \frac{1}{2}\sqrt{\alpha^2 + 1}$, i.e. at the points O and O'. The roots of the second factor define the abscissas of B and B':

$$\nu_{B'} = \tfrac{1}{4}\left(\alpha\left(\alpha^2 + 5\right) - \left(1 + \alpha^2\right)\sqrt{\alpha^2 + 5}\right)$$
$$\nu_B = \tfrac{1}{4}\left(\alpha\left(\alpha^2 + 5\right) + \left(1 + \alpha^2\right)\sqrt{\alpha^2 + 5}\right)$$

The corresponding λ coordinates are easily obtained by replacing the ν-values in Eq. (7.49):

$$\lambda_{B'} = \tfrac{1}{2\sqrt{2}}\sqrt{1 + \tfrac{1}{4}\left(\alpha^3 + 3\alpha - \left(\alpha^2 + 1\right)\sqrt{\alpha^2 + 5}\right)^2}$$
$$\lambda_B = \tfrac{1}{2\sqrt{2}}\sqrt{1 + \tfrac{1}{4}\left(\alpha^3 + 3\alpha + \left(\alpha^2 + 1\right)\sqrt{\alpha^2 + 5}\right)^2}$$

As it is said for an analogous situation in (Glendinning and Proctor, 1986), an important particular case occurs when α is such that the points A, O and B converge in a unique bifurcation point of codimension 3. This particular α value can be computed by imposing the equality $\nu_O = \nu_A$, with the values taken from Tables 7.1 and 7.2, respectively. This leads to

$$\alpha = -\sqrt{3}/3, \quad \nu_A = \nu_O = \nu_B = 0 \quad \text{and} \quad \lambda_A = \lambda_O = \lambda_B = 1/\sqrt{6}$$

Likewise, the points O', A' and B' coincide when

$$\alpha = \sqrt{3}/3, \quad \nu_{A'} = \nu_{O'} = \nu_{B'} = 0 \quad \text{and} \quad \lambda_{A'} = \lambda_{O'} = \lambda_{B'} = 1/\sqrt{6}$$

The values $\alpha = \pm\sqrt{3}/3$ bound the so-called *small isochronicity region* (Pikowski et al., 2001).

The curves defining the different kinds of bifurcations have been defined. Let us now analyze the regions of the $\nu - \lambda$ plane delimited by these curves. Three types of regions are distinguished:

- Type I regions: outside the saddle-node bifurcation B_S (Eq. (7.47)) and such that $\lambda > \lambda_H(\nu, \alpha)$ (Eq. (7.49)).
- Type II regions: inside the saddle-node bifurcation B_S (Eq. (7.47)).
- Type III regions: outside the saddle-node bifurcation B_S (Eq. (7.47)) and such that $0 < \lambda < \lambda_H(\nu, \alpha)$ (Eq. (7.49)).

Each point (ν, λ) of the regions of type II (for given α), is associated with *three* solutions of the form (7.6)-(7.10), i.e. three values of the squared non-dimensional amplitude $z = r^2$. Conversely, each point of the regions I and III is associated with one solution. The number of sub-regions and the nature and stability of the associated solution(s) varies with the value of the parameter α. Let us analyze the following cases:

(a) $\alpha = 0$ (see Figure 7.7 and Table 7.3). This situation corresponds to the standard Van der Pol and/or Rayleigh oscillators. It is the so-called *isochronous* case (Pikowski et al., 2001). There are two regions of type I, where each point (ν, λ) is associated with a stable node (I_1) or a stable spiral (I_2). In both regions, the entrained solution (Eq. (7.6) or (7.10)) is stable. The region III is characterized by an unstable spiral. Therefore, the entrained solution is not stable. The transition from I_2 and III occurs via the Hopf bifurcation (7.49). In the four regions of type II, each point is associated with a saddle and two other solutions, whereof at least one is stable (Table 7.3). In summary, in the regions I and II a stable entrained solution exists, while in the region III the entrained solution is unstable. The upper bounds of the region III are the lower branch of B_S ($\lambda = \lambda_Q$) and B_H, that intersect at the point B for positive ν and at B' for negative ν.

(b) $0 < |\alpha| \leq \sqrt{3}/3$. In this case, the region II is "stretched" with respect to the basic isochronous case $\alpha = 0$, with a consequent loss of symmetry with respect to

the λ-axis. The bifurcation diagram remains substantially unchanged, with the exception of the new region III_1, associated with an unstable node; see the first column of Table 7.4 and, for the particular case α = 0.5, Fig. 7.8.

(c) $\sqrt{3}/3 < |\alpha| < \sqrt{3}$. With respect to the case (b), three new regions of type II appear (see Table 7.4 and, for the particular case α = 1, Fig. 7.9). The regions II_6 and II_7 are characterized by three unstable solutions. For positive α, the left branch of the Hopf bifurcation is tangent to the lower branch λ_Q of the saddle-node bifurcation at O', while in the cases (a) and (b) it is tangent to the upper branch λ_P. The unstable domain, constituted by the regions II_6, II_7, III and III_1, is still delimited by the curves B_S ($\lambda = \lambda_Q$) and B_H, but the relevant intersection point for negative ν is O', instead of B'. An analogous situation occurs for negative α, for points O and B.

(d) $|\alpha| \geq \sqrt{3}$. In this case, the regions II_3 and II_4 become open, and the cusp A' no longer exists (see Figure 7.10, for the case α = 2). The new region II_8 appears: it contains points associated with three solutions, one of which is stable (Table 7.4). The other regions are the same as in the case (c).

Table 7.3: Description of the fixed points in the different regions of the bifurcation diagrams. First part. (s.n.=stable node; s.s.= stable spiral; sd.= saddle; u.n.= unstable node; u.s.= unstable spiral).

Region	I_1	I_2	II_1	II_2	II_3	II_4	III
p	< 0	< 0	< 0, (-), > 0	< 0, (-), > 0	< 0, (-), < 0	< 0, (-), < 0	> 0
q	> 0	> 0	$> 0, < 0, > 0$	$> 0, < 0, > 0$	$> 0, < 0, > 0$	$> 0, < 0, > 0$	> 0
Δ	> 0	< 0	$> 0, > 0, > 0$	$> 0, > 0, < 0$	$> 0, > 0, < 0$	$> 0, > 0, > 0$	< 0
	s.n.	s.s.	s.n., sd., u.n.	s.n., sd., u.s.	s.n., sd., s.s.	s.n., sd., s.n.	u.s.

$-$ for both signs

Collecting the conditions corresponding to the four cases, i.e. for all α, it is possible to distinguish the regions where there is at least a solution of the form (7.10) which

Table 7.4: Description of the fixed points in the different regions of the bifurcation diagrams. Second part. (s.n.=stable node; s.s.= stable spiral; sd.= saddle; u.n.= unstable node; u.s.= unstable spiral).

Region	III_1	II_5	II_6	II_7	II_8
p	> 0	< 0, (-), > 0	> 0, (-), > 0	> 0, (-), > 0	< 0, (-), > 0
q	> 0	$> 0, < 0, > 0$	$> 0, < 0, > 0$	$> 0, < 0, > 0$	$> 0, < 0, > 0$
Δ	> 0	$< 0, > 0, > 0$	$< 0, > 0, > 0$	$> 0, > 0, > 0$	$> 0, > 0, < 0$
	u.n.	s.s., sd., u.n.	u.s., sd., u.n.	u.n., sd., u.n.	s.s., sd., u.s.

$-$ for both signs

Table 7.5: Inequalities defining the stability domain for the entrained solutions (7.6)-(7.10) of the non-autonomous MHVR oscillator (7.5), according to the analytical approximation based on the harmonic balance method. $\lambda_Q = \lambda_Q(\alpha, \nu)$ and $\lambda_H = \lambda_H(\alpha, \nu)$ are defined by Eqs. (7.48) and (7.49), respectively.

	$\alpha < -\frac{\sqrt{3}}{3}$	$\lvert\alpha\rvert \leq \frac{\sqrt{3}}{3}$	$\alpha > \frac{\sqrt{3}}{3}$
$\lambda \geq \lambda_H$ when	$\nu \leq \nu_{B'(\alpha)}$	$\nu \leq \nu_{B'(\alpha)}$	$\nu \leq \nu_{O'(\alpha)}$
$\lambda \geq \lambda_Q$ when	$\nu_{B'(\alpha)} \leq \nu \leq \nu_{O(\alpha)}$	$\nu_{B'(\alpha)} \leq \nu \leq \nu_{B(\alpha)}$	$\nu_{O'(\alpha)} \leq \nu \leq \nu_{B(\alpha)}$
$\lambda \geq \lambda_H$ when	$\nu \geq \nu_{O(\alpha)}$	$\nu \geq \nu_{B(\alpha)}$	$\nu \geq \nu_{B(\alpha)}$

is stable, viz. synchronization occurs, and the regions where synchronization is not possible. A summary of these conditions is given in Table 7.5. This Table defines a three-dimensional stability domain in the space (ν, λ, α). Accounting for the previous discussion, the transition between stable and unstable domains occurs either *via* the Hopf bifurcation ($\lambda = \lambda_H$) or *via* the bottom branch of the saddle-node bifurcation ($\lambda = \lambda_Q$). The graphical representation of this boundary as a surface in the space (ν, λ, α) is given in Figure 7.11, where the stability region is over the surface. Actually, the representation is made with a translated $\nu-$axis, i.e. $(\nu - \alpha, \lambda, \alpha)$.

The domains described above are related with the *local* stability of the solution (7.6). However, it is well-known that some non-local bifurcations also exist for systems like Eq. (7.15); see e.g. (Glendinning and Proctor, 1986). The study of non-local bifurcations for the MHVR oscillator is beyond the purposes of this paper. One also observes that the transition between stable and unstable spirals across the Hopf bifurcation does not occur suddenly: around an unstable spiral defined by the coordinates ($x_1 = R\cos\theta, x_2 = R\sin\theta$), a limit cycle always raises Jordan and Smith (2007). If the spiral of coordinates (x_1, x_2) is close to the Hopf bifurcation, this limit cycle is small and does not envelope the origin of the plane (x_1, x_2): in this case the frequency of the solution u_y (Eq. (7.6)) is still that of the external force, but the amplitude is modulated, i.e. u_y is not of the form predicted by Eq. (7.6). This situation is sometimes called ”nearly synchronous” regime (Pikowski et al., 2001). When the spiral is far enough from the Hopf bifurcation, the limit cycle around the spiral also envelops the origin of the plane (x_1, x_2) and the frequency of the solution becomes different from that of the excitation and synchronization is completely lost. For simplicity, these two situations are not distinguished in this presentation and they are both considered as non-synchronized.

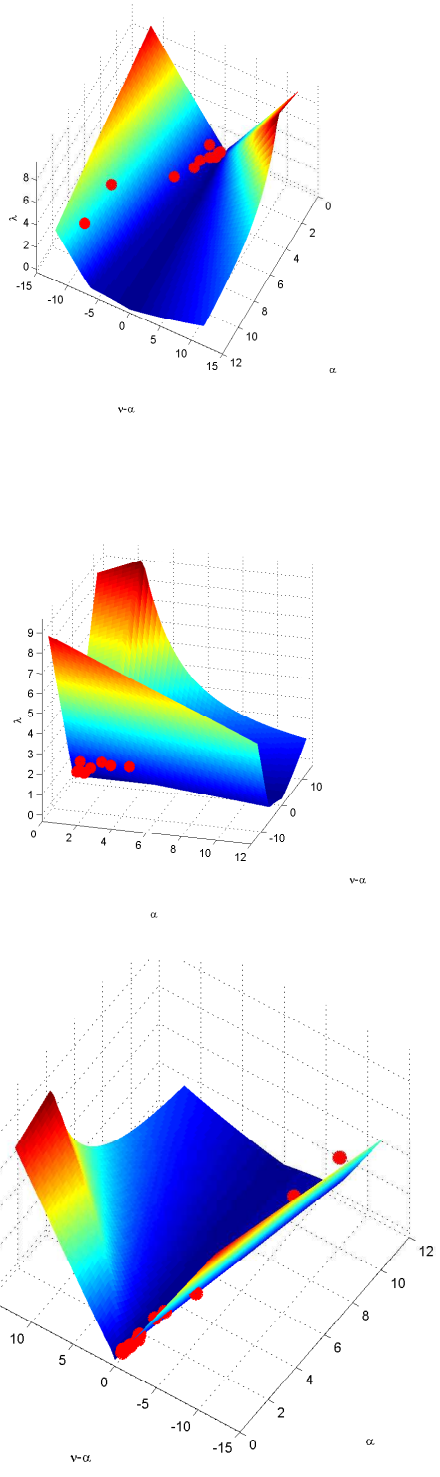

Figure 7.11: Surface representing the lower boundary of the stability domain, according to the analytical approximation defined in Table 7.5. Each point *over* the surface represents a pedestrian synchronized with the harmonically moving floor.

7.5 The use of the stability domain for predicting the pedestrian synchronization

In this Section, the theoretical notions previously discussed are used to illustrate experimental results about the lateral oscillations of pedestrians walking on a moving floor. Several studies have been performed in this situation. In particular, in (Dallard et al., 2001a; Nakamura et al., 2008; Sun and Yuan, 2008) experimental results on a shake table with *harmonic* motion are discussed and some percentages of synchronized pedestrians are found. In view of the fact that different authors used different terminology to represent or to consider the effect of synchronized pedestrians, we discuss these terminologies to correlate them. Fujino (Fujino et al., 1993) used the term 'percentage of synchronized pedestrians'. By analysing video recordings of pedestrians' head movements, he concluded that 20 percent of the pedestrians on the T-bridge were synchronized to the girder lateral vibration. Dallard (Dallard et al., 2001a) introduced the term 'probability of lock-in' or 'probability of synchronization' (Newland, 2004) based on the tests performed at Imperical college, London. A person walked along the specially built 7.2 m long platform, which could be driven laterally at different frequencies and amplitudes. The objective was to establish the probability that a pedestrian will synchronize his footfall rate to the frequency of the swaying platform (lock-in), as a function of the frequency and amplitude of the sway. Because the laboratory test included a limited number of steps (7-8), no normal walking conditions could be reproduced. Nonetheless, it was not possible to investigate the effects of psychological crowd-related factors that might influence the correlation between individuals: as a reason for lock-in to appear, there was only deck amplitude investigated at different frequencies, but the probability of lock-in might become more important due to visual and comfort issues when walking in a large crowd (Franck, 2009). Nakamura (Nakamura, 2004; Nakamura and Kawasaki, 2006) proposed a load model for the T-bridge. In that load model the coefficient k_2 is the percentage of pedestrians who synchronized the girder vibration. The value of k_2 was determined by using the results of the laboratory tests made by Dallard (Dallard et al., 2001a). In the shaking table experiment, Nakamura used terms 'rate of synchronized people' (Nakamura et al., 2008) and 'synchronization rate'(Nakamura and Kawasaki, 2009).

A person walked 'on the spot' on an oscillating shaking table, which was driven laterally at different frequencies and amplitudes. In (Nakamura and Kawasaki, 2009), Nakamura determined values of the coefficient k_2 of his load model from the shaking table tests performed in (Nakamura et al., 2008). Sun (Sun and Yuan, 2008) performed a shaking table test similar to Nakamura (Nakamura et al., 2008), however he used the term 'probability of synchronization' and gave a graphical comparison with Fujino (Fujino et al., 1993) and Dallard (Dallard et al., 2001a). The above summary indicates that different terminologies, e.g. probability of lock-in, probability of synchronization, percentage of synchronized people/pedestrians, rate of synchronized people/pedestrians and synchronization rate, used in various literature carry the similar meaning. And basically these are the graph between number ratio of synchronized people to total tested people and floor amplitude at one or more than one floor frequencies. The further concern involves in incorporating the results from lab tests to the real structures. Though all the mentioned lab tests involved only one person walking at one time, and not a crowd, synchronization tests with more people will be necessary for more realistic predictions. Here we use the term 'percentages of synchronized pedestrians' showing the number ratio of synchronized people to the total tested people in a particular excitation and walking condition.

7.5.1 Analytical viewpoint: a 3D normalized synchronization domain

Let us suppose in this Subsection that the *analytical* approximation of the synchronization domain (Table 7.5) is very close to the exact domain. According to the definition (7.5) of the MHVR oscillator, the motion of a pedestrian on a laterally moving deck is represented by the seven 'physical' parameters $\mu, \omega_0, \beta, \gamma, \delta$, A_{acc} and ω. Nonetheless, it is possible to use Eqs. (7.12) and (7.13) to reduce to *three* the number of (non-dimensional) parameters necessary and sufficient to represent a pedestrian walking on a floor with a given harmonic motion. These parameters can be thought as the coordinates of a point in the 3D (ν, λ, α) space. In the same space, the synchronization domain has been defined by the conditions collected in Table 7.5 and it has been represented in Fig. 7.11, with the translation $\nu \to \nu - \alpha$. When the point is outside this domain, i.e. it is under the surface plotted in Fig. 7.11, synchronization

cannot occur. Conversely, when the point is inside this domain, the synchronization of the pedestrian with the floor is possible. For instance, Fig. 7.11 shows twelve points, corresponding to twelve pedestrians (see (Erlicher et al., 2010), test with nominal longitudinal speed v_x = 4.5 km/h) on a laterally moving floor with A_{acc} = 0.15 m/s^2 and $f = \omega/2\pi$ = 0.75 Hz. The ratio between the number of points over the surface and the total number of points gives the synchronization percentage.

Looking at Fig. 7.11, one notices that when $\lambda = 0$ the synchronization domain touches the axis $\nu - \alpha = 0$. This indicates that also for very small excitations, synchronization is possible provided that the difference $\nu - \alpha$ is close enough to zero. In terms of dimensional parameters, $\lambda = 0$ entails $A_{acc} = 0$ according to (7.13) : it is the rigid floor condition. Moreover, it can be proven that, in terms of dimensional parameters, $\nu - \alpha = 0$ corresponds to $\omega = \omega_1$, where ω_1 is the walking frequency of the pedestrian on a rigid floor. Hence, synchronization is possible even for small excitation amplitudes, provided that the floor frequency ω is very close to ω_1. Conversely, if the difference $\nu - \alpha$ is large, the synchronization occurs only when the excitation amplitude λ is large. According to this interpretation, it makes no sense to speak about an absolute threshold value of the excitation amplitude acting on a single pedestrian, without referring to the detuning $\nu - \alpha$, correlated with the frequency difference $\omega - \omega_1$.

Fig. 7.11 as well as Figs. 7.8-7.10 show that for a given non-zero α value, the lower boundary of the stability/synchronization domain *is not an even function of* $\nu - \alpha$. Therefore, the *sign* and not only the amplitude of the frequency detuning is important. If $\alpha > 0$, the tendency to have synchronization is greater when the floor frequency is larger than the pedestrian natural frequency ($\omega - \omega_1 > 0 \Leftrightarrow \nu - \alpha > 0$). This asymmetric behaviour is correlated with the term proportional to γ in the MHVR oscillator, that is in turn proportional to α. The model identification presented in (Erlicher et al., 2010) shows that the identified values of γ are always positive and that this parameter is essential to have a good fitting of experimental lateral forces in rigid floor regime.

Concerning the test results available in the literature for the moving floor regime (e.g. (Dallard et al., 2001a; Nakamura et al., 2008; Sun and Yuan, 2008)), it is actually not easy to extract some information about the synchronization behaviour of *each single pedestrian* for different frequency detunings. The measurement results are often given under the form of percentages of synchronization, without referring to the

single individual. For this reason, it is not easy to detect this asymmetric synchronization effect. Further experimental analyses might help to get a better understanding of this aspect.

7.5.2 Analytical vs. numerical synchronization domain

The analytical approximation of the stability domain presented in the previous Subsection is insightful, *however*, the assumption made is not always fulfilled. Actually, Eqs. (7.44), (7.45), (7.46) and the relationships of Table 7.5 defining the analytical approximation of the stability domain have been obtained supposing that the solution of the forced MHVR model is of the form (7.6)-(7.10), where superharmonics components of the response are neglected. Hence, this analytical representation has to be used with caution. In order to avoid an important effect of the higher harmonics, the amplitude of the force has to be small. For the same reason, the parameters μ and α related to the nonlinear damping and the frequency detuning ν should be small (Jordan and Smith, 2007). In addition, it should not be forgotten that this domain concerns the 1:1 synchronization only (Pikowski et al., 2001).

Accounting for these remarks, a comparison between analytical predictions and numerical results is presented in Figs. 7.12, 7.13 and 7.14. Three cases are considered: (a) α = 0; (b) α = 0.5; and (c) α = 1. Each point in these figures gives the numerical estimation of the boundary of the stability domain for a given ν value. It has been obtained doing several numerical simulations at a given value of ν and modifying the λ value. In detail, Eq. (7.5) is solved with the parameters μ = 0.15, β = 1, δ = 1, ω_0 = 1; the excitation frequency ω is computed using the third identity in Eq. (7.13) for the given ν value, while γ is computed for the given α value (constant in each Figure) using the second relationship in Eq. (7.12). Finally, A_{acc} is modified according to the second identity in Eq. (7.13) in order to modify the λ value. For small λ values, the computed response is not synchronized (like in the example of Fig. 7.15a). By increasing λ, this behaviour changes at the transition across the stability domain and a solution with constant amplitude and frequency ω appears (like in the example of Fig. 7.15b). The transition value of λ, together with the given ν, defines one point. As it can be seen from Figs. 7.12, 7.13 and 7.14, the difference between analytical

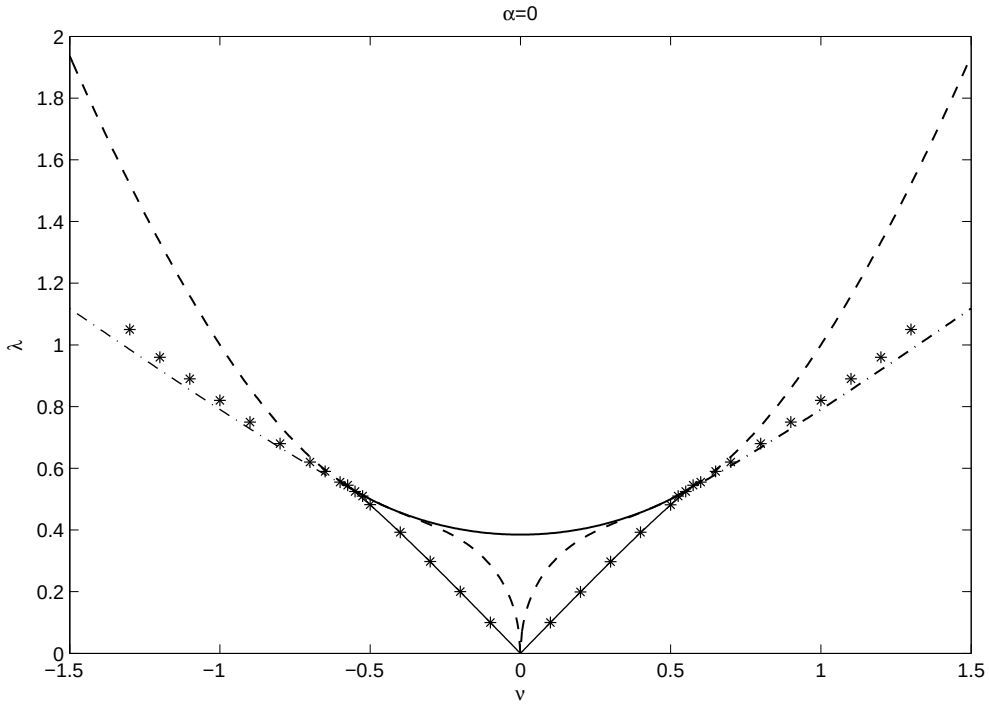

Figure 7.12: Comparison between the analytical and numerical estimations of the boundary of the stability domain of the MHVR oscillator. Case α = 0.

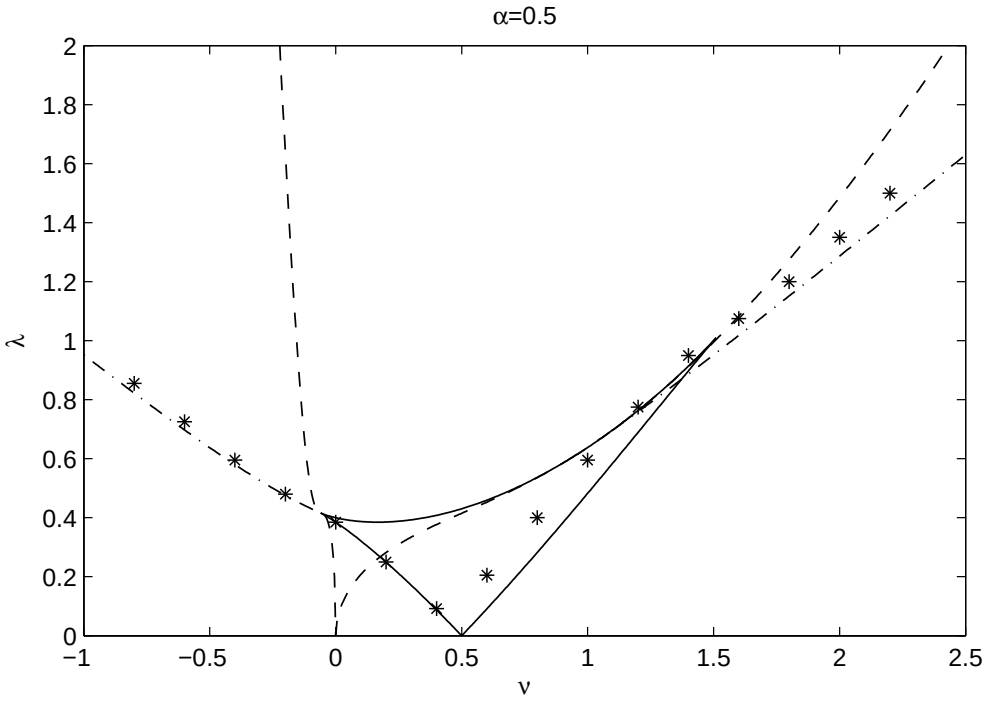

Figure 7.13: Comparison between the analytical and numerical estimations of the boundary of the stability domain of the MHVR oscillator. Case α = 0.5.

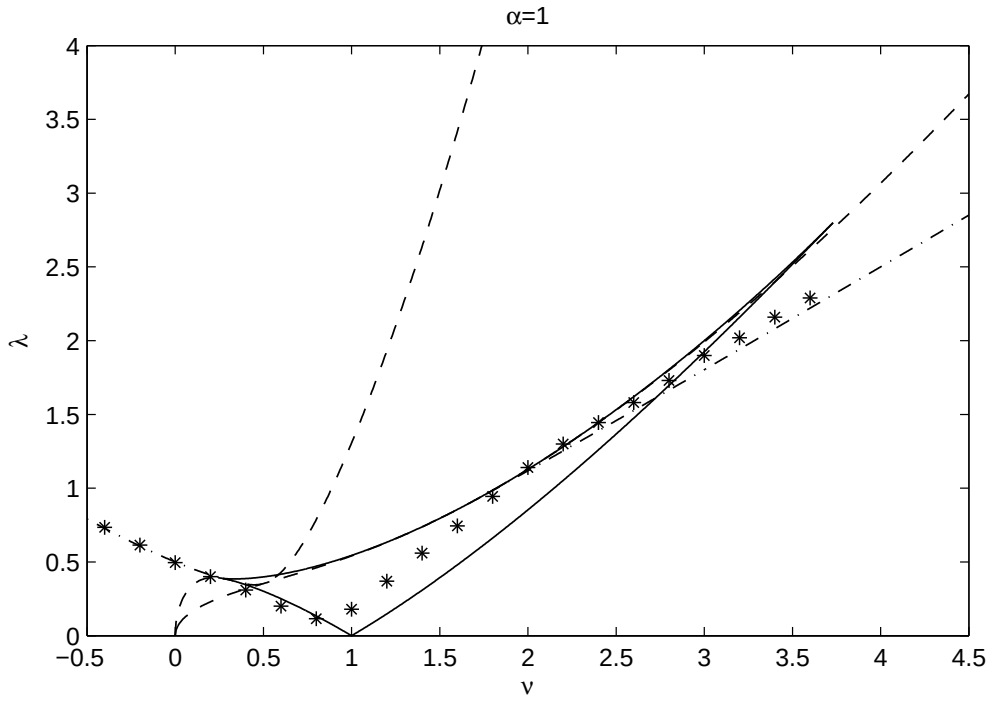

Figure 7.14: Comparison between the analytical and numerical estimations of the boundary of the stability domain of the MHVR oscillator. Case α = 1.

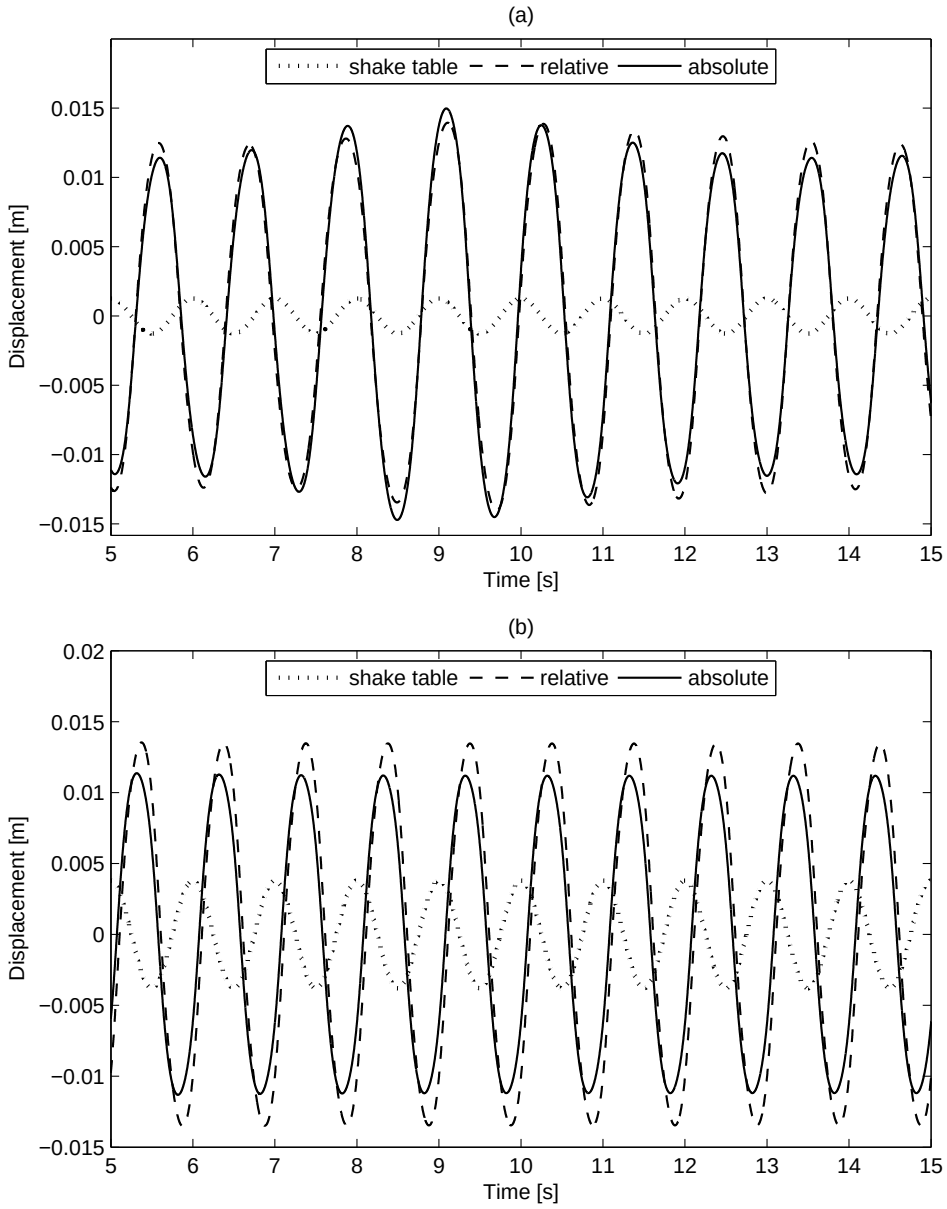

Figure 7.15: Time-evolution of the displacements of the center of mass of pedestrian "2" (v_x = 3.75 km/h Erlicher et al. (2010)) in the case of (a) *non-entrained* oscillation (A_{acc} = 0.05 m/s^2, $\omega/(2\pi)$ = 1 Hz) and (b) *entrained* oscillation (A_{acc} = 0.15 m/s^2, $\omega/(2\pi)$ = 1 Hz). u_y : relative displacement; $U_y + u_y$: absolute displacement; U_y : shake table displacement.

and numerical results is not always small, above all for the highest values of ν and α. For this reason, only the numerical results should be used for the comparison of the model predictions with the experimental results, if any.

7.5.3 Percentages of synchronization for a group of pedestrians

We consider here two populations of twelve pedestrians, represented by two groups of twelve MHVR oscillators. The parameters defining these pedestrians have been identified from *rigid floor* walking tests (Erlicher et al., 2010). Actually, the pedestrians of the first population were asked to walk on a treadmill with a nominal speed v_x = $3.75 km/h$. Each pedestrian has a natural walking frequency corresponding to this longitudinal speed. The average of the natural frequencies of this group is 0.848 *Hz* with a standard deviation of 0.055 *Hz*. The same pedestrians were also asked to walk at the nominal speed v_x = $4.5 km/h$. The average frequency in this case is 0.923 *Hz* with a standard deviation of 0.053 *Hz*.

For each oscillator/pedestrian a numerical simulation is made with an periodic excitation corresponding to a floor motion with given acceleration amplitude A_{acc} and frequency ω. The response is computed considering zero initial conditions: if a steady response with constant amplitude and frequency equal to ω is reached after a transient (see Fig. 7.15b), then the oscillator/pedestrian is considered synchronized with the floor. It is non-synchronized in the opposite case (see Fig. 7.15a). In the non-synchronized case the amplitude and frequency of the pedestrian-oscillator is varying with respect to the floor, while in the synchronized condition these parameters are constatnt.

Table 7.6 concerns the first population and shows the percentages of synchronized pedestrians for several amplitudes and frequencies of the floor motion. Table 7.7 concerns the second population, characterized by a slightly higher averaged frequency. It can be seen that the highest percentages of synchronization occur for the highest floor acceleration amplitudes and for floor frequencies close to the average value of the population.

Table 7.6: Percentages of synchronized pedestrians in a population of twelve people. The average of the natural walking frequencies of all pedestrians is $\overline{f_1}$ = 0.848 *Hz* with a standard deviation of 0.055 *Hz*.

$A_{acc}[m/s^2]$ \ f [Hz]	0.5	0.75	1.0	1.25
0.05	0/12	5/12	1/12	0/12
0.15	0/12	12/12	7/12	0/12
0.30	9/12	12/12	12/12	3/12

Table 7.7: Percentages of synchronized pedestrians in a population of twelve people. The average of the natural walking frequencies of all pedestrians is $\overline{f_1}$ = 0.923 *Hz* with a standard deviation of 0.053 *Hz*.

$A_{acc}[m/s^2]$ \ f [Hz]	0.5	0.75	1.0	1.25
0.05	0/12	0/12	5/12	0/12
0.15	0/12	10/12	11/12	0/12
0.30	9/12	12/12	12/12	7/12

7.6 Phase analysis

A phase difference during synchronized motion between pedestrian(s) and floor has already been noticed in several experimental studies, e.g. (Dallard et al., 2001a; Nakamura and Kawasaki, 2006; Nakamura et al., 2008; Sun and Yuan, 2008). The studies made on Millennium bridge by Dallard (Dallard et al., 2001a) show a linear relationship (zero phase difference) between lateral force and the local bridge velocity during synchronization. The experimental studies made on the T-bridge (Nakamura and Kawasaki, 2006) identified the synchronization phenomenon but the phase difference between the girder and the pedestrians was not clarified. In case of M-bridge (Nakamura and Kawasaki, 2006) pedestrian's lateral displacement phase during synchronization is between 120-160 degrees ahead of the girder. In the shaking table experiment by Nakamura (Nakamura et al., 2008) the phase difference between floor and pedestrian displacement during synchronization lies between 120-140 degrees with pedestrian lagging the floor. The experiment performed by Sun and Yuan (Sun and Yuan, 2008) on a shaking table shows that the synchronization occurs at a steady phase difference and finds the steady phase lag of the lateral force with respect to the displacement of shaking table with a mean value of 140.8 degrees and standard deviation of 17.9 degrees. The tests performed for three crowd densities, i.e. 0.3, 0.7 and 0.9 pedestrians/m^2 on a reinforced concrete prototype footbridge Araujo Jr et al. (2009) could not observe the synchronization phenomenon. Nevertheless, the phase angle among pedestrians was found with a mean of 90.45 degrees and standard deviation 50.74 degrees for crowd density 0.7.

The above outcomes show that some individual studies were made on different footbridges and models, each considering a different type of phase difference. In this condition, it is difficult to find a general agreement on the experimental values of the phase-difference. Nevertheless, it is easier to study all possible types of phase differences during synchronization on an analytical model. The phase difference during synchronization is an important aspect of pedestrians-structure interaction phenomenon. However, in our knowledge no detailed analysis of this problem can be found in the literature. The study presented in this Section gives a contribution to

fill this dearth, aiming to a better understanding of the pedestrians-structure interaction. The modified hybrid Van der Pol/Rayleigh (MHVR) model has been used for a theoretical study of the phase-difference.

7.6.1 Phase difference θ between relative displacement response and displacement excitation

As already mentioned in the previous section, Eq.(7.6) represents the motion of a pedestrian relative to the floor and θ represents the phase difference between the relative pedestrian displacement and the floor displacement. The analytical estimation of θ comes from Eqs. (7.20)-(7.21) after choosing the values of the non-dimensional parameters ν, λ and α. The relative phase θ has been represented in bidimesional plot $\nu - \theta$ in Fig. 7.16 for fixed α and λ values. According to our sign convention a negative value of θ indicates that the pedestrian is lagging to the floor motion by $|\theta|$ angle or with a time lag $\triangle\ t = |\theta/\omega|$, where ω is the angular frequency, and viceversa when θ is positive.

7.6.1.1 Analytical vs. numerical results

A comparison between numerical solution and the analytical phase difference predicted by Eq. (7.21) is reported in Fig. 7.16. The numerical solution is obtained for the stable entrained periodic responses by solving Eq. (7.5) by ODE23 solver in Matlab and then computing the phase of the first harmonic of the periodic response. The numerical simulations are performed with the parameters ω_0 = 1 rad/s, $\epsilon = 2\mu$ = 0.05, β = 1 m^{-2}, δ = 1 m^{-2}. The non-dimensional parameter α is taken constant (α = 1), while three values of λ are considered (λ = 0.35, λ = 1.5, λ = 2.5). As a result, for each fixed value of ν , the remaining parameters ω, A_{acc} and γ needed for numerical integration of Eq. (7.5) are computed using Eqs. (7.12)-(7.13) and the identity $A_{acc} = \omega^2 A_d$. Fig. 7.16 shows that there is a good agreement between numerical and analytical results. Actually, the good approximation obtained in this example concerns values of z less than 2.5, while λ is less than 2.5 and μ is small. The accuracy of analytical predictions diminishes for higher values of these quantities and the modulus

of α.

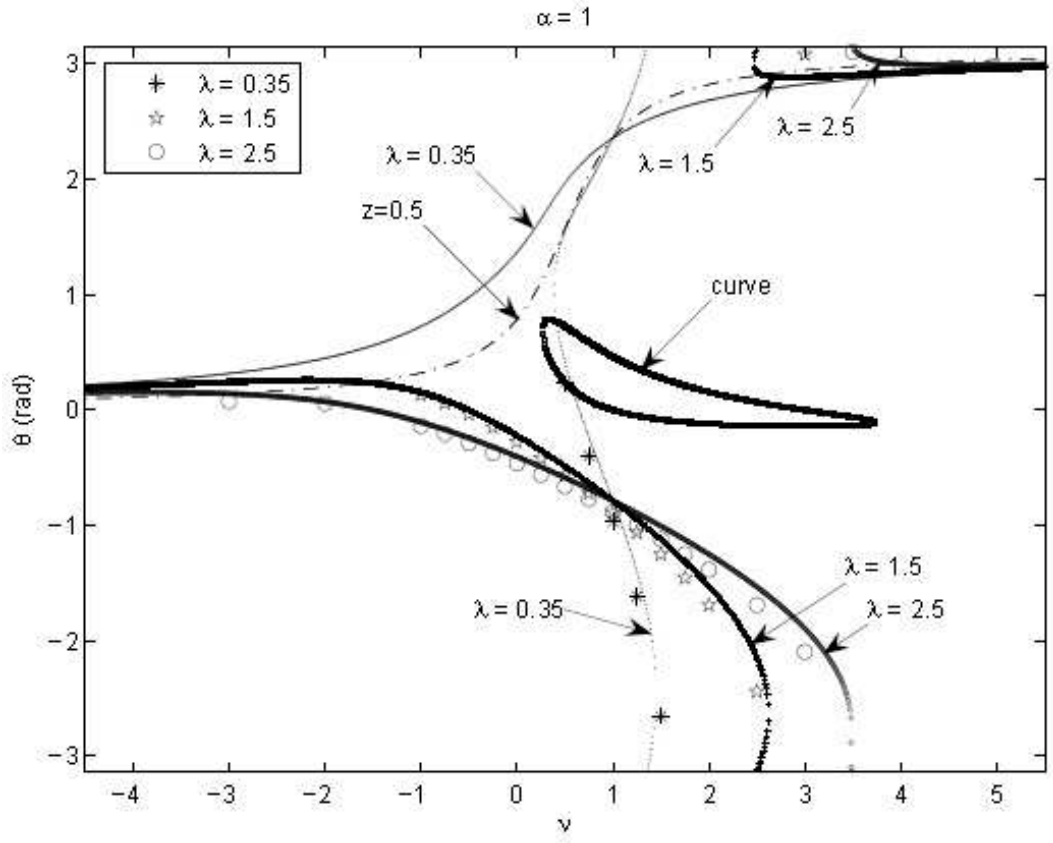

Figure 7.16: Analytical and numerical comparison of the phase difference between relative displacement response and and displacement excitation for α = 1.and λ = 0.35, 1.5 and 2.5

As θ in Eq. (7.21) is a function of z, ν and α, the number of values of θ will depend on the number of roots of $p_{\nu,\alpha,\lambda}(z)$ for any set of ν, λ and α values. In Fig. 7.16, θ is plotted between $-\pi$ and π. In addition to the phase difference (θ) curves for three λ values there is a line corresponding to $z = \frac{1}{2}$ and a close curve corresponding to Eq. (7.23). For λ = 0.35, two curves exist, one is continuous over all values of ν while another curve is continuous in a small range of ν values. For larger negative values of ν, θ is positive and approaches to a constant value regardless of the values of λ. However, θ is negative for positive and smaller negative values of ν.

7.6.2 Phase difference ϕ between absolute displacement response and displacement excitation

In this Section, another interpretation of phase is discussed in order to make an easier comparison with experimental results. According to Eq. (7.6), $u_y(t)$ has a constant amplitude and frequency and is entrained by the external excitation frequency. A solution of this kind represents a pedestrian synchronized with the floor motion. In synchronized condition, the absolute displacement of the pedestrian can be written as the sum of the (absolute) displacement of the floor and the relative displacement of the pedestrian with respect to the floor.

$$\begin{aligned} u_{yA}(t) &= U_y(t) + u_y(t) \\ &= A_d \cos(\omega t) + R\cos(\omega t + \theta) \end{aligned} \tag{7.51}$$

Using some trigonometric identities, one has

$$\begin{aligned} u_{yA}(t) &= [A_d + R\cos(\theta)]\cos(\omega t) - [R\sin(\theta)]\sin(\omega t) \\ &:= A\cos(\omega t + \phi) \end{aligned} \tag{7.52}$$

Hence, the squared absolute displacement amplitude is given by

$$A^2 = [A_d + R\cos(\theta)]^2 + [R\sin(\theta)]^2 \tag{7.53}$$

The phase is given by

$$\tan\phi = \frac{R\sin\theta}{A_d + R\cos\theta} \tag{7.54}$$

Putting the values of R and A_d from Eq.(7.13), after simplification the phase is given by

$$\tan\phi = \frac{\omega r^2(1-r^2)}{\epsilon\omega_0\lambda^2 + \omega r^2(-\nu + \alpha r^2)} = \frac{\omega z(1-z)}{\epsilon\omega_0\lambda^2 + \omega z(-\nu + \alpha z)} \tag{7.55}$$

Eq.(7.52) represents the absolute motion of the pedestrian with amplitude A and phase ϕ. The motion of the floor is represented by Eq.(7.4), having zero phase; therefore, ϕ also represents the phase difference between the absolute pedestrian

displacement and the floor displacement. According to our sign convention a negative value of ϕ indicates that the pedestrian is lagging to the floor motion by $|\phi|$ angle or with a time lag $\triangle\ t = |\phi/\omega|$, where ω is the angular frequency, and viceversa when ϕ is positive.

7.6.2.1 Analytical vs. numerical results

In this Subsection, numerical and analytical plots of the relationships $\nu - \phi$ are compared in Fig. 7.17. The same example is chosen as in the case of analytical-numerical comparison of θ. The same procedure is followed for the numerical integration and to get the first harmonic of the entrained periodic response of Eq. (7.5).

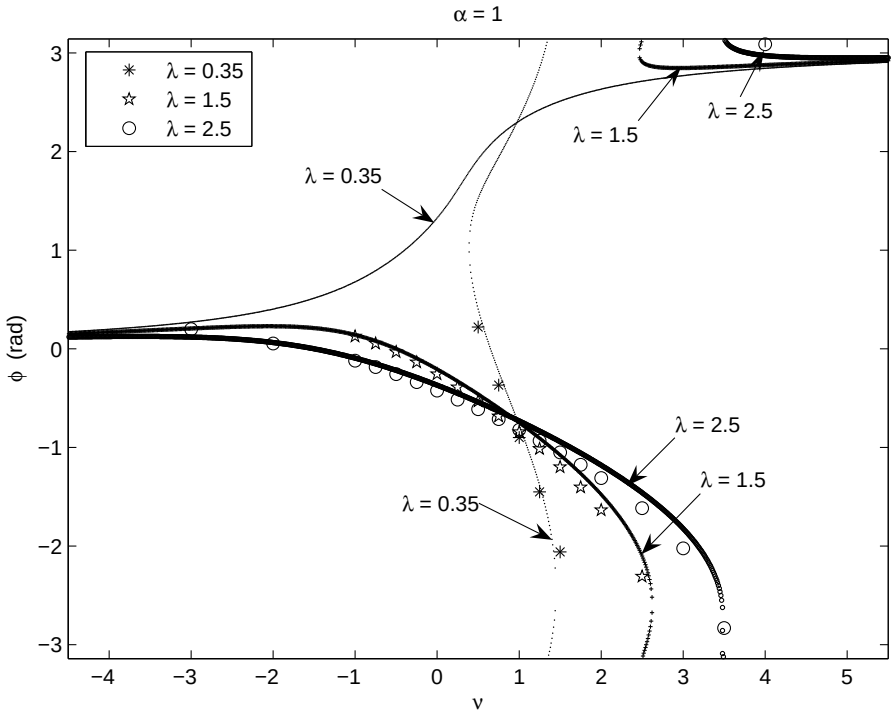

Figure 7.17: Analytical and numerical comparison of the phase difference between absolute displacement response and displacement excitation for α = 1 and λ = 0.35, 1.5 and 2.5

In Eq. (7.55), ϕ is a function of $z, \nu, \lambda, \alpha, \omega, \omega_0$ and ϵ. From Eq.(7.13) for known parameters ω_0 and ϵ; ω is a function of ν. So finally, ϕ is a function of z, ν, λ and α. The number of values of ϕ depends on the number of roots of $p_{\nu,\alpha,\lambda}(z)$ for any set of ν, λ and α values. In Fig. 7.17, ϕ is plotted between $-\pi$ and π. For λ = 0.35, two curves exist, one is continuous over all values of ν and another curve is continuous in a small range of ν values. For larger negative values of ν, ϕ is positive and approaches to a constant value regardless of the values of λ. However, ϕ is negative for positive and smaller negative values of ν.

7.6.3 Phase difference ϕ_{vf} between restoring force and external excitation (floor) velocity

In this Section, another interpretation of phase is discussed: the phase difference between force and floor velocity. In case of pedestrians-footbridge behaviour, this phase is often considered as the most significant in experimental testings (Dallard et al., 2001a; Nakamura and Kawasaki, 2006). Accounting for Eqs. (7.2), (7.4) and (7.6), the lateral force applied by the walker on the moving floor is given by

$$\begin{aligned} F_y(t) &= F_y\left(u_y(t), \tfrac{du_y}{dt}(t)\right) = m\left(-\tfrac{d^2U_y(t)}{dt^2} - \tfrac{d^2u_y(t)}{dt^2}\right) = m\left(\omega^2 A_d \cos(\omega t) - \tfrac{d^2u_y(t)}{dt^2}\right) \\ &= m\left(\omega^2 A_d \cos(\omega t) + R\omega^2 \cos(\omega t + \theta)\right) \end{aligned} \tag{7.56}$$

Using some trigonometric identities, one has

$$\begin{aligned} F_y(t) &= m\left[\omega^2 A_d + R\omega^2 \cos(\theta)\right]\cos(\omega t) - m\left[R\omega^2 \sin(\theta)\right]\sin(\omega t) \\ &:= C_{1,dyn}\cos\left(\omega t + \phi_{1,dyn}\right) \end{aligned} \tag{7.57}$$

Hence, the squared force amplitude is given by

$$C_{1,dyn}^2 = \left(m\,\omega^2\right)^2\left([A_d + R\cos(\theta)]^2 + [R\sin(\theta)]^2\right) \tag{7.58}$$

The phase is given by

$$\tan\phi_{1,dyn} = \frac{m\omega^2 R\sin\theta}{m\omega^2 A_d + m\omega^2 R\cos\theta} = \frac{R\sin\theta}{A_d + R\cos\theta} = \tan\phi \tag{7.59}$$

Hence,

$$\phi_{1,dyn} = \phi \tag{7.60}$$

By definition, $\phi_{1,dyn}$ represents the phase difference between the lateral force and the floor displacement and according to Eq.(7.60), it is equal to the phase difference (ϕ) between absolute pedestrian displacement and the floor displacement. According to our sign convention a negative value of $\phi_{1,dyn}$ indicates that the lateral force is lagging to the floor displacement by $|\phi_{1,dyn}|$ angle or with a time lag $\triangle\ t = |\phi_{1,dyn}/\omega|$, where ω is the angular frequency, and viceversa when $\phi_{1,dyn}$ is positive.

The floor velocity, $V_y(t)$ is given by one time differentiation of floor displacement $U_y(t) = A_d \cos(\omega t)$.

$$V_y(t) = A_d \omega \cos\left(\omega t + \frac{\pi}{2}\right) \tag{7.61}$$

The phase difference between the lateral force and the floor velocity reads

$$\phi_{vf} = \phi_{1,dyn} - \frac{\pi}{2} = \phi - \frac{\pi}{2} \tag{7.62}$$

According to our sign convention the negative value of ϕ_{vf} indicates that the lateral force is lagging to the floor velocity by $|\phi_{vf}|$ angle or with a time lag $\triangle\ t = |\phi_{vf}/\omega|$, where ω is the angular frequency, and viceversa when ϕ_{vf} is positive.

7.6.3.1 Analytical vs. numerical results

In this Subsection, numerical and analytical plots of the relationships $\nu - \phi_{vf}$ are compared in Fig. 7.18. The same example is chosen as in the case of analytical-numerical comparison of θ and ϕ. The same procedure is followed for the numerical integration of the entrained periodic response of Eq. (7.5). The value of the total lateral force is obtained from Eq. (7.3). The numerical counterpart of $F_y(t)$ defined in Eq. (7.57) has been obtained by extracting the first harmonic of the total lateral force using the Fourier series definition.

In Fig. 7.18, ϕ_{vf} is plotted between $-\pi$ and π for the same three values of λ i.e.$\lambda = 0.35, 1.5$ and 2.5. For larger negative values of ν, ϕ_{vf} approaches to a constant negative value regardless of the values of λ. For the MHVR model with the parameters of Fig. 7.18, ϕ_{vf} is never null for a stable entrained periodic response.

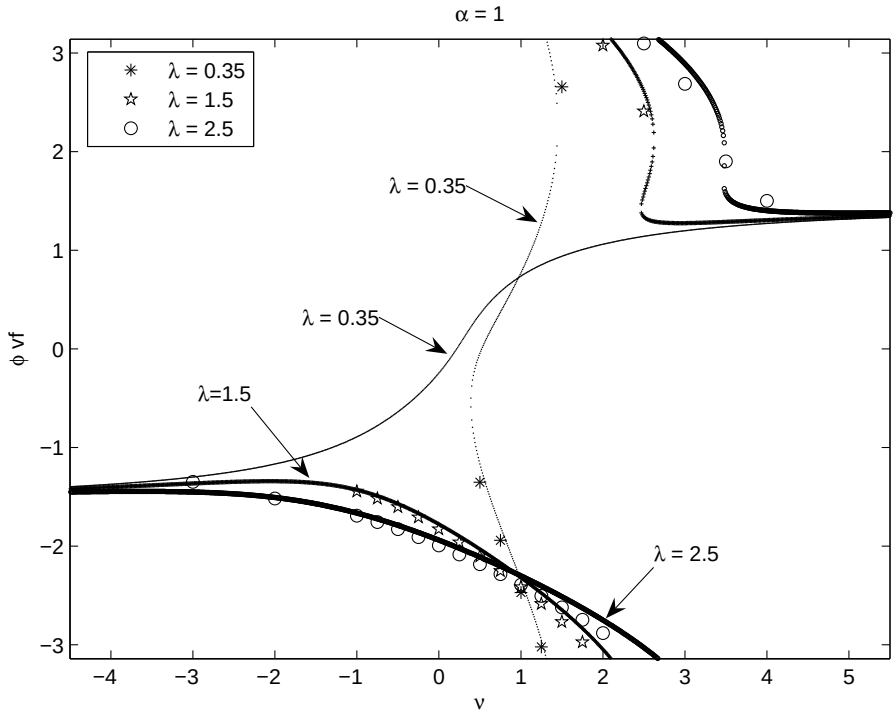

Figure 7.18: Analytical and numerical comparison of phase difference between lateral force and floor velocity. For α = 1.and λ = 0.35, 1.5 and 2.5

In this Section, we present the numerical results showing the effect of variation of excitation (floor) frequency and amplitude on phase and amplitude of the motion of the MHVR oscillator. The MHVR parameters are those defined for pedestrian "2" and shown in Table 7.8 (Erlicher et al., 2010).

Table 7.8: Model parameters for the two MHVR pedestrians

Pedestrian No.	$\omega_0 \ [rad/s]$	μ	$\beta \ [m^{-2}]$	$\gamma \ [m^{-2}]$	$\delta \ [m^{-2}]$	m [kg]
"2" Erlicher et al. (2010)	4.622	0.5536	4780	7420	3430	68.1
"5" Erlicher et al. (2010)	4.27	0.3775	0	4180	2390	72.4
"a" Nakamura et al. (2008)	-	-	-	-	-	81.5

Fig. 7.19(a) shows that the absolute values of the phase differenc ϕ are larger at high frequencies and smaller at low frequencies for all amplitudes.

Fig. 7.19(b) shows that the force-velocity phase difference ϕ_{vf}, at large amplitudes, tends towards a unique value for all frequencies, for instance $\mid \phi_{vf} \mid \rightarrow$ about 115 degrees in this case. By virtue of Eq. (7.62) also ϕ tends towards a constant value. This means that at large excitation amplitudes; the phase difference becomes independent of the synchronized frequency. Fig. 7.19(c) shows that the relative amplitude ratio R/A_d is larger at low frequencies and smaller at high frequencies. The ratio R/A_d increases almost linearly with amplitude A_d at almost same slope for all the considered frequencies. Fig. 7.19(d), shows that the absolute amplitude ratio A/A_d is larger at low frequencies and smaller at high frequencies. However, at large floor amplitudes A_d, the ratio A/A_d tends towards a unique value for all frequencies, for instance about 1.2 in this case. It means that at larger excitation amplitudes; amplitude ratio becomes independent of the synchronized frequency.

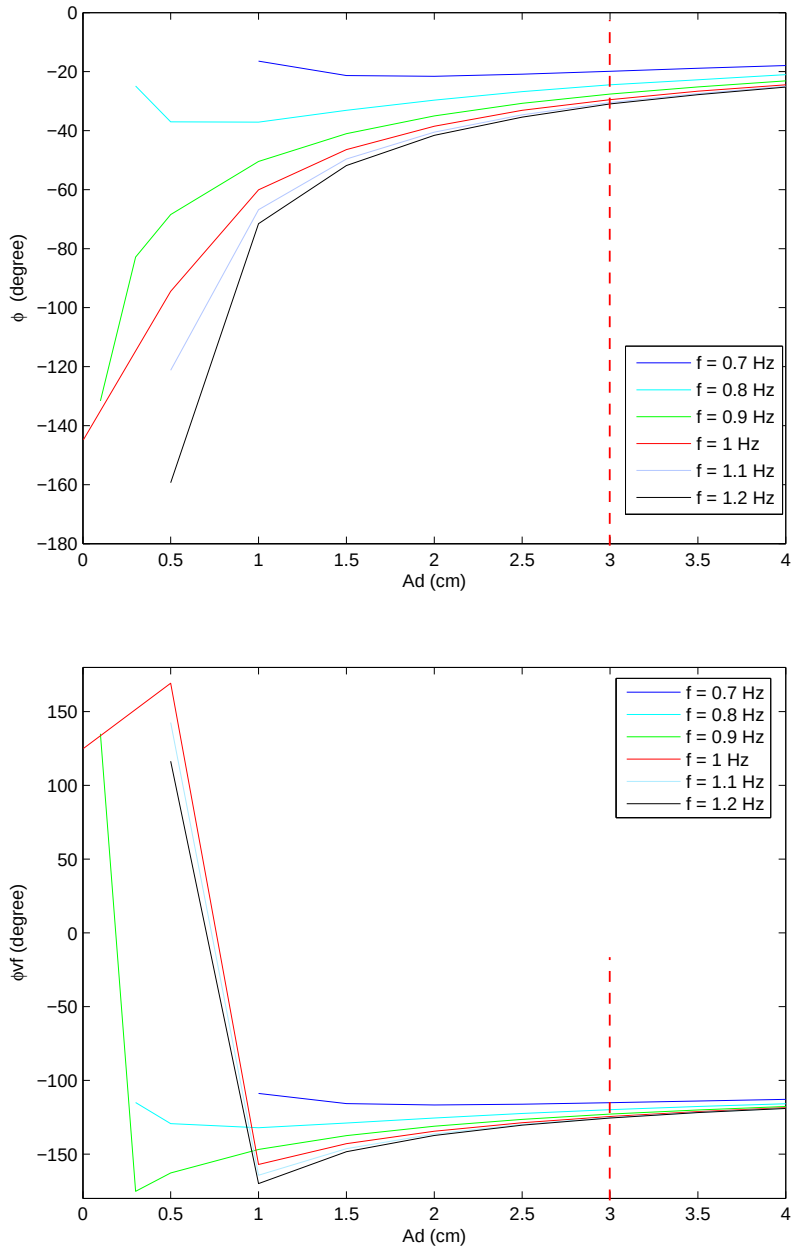

Figure 7.19: Pedestrian ”2”- effect of varying frequency (f) and amplitude (A_d) on (a) ϕ (b) ϕ_{vf}

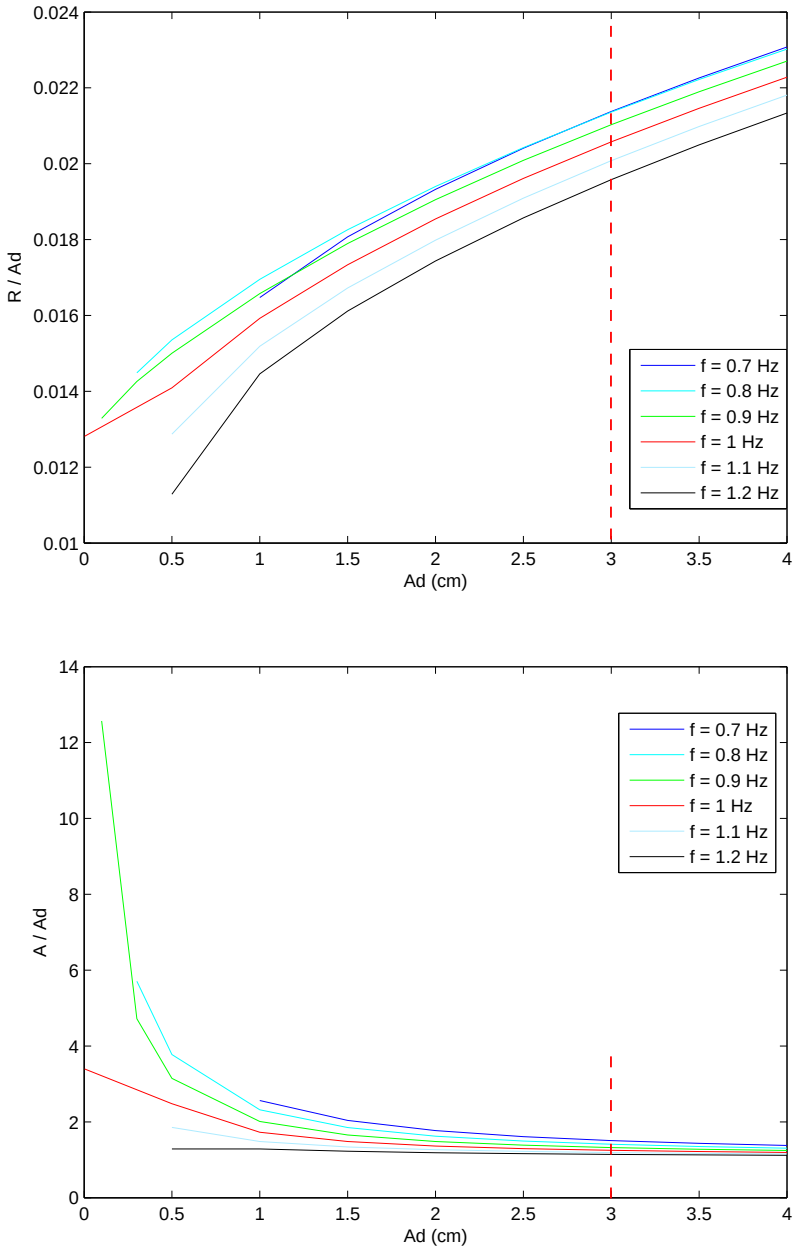

Figure 7.19: Pedestrian ”2”- effect of varying frequency (f) and amplitude (A_d) on (c) R/A_d (d) A/A_d

In the Section 7.6, it has been illustrated the phase variations as a function of ν and λ and shown by some examples that the analytical and numerical solutions are under good agreements in certain intervals of ν, α and λ. In order to make a comparison with the experimental results available in the literature (Nakamura et al., 2008; Sun and Yuan, 2008), the model behaviour is represented by the numerical solutions.

In the shaking table experiment of Nakamura (Nakamura et al., 2008), a pedestrian walked on the spot on a reaction plate (0.8 m wide and 0.5 m long) put on a shaking table (1.5 m wide and 1 m long) under harmonic motion of known amplitude and frequency. In the numerical solution, the floor motion amplitude and frequency are chosen as 3 cm and 1 Hz respectively, only in this case a comparison is possible with experimental data of Nakamura (Nakamura et al., 2008). Table 7.8 presents the MHVR model parameters of the two (no. 2 and 5) out of 12 pedestrians observed in the rigid floor case at the walking speed 3.75 m/s (Erlicher et al., 2010). The numerical results of the same two pedestrians are plotted in Figs. 7.20 and 7.21 respectively, and presented in Table 7.9. In Figs. 7.20 and 7.21, the contours of the plots are similar to the shaking table experiment (Nakamura et al., 2008) with the lateral force containing superharmonics and both the pedestrians lagging the floor.

In the shaking table experiment of Sun and Yuan (Sun and Yuan, 2008), the steady phase lag between the lateral pedestrian force and the displacement of shaking table during synchronization was found with a mean value of 140.8 degrees and standard deviation of 17.9 degrees. In the MHVR model, this phase difference is denoted as $\phi_{1,dyn}$ and defined by Eqs. (7.59) and (7.60). According to Eq. (7.60), $\phi_{1,dyn}$ must be equal to the phase difference (ϕ) between absolute pedestrian displacement and the floor displacement. In the Nakamura's experiment (Nakamura et al., 2008) ϕ is between 120-140 degrees. In Table 7.9, the maximum amplitude ratio$\left(A/A_d\right)$ is very close to that of Nakamura (Nakamura et al., 2008), but the phase difference(ϕ) is smaller and the force to weight ratio$\left(F_{\max}/mg\right)$ is larger. The reason behind this, according to our view, is that the pedestrians in both the cases are not the same. The parameters of MHVR model were not identified for the pedestrian walking on the

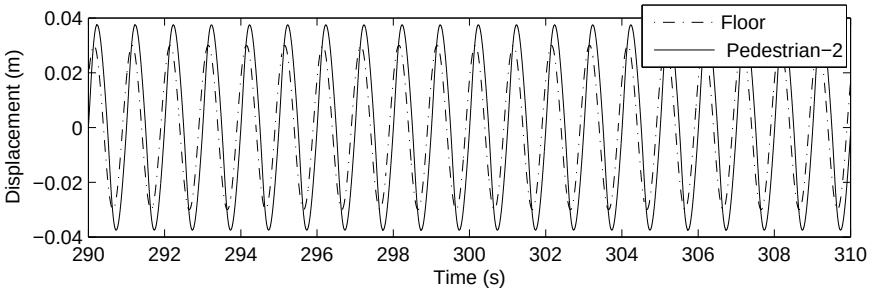

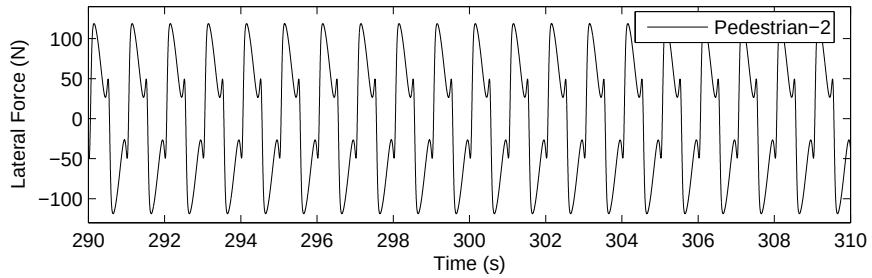

Figure 7.20: Displacement and force-time plot for pedestrian no. ”2” at floor excitation amplitude 3 cm and frequency 1 Hz

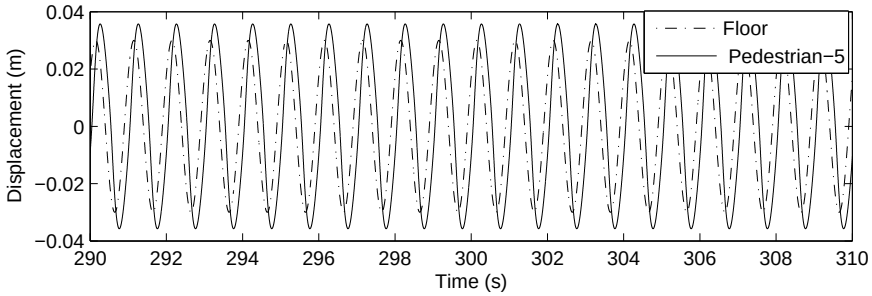

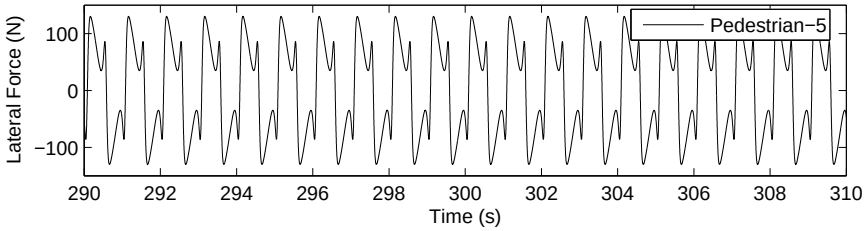

Figure 7.21: Displacement and force-time plot for pedestrian no. ”5” at floor excitation amplitude 3 cm and frequency 1 Hz

shake table, but for a different person walking on a rigid floor because exploitable experimental data were available only in this case (Erlicher et al., 2010). Therefore, more experiments are sought on the shaking table with the same pedestrians as used in the numerical model.

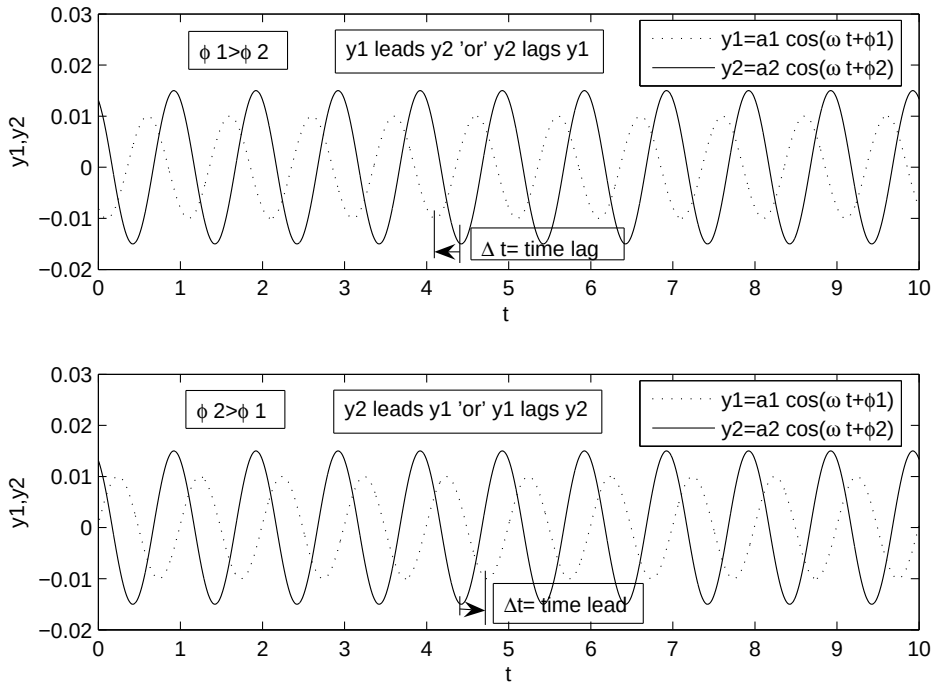

Figure 7.22: Phase sign convention- Case(1) y1 leads y2 Case(2) y2 leads y1

Table 7.9: Comparison of numerical and experimental results

Pedestrian No.	ϕ [*degrees*]	A/A_d	F_{max} [N]	F_{max}/m [m/s^{-2}]	$F_{max}/(mg)$
”2” Erlicher et al. (2010)	-29.43	1.25	119.63	1.757	0.179
”5” Erlicher et al. (2010)	-42.32	1.19	131.21	1.812	0.185
”a” Nakamura et al. (2008)	-120	1.33	85	1.042	0.106

7.9 Conclusions

In this Chapter, an approach where the lateral pedestrian oscillations during walking are modelled by a self-sustained oscillator was presented. This MHVR oscillator is a new extension of the classical Van der Pol/Rayleigh model. The non-autonomous case is analyzed here with particular emphasis on the stability and phase of the entrained response. The theoretical analysis and a comparison with numerical results are presented. In detail, the amplitude, stability and phase of the MHVR oscillator solution under a harmonic external force associated with the floor motion is analytically evaluated by the harmonic balance method and compared with numerical results. It is shown that the phase difference tends to become constant at high excitation (floor) amplitude. The numerical results of MHVR oscillator have been compared with the experimental results on a shake table with harmonic floor motion. There is a good agreement in amplitude ratio. The phase difference evaluated by the MHVR model is lower than the experimental value. A possible reason might be that, the parameters of MHVR model were not identified for the pedestrian walking on the shake table, but for a different person walking on a rigid floor. Experimental data on both rigid and moving floor conditions for the same person are necessary to clarify the differences.

CHAPTER 8

SUMMARY, CONCLUSIONS AND FUTURE PERSPECTIVES

8.1 Summary

This thesis dealt with several issues crucial to the performance of cable-stayed footbridges. In particular, it focussed on the: i) investigation of the effectiveness of the vibration reduction system in a complex cable-stayed footbridge characterised by two curved decks; ii) model updating of the 'Ponte del mare' cable-stayed footbridge in Pescara, Italy; iii) nonliner-identification of stay cables; and iv) modeling the synchronous lateral excitation phenomenon in a pedestrian-footbridge interaction.

A passive control system, already designed, was installed to avoid premature aeroelastic instability and to control human-induced vibrations on a recently built cable-stayed footbridge, i.e. the 'Ponte del mare' in Pescara, Italy. The complex dynamic behaviour and the uncertainties related to the numerical modelling led to a modal testing campaign of the bridge without and with dampers. Output-only ambient and free decay vibration tests were chosen based on the state-of-the-art presented in chapter 3. Output-only ambient vibration tests, associated with low vibration levels, showed that the damping devices were basically inactive. Free decay tests, which were performed by released masses, did produce high vibration levels. In the latter tests, dampers showed a good absorption capacity and the damping doubled or even trebled on some of the modes. In order to clarify these outcomes, modal quantities were instantaneously calculated, based on time-frequency identification techniques.

The modal properties estimated from the modal testing campaign did not match

that of the numerical model. In order to get a robust FE model capable to simulate the actual behaviour of the footbridge, a model updating was performed. Firstly, the initial FE model was modified considering the changes during construction. The major changes were: the use of lightened concrete in the cyclic deck; the use of five different thicknesses of concrete in the pedestrian deck; additional short and long diagonals in the two decks. Moreover, the modified model considered some issues that were left out in the initial model. In a greater detail considerations were made to: the contribution of the two side blocks; of the presence of metal steel sheeting; the concrete present between the outlines of the metal steel sheeting and different thicknesses of the paving; variation of the section of the tubular mast along its length and the concrete inside; mass of the metallic plates at the junction in the deck; the and refinement of the model at the two supports. Then, the tensions in the stay cables were updated by an iterative procedure to match that obtained from the experiment. These were the characteristics of the model ready for updating. The modified model also showed discrepancies in the modal properties with respect to experimental values. In order to perform the updating, the sensitivity-based MU technique and Powell's Dog-Leg method of optimisation based on the Trust-Region approach were used. The sensitivity matrix was calculated and the nine most sensitive parameters were selected. The sensitive parameters were the elastic modulii of the concrete and steel, the densities of the two types of concrete, and the C coefficients of the two decks. Then, the automatic updating was performed in the Ansys Parametric Design Language (APDL). The model was updated for nine frequencies. Eventually, the applicability of the updated model was examined by simulating the behaviour of the footbridge in a recorded high wind loading.

The revealed cable-deck interaction phenomenon was a motivation to investigate in depth the dynamics of long stay cables. Therefore, efforts were made towards the identification of the nonlinear behaviour of stay cables from measured response data. Although, there are several nonlinear identification methods available, non-parametric methods of polynomial form were used owing to their advantages. In view of the fact that the actual measured data contained the response of a MDoF system, the first step in this direction was to investigate the functionality of the nonlinear identification methods for a SDoF cable system. Due to the lack of experimental data for the SDoF

cable response, a simple numerical model of the in-plane cable element with zero initial sag was get in the ANSYS structural software. To get the SDoF response, the model was reduced to a SDoF system, by applying a harmonic force in the first modal frequency and the first mode shape. In doing so, we assumed that the system was weakly nonlinear and that most of the energy was in the primary resonance associated to the first mode. Consequently, data were forced to fit the model of a weakly nonlinear SDoF system. In this manner, distortions due to the discrepancy between the assumed model and the actual structure were perceived as noise in the optimisation procedure.

Approaching towards a more complete understanding of the performance of cable-stayed footbridges, it was realized that the modern footbridges are more prone to pedestrian-induced vibrations that, eventually, degrades their serviceability performance. In the case of the 'Ponte del mare' footbridge, the undergoing monitoring results disclosed the acceleration levels exceeding comfort level for some running competitions consisting of about 800 participants. Moreover, several researchers tried to investigate the problem of synchronous lateral excitation of footbridges; but there is no general consensus on the models already reviewed in the state-of-the-art chapter 2. Therefore, in the last part of the thesis, an effort was made to model the pedestrian-footbridge interaction phenomenon. A pedestrian was considered as a self-sustained oscillator represented by a modified hybrid Van der Pol/Rayleigh (MHVR) model. In detail, the amplitude, stability and the phase of the MHVR oscillator solution under a harmonic external force associated with the floor motion was analytically evaluated by the harmonic balance method and compared with numerical results. Moreover for an illustrative purpose, a comparison was made between numerical and experimental results available in the literature.

8.2 Conclusions

Major conclusions are summarised herein.

An amplitude dependent behaviour of the passive damper system of the ‘Ponte del mare’ of Pescara was found both with the output-only ambient vibration and free decay tests. In order to clarify these outcomes, modal quantities were instantaneously calculated, based on time-frequency identification techniques. A thorough analysis of dynamic response signals revealed that the structure with dampers actually behaved like a threshold system: i) for low vibration levels the dampers were still, so that they performed as constraints that stiffen the structure; ii) for high vibration levels, the dampers became fully working. Moreover, a deck-cable interaction between one of the longest cables and the first global mode was detected.

Initially, the modal properties estimated from dynamic tests did not match those of the numerical model. In order to have a robust FE model capable to simulate the actual behaviour of the footbridge, model updating was performed. The sensitivity-based model updating techniques and Powell’s Dog-Leg method of optimisation based on the Trust-Region approach were used. The final updated model showed a considerable reduction of errors relevant to frequencies. The updated model was also able to reproduce the response of the footbridge under actual wind conditions.

The proposed non-parametric method exhibited a good capability in the nonlinear parameter identification of a SDoF cable. Only a cubic-type of nonlinearity was identified. The quadratic type of nonlinearity was not present due to zero initial-curvature or sag. Moreover, an increase of the parameter related to damping and a decrease of the parameter relevant to linear-frequency were observed versus the loading amplitude. However, the values of the parameters stabilised at higher load amplitudes. Superharmonics were present in the response at higher loading amplitudes. However, the major challenges in the application of the proposed identification method was the computational burden related to the calculation both of the solution of the polynomial equation and of the Short Time Fourier Transform (STFT) at each instant of time.

A model of pedestrian-footbridge interaction was proposed. In detail, a pedestrian was represented by a modified hybrid Van der Pol/Rayleigh (MHVR) self-sustained oscillator. Amplitude, stability and phase of the MHVR oscillator solution under a harmonic external force associated with the floor motion was analytically evaluated by the harmonic balance method and was compared with numerical results. It was

shown that the phase difference tended to become constant at high excitation amplitudes. Moreover, the stability domain was found useful in predicting the precentage of pedestrians synchronized to a given oscillating floor. The numerical results of MHVR oscillator was, then, compared with the experimental result of a shake table with harmonic floor motion. A good agreement in amplitude ratio was found; however, the phase difference resulted to be underestimated by the MHVR model.

8.3 Future perspectives

As presented in the previous sections, the research analysed in depth only some aspects related to the performance of cable-stayed footbridges. We believe that this effort was worthy. Although, the investigation was focussed on the 'Ponte del mare' cable-stayed footbridge, we believe that the numerical and analytical tools developed are robust and applicable to other analogous structures.

The following future developments are envisioned relevant to the investigated subjects.

1. In view of the fact that the 'Ponte del mare' is complex, we performed the model updating in the most feasible manner; however, there are several issues still open. The following factors could be taken into account in the relevant FE model:

i) the FE model considered a smooth curvature for the cycle deck according to the drawing, but in reality it looks distorted. An accurate measurement of the distortion in the deck geometry and its implementation in the FE model can be worthwhile.

ii) Bolts and plates in the deck joints were not modelled in detail. They could alter the stiffness and damping properties.

iii) The connection of each stay cable to the deck was not modelled in detail.

iv) The deck covering elements were not modelled.

v) The modelling of the wind and pedestrian actions is difficult and needs further refinements.

vi) The FE model considered wind direction orthogonal to the deck surface, but in

reality, the wind direction might be inclined to the surface.

vii) Flutter derivatives were estimated assuming wind direction orthogonal to the bridge; however, in reality, the wind direction might be inclined.

viii) The model updating was carried out without considering dampers, but the footbridge is connected with dampers. Therefore, an additional model updating is suggested.

2. With regard to the nonlinear identification of stay cables, the proposed method should be applied to experimental data. The long term perspective could be to develop an identification method based on a MDoF system.

3. In the case of pedestrian-footbridge interaction the following developments are possible:

i) to study the phase equation obtained from the MHVR model and to correctly define the parameters appearing within this equation from experiments (lateral motion).

ii) A systematic comparison of predictions with those of French, British and European standards.

iii) To couple this phase equation with a particle model (the crowd as a set of particles with given interaction rules), in order to simultaneously model the pedestrian-footbridge interaction (and possible synchronization) and the crowd motion (with pedestrian-pedestrian interactions and possible synchronization) in case of lateral motion.

iv) After the phase equation for the pedestrian, it is important to propose an amplitude equation describing the amplitude variation of a pedestrian under the external force (lateral motion).

v) To study the pedestrian-footbridge interaction owing to vertical oscillations in order to account for vertical and torsional modes.

BIBLIOGRAPHY

A.M. Abdel-Ghaffar and M.A. Khalifa. Importance of cable vibrations in dynamics of cable-stayed bridges. *Journal of Engineering Mechanics*, 117 (11):2571–2589, 1991.

A.M. Abdel-Ghaffar and A.S. Nazmy. 3-d nonlinear seismic behavior of cablestayed bridges. *Journal of Structural Engineering*, 117 (11):3456–3476, 1991.

D.M. Abrams. *Two coupled oscillator models: the Millennium Bridge and the chimera state*. PhD thesis, Cornell University, Ithaca, NY, 2006.

G. Achs and C. Adam. Control of vibration prone cable-stayed bridges under construction by tuned liquid column dampers. In *22nd DANUBIA-ADRIA Symposium on Experimental Methods in Solid Mechanics*, Monticelli Terme / Parma, Italy, 2005.

Poulimenos A.G. and Fassois S.D. Output-only stochastic identification of a time-varying experimental structure via functional series tarma models. *Mechanical Systems and Signal Processing*, 234:11801204, 2008.

A.A. Al-Qaisia and M.N. Hamdan. On the steady state response of oscillators with static and inertia non-linearities. *Journal of Sound and Vibration*, 223 (1):49–71, 1999.

A.A. Al-Qaisia and M.N. Hamdan. Bifurcations and chaos of an immersed cantilever beam in a fluid and carrying an intermediate mass. *Journal of Sound and Vibration*, 253 (4):859–888, 2002.

M. Al-Qassab and S. Nair. Wavelet-galerkin method for free vibrations of elastic cable. *J. Eng. Mech. Div.*, 129:350357, 2003.

M. Al-Qassab and S. Nair. Wavelet-galerkin method for the free vibrations of an elastic cable carrying an attached mass. *J. Sound Vib.*, 270:191206, 2004.

Algalink. Appoggi in gomma armata. Technical report, Alga technical thinking, 2009.

H.M. Ali and A.M. Abdel-Ghaffar. Modeling the nonlinear seismic behavior of cable-stayed bridges with passive control bearings. *Computers & Structures*, 54 (3): 461–492, 1995.

R.J. Allemang. The modal assurance criterion (mac) twenty years of use and abuse. In *IMAC XX*, Los Angeles, CA, U.S.A., 2002.

R.J. Allemang and D.L. Brown. A unified matrix polynomial approach to modal identification. *Journal of Sound and Vibration*, 211:301322, 1998.

R.J. Allemang and A.W. Phillips. The unified matrix polynomial approach to understanding modal parameter estimation: an update. In *Proceedings of the International Seminar on Modal Analysis ISMA*, Leuven, 2004.

S. Anusas, A.J. Notkus, and Z. Kamaitis. Stabilization of vibrations of footbridges. In *9th International Conference on Modern Building Materials, Structures and Techniques*, Vilnius, Lithuania, May 1618 2007.

M.C. Araujo Jr, H.M.B.F. Brito, and R.L. Pimentel. Experimental evaluation of synchronisation in footbridges due to crowd density. *Structural Engineering International*, 3, 2009.

W. C. Arrol and S. Chatterjee. Implications of the rules on bridge design-past and future. In *Proceedings of conference at Institution of Civil Engineers*, London, March 25-26 1981.

H. Auweraer Van Der. Testing in the age of virtual prototyping. In *Proceedings of International Conference on Structural Dynamics Modelling*, Funchal, 2002.

H. Bachmann. Lively footbridges - a real challenge. In *Proc. Footbridge*, Paris, 2002.

H. Bachmann and W. Ammann. Vibrations in structures- induced by man and machines. In *Structural Engineering Documents*, volume 3e (2), Zrich, 1987. IABSE.

M. Baruch and I.Y. Bar-Itzhack. Optimal weighted orthogonalization of measured modes. *AIAA Journal*, 16(4):346–351, 1978.

C.E. Bauby and A.D. Kuo. Active control of lateral balance in human walking. *J Biomech*, 33:14331440, 2000.

E. Bedrossan and S.O. Ricand. The output properties of volterra systems driven by harmonic and gaussian inputs. In *Proceedings IEEE*, volume 59, pages 1688–1707, 1971.

A. Belli, P. Bui, A. Berger, A. Geyssant, and J.R. Lacour. A treadmill ergometer for three-dimensional ground reaction forces measurement during walking. *J Biomech*, 34(1):105112, 2001.

S. Bellizzi and M. Defilippi. Non-linear mechanical systems identification using linear systems with random parameters. *Mechanical Systems and Signal Processing*, 17: 203210, 2003.

F. Benedettini and G. Rega. Nonlinear dynamics of an elastic cable under planar excitation. *Int. J. Non-Linear Mech.*, 22:497509, 1987.

F. Benedettini, G. Rega, and R. Alaggio. Nonlinear oscillations of a four-degree-of freedom model of a suspended cable under multiple internal resonance conditions. *J. Sound Vib.*, 182:775798, 1995.

Friswell M.I. Benhafsi Y., Penny J.E. A parameter identification method for discrete nonlinear systems incorporating cubic stiffness elements. *Journal of Analytical and Experimental Modal Analysis*, 7:179195, 1992.

A. Berman and E.J. Nagy. Improvement of large analytical model using test data. *AIAA Journal*, 21(8):1168–1173, 1983.

S.A. Billings and K.M. Tsang. Spectral analysis for nonlinear systems, part i: parametric non-linear spectral analysis. *Mechanical Systems and Signal Processing*, 3: 319–339, 1989a.

S.A. Billings and K.M. Tsang. Spectral analysis for nonlinear systems, part ii: interpretation of nonlinear frequency response functions. *Mechanical Systems and Signal Processing*, 3:341–359, 1989b.

S.A. Billings, H.B. Jamaluddin, and S. Chen. Properties of neural networks with applications to modelling non-linear dynamical systems. *International Journal of Control*, 55:193224, 1991.

A.N. Blekherman. Swaying of pedestrian bridges. *Journal of Bridge Engineering*, 10(2):142–150, 2005.

A.N. Blekherman. Autoparametric resonance in a pedestrian steel arch bridge: Solferino bridge, paris. *Journal of Bridge Engineering*, 12 (6):669676, 2007.

J. Bodgi, P. Argoul, and S. Erlicher. Lateral vibration of footbridges under crowd-loading: continuous crowd modelling approach. *Key Engineering Materials*, 347: 685–690, 2007.

P. Bonato, R. Ceravolo, and A. De. Stefano. Time-frequency and ambiguity function approaches in structural identification. *Journal of Engineering Mechanics*, 12: 12601267, 1997.

C. Borri and R. Hffer. Aeroelastic wind forces on flexible bridge girders. *Meccanica*, 35:1–28, 2000.

R. Brincker and N. Moller (eds.). In *Proceedings of the 2nd International Operational Modal Analysis Conference IOMAC*, Copenhagen, 2007.

R. Brincker, L. Zhang, and P. Andersen. Modal identification from ambient response using frequency domain decomposition. In *Proc. of the 18th International Modal Analysis Conference*, Kissimmee, USA, 2001.

J.M.W. Brownjohn and P.. Xia. Dynamic assessment of curved cable-stayed bridge by model updating. *Journal of Structural Engineering*, 126(2), 2000.

J.M.W. Brownjohn, J. Lee, and B. Cheong. Dynamic performance of a curved cable-stayed bridge. *Engineering structures*, 21:1015–1027, 1999.

J.M.W. Brownjohn, P. Xia, H. Hao, and Y. Xia. Civil structure condition assessment by fe model updating: methodology and case studies. *Finite Elements in Analysis and Design*, 37:761–775, 2001.

D. Bruno, F. Greco, and P. Lonetti. Dynamic impact analysis of long span cable-stayed bridges under moving loads. *Engineering Structures*, 30:11601177, 2008.

J.J. Burgess and M.S. Triantafyllou. The elastic frequencies of cables. *J. Sound Vib.*, 120:153165, 1988.

O.S. Bursi, M. Molinari, R. Ceravolo, G.V. Demarie, L.Z. Fragonara, and S. Erlicher. Non-linear identification of a benchmark steel-concrete composite structure subjected to pseudo-dynamic tests. In *14th ECEE Conference*, Ohrid, Republic of Macedonia, 30 Aug-3 Sep, 2010.

O.S. Bursi et al. Identification of the damage evolution in a benchmark steel-concrete composite structure during pseudo-dynamic testing. In *Proceedings of Compdyn*, Rhodes, 2009.

B. Caesar. Update and identification of dynamic mathematical models. In *IMAC IV*, Las Vegas, 1986.

E. Caetano, A. Cunha, and C.A. Taylor. Investigation of dynamic cable-deck interaction in a physical model of a cable-stayed bridge part i: modal analysis. *Earthquake Engineering and structural Dynamics*, 29:481–498, 2000.

E. Caetano, A. Cunha, V. Gattulli, and R. Lepidi. Cabledeck dynamic interactions at the international guadiana bridge: On-site measurements and finite element modeling. *Structural Control and Health Monitoring*, 2008. DOI: 10.1002/stc.241.

F.J. Carrin-Viramontes, J.A. Lpez-Lpez, J.A. Quintana-Rodrguez, and A. Lozano-Guzmn. Nonlinear assessment of cable vibration in a stayed bridge. *Experimental Mechanics*, 48:153–161, 2008.

J. R. Casas. Full-scale dynamic testing of the alamillo cable-stayed bridge in sevilla (spain). *Earthquake Engineering and Structural Dynamics*, 24:35–51, 1995.

J.R. Casas and A.C. Aparicio. Rain-wind-induced cable vibrations in the alamillo cable-stayed bridge (sevilla, spain). assessment and remedial action. *Structural and Infrastructure Engineering*, 6(5):549–556, 2010.

R. Ceravolo. Use of instantaneous estimators for the evaluation of structural damping. *Journal of Sound and Vibration*, 274:385–401, 2004.

R. Ceravolo. *Time-frequency analysis (eds. Boller, C., Chang, F.K. & Fujino, Y.)*, chapter Encyclopedia of Structural Health Monitoring. Wiley & Sons Ltd, Chichester, UK, 2009.

R. Ceravolo, G.V. Demarie, and S. Erlicher. Instantaneous identification of degrading hysteretic oscillators under earthquake excitation. *Structural Health Monitoring*, 0(0):1–18, 2010.

C.C. Chang, M. Gu, and K.H. Tang. Tuned mass dampers for dual-mode buffeting control of bridges. *Journal of Bridge Engineering*, 8(4), 2003.

Masri S.F. Chassiakos A.G. Modelling unknown structural systems through the use of neural networks. *Earthquake Engineering and Structural Dynamics*, 25:117128, 1996.

A. Chatterjee and N.S. Vyas. Non-linear parameter estimation through volterra series using the method of recursive iteration through harmonic probing. *Journal of Sound and Vibration*, 268:657–678, 2003.

L.K. Chedjou, J.C.and Kana, K. Moussa, I. and. Kyamakya, and A. Laurent. Dynamics of a quasiperiodically forced rayleigh oscillator. *Journal of Dynamic Systems, Measurement and Control*, 3 (128):600–607, 2006.

S.H. Cheng and D.T. Lau. Modeling of cable vibration effects of cable-stayed bridges. *Earthquake Engineering and Engineering Vibration*, 1 (1):ID: 1671–3664(2002)01–0074–12, 2002.

K. Christodoulou, E. Ntotsios, C. Papdimitriou, and P. Panetsos. Structural model updating and prediction variability using pareto optimal models. *Computer Methods in Applied Mechanics and Engineering*, 198:138–149, 2008.

L. Cohen. *Time-Frequency Analysis*. Prentice-Hall PTR, Inc., Englewood Cliffs, New Jersey, 1995.

A. Cunha and E. Caetano (eds). In *Proc. of the experimental vibration analysis for civil engineering structures EVACES07 conference*, FEUP, Porto, 2007.

A. Cunha, E. Caetano, and R. Delgado. Dynamic tests on a large cable-stayed bridge. an efficient approach. *Journal Bridge Engineering*, 6(1):54–62, 2001.

A. Cunha, E. Caetano, F. Magalhaes, and C Moutinho. From input-output to output-only modal identification of civil engineering structures. *SAMCO Final Report*, 2006.

A. Cunha, E. Caetano, and F. Magalhaes. Output-only dynamic testing of bridges and special structures. *Structural Concrete*, 8(1), 2007.

T.B. Dack, F. Hoffmeistert, and H.P. Schwefel. A survey of evolutionary strategies. In *Proceeding of the international conference of Genetic Algorithms*, San Diego, 1991.

P. Dallard, A.J. Fitzpatrick, A. Flint, S. Le Bourva, A. Low, R.M. Ridsdill Smith, and M. Willford. The london millennium footbridge. *The Structural Engineer*, 79 (22): 19–33, 2001a.

P. Dallard, A.J. Fitzpatrick, A. Flint, A. Low, R.M. Ridsdill Smith, M. Willford, and M. Roche. London millennium bridge: pedestrian-induced lateral vibration. *Journal of Bridge Engineering*, 6 (6):412–417, 2001b.

G.V. Demarie, R. Ceravolo, and A. De Stefano. Instantaneous identification of polynomial nonlinearity based on volterra series representation. *Key Engineering Materials*, 293-294:703–710, 2005a.

G.V. Demarie, R. Ceravolo, and A. De Stefano. Instantaneous identification of rigid bodies on nonlinear support based on volterra series representation. In *2nd International Conference on Structural Health Monitoring and Intelligent Infrastructure Ou, Li & Duan (eds), Taylor & Francis Group*, Shenzhen, Guangdong, 16-18 November 2005b.

G.V. Demarie, R. Ceravolo, D. Sabia, and P. Argoul. Experimental identification of beams with localized nonlinearities. *Journal of Vibration and Control*, 0(0):1–12, 2010.

X. Du and F. Wang. New modal identification method under the non-stationary gaussian ambient excitation. *Appl. Math. Mech*, 30(10):12951304, 2009.

B. Eckhardt, E. Ott, S.H. Strogatz, D.M. Abrams, and A. McRobie. Modeling walker synchronization on the millennium bridge. *Physical Review E*, 75:021110, 2007.

F. Ehsan and R. H. Scanlan. Damping stay cables with ties. In *Proceedings of the 5th U.S.-Japan Bridge Workshop*, 1990.

S. Erlicher and P. Argoul. Modal identification of linear non-proportionally damped systems by wavelet transform. *Mechanical Systems and Signal Processing*, 21: 13861421, 2007.

S. Erlicher, A. Trovato, and Argoul P. Modeling the lateral pedestrian force on a rigid floor by a self-sustained oscillator. *Mechanical Systems and Signal Processing*, 24: 1579–1604, 2010.

D. J. Ewins. *Modal testing theory and practice*. Research Studies Press LTD, UK, 2000.

Y. Fan and C.J. Li. Non-linear system identification using lumped parameter models with embedded feedforward neural networks. *Mechanical Systems and Signal Processing*, 16:357372, 2002.

H.J. Farran. Wind & earthquake response in very long span cable-stayed and suspension bridges. `http://www.csupomona.edu/ jis/1999/farran.pdf`, 1999.

C.R. Farrar, T.A. Duffey, P.J. Cornwell, and S.W. Doebling. Excitation methods for bridge structures. In *Proc. of the 17th International Modal Analysis Conference*, Kissimmee, FL, Feb 1999.

S. D. Fassois and J. E. Lee. On the problem of stochastic experimental modal analysis based on multiple-response data, part ii: the modal analysis approach. *Journal of Sound and Vibration*, 16(11):57–87, 1993.

A.J. Felber and C.E. Ventura. Frequency domain analysis of the ambient vibration data of the queensborough bridge main span. In *14th International Modal Analysis Conference, Dearborn*, Dearborn, Michigan, February 12-15 1996.

M. Feldman. Nonlinear system vibration analysis using the hilbert transformi. free vibration analysis method freevib. *Mechanical Systems and Signal Processing*, 8: 119127, 1994a.

M. Feldman. Nonlinear system vibration analysis using the hilbert transformi. forced vibration analysis method forcevib. *Mechanical Systems and Signal Processing*, 8: 309318, 1994b.

M. Feldman. Non-linear free vibration identification via the hilbert transform. *Journal of Sound and Vibration*, 208:475489, 1997.

M. Feldman and S. Braun. Identification of non-linear system parameters via the instantaneous frequency: application of the hilbert transform and wignerville technique. 1995.

O. Flamand. Rain/wind-induced vibration of cables. In *Proceedings of the International Conference on Cable-Stayed and Suspension Bridges (AFPC)*, Deauville, France, 2 October 1994.

H. Forsterling and P. Furtner. Applications of hydraulic actuators for damping and isolation of structural oscillations. In *Third European Conference on Structural Control 3ECSC*, Vienna, Austria, July 12-15 2004.

L. Franck. Synchronous lateral excitation of footbridges. In *cole polytechnique fdrale de Lausanne (EPFL)*, Lausanne, Switzerland, February 2009.

M.I. Friswell and J.E. Mottershead. *Finite Element Model Updating in Structural Dynamics*. Kluwer Academic Publishers, 1995.

Y. Fujino, B.M. Pacheco, S. Nakamura, and P. Warnitchai. Synchronization of human walking observed during lateral vibration of a congested pedestrian bridge. *Earthquake Engineering & Structural Dynamics*, 22 (9):741–758, 1993.

J.P. Fuzier and J. Stubler. The normandie bridge stays. In *Conference on cable-stayed and suspension bridges*, 1994.

V. Gattulli, A. Paolone, and G. D'Amore. Nonlinear quadratic interactions in cable-stayed beams. In *15th ASCE Engineering Mechanics Conferenc*, Columbia University, New York, 2-5 June, 2002.

C. Gentile, F. Martinez, and Y. y Cabrera. Dynamic performance of twin curved cable-stayed bridges. *Earthquake Engineering and Structural Dynamics*, 33:15–34, 2004. DOI: 10.1002/eqe.332.

R. Ghanem and M. Shinozuka. Structural-system identification Theory. *Journal of Engineering Mechanics*, 121:255–264, 1995.

D F. Giraldo, W. Song, S. J. Dyke, and J. M. Caicedo. Modal identification through ambient vibration Comparative study. *Journal of Engineering Mechanics*, 135: 759–770, 2009.

G.M.L. Gladwell. *Inverse Problems in Vibration*. Springer, Dordrecht, 1986.

P. Glendinning and M. Proctor. Travelling waves with spatially resonant forcing: bifurcations of a modified landau equation. *International Journal of Bifurcation and Chaos*, 3 (6):1447 – 1455, 1986.

J. Guckenheimer and P. Holmes. *Nonlinear Oscillations, Dynamical Systems, and Bifurcation of Vector Fields*. Springer-Verlag, New York, 1983.

R. Guyan. Reduction of stiffness and mass matrices. *AIAA Journal*, 3(2):380–380, 1965.

P. Hagedorn and J. Wallaschek. On equivalent harmonic and stochastic linearization. In *On equivalent harmonic and stochastic linearization*, page 2332, Berlin, 1987.

M.N. Hamdan and N.H. Shabaneh. On the large amplitude free vibrations of a restrained uniform beam carrying an intermediate lumped mass. *Journal of Sound and Vibration*, 199 (5):711–736, 1997.

J.K. Hammond and T.P. Waters. Signal processing for experimental modal analysis. *Philosophical Transactions of the Royal Society of London, Series A: Mathematical, Physical and Engineering Sciences*, 359:4159, 2001.

J.K. Hammond and P.R. White. The analysis of non-stationary signals using timefrequency methods. *Journal of Sound and Vibration*, 190:419447, 1996.

A. Hassan and T.D. Burton. Extraneous solutions predicted by the harmonic balance method. *Journal of Sound and Vibration*, 182:523–538, 1995.

T.K. Hasselman, M.C. Anderson, and W.G. Gan. Principal component analysis for nonlinear model correlation. In *Proceedings of the 16th International Modal Analysis Conference*, page 644651, Santa Barbara, 1998.

F.M. Hemez and S.W. Doebling. Review and assessment of model updating for non-linear, transient dynamics. *Mechanical Systems and Signal Processing*, 15:4574, 2001.

W. Heylen, S. Lammens, and P. Sas. *Modal Analysis Theory and Testing*. KUL Press, Leuven, 1997.

Y. Hikami. Rain vibration of stayed bridges. *Journal of Wind Engineering*, 27 (3): 23–34, 1986.

HIVOSS. Human induced vibrations of steel structures. Technical report, Research fund for Coal & Steel, 2008.

A.L. Hof, M.G.J. Gazendam, and W.E. Sinke. The condition for dynamic stability. *J Biomech*, 38:18, 2005.

A.L. Hof, R.M. van Bockel, T. Schoppen, and K. Postema. Control of lateral balance in walking: experimental findings in normal subjects and above-knee amputees. *Gait Posture*, 25:250258, 2007.

N.E. Huang, Z. Shen, S.R. Long, M.C. Wu, H.H. Shih, Q. Zheng, N.C. Yen, C.C. Tung, and H.H. Liu. The empirical mode decomposition and the hilbert spectrum for non-linear and non-stationary time series analysis. In *Proceedings of the Royal Society of London Series AMathematical, Physical and Engineering Sciences*, volume 454, page 903995, 1998.

S. R. Ibrahim and E. C. Mikulcik. A method for the direct identification of vibration parameters from the free response. *The Shock and Vibration Bulletin*, 183:183–198, 1977.

FIP Industriale. Ponte del mare a pescara. smorzatori viscoelastici. certificati di collaudo. internal report (in italian). Technical report, Selvazzano Dentro (PD), 2009.

H.M. Irvine and T.K. Caughey. The linear theory of free vibrations of a suspended cable. *Proc. R. Soc. London*, Ser. A 341:299–315, 1974.

H.M. Irvine and J.H. Griffin. On the dynamic response of a suspended cable. *Earthquake Eng. Struct. Dyn.*, 4:389402, 1976.

G.H. James, G.T. Carne, and J.P. Lauffer. The natural excitation tecnique next for modal parameter extraction from operating structures. *Modal Analysis*, 10:260–277, 1995.

D. Janjic. Structural analysis of the sutong bridge. `http://www.bentley.com/BrIM`.

D.S. Johnson, C.R. Aragon, L.A. McGeoch, and C. Schevon. Optimization by simulated annealing: an experimental evaluation. part i: graph partitioning. *Operations Research*, 37:865892, 1989.

E.A. Johnson, R.E. Christenson, and B.F. Spencer Jr. Semiactive damping of cables with sag. *Computer Aided Civil and Infrastructure Engineering*, 18(2):132146, 2003.

A.J. Jones, R.T. and. Pretlove and R. Eyre. Two case studies in the use of tuned vibration absorbers on footbridges. *The Structural Engineer*, 59B(2):27–32, 1981.

D.W. Jordan and P. Smith. *Nonlinear Ordinary Differential Equations*. Oxford University Press Inc, New York, 4 edition, 2007.

J. N. Juang. and R. S. Pappa. An eigensystem realisation algorithm era for modal parameter identification and modal reduction. In *NASA/JPL Workshop on Identification and Control of Flexible Space Structures*, 1984.

A. Juditsky, H. Hjalmarsson, A. Beneviste, B. Delyon, L. Ljung, J. Sjo berg, and Q. Zhang. Nonlinear black-box models in system identification: mathematical foundations. *Automatica*, 31:17251750, 1995.

H. Kauderer. *Nichtlinear Mechanik*. Springer-Verlag, Berlin, 1958.

A.A. Khan and N.S. Vyas. Non-linear parameter using volterra and wiener theories. *Journal of Sound and Vibration*, 221:805–821, 1999.

S.B. Kim and E.J. Powers. Frequency-domain volterra kernel estimation via higher-order statistical signal processing. *IEEE Transactions on Signal Processing*, pages 446–450, 1993.

S. Kirkpatrick, C.D. Gelatt, and M.P. Vecchi. Optimization by simulated annealing. *Science*, 1(220):671–680, 1983.

R. Kiviluoma. Coupled-mode buffeting and flutter analysis of bridges. *Computer & Structures*, 70:219–228, 1998.

M. Kominek. The marian bridge, czech republic. *Structural Engineering International*, 8(4):283284, 1998.

E.B. Kosmatopoulos, A.W. Smyth, S.F. Masri, and A.G. Chassiakos. Robust adaptive neural estimation of restoring forces in nonlinear structures. *Journal of Applied Mechanics*, 68:880893, 2001.

P. Koukoulakis and N. Kalouptsidis. Second-order volterra system identification. *IEEE Trans. on Signal Processing*, 48(12):3574–3577, 2000.

P. Koukoulas and N. Kalouptsidis. Second-order volterra system identification. *IEEE Transactions on Signal Processing*, 48:3574–3577, 2000.

S. Kumarasena, N.P. Jones, P. Irwin, and P. Taylor. Wind induced vibration of stay cables. Technical Report RI98-034 RDT05-004, Federal Highway Administration, McLean, Virginia, 2005.

Y. Kuramoto. *Chemical Oscillations, Waves, and Turbulence*. Dover Publications, Mineola, New York, 2000.

I.J. Leontaritis and S.A. Billings. Input-output parametric models for nonlinear systems, part i deterministic nonlinear systems. *International Journal of Control*, 41: 303328, 1985a.

I.J. Leontaritis and S.A. Billings. Input-output parametric models for nonlinear systems, part ii stochastic nonlinear systems. *International Journal of Control*, 41: 329344, 1985b.

G.V. Levina and A.A. Nepomnyaschiy. Analysis of an amplitude equation for autovibrational flow regimes at resonance external forces. *Zeitschrift fr angewandte Mathematik und Mechanik*, 66 (6):241–246, 1986.

J. S. Lew, J. N. Juang, and R. W. Longman. Comparison of several system identification methods for flexible structures. *Journal of Sound and Vibration*, 1673:461–480, 1993.

Y.C. Liang, D.P. Feng, and J.E. Cooper. Identification of restoring forces in non-linear vibration systems using fuzzy adaptive neural networks. *Journal of Sound and Vibration*, 242:4758, 2001.

Liu. *Wind Engineering: A Handbook for structural Engineers*. Prentice Hall, New Jersey, 1991.

H. Liu, T. Vinh, T. Chouychai, and M. Djouder. Second order transfer function: computation and physical interpretation. In *Proceedings of the 5th International Modal Analysis Conference*, London, 1987.

L. Ljung. *System identification theory*. Prentice Hall, 1999.

C. H. Loh, C. Y. Lin, and C. C. Huang. Time domain identification of frames under earthquake loadings. *Journal of Engineering Mechanics*, 1267:693–703, 2000.

A. Luongo, G. Rega, and F. Vestroni. Planar non-linear free vibrations of an elastic cable. *Int. J. Non-Linear Mech.*, 19:39–52, 1984.

J.H.G. Macdonald. Lateral excitation of bridges by balancing pedestrians. *Proceedings of the Royal Society A*, 2008. doi:10.1098/rspa.2008.0367.

J.H.G. Macdonald and W.E. Daniell. Variation of modal parameters of a cable-stayed bridge identified from ambient vibration measurements and fe modeling. *Engineering Structures*, 27:19161930, 2005.

N. M. M. Maia and J. M. M. Silva. *Theoretical and experimental modal analysis*. Research Studies Press LTD, 1998.

M. Malanka, B. Sapiski, and J. Snamina. Experimental study of vibration control of a cable with an attached mr damper. *Journal of Theoretical and Applied Mechanics*, 45 (4):893–917, 2007.

L. Marcheggiani and S. Lenci. On a model for the pedestrians-induced lateral vibrations of footbridges. *Meccanica*, 45:531551, 2010.

S. F. Masri, H. Sassi, and T.K. Caughey. Nonparametric identification of early arbitrary nonlinear system. *J. Appl. Mech. ASME*, 49:619–628, 1982.

M. Matsumoto, N. Shiraishi, and H. Shirato. Rain/wind-induced vibration of cables of cablestayed bridges. In *Proceedings of the 8th International conference on Wind Engineering*, London, 1992.

Y. Matsumoto, T. Nishioka, H. Shiojiri, and K. Matsuzaki. Dynamic design of footbridges. In *Proceedings IABSE*, Zurich, Switzerland, 1978.

C. Menn. The place of aesthetics in bridge design. *Structural Engineering International*, 6(2):93–95, 1996.

S. Meyer, M. Weiland, and M. Link. Modelling and updating of local non-linearities using frequency response residuals. *Mechanical Systems and Signal Processing*, 17:219226, 2003.

C. Minas and D. Inman. Correcting finite element models with measured modal results using eigenstructure assignment methods. In *Proceedings of the 6th International Modal Analysis Conference*, volume 2, pages 583–587, 1988.

M. Molinari. *Model updating of a steel-concrete composite MR frame structure under severe seismic loading via forced dynamic tests*. PhD thesis, University of Trento, 2007.

M. Molinari, A.T. Savadkoohi, O.S. Bursi, M.I. Friswell, and D. Zonta. Damage identification of a 3d full scale steel-concrete composite structure with partial-strength joints at different pseudo-dynamic load levels. *Earthquake Engineering Structural Dynamics*, 38:1219–1236, 2009.

S. Nakamura. Model for lateral excitation of footbridges by synchronous walking. *Journal of Structural Engineering*, 2004. doi: 10.1061/(ASCE)0733-9445(2004)130:1(32).

S. Nakamura and Y. Fujino. Lateral vibration on a pedestrian cable-stayed bridge. *Structural Engineering International*, 12(4):295300, 2002.

S. Nakamura and T. Kawasaki. Lateral vibration of footbridges by synchronous walking. *Journal of Constructional Steel Research*, 62:1148–1160, 2006.

S. Nakamura and T. Kawasaki. A method for predicting the lateral girder response of footbridges induced by pedestrians. *Journal of Constructional Steel Research*, 65: 1705–1711, 2009.

S. Nakamura, T. Kawasaki, H. Katsuura, and K. Yokoyama. Experimental studies on lateral forces induced by pedestrians. *Journal of Constructional Steel Research*, 64:247–252, 2008.

H.G. Natke, G.R. Tomlinson, and J.T. Yao. *Safety Evaluation Based on Identification Approaches*. Vieweg & Sohn, Braunschweig/Wiesbaden, 1993.

A.H. Nayfeh and D.T. Mook. *Nonlinear Oscillations*. John Wiley & Sons, Inc., New York, 1995.

A.S. Nazmy and A.M. Abdel-Ghaffar. Nonlinear earthquake response analysis of long span cable-stayed bridges: Theory. *Earthquake Engineering & Structural Dynamics*, 19:45–62, 1990.

D.E. Newland. Ridge and phase identification in the frequency analysis of transient signals by harmonic wavelets. *Journal of Vibration and Acoustics*, 121:149155, 1999.

D.E. Newland. Pedestrian excitation of bridges - recent results. In *Proceedings of the Tenth International Congress on Sound and Vibration*, volume 3e (2), Stockholm, July 2003. IABSE.

D.E. Newland. Pedestrian excitation of bridges. *Proceedings of the Institution of Mechanical Engineers, Part C: Journal of Mechanical Engineering Science*, 218: 477–492, 2004. doi:10.1243/095440604323052274.

D. Nyawako and P. Reynolds. Technologies for mitigation of human-induced vibrations iin civil engineering structures. *The Shock and Vibration Digest*, 39(6):465–493, 2007.

J. O'Callahan. A new procedure for and improved reduced system irs. In *IMAC VII*, Las Vegas, 1989.

J. O'Callahan, P. Avitabile, and R. Riemer. System equivalent reduction expansion process serep. In *IMAC VII*, Las Vegas, 1989.

M.E. Ozer, H.N. Ven, T.J. Ozgu, and Royston. Identification of structural nonlinearities using describing functions and shermanmorrison method. In *Proceedings of the 23rd International Modal Analysis Conference*, Orlando, 2005.

B.M. Pacheco, Y. Fujino, and A. Sulekh. Estimation curve for modal damping in stay cables with viscous damper. *Journal of Structural Engineering*, 119(6):1961–79, 1993.

G. Palm and T. Poggio. The volterra representation and the wiener expansion: validity and pitfalls. *SIAM Journal on Applied Mathematics*, 33(2)., 1977.

B. Peeters and G. DeRoeck. Reference-based stochastic subspace identification for output-only modal analysis. *Mechanical Systems and Signal Processing*, 13:855–878, 1999.

J.C. Peyton Jones and S.A. Billings. Recursive algorithm for computing the frequency response of a class of non-linear difference equation models. *International Journal of Control*, 50:1925–1940, 1989.

R.S. Phelan, P.P. Sarkar, and K.C. Mehta. Full-scale measurements to investigate rain–wind induced cable-stay vibration and its mitigation. *Journal of Bridge Engineering*, 11(3), 2006. DOI: 10.1061/ ASCE 1084-0702 2006 11:3 293.

G. Piccardo and F. Tubino. Parametric resonance of flexible footbridges under crowd-induced lateral excitation. *Journal of Sound and Vibration*, 311 (1-2):353–371, 2008.

A. Pikowski, M. Rosenblum, and J. Kurths. *Synchronization. A universal concept in nonlinear sciences*. Cambridge University Press, Cambridge, UK, 1 edition, 2001.

R. Pimentel, A. Pavic, and P. Waldron. Vibration performance of footbridges established via modal testing. In *IABSE Symposium: Structures for the Future–The Search for Quality*, volume 209, pages 602–609, Rio de Janeiro, Brazil, 25-27 August 1999. IABSE.

A.J. Pretlove and J.H. Rainer. *Human response to vibrations. In: Vibration Problems in Structures: Practical Guidelines,*, page Appendix I. Birkhuser Verlag, Basel, Switzerland, 1995.

M.B. Priestley. Power spectral analysis of nonstationary processes. *Journal of Sound and Vibration*, 6:8697, 1967.

R.H. Rand. Lecture notes on nonlinear vibrations, version 52. 2005.

C. Rebelo, E. Julio, H. Varum, and A. Costa. Cable tensioning control and modal identification of a circular cable-stayed footbridge. *Experimental Techniques*, 2010. doi: 10.1111/j.1747-1567.2009.00539.x.

G. Rega. Nonlinear vibrations of suspended cables. part i: modeling and analysis. *J. Appl. Mech. Rev.*, 57:443–478, 2004a.

G. Rega. Nonlinear vibrations of suspended cables. part ii: deterministic phenomena. *J. Appl. Mech. Rev.*, 57:479–514, 2004b.

W-X. Ren and Z-H. Zong. Output-only modal parameter identification of civil engineering structures. *Structural Engineering and Mechanics*, 17(3-4):00, 2004.

E. Reynders, R. Pintelon, and G. De Roeck.

F. Ricciardelli and A.D. Pizzimenti. Experimental evaluation of the dynamic lateral loading of footbridges by walking pedestrians. In *Proceedings Eurodyn*, 2005.

F. Ricciardelli and A.D. Pizzimenti. Lateral walkinginduced forces on footbridges. *Journal of Bridge Engineering*, 12 (6):677688, 2007.

R. Le Riche, D. Gualandris, J.J. Thomas, and F.M. Hemez. Neural identification of non-linear dynamic structures. *Journal of Sound and Vibration*, 248:247265, 2001.

A. Rito. Aesthetics and bridge design. *Structural Engineering International*, 6(2): 91–92, 1996.

Rosenberg R.M. On nonlinear vibrations of systems with many degrees of freedom. *Advances in Applied Mechanics*, 9:155242, 1966.

J.B. Roberts and P.D. Spanos. *Random Vibrations and Statistical Linearization*. Wiley, New York, 1990.

T.M. Roberts. Lateral pedestrian excitation of footbridges. *Journal of Bridge Engineering*, 10 (1):107–112, 2005.

E.J. Routh. *The Advanced Part of a Treatise on the Dynamics of a System of Rigid Bodies*. Dover Publ., New York, 6 edition, 1955.

F.R. Rutz and K.L. Rens. Wind loads for 19th century bridges: Design evolution, historic failures, and modern preservation. *Journal of Performance of Constructed Facilities*, 21(2), 2007. DOI: 10.1061/ ASCE 0887-3828 2007 21:2 157.

E Safak. Identification of linear structures using discrete-time filters. *Journal of Structural Engineering*, 11710:3064–3085, 1991.

E Safak and M. Celebi. Seismic response of transamerica building. ii: System-identification. *Journal of Structural Engineering*, 1178:2405–2425, 1991.

R.H. Scanlan. Problematics in formulation of wind force models for bridge decks. *Journal of Engineering Mechanics*, 119(7):1353–73, 1993.

R.P. Selvam and S. Govindaswamy. Aeroelastic analysis of bridge girder section using computer modeling. Technical report, Mack Blackwell Transportation Center, University of Arkanas, 2001.

Tarini M. J. Larsen A. Selvam, R. P. Computer modeling of flow around bridges using les and fem. *Journal of Wind Engineering and Industrial Aerodynamics*, 77-78: 643–651, 1998.

SETRA. Assessment of vibrational behaviour of footbridges under pedestrian loading. Technical report, service d'tudes techniques des routes et autoroutes, Paris, France, 2006.

B. Shih and I.G. Tadjbakhsh. Small-amplitude vibrations of extensible cables. *J. Eng. Mech. Div.*, 110:569576, 1984.

M. Shinozuka, C. B. Yum, and H. Imai. Identification of linear structural dynamic systems. *J. Engrg. Mech. Div., ASCE*, 1086:1371–1390, 1982.

E. Simiu and R.H. Scanlan. *Wind effects on Structures*. Wiley Interscience, New York, 3 edition, 1996.

SISTRAL. Rilievo delle forze di tiro nelle funi spiroidali. Technical Report PNP112/09, Sistemi di Ingegneria Strutturale Applicati, 2009.

T. Soderstrom and P. Stoica. *System Identification*. Prentice-Hall, Englewood Cliffs, 1989.

O. Le. Soize C., Fur. Modal identification of weakly non-linear multidimensional dynamical systems using a stochastic linearization method with random coefficients. *Mechanical Systems and Signal Processing*, 11:3749, 1997.

Y. Song, C.J. Hartwigsen, D.M. McFarland, A.F. Vakakis, and L.A. Bergman. Simulation of dynamics of beam structures with bolted joints using adjusted iwan beam elements. *Journal of Sound and Vibration*, 273:249276, 2004.

D Spina, C. Valente, and G.R. Tomlinson. A new procedure for detecting nonlinearity from transient data using gabor transform. *Nonlinear Dynamics*, 11:235254, 1996.

N. Srinil, G. Rega, and S. Chucheepsakul. Nonlinear interaction in the 3d free vibrations of horizontal and inclined sagged cables. In *Proc. 5th Int. Symp. Cable Dynamics*, volume 7784, Santa Margherita Ligure, AIM, Lie'ge, 7784, 2003.

N. Srinil, G. Rega, and S. Chucheepsakul. Three-dimensional nonlinear coupling and dynamic tension in the large amplitude free vibrations of arbitrarily sagged cables. *J. Sound Vib.*, 269:823–852, 2004.

M. Srinivas and L.M. Patnaik. Genetic algorithms a survey. *IEEE Computer Magazines*, pages 17–24, 1994.

W.J. Staszewski. Analysis of non-linear systems using wavelets. *Journal of Mechanical Engineering Science*, 214:13391353, 2000.

D.M. Storer. *Dynamic Analysis of Non-Linear Structures Using Higher Order Frequency Response Functions*. PhD thesis, University of Manchester, 1991.

D.M. Storer and G.R. Tomlinson. Higher order frequency response functions and their relation to practical structures. In *Proceedings of the 16th International Seminar on Modal Analysis*, Florence, Italy, 1991.

S.H. Strogatz. *Nonlinear dynamics and chaos, with applications to physics, biology, chemistry, and engineering*. Perseus Books, Cambridge, 2000.

S.H. Strogatz, D.M. Abrams, A. McRobie, B. Eckhardt, and E. Ott. Crowd synchrony on the millennium bridge. *Nature*, 438:43–44, 2005.

L. Sun and X. Yuan. Study on pedestrian-induced vibration of footbridge. In *Footbridge 2008, Third International Conference*, Porto, Portugal, 2008.

H. Tabatabai and A.B. Mehrabi. Design of mechanical viscous dampers for stay cables. *Journal of Bridge Engineering*, 5(2), 2000.

K. Takahashi and Y. Konishi. Non-linear vibration of cables in three dimensions: Part i: non-linear free vibrations. *Journal of Sound and Vibration*, 118:69–84, 1987.

K. Takenouchi. Single pylons for curved cable-stayed bridges. *Structural Engineering International*, 8(4):269272, 1998.

I. Tawfiq and T. Vihn. Contribution to the extension of modal analysis to non-linear structures using volterra functional series. *Mechanical Systems and Signal Processing*, 17:379–407, 2003.

L.J. Tick. The estimation of transfer functions of quadratic system. *Technometrics*, 3: 563–567, 1961.

S. Tinazzi. Generazione di storie di vento turbolento e analisi dinamica strutturale di un ponte ciclo-pedonale strallato. Master's thesis, University of Trento, 2009.

N. Tondini, A. Bonelli, S. Santini, and T. Dusatti. Dynamic behaviour of steel footbridges: the "ponte del mare" case study. *Costruzioni Metalliche*, 2010.

A. Trovato, S. Erlicher, and Argoul P. A modified van der pol oscillator for modelling the lateral force of a pedestrian during walking. In *Proceeding of the Conference "Vibrations, Chocs & Bruit*, Lyon, France, 2008.

A. Trovato, S. Erlicher, and Argoul P. Modeling the lateral pedestrian force on rigid and moving floors by a self-sustained oscillator. In *Proceeding of the International Conference COMPDYN 2009*, Island of Rhodes, Greece, June 2009.

L. F. Troyano, J. M. Armisen, and M. A. A. Suarez. The inclined towers of the ebro and lerez bridge. *Structural Engineering International*, 8(4):258260, 1998.

A.F. Vakakis. Non-linear normal modes and their applications in vibration theory: an overview. *Mechanical Systems and Signal Processing*, 11:322, 1997.

P. Van Overschee and B. De Moor. *Subspace identification for linear systems: theory implementation applications*. Kluwer Academic Press, Dordrecht, The Netherlands, 1996.

C.L. Vaughan. Theories of bipedal walking: an odyssey. *J Biomech*, 36:513523, 2003.

J. A. Vazquez Feijoo, K. Worden, and R. Stanway. System identification using associated linear equations. *Mechanical Systems and Signal Processing*, 18(3):431–455, 2004.

F. Venuti and L. Bruno. Crowd-structure interaction in lively footbridges under synchronous lateral excitation: A literature review. *Physics of Life Reviews*, 6:176206, 2009.

F. Venuti and L. Bruno. Pedestrian loads and dynamic performances of lively footbridges: an overview on measurement techniques and codes of practice. In *Load Capacity and Bridge Performance*, Roma, 2010.

F. Venuti, L. Bruno, and N. Bellomo. Crowd dynamics on a moving platform: Mathematical modelling and application to lively footbridges. *Math Comput Model*, 45: 252269, 2007.

M. Virlogeux. Recent evolution of cable-stayed bridges. *Engineering Structures*, 21: 737755, 1993.

H. Vold, J. Kundrat, G. T. Rocklin, and R. Russell. A multi-input modal estimation algorithm for mini-computers. *SAE Paper*, (820194), 1982.

V. Volterra. *Theory of Functionals and Integral equations*. Dover Publications, New York, 1959.

L. Wang, J. Zhang, C. Wang, and S. Hu. Time-frequency analysis of nonlinear systems: the skeleton linear model and the skeleton curves. *Journal of Vibration and Acoustics*, 125:170177, 2003.

P. Warnitchai, Y. Fujino, and T. Susumpow. A non-linear dynamic model for cables and its application to a cable-structure system. *Journal of Sound and Vibration*, 187 (4):695–712, 1995.

F. Weber, G. Feltrin, and O. Huth. Guidelines for structural control. Technical Report F05, SAMCO, Dbendorf, Switzerland, 2006.

F.S. Wei. Structural dynamic model improvement using vibration test data. *AIAA Journal*, 28:175–177, 1990.

R.H. Wood. Some notes on vibrations in structures. *The Journal of Royal Institute of British Architects*, 55(12):553–555, 1948.

K. Worden and G. Manson. Random vibrations of a duffing oscillator using the volterra series. *Journal of Sound and Vibration*, 217:781–789, 1998.

K. Worden and G. Manson. Random vibrations of a multi-degree-of-freedom non-linear system using the volterra series. *Journal of Sound and Vibration*, 226:397–405, 1999.

K. Worden and G.R. Tomlinson. *Nonlinearity in Structural Dynamics: Detection, Identification and Modelling*. IOP Publishing Ltd, New York, 1 edition, 2001.

K. Worden, G. Kerschen, A.F. Vakakis, and J.C. Golinval. Nonlinear system identification in structural dynamics: A short history. In *Proceedings of IMAC XXV*, Orlanddo, 2007.

J. Wray and G.G.R. Green. Calculation of the volterra kernels of nonlinear dynamic systems using an artificial neural network. *Biological Cybernetics*, 71:187–195, 1994.

W.J. Wu, C.S. Cai, and S.R. Chen. Experiments on reduction of cable vibration using mr dampers. In *17th ASCE Engineering Mechanics Conference*, Newark, DE, June 13-16 2004.

J.I. Xiaodong, Q. Jiaru, and X.U. Longhe. Experimental study of modal parameter identification in a simulated ambient-excited structure. *Front. Archit. Civ. Eng. China*, 1(3):281285, 2007.

H. Yamaguchi and Y. Fujino. Stayed cable dynamics and its vibration control. In *Proc. of the International Symposium on Advances in Bridge Aerodynamics*, Copenhagen, 1999.

H Yamaguchi and M. Ito. Mode-dependence of structural damping in cable-stayed bridges. *Journal of Wind Engineering and Industrial Aerodynamics*, 72:289–300, 1997.

J.N. Yang, Y. Lei, S.W. Pan, and N. Huang. System identification of linear structures based on hilberthuang spectral analysis; part 1: Normal modes. *Earthquake Engineering and Structural Dynamics*, 32:14431467, 2003a.

J.N. Yang, Y. Lei, S.W. Pan, and N. Huang. System identification of linear structures based on hilberthuang spectral analysis; part 2: Complex modes. *Earthquake Engineering and Structural Dynamics*, 32:15331554, 2003b.

Lin S. Yang J.N. Hilberthuang based approach for structural damage detection. *Journal of Engineering Mechanics*, 32:1308595, 2004.

K. Yasuda, S. Kawamura, and K. Watanabe. Identification of nonlinear multi-degree-of-freedom systems presentation of an identification technique. *JSME International Journal Series III*, 31:814, 1988.

Z. Yu and Y.L. Xu. Non-linear vibration of cable-damper systems part i: formulation. *Journal of Sound and Vibration*, 225 (3):447–463, 1999.

Beck J.L. Yuen, K-V. and L.S. Katafygiotis. Probabilistic approach for modal identification using non-stationary noisy response measurements only. *Earth. Eng. Struc. Dyn.*, 314:1007–1023, 2002.

A. Zasso, M. Belloli, and S. Muggiasca. Wind tunnel study on the pescara footbridge. In *FACWE 5*, Florence, Italy, July 19-23 2009.

H.P. Zeiger and A.J. McEwen. Approximate linear realisations of given dimension via ho's algorithm. *IEEE Transactions on Automatic Control*, 19(2):153, 1974.

N. Zhang. Dynamic condensation of mass and stiffness matrices. *Journal of Sound and Vibration*, 188(4):601–615, 1995.

Q.W. Zhang, T.Y.P. Chang, and C.C. Chang. Finite element model updating for the kap shui mun cable-stayed bridge. *Journal Bridge Engineering*, 6(4):285–293, 2001.

G Zheng, J. M. Ko, and Y. Q. Ni. Super-harmonic and internal resonances of a suspended cable with nearly commensurable natural frequencies. *Nonlinear Dynamics*, 30:55–70, 2002.

S. Zivanovic, A. Pavic, and P. Reynolds. Vibration serviceability of footbridges under human-induced excitation a literature review. *Journal of sound and vibration*, 279(1-2):1–74, 2005.

S. Zivanovic, A. Pavic, and P. Reynolds. Finite element modelling and updating of a lively footbridge The complete process. *Journal of sound and vibration*, 301(1-2): 126–145, 2007.

D. Zuo and N.P. Jones. Stay-cable vibration monitoring of the fred hartman bridge (houston, texas) and the veterans memorial bridge (port arthur, texas). Technical Report FHWA/TX-06/0-1401-2, Federal Highway Administration, McLean, Virginia, 2005.